



**HAL**  
open science

# Mechanical and Materials Development of Radio-Frequency Contact for the ITER Ion Cyclotron Resonance Heating Antenna

Zhaoxi Chen

► **To cite this version:**

Zhaoxi Chen. Mechanical and Materials Development of Radio-Frequency Contact for the ITER Ion Cyclotron Resonance Heating Antenna. Electromagnetism. l'Université Toulouse 3 - Paul Sabatier, 2018. English. NNT: . tel-02052920

**HAL Id: tel-02052920**

**<https://cea.hal.science/tel-02052920>**

Submitted on 28 Feb 2019

**HAL** is a multi-disciplinary open access archive for the deposit and dissemination of scientific research documents, whether they are published or not. The documents may come from teaching and research institutions in France or abroad, or from public or private research centers.

L'archive ouverte pluridisciplinaire **HAL**, est destinée au dépôt et à la diffusion de documents scientifiques de niveau recherche, publiés ou non, émanant des établissements d'enseignement et de recherche français ou étrangers, des laboratoires publics ou privés.



# THÈSE

## En vue de l'obtention du DOCTORAT DE L'UNIVERSITÉ DE TOULOUSE

Délivré par l'Université Toulouse 3 - Paul Sabatier

---

Présentée et soutenue par

**Zhaoxi CHEN**

Le 6 novembre 2018

### Développement d'un contact Haute-Fréquence pour les antennes à Résonance Cyclotronique Ionique d'ITER : validation mécanique et matériaux

---

Ecole doctorale : **SDM - SCIENCES DE LA MATIERE - Toulouse**

Spécialité : **Sciences et Génie des Matériaux**

Unité de recherche :

**CIRIMAT - Centre Interuniversitaire de Recherche et d'Ingénierie des  
Matériaux**

Thèse dirigée par

**Viviane TURQ et Julien HILLAIRET**

Jury

Mme Cécile LANGLADE, Rapporteur  
M. Mauro TABORELLI, Rapporteur  
M. Jean DENAPE, Examineur  
M. Olivier PASCAL, Examineur  
M. Philippe DJEMIA, Examineur  
Mme Viviane TURQ, Directeur de thèse









# THÈSE

## En vue de l'obtention du DOCTORAT DE L'UNIVERSITÉ DE TOULOUSE

Délivré par l'Université Toulouse 3 - Paul Sabatier

---

Présentée et soutenue par

**Zhaoxi CHEN**

Le 6 novembre 2018

**Mechanical and Materials Development of Radio-Frequency  
Contact for the ITER Ion Cyclotron Resonance Heating Antenna**

---

Ecole doctorale : **SDM - SCIENCES DE LA MATIERE - Toulouse**

Spécialité : **Sciences et Génie des Matériaux**

Unité de recherche :

**CIRIMAT - Centre Interuniversitaire de Recherche et d'Ingénierie des  
Matériaux**

Thèse dirigée par

**Viviane TURQ et Julien HILLAIRET**

Jury

Mme Cécile LANGLADE, Rapporteur  
M. Mauro TABORELLI, Rapporteur  
M. Jean DENAPE, Examineur  
M. Olivier PASCAL, Examineur  
M. Philippe DJEMIA, Examineur  
Mme Viviane TURQ, Directeur de thèse



## **Acknowledgment**

First of all, I would like to express my sincere thanks to my thesis director Dr. Viviane TURQ and thesis supervisor Dr. Julien HILLAIRET, who were providing their enthusiastic help during the past three years. Dr. Viviane TURQ and Dr. Julien HILLAIRET are knowledgeable experts in tribology and RF engineering. With their patient guidance, I enriched my knowledge in material science and finished my Ph.D. study in material field successfully. For me, they are more than my thesis director and supervisor, they are also my mentors of life. The research and working attitude that I learned from them will benefit me all my life. It's really my honor to be their Ph.D. student.

I would like to show my special thanks to Prof. Yuntao SONG, who is my master director and the co-director of ASIPP-CEA associated laboratory. Without his help, I may have no chance to study and work in CEA and ITER. I was deeply infected and inspired by his passion for work. Prof. SONG can always give me constructive suggestions and encourage me to conquer difficulties.

I would like to thank Dr. Caroline HERNANDEZ, Mr. Karl VULLIEZ who had the first discussion about material characterization with me and helped me to make the test planning for my first-year study. Their encouragement during these years is really important for me to finish my Ph.D. study successfully.

I would like to sincerely thank the two thesis reviewers Prof. Cécile LANGLADE and Dr. Mauro TABORELLI and jury members: Prof. Jean DENAPE, Prof. Olivier PASCAL and Prof. Philippe DJEMIA, thanks for their time and carefully review work towards my thesis. The thesis was improved significantly based on their useful comments.

I would like to acknowledge the laboratory, department and group heads: Dr. Alain BECOULET, Mr. Philippe MAGAUD, Mr. Jean-Michel BERNARD, and Dr. Tuong HOANG. Especially Mr. Jean-Michel BERNARD and Dr. Tuong HOANG, they made a lot of effort for the funding application of my Ph.D. subject and my future career after my Ph.D. graduation.

I am grateful to all the colleagues who were working with me during these three years at CEA, CIRIMAT, ASIPP and LICP: Xiaolan ZOU, Gilles LOMBARD, Patrick MOLLARD, Robert VOLPE, Walid HELOU, Fabien FERLAY, Raphael LALOO, Pierre-Louis TABERNA, Julien WAGNER, Sandrine DULUARD, Marie-Claire BARTHELEMY, Benjamin DUPLOYER, Jean-Jacques DEMAI, Hui SHAO, Kun LU, Qingxi YANG, Yong CHENG, Xuebing PENG, Prof. Peng WANG and Li QIAO.

## Acknowledgement

---

Last but not least, I would like to express my deepest thanks to my parents, my three sisters and my girlfriend, thanks for their permanent love, understanding and unreserved support.

20/12/2018

CEA, Cadarache

## **Acronyms**

AC: Alternating Current

AE: Acoustic Emission

a-C: amorphous Carbon

CoF: Coefficient of Friction

CTE: Coefficient of Thermal Expansion

CEA: Commissariat à l'énergie atomique et aux énergies alternatives

DC: Direct Current

DLC: Diamond-Like Carbon

EDS: Energy-Dispersive Spectrometer

FEM: Finite Element Method

FWHM: Full-Width at Half-Maximum

FM: Front Modules

FCC: Face-Centered Cubic

FFT: Fast Fourier Transform

GLC: Graphite-Like Carbon

HTC: Heat Transfer Coefficient

HRTEM: High-Resolution Transmission Electron Microscopy

HV-MTEST: Heatable Vacuum Material Tribological & Electrical Study Testbed

HCP: Hexagonal Close-Packed

IACS: International Annealed Copper Standard

ITER: International Thermonuclear Experimental Reactor

ICRH: Ion Cyclotron Resonance Heating

JET: Joint European Tokamak

LHC: Large Hadron Collider

LSV: Linear sweep voltammetry

OFHC: Oxygen-Free High Conductivity

PVD: Physical Vapor Deposition

PP: Port Plug

Rc: Contact Resistance

RVTL: Removable Vacuum Transmission Lines

RF: Radio-Frequency

SEM: Scanning Electron Microscopy

TSL: Turbiscan stability index

TL: Transmission Lines

TEM: Transmission Electron Microscopy

XPS: X-ray Photoelectron Spectroscopy

XRD: The X-ray Diffraction

## Résumé

L'objectif du projet ITER est de démontrer la faisabilité scientifique et technique de la fusion nucléaire à des fins énergétiques. Pour obtenir les réactions de fusion, un plasma chauffé à 150 millions de degrés doit être confiné par un champ magnétique de plusieurs teslas en quasi-continu. Pour obtenir ces températures, des antennes radiofréquences (RF) injectent des ondes électromagnétiques de forte puissance dans le plasma, en particulier entre 40 et 55 MHz aux fréquences de résonance cyclotron des ions. L'assemblage et la dilatation thermique en fonctionnement de ces antennes sont rendus possibles par des contacts électriques glissants. Ces contacts doivent supporter un courant RF crête de 2.25 kA en régime stationnaire, dans un environnement sous vide et pendant toute la durée de fonctionnement de l'antenne. De plus, les matériaux de ces contacts doivent être compatibles avec la température de 250°C utilisée pour l'étuvage de la machine pendant plusieurs milliers d'heures cumulées. Ces contacts RF sont donc des composants critiques pour les performances de l'antenne. Aucun contact électrique du commerce n'a jusqu'à présent été qualifié pour ces spécifications et un effort particulier a donc été porté dans le cadre de ce travail de thèse afin de développer une solution satisfaisante.

Le choix des matériaux et des revêtements utilisés pour ces contacts a fait l'objet de la première partie de cette étude. Pour ce faire, un modèle multi-physique tenant compte des paramètres RF, mécaniques et thermiques a été développé. À la suite de cette étude, des premiers couples de matériaux et de revêtements ont été sélectionnés. Les propriétés d'échantillons représentatifs ont été caractérisées par des mesures réalisées au laboratoire CIRIMAT avant et après un vieillissement thermique simulé.

Afin d'évaluer le comportement électrique et tribologique de ces paires de matériaux dans les conditions de fonctionnement d'ITER, un tribomètre sous vide a été spécifiquement conçu et utilisé pendant ce travail de thèse. Ce tribomètre permet de mesurer l'évolution du coefficient de frottement et de la résistance de contact entre deux échantillons en mouvement relatif linéaire, sous vide ( $10^{-5}$  Pa) et jusqu'à 350°C. Des couples d'échantillons de 316L/CuCrZr non revêtus ont été comparés à des couples revêtus d'argent et de rhodium ou d'or et de rhodium. La force normale de contact optimale a d'abord été déterminée par rapport à la résistance de contact et au coefficient de frottement. L'évolution dynamique de ces paramètres et la durée de vie des revêtements ont ensuite été mesurées sur le cycle de vie attendu des contacts de l'antenne ICRH d'ITER.

Enfin, la faisabilité d'une nouvelle méthode de lubrification compatible avec le vide a été développée à partir de revêtements composites or/nickel/carbone et or/cobalt/WS<sub>2</sub>.

Ces nouveaux revêtements ont été élaborés par des méthodes de dépôt en phase vapeur et d'électrodéposition respectivement. Leurs performances tribologiques ont été caractérisées dans des conditions représentatives de celles d'ITER.

**ABSTRACT**

Ion Cyclotron Resonance Heating (ICRH) is one of the most important plasma heating methods in magnetically confined fusion experiments. In ITER, two ICRH antennas are designed to supply 20 MW of Radio-Frequency (RF) power at 40-55 MHz to heat the plasma. RF sliding contacts are used in the antennas to allow their remote handling assembly and to improve their maintainability, as well as to absorb the thermal expansion of the RF conductors during operations. One of the RF contacts is designed to be operated at 2.25 kA in steady-state (1200 s), with a current density of 4.8 kA/m. With such current levels, high heating occurs at the contact area which threatens the structural and material safety of the RF contacts and constrain their life time. In addition, before operation of the ITER ICRH antennas, all the in-vessel structures will be baked at 250°C during thousands of cumulated hours for outgassing.

In CEA, R&D work on RF contact development has been carried out for 10 years. Recently, Ag-coated CuCrZr louvers RF contact prototype based on Multi-Contact LA-CUT commercial contact configuration was tested on TITAN test-bed. 1500 A, 1200 s steady-state operation was achieved. However, due to burn failure, the RF contact prototype couldn't reach 1200 s steady-state under 2 kA as expected. In order to improve the performances of the RF sliding contacts to match ITER requirements, failure mechanisms of RF contacts during RF operations were analyzed and possible materials or coated systems that can be used for RF sliding contacts compatible with the ITER environment have been studied in detail within this thesis work. The effects of material selection, cooling parameter and contact resistance on louvers temperature have been modelled and simulated through finite element methods.

Moreover, functional coatings like Ag, Au, Rh and their alloys were manufactured by electroplating on 316L and CuCrZr, which are commonly used as base materials on tokamak. By mimicking the ITER baking conditions, the coated samples were thermal aged under vacuum at 250°C for 500 h, after which the materials properties evolution such as hardness, grain size and adherence was characterized. In addition, the coating life time has been evaluated through cross-sectional diffusion characterizations.

In order to evaluate the electrical and tribological behavior of the coated material pairs, a dedicated and innovative test bed was designed during this thesis and used successfully. On this test bed the samples can be heated up to 350°C and the vacuum can reach  $10^{-5}$  Pa. Static contact resistance as well as transient contact resistance/friction coefficient of sliding pairs can be measured. Sliding and electrical tests of uncoated 316L/CuCrZr pair and coated pairs Ag/Rh and Au-Ni/Rh were

## ABSTRACT

---

carried out. The relationships between vacuum condition, temperature, contact force and the static contact resistance have been studied and an optimal contact force was selected. Under this optimal contact force, the sliding tests were launched and the evolutions of friction coefficient as well as contact resistance were analyzed. Through wear characterizations, the life times of the coatings were evaluated.

Finally, based on the first tribological results obtained on commercial Au-Ni and Au-Co alloy coatings, the feasibility of depositing solid lubricant containing Au-Ni and Au-Co composite coatings to minimizing wear and friction coefficient was evaluated. Au-Ni/a-C and Au-Co/WS<sub>2</sub> composite coatings were successfully developed by using magnetron sputtering and electroplating methods respectively. Their tribological performance under ITER relevant vacuum condition had been studied.

## Contents

Chapter 1	Context and objectives.....	1
1.1	Energy and nuclear fusion .....	1
1.1.1	Global Energy Situation .....	1
1.1.2	Nuclear fusion .....	1
1.2	ITER and ITER ICRH antenna.....	2
1.2.1	Magnetic confined fusion and Tokamak .....	2
1.2.2	ITER project .....	3
1.2.3	ITER ICRH antenna and RF contacts.....	4
1.2.3.1	Mechanical design of ICRH antenna .....	4
1.2.3.2	RF contact design specifications.....	5
1.2.3.3	RF contact design challenges.....	6
1.3	RF sliding contact development status .....	6
1.4	Research aims and objectives .....	8
Chapter 2	Coating deposition and characterization techniques.....	11
2.1	Coating deposition techniques.....	11
2.1.1	Overview .....	11
2.1.2	Electroplating .....	12
2.1.2.1	Faraday’s Law.....	12
2.1.2.2	Main factors that affect electroplating process .....	13
2.1.3	Magnetron sputtering deposition .....	14
2.2	Characterization techniques.....	14
2.2.1	3D optical profiler .....	15
2.2.2	SEM/EDS .....	15
2.2.3	TEM.....	16
2.2.4	Micro-scratch tester .....	17
2.2.5	Nanoindentation tester.....	18
2.2.6	Microharness tester.....	19
2.2.7	XRD.....	19

## Contents

---

2.2.8	XPS.....	20
2.2.9	Raman spectroscopy .....	21
2.3	Tribology of conductive contact.....	22
2.3.1	Electrical contact resistance.....	22
2.3.2	Friction and wear .....	26
2.3.2.1	Source of friction .....	26
2.3.2.2	Wear.....	26
2.3.2.3	Lubrication.....	28
2.4	Tribological study tools.....	30
2.4.1	Tribometer configuration and parameters .....	30
2.4.2	Ball on disc tribometers.....	31
2.4.3	Pin on plate ITER RF contact specific tribometer.....	32
2.4.3.1	System design .....	32
2.4.3.2	Modeling and simulations results .....	39
2.4.3.3	Calibration of the CoF measurement system .....	44
2.4.3.4	Precision Measurements .....	45
2.4.4	Overview of tribological test parameters.....	49
Chapter 3	Experimental study and failure analysis of Multi-Contact LA-CUT contact...	51
3.1	ITER RF sliding contact prototype design .....	51
3.1.1	RF sliding contact configuration selection .....	51
3.1.2	Base material selection for the RF contact .....	53
3.2	RF tests of LA-CUT prototype.....	54
3.2.1	T-Resonator Setup .....	55
3.2.2	RF Contact holder.....	56
3.2.2.1	RF contact holder design.....	56
3.2.2.2	Thermal-hydraulic analysis.....	57
3.2.3	LA-CUT prototype RF test results .....	61
3.2.4	LA-CUT RF contact failure analysis.....	63
3.2.5	LA-CUT RF contact operating temperature study .....	65

## Contents

---

3.2.5.1	Theoretical model .....	66
3.2.5.2	Finite element analysis model.....	67
3.2.5.3	Analysis procedure and results .....	67
3.3	Discussion.....	71
Chapter 4	Thermal stability, electrical and tribological characterization of coatings .....	73
4.1	Materials and samples preparation .....	73
4.1.1	Material selection .....	73
4.1.1.1	Au and Au alloys .....	74
4.1.1.2	Ag and Ag alloys .....	74
4.1.1.3	Rhodium.....	75
4.1.2	Sample manufacturing.....	75
4.1.3	Characterizations and sample preparation .....	76
4.1.3.1	Thermal aging process .....	76
4.1.3.2	Tests planning .....	77
4.2	Characterization results of thermal stability .....	78
4.2.1	Coating properties changes and diffusion with substrate .....	78
4.2.1.1	Au-Ni on CuCrZr .....	78
4.2.1.2	Ag-Sb on CuCrZr.....	86
4.2.1.3	Rh on CuCrZr .....	89
4.2.1.4	Rh on 316L .....	95
4.2.2	Diffusion between coatings .....	99
4.2.2.1	Au-Ni on CuCrZr vs. Rh on 316L .....	99
4.2.2.2	Au-Ni on CuCrZr vs. Rh on CuCrZr .....	100
4.2.2.3	Ag-Sb on CuCrZr vs. Rh on 316L .....	101
4.2.2.4	Ag-Sb on CuCrZr vs. Rh on CuCrZr .....	102
4.2.3	Discussion.....	102
4.3	Electrical/tribological characterizations under ITER relevant conditions .....	103
4.3.1	CuCrZr vs. 316L.....	103
4.3.1.1	Static contact resistance .....	103

## Contents

---

4.3.1.2	Evolution of Rc and CoF during sliding cycles .....	105
4.3.1.3	Wear surface morphology .....	106
4.3.2	Au-Ni on CuCrZr vs. Rh on 316L .....	107
4.3.2.1	Static contact resistance .....	107
4.3.2.2	Evolution of Rc and CoF during sliding cycles .....	108
4.3.2.3	Wear surface morphology .....	108
4.3.3	Au-Ni on CuCrZr vs. Rh on CuCrZr .....	110
4.3.3.1	Evolution of Rc and CoF during sliding cycles .....	110
4.3.3.2	Wear surface morphology .....	111
4.3.4	Ag on CuCrZr vs. Rh on 316L .....	112
4.3.4.1	Static contact resistance .....	112
4.3.4.2	Evolution of Rc and CoF during sliding cycles .....	112
4.3.4.3	Wear surface morphology .....	113
4.3.5	Ag on CuCrZr vs. Rh on CuCrZr .....	114
4.3.5.1	Evolution of Rc and CoF during sliding cycles .....	114
4.3.5.2	Wear surface morphology .....	114
4.3.6	Discussion.....	115
Chapter 5	Self-lubricating coating development.....	117
5.1	Au-Ni/a-C deposition and coating characterizations .....	117
5.1.1	Magnetron sputtering process of Au-Ni/a-C .....	117
5.1.2	Coating characterizations .....	118
5.1.2.1	Surface morphology .....	118
5.1.2.2	Coating composition and crystal structure .....	119
5.1.2.3	Mechanical performance.....	123
5.1.2.4	Electrical performance .....	126
5.1.2.5	Tribological performance.....	127
5.1.3	Summary.....	128
5.2	Au-Co/WS <sub>2</sub> deposition and coating characterizations.....	129
5.2.1	Electroplating process of Au-Co/WS <sub>2</sub> .....	129

## Contents

---

5.2.1.1	Ni interlayer plating .....	129
5.2.1.2	Au-Co/WS <sub>2</sub> plating .....	133
5.2.2	Coating characterizations .....	140
5.2.2.1	Coating composition .....	140
5.2.2.2	Coating morphology and topography .....	141
5.2.2.3	Crystal structure .....	144
5.2.2.4	Tribological performance.....	145
5.2.2.5	Summary .....	148
5.3	Tribological performance comparison of different coatings .....	149
5.4	Discussion.....	150
Chapter 6	Conclusions and prospect .....	153
6.1	Conclusions of this thesis .....	153
6.2	Future work .....	155
References	.....	157
Appendix A: HV-MTEST Plotting Methods	.....	173
Appendix B: Binary phase diagram	.....	175
Appendix C: Investigation of the generation of the top layer	.....	181
Publications:	.....	183

## Contents

---

## Chapter 1 Context and objectives

### 1.1 Energy and nuclear fusion

#### 1.1.1 Global Energy Situation

Energy sources are fundamental for human society and the global energy consumption is increasing rapidly nowadays. Currently, available world energy resources are based mostly on fossil fuels such as coal, oil and gas. However, as un-renewable sources, fossil fuels can run out in the future and the pollution caused by their consumption is a serious problem. In the past decades, renewable energy sources such as wind and solar energy were widely studied and applied all over the world. Although renewable energy sources are replacing part of traditional fossil fuels role, their intermittent natures let them impossible to fully satisfy the world's energy requirements.

Nuclear fission was first investigated and explained in the late 1930's and the first commercial fission power plant was built in the 1950's. As a reliable and high efficiency energy source, nuclear fission is well developed in many countries. In France for instance, 78% of electricity is generated from fission power plants. After the Fukushima Daiichi accident on 11 March 2011 that was caused by an earthquake and a subsequent tsunami, several countries with operational nuclear power plants decided to phase-out the use of the technology over the next two decades [1]. Due to the high safety risk of radioactive pollution caused by accidents of fission power plants, the fever of fission energy application cold down all over the world. Therefore, energy sources that can offer safe and renewable energy still have to be found.

#### 1.1.2 Nuclear fusion

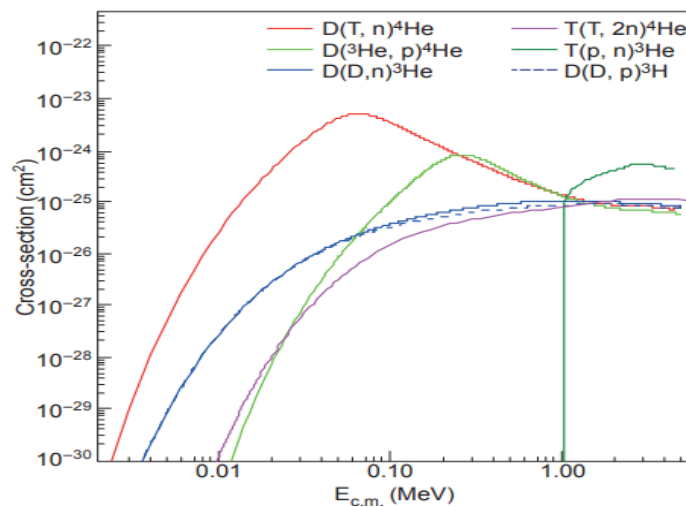
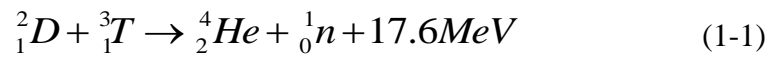


Figure 1-1 Effective cross sections of major fusion reactions [2]

Nuclear fusion is another nuclear reaction which is happening in stellar cores. In the fusion process, the nuclei are fused together and release energy. On earth, the technically easiest achievable nuclear fusion reaction is the fusion between hydrogen isotopes deuterium (D) and tritium (T) due to their high cross-section and the greatest yield of energy per reaction (Figure 1-1).

The fusion reaction of deuterium and tritium is expressed as:



In order to achieve fusion reactions between deuterium and tritium, one has to bring the nuclei (which are positively charged) close enough ( $<10^{-15}$  m) to overcome the electrostatic repulsion, so that the nuclear strong force can bind the nucleons together in a nucleus[3, 4]. In practice, the D-T nuclei should be heated to about 100 million Kelvin, which is much higher than the ionization temperature of the hydrogen atom which is in the order of 10000 K. In other words, the fusion reaction can only occur in a fully ionized plasma state.

Compared with nuclear fission, the nuclear fusion reaction itself does not produce radioactive wastes. Moreover, since the Deuterium isotope can be found in abundance in seawater and the Tritium could be generated from the interaction of the high energy neutron with Lithium, fusion energy would have no shortage of fuels. All these advantages make fusion energy a candidate for the future energy supply and fusion development is carried out in many countries all over the world.

## 1.2 ITER and ITER ICRH antenna

### 1.2.1 Magnetic confined fusion and Tokamak

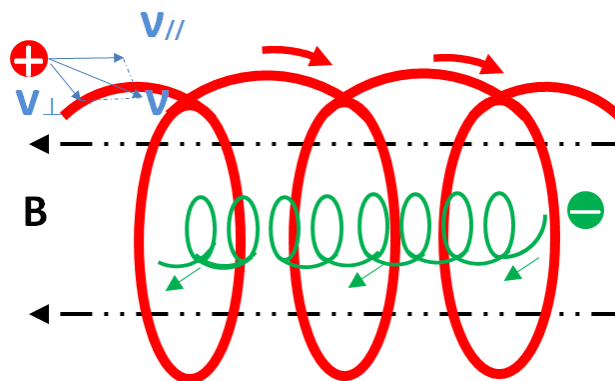


Figure 1-2 Diagram of ions and electrons trajectories in a DC magnetic field

No container exists that can hold hot plasma which is in the order of 100 million

Kelvin. The idea is to use a magnetic field to trap the charged plasma particles in order to control the contact with the wall of the container. In a steady magnetic field, electrically charged moving plasma particles move in spiral orbits along magnetic field lines (Figure 1-2). Trapping the plasma particles along the magnetic field lines has been successfully achieved by some magnetic confinement concepts, such as reversed field pinch, stellarator and tokamak.

In the world, tokamak has been the most developed magnetic confinement system and is presently the basis for a future fusion reactor design in many countries [5-7]. As shown in Figure 1-3, plasma is contained in a torus-shaped vacuum vessel and confined by a specially designed magnetic field configuration [8]. A set of Toroidal Field (TF) coils are installed along the torus to generate the toroidal magnetic field. However, toroidal field is not sufficient to confine the plasma alone, due to the curvature of the magnetic field lines which produces opposite particle drifts for ions and electrons. Due to this particle drift, plasma shifts rapidly toward the wall and gets lost. In order to avoid this particle drift phenomenon, an additional poloidal magnetic field is necessary, which combines with the toroidal field and forms spiral magnetic lines. The poloidal magnetic field is generated by a flowing current in the plasma, magnetically induced by the inner poloidal field coils. In addition, External Poloidal Field (PF) coils are designed for plasma positioning and shaping.

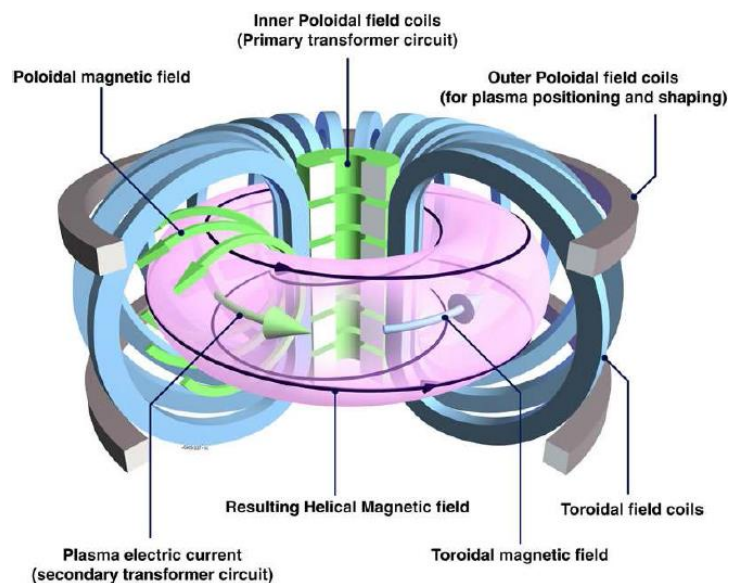


Figure 1-3 Schematic of tokamak [9]

### 1.2.2 ITER project

In the past 50 years, tokamak-based magnetic confinement fusion research achieved impressive progress: on JET and TFTR tokamaks, total fusion powers of 16MW and

11MW were produced respectively [10]. However, based on confinement scaling laws, in order to generate enough power to sustain the fusion reaction itself, the size of the machine should be enlarged almost twice as large as any tokamak machine existing. So, large size tokamak machine needs to be built to get further progress.

In order to demonstrate the scientific and technological feasibility of fusion energy, the ITER Project was launched in 1988. As an international project, China, the European Union, India, Japan, Korea, Russia and the United States firmly committed to building the International Thermonuclear Experimental Reactor (ITER), which is the world largest tokamak[10-12].

The primary objectives of ITER tokamak are 1). achieving the out-versus-in power amplification ratio of the fusion reaction ( $Q$ ) no less than 10 and generating 500MW output power for 400 s. Thus, ITER will be the first machine that could gain net energy after subtracting the energy to initiate the fusion reaction. 2). to demonstrate steady-state operation non-inductive current drive at  $Q \geq 5$ . 3). to demonstrate availability and integration of essential fusion technologies. 4). to test components for a future power reactor including high temperature tritium breeding blanket module concepts with the 14 MeV neutron power load.

### **1.2.3 ITER ICRH antenna and RF contacts**

To heat the deuterium and tritium fuel to fusion temperatures, ITER relies in part on Ion Cyclotron Resonance Heating (ICRH) power. ITER ICRH system is one of the three heating systems that are anticipated to be used during plasma experiments and two antennas will be installed in ITER equatorial ports with a total heating power of 20 MW (40-55 MHz) up to one-hour steady-state operation for a variety of ITER plasma scenarios [13-16].

#### **1.2.3.1 Mechanical design of ICRH antenna**

As shown in Figure 1-4, each of the ITER ICRH antennas was designed as port plug structure with a total weight of 45 tons [14]. In order to ease the assembly, each port plug was split into four symmetric pieces in a  $2 \times 2$  array. In the front of the port plug (PP), front modules (FM) transfer and couple the RF power to ITER plasma. This RF power is generated by sources that will be installed far from the ITER machine and transferred through transmission lines (TL). In the port plug, there are eight removable vacuum transmission lines (RVTL) designed to connect the FM and TL [17]. The RVTL has been designed to be maintained or replaced using remote handling system without extracting all the heavy and complex PP. For the RF plasma coupling adjusting consideration, a shimming process has also been foreseen to allow

FM radial displacement of few centimeters relative to the RVTL [14, 15]. Besides, due to uniform temperature distribution, large thermal stress can generate inside the RVTL, which will threaten the RVTL's structural safety.

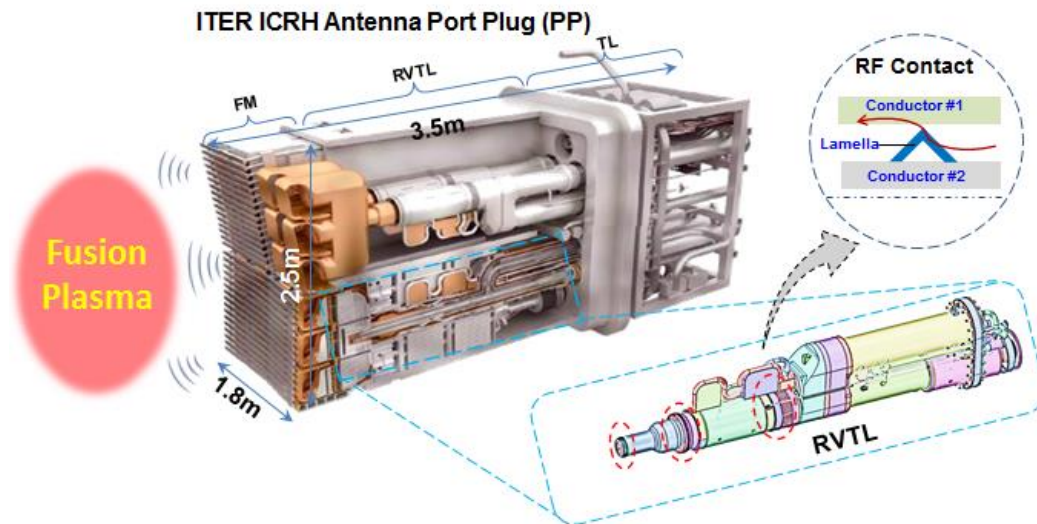


Figure 1-4 Overview of ITER ICRH antenna

To allow the relative displacement between FM and RVTL as well as to release the thermal stress in the RVTL, flexible connection joints named RF contacts were added at some different locations. The most stringent operation conditions of three of these RF contacts are reported in Table 1-1.

Table 1-1 General parameters of the three locations' RF contact on the ITER ICRH

Contact	Max $I_{RF}$ [kA]	Diam. [mm]	Max $J_{RF}$ [kA/m]*
#1 :	2.0	140	4.6
#2 :	2.5	260	3.1
#3 :	2.3	218	3.4

(\* The current density is defined as  $J_{RF} = I_{RF} / \pi \cdot \text{Diam.}$ )

### 1.2.3.2 RF contact design specifications

These contacts must satisfy the following constraints:

- The RF contact (#3) should work normally under 2.25 kA (+20% of safety margin) at 40-55 MHz for 1200 s steady-state operation without any failure.
- The structural and material of the RF contact should be compatible with the ITER vacuum condition which is a pressure lower than  $10^{-4}$  Pa.
- The RF contact should sustain high temperature baking at 250°C during ITER baking phase for  $2 \times 10^4$  hours without structure problem caused by creeping

and diffusion.

- The RF contact should sustain linear sliding under two sliding modes: thermal expansion happens during RF operation and baking or insertion during assembly. For the first mode, based on the calculation, the sliding speed is 0.05 mm/s with a sliding stroke of 2 mm. For the assembly insertion, the total stroke is about 50 mm and the speed is 1 mm/s-5 mm/s (should be compatible with the remote handling system).

### **1.2.3.3 RF contact design challenges**

Based on the relative motion between electrical contact parts, electrical contacts can be divided in general into two basic types: stationary contacts and moving contacts[18]. According to the property of current that flows through, electrical contacts can be classified as direct current (DC) contacts and alternating current (AC) contacts. ITER RF contacts are sliding contacts that will work under a heavy current load with a current frequency of 40-55 MHz.

One of the biggest challenges for the ITER ICRH RF contact design is the large current or current density (4.6 kA/m Max.) which will induce large thermal load, especially at contact areas due to Ohmic loss, where the contact resistance generated. Even if active cooling is designed below the RF contact, confined by the flexible RF contact's mechanical design, the distance between the contact to the cooling channel can be few centimeters and the cooling efficiency reduced. During steady-state operation, heat will accumulate and temperature will increase which would induce structure and material failures. For this reason, the mechanical structure design and contact material selection which can ensure the function stability are the most important aspects. Compared with stationary electrical contacts, sliding contacts are facing much critical working conditions: severe wear and corrosion. Moreover, the RF condition makes the sliding contact design more challenging, as “skin effect” increases the bulk resistance, thus increases the Ohmic loss accordingly.

## **1.3 RF sliding contact development status**

Although RF contacts are commonly used in the electronic industry as well as on scientific research facilities, however, their application on high RF current load under vacuum is very limited. Before the RF sliding contact development for fusion applications, almost no research experience existed regarding such components. Commercial RF contact LA-CUT produced by the Multi-Contact® company (now part of Stäubli) [19] was selected as a possible design concept for various ICRH systems, in particular for ITER [20]. During the last 15 years, such contacts have been

tested in various operating conditions in IPP [21] or CEA [22] and are currently used in the JET ICRH ITER-like antenna [23]. The experiments results obtained at CEA under vacuum are summarized in Figure 1-5.

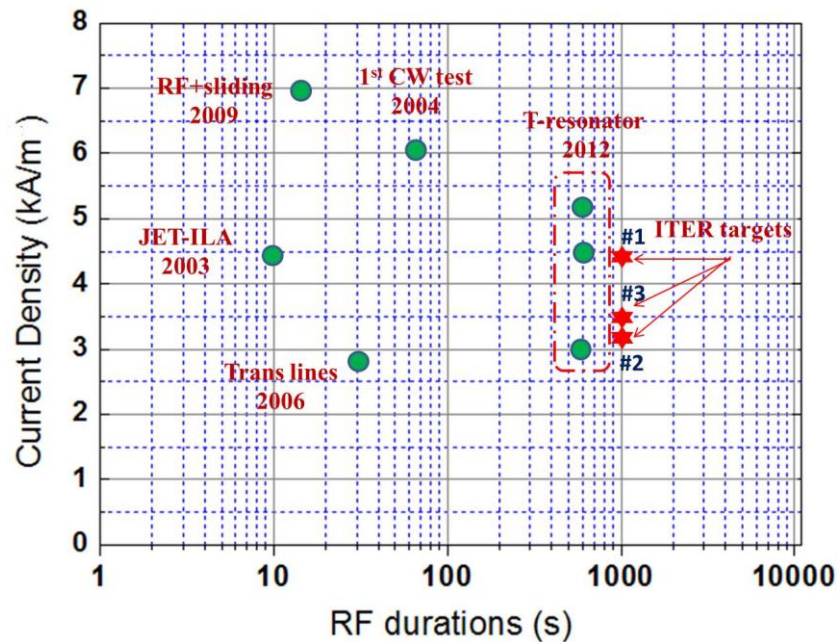


Figure 1-5 Summary of Multi-Contact LA-CUT RF experiment results in CEA

CEA started to investigate the electrical performance and reliability of flexible finger contacts since 2002. The first RF sliding contact prototype was designed based on the Multi-Contact LA-CUT configuration and installed in the JET-EP ITER-like antenna to provide a separable electrical coupling between tuning capacitors and current straps [22]. In this work, Multi-Contact LA-CUT had been tested under vacuum condition, up to 36 kV and 1.75 kA peak (1.24 kA RMS) during 10 s with a current density around 4.5 kA/m. In 2004, these same contacts were successfully tested for 60 s steady state operation under the current density of 6.16 kA/m in vacuum at 59 MHz. The feasibility of applying Multi-Contact LA-CUT commercial RF contact in ITER vacuum condition was proved.

In 2009, Multi-Contact LA-CUT contact was tested in a vacuum environment up to 60 s. Moreover, sliding tests were first performed to investigate the feasibilities of contact sliding during RF shot [24]. The mock-up consists of a  $\Phi 54$  mm strip holder, where louvers faced a thick 500  $\mu\text{m}$  copper electroplated steel part. During the mechanical sliding test, the abrasion on the copper plated part was so serious that the sliding was blocked due to wear debris generated. At last, the copper coated cylinder was changed to CuCr (with higher hardness than copper) and wear problem solved. Based on this prototype, RF tests had been performed at 57 MHz up to 32 kV / 1.2 kA peak (7.07 kA/m) under vacuum during 16 s with a sliding speed of 5 mm/s over a

50 mm range. From this test, the capability of Multi-Contact LA-CUT to support RF operation during sliding was demonstrated. But its steady state operation capability still required further investigations.

For that purpose, RF tests have been performed on Multi-Contact LA-CUT under vacuum on a newly developed facility (T-resonator), which is a dedicated testbed for ITER RF components development. These contacts have been tested under 2 kA/600 s (4.54 kA/m) and ultimately up to 2.28 kA (5.18 kA/m) peak during 600 s at 62 MHz on both a  $\Phi 140$  mm holders, after which the contact band was destroyed (Figure 1-6).

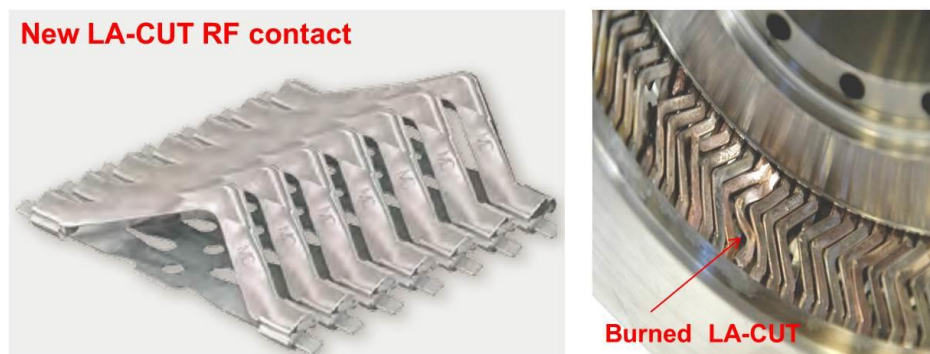


Figure 1-6 Multi-Contact LA-CUT RF contact before and after RF tests<sup>1</sup>

Even though significant progress about the mechanical design of RF sliding contacts and the necessary knowledge about their material had been achieved in the previous R&D phase, there is still a large gap between the obtained results and the ITER RF sliding contact design specifications.

#### 1.4 Research aims and objectives

The development of an ITER RF sliding contact is the combination of mechanical structure design and material selection. The previous studies [21-24] mainly focused on the RF current carrying capability of the LA-CUT commercial product. However, the failure mechanism of the RF contact was not deeply researched. As a result, the main parameters or factors that can affect the RF contact's stability were not clearly understood.

<sup>1</sup> I would like to add that LA-CUT is a widely used and high-tech commercial electrical contact. It was not designed specifically for ITER application. In this thesis study, LA-CUT was selected to test under ITER relevant conditions. The failure presented in this figure doesn't present the quality of the LA-CUT product and the test results are significantly affected by the test conditions as well as the performance of the conductor that the LA-CUT was installed in. The test conditions were out of its manufacturing specifications.

Meanwhile, as commercial RF contact, LA-CUT was designed mainly for civil (and DC) applications. However, the ITER RF sliding contacts will be facing in ITER specific nuclear fusion conditions which include high vacuum, high temperature and neutron radiation. The thermal effects and metal diffusion induced by thermal aging to the materials mechanical and electrical property changes should be investigated. Besides, as a sliding electrical contact, the understanding of the tribological performance of contact materials under ITER operation conditions is also essential to direct the material selection. The neutron irradiation effects on the materials will not be investigated in this work.

The aims of this thesis are:

- 1) Understanding the failure mechanisms of RF sliding contacts in the context of ITER ICRH system. Creating multi-physics analysis model of the contact and analyzing the main factors and parameters that can affect the operating temperature of the RF contact louvers through Finite Element Analysis (FEA) method.
- 2) Selecting electrical contact materials which are expected to have good performance of electrical conductivity and wear resistivity in ITER operating conditions. Mimicking ITER high temperature baking periods and investigating the selected materials' thermal stabilities and diffusion phenomena after thermal aging treatment at 250°C for 500 h.
- 3) Developing an electrical and tribological multi-functional test bed with ITER relevant conditions such as vacuum and temperature. Investigating the electrical contact and wear performance of the material pairs on the test bed and analyzing the effects of wear to the contact resistance.
- 4) From the acquired knowledge, designing a new ITER RF sliding contact prototype to be tested on the IRFM RF T-resonator
- 5) Studying the feasibility of applying advanced self-lubricating coatings on RF sliding contact to improve their wear performance in ITER. Investigating the possibility of co-depositing nanoparticles of solid lubricants (WS<sub>2</sub>, carbon) within the electrical contact functional coatings.

In summary, in this thesis study, the failure mechanisms of the LA-CUT commercial electrical contact under ITER ICRH application conditions are expected to be investigated and the relationship between the LA-CUT operational performance with the material selection will be analyzed. Based on the material properties requirements obtained from the LA-CUT prototype failure analysis, the proper material candidates

(commercial and self-developed) were evaluated under ITER relevant conditions, which can give a direction to the material selection for the ITER ICRH RF sliding contact development.

Therefore, this manuscript will be divided into 5 parts: after the thesis general introduction (chapter 1), in chapter 2, the coating deposition techniques, material characterization techniques and background of wear and contact resistance were introduced. In this thesis, not only commercial material characterization tools were used, a multi-functional tribometer that can mimic ITER conditions to perform the materials' electrical/tribological characterizations was developed during the thesis. So, the engineering details of the multi-functional tribometer development were also introduced in chapter 2. Chapter 3 introduces the RF test results and the failure mechanisms of the LA-CUT electrical contact under ITER relevant conditions. During the failure mechanism analysis, both the material characterization by commercial material characterization techniques and the FEM analysis were applied. Based on the failure mechanism analysis, CuCrZr and 316L were selected to be the base material candidates for the ITER RF conductor and CuCrZr was selected as the base material candidate for the RF contact louver. Functional coatings were also proved to be necessary which can help to improve the base materials' electrical and tribological performance. In chapter 4, various of commercial functional coatings that were electroplated on CuCrZr and 316L substrates were evaluated under ITER relevant working conditions and wear was observed to be a problem which shortened their life time. The possibility of applying solid lubricants to improve the coatings' wear performance was evaluated in chapter 5 by developing and testing two kinds of self-lubricating coatings. Chapter 6 will finally conclude this manuscript.

## **Chapter 2 Coating deposition and characterization techniques**

ITER RF sliding contact is a critical component that has both harsh mechanical and electrical design requirements. Applying suitable coatings on proper substrates is a possible material solution. Material selection and the following characterizations in mechanical, electrical and diffusion properties are major steps for the ITER RF sliding contact development. In this chapter, the coating techniques and the coating characterization techniques (morphology, composition, mechanical properties, crystal structure) that are used in this study are introduced. The background knowledge of wear and contact resistance between coating surfaces in vacuum which can help to understand the ITER RF sliding contact's failure mechanism is discussed. The engineering design of the dedicated testbed for coatings' electrical and tribological performance characterization is also presented.

### **2.1 Coating deposition techniques**

The performance of an electrical contact is mainly the consequences of the phenomena occurring at its surface, such as contamination, oxidation, re-oxidation, wear, etc. [18] The above factors can increase the contact resistance so as to threaten the reliability of the connection. As a commonly used surface engineering method, applying coating is an effective practical solution for various electrical contacts, on which thin coating layers play a major role in dealing with corrosion, wear and metal diffusion. Based on the coating material's characteristics and operating conditions, the coating thickness varies from 0.1–0.3  $\mu\text{m}$  to 20–30  $\mu\text{m}$ .

#### **2.1.1 Overview**

Generally speaking, the majority of contact materials that help to improve electrical contact quality, are noble metal materials. Depositing them as micron scale coatings on common structural metal materials is common practice for high-power RF components. The practical coating methods include electroplating, electroless plating, spraying and Physical Vapor Deposition (PVD). Hardness and surface quality can affect the electrical contact's wear performance. Generally, hard coatings with smooth surfaces have higher wear resistance. Electroplating and PVD deposition methods can generate fine grain size coating, which has better hardness performance than spraying and electroless plating. Moreover, by using electroplating and PVD methods, alloy coatings and composite coatings can be achieved, which is beneficial for advanced coating development in which solid lubricant materials are expected to be co-deposited. In this thesis, two self-lubricating composite coatings were developed. The Au-Ni/C coatings were deposited by magnetron sputtering under the collaboration with Lanzhou Institute of Chemical Physics in China (discussed in

section 5.1). The Au-Co/WS<sub>2</sub> coatings were electrodeposited at CIRIMAT laboratory in France (discussed in section 5.2).

### 2.1.2 Electroplating

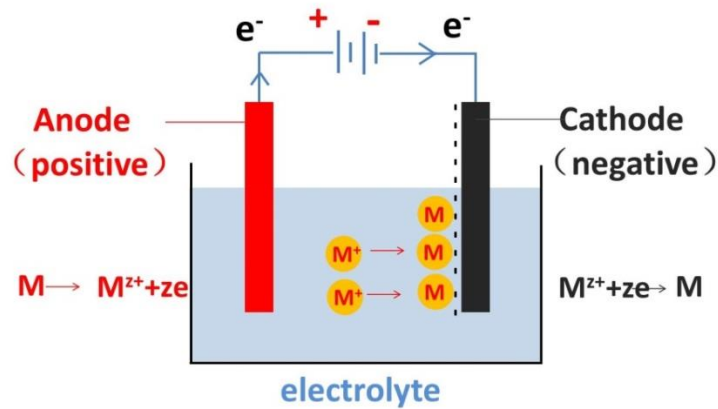


Figure 2-1 Schematic of electrodeposition

Electroplating is a process of depositing metal or conductive metal oxides thin films on conductive substrates by applying an electric current to reduce the metal cations dissolved into the electrolyte [25, 26]. A generic electroplating cell setup is shown in Figure 2-1.

There are two electrodes applied during the plating process: the anode and the cathode. The cathode is the piece to be plated and the anode is either a sacrificial anode or an inert anode (normally either platinum or carbon). For a sacrificial anode, the metal ions  $M^{z+}$  are exchanged between two phases, the solid metal and the solution contains  $M^{z+}$ . The metallic ions in salt carry positive charges and get attracted to the cathode when passing a negative current. When they reach the surface of the cathode, it provides electrons to reduce the positively charged ions into metallic form [27, 28]. On the anode, the reaction is reversed. The reactions of electrodeposition are expressed as:



If the anode is an inert anode, oxygen evolution takes place at the anode:



#### 2.1.2.1 Faraday's Law

Faraday's law states the relationship between the coating production and the quantity of electric charge passed through the electroplating cell. It's a useful method to

calculate the coating thickness. The weight of coating product is:

$$m = n \cdot M = \frac{I \cdot t \cdot M}{z \cdot F} \quad (2-3)$$

where,  $I$  is the current (A),  $t$  is the coating time (s),  $M$  is the molecular weight (g/mol),  $z$  is the number of electrons transferred,  $F$  is the Faraday constant (96487 C/mol).

The coating thickness ( $\mu\text{m}$ ) can be calculated through:

$$d = 100KD_k t \eta_k / 60\rho \quad (2-4)$$

where  $K$  is the coating metal's electrochemical equivalent ( $\text{g} \cdot \text{A}^{-1} \cdot \text{h}^{-1}$ ),  $D_k$  is the current density ( $\text{A}/\text{dm}^2$ ),  $t$  is the coating time (min),  $\eta_k$  is the cathode current efficiency and  $\rho$  is the density of the coating material ( $\text{g}/\text{cm}^3$ ).

### 2.1.2.2 Main factors that affect electroplating process

#### 1) Temperature

Generally, increasing the temperature of the electrolyte can increase the solubility of the metal salts and improve the conductivity of the solution accordingly [27, 29]. Increasing temperature can decrease the viscosity of the solution, thereby replenishing the double layer relatively faster. Besides, with high plating temperature one can achieve low stress and low cracking tendency coating as the hydrogen absorption on the coating is decreased. However, high temperature may increase the crystal size and sometimes impairs the coating quality. So, in practice, the plating temperature is selected by compromising the deposition rate and coating quality.

#### 2) Agitation

Agitation provides sufficient mixing of electroplating bath and replenishes metal ions at the cathode surface which reduces the thickness of diffusion layer. Under agitation, high current density can be used during the plating process to achieve high productivity. Meanwhile, agitation helps to remove hydrogen bubbles from the coating surface, which prevents voids defects in the coating [30]. Many types of stirring can be used such as mechanical swing, electric shock, gas vibration and so on.

#### 3) Current density

In electroplating, current density plays an important role in the coating rate and coating quality. The selection of current density must take the bath composition and temperature into consideration. Insufficient current density will result in poor coating, while excessive current density may induce burn defects [31].

### 2.1.3 Magnetron sputtering deposition

Magnetron sputtering is a plasma-based deposition process in which energetic ions are accelerated towards a target. The ions strike the target and atoms are ejected or sputtered from the target surface and deposited on the substrate to generate film. Magnetron sputtering belongs to PVD deposition method.

The scheme of the J450 magnetron co-sputtering system used in this thesis study is shown in Figure 2-2. The coating substrate and target are installed in a chamber. During the plating process, a DC power supply or RF power supply is used between the target (cathode) and substrate (anode) [32, 33]. Ar plasma is generated between the electrodes and  $\text{Ar}^+$  ions are accelerated to bombard the target surface. What differentiates a magnetron cathode from a conventional cathode is the presence of a magnetic field. The magnetic field in the magnetron is oriented parallel to the cathode surface. The local polarity of the magnetic field is oriented such that  $\text{E} \times \text{B}$  drift of the emitted secondary electrons forms a closed loop. Due to the increased confinement of the secondary electrons in this  $\text{E} \times \text{B}$  drift loop, the ionization efficiency of Ar gas is increased and the plasma density near the target surface is increased too. With ionization of Ar gas, the energy of the electrons decreased, which eliminates the heating problem of the substrate due to electron bombardment. More deposition details are introduced in Chapter 5 (section 5.1.1).

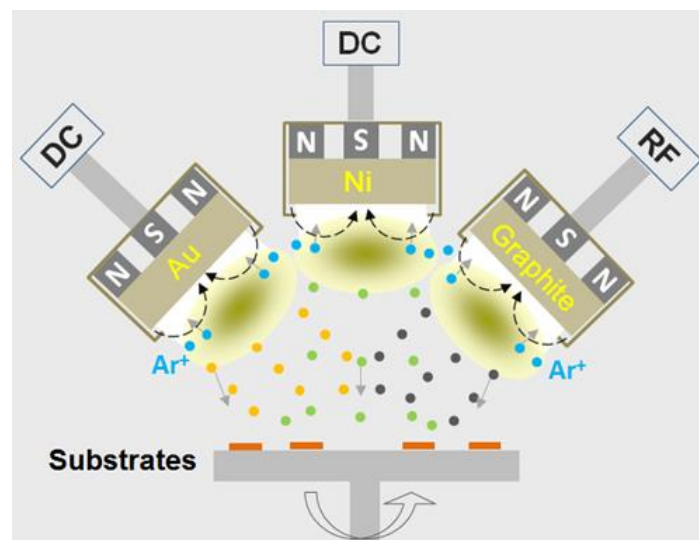


Figure 2-2 Schematic configuration of the magnetron sputtering system

## 2.2 Characterization techniques

Several different techniques were used to analyze or characterize the coating materials aiming for ITER RF sliding contact development. The coatings' morphology, coatings' mechanical properties (adhesion, hardness and elastic modulus), coatings' chemical

composition and crystal structure were characterized. The techniques used in this study include: 3D optical profiler, Scanning Electron Microscopy (SEM), Energy-Dispersive Spectrometer (EDS), Transmission Electron Microscopy (TEM), micro-scratch tester, nanoindentation tester, X-ray Photoelectron Spectroscopy (XPS), The X-ray Diffraction (XRD) and Raman spectroscopy.

### 2.2.1 3D optical profiler

Optical profilers are interference microscopes used to accurately measure the three-dimensional height variations on surfaces of a given test material. As Figure 2-3 shows, optical profilers manipulate the wave properties of light entering the microscope and compare the path differences between the test subject and a reference object of a known flatness. Once light enters the optical profiler, the light beam will split, where one-half of the beam reflects the focal plane of a microscope objective for the object of interest and the other half is reflected from the reference mirror. Interference between these two beams is then measured to form an interferogram from which height calculations can be obtained [34]. The main advantage of the 3D optical profiler is the non-contact measurement.

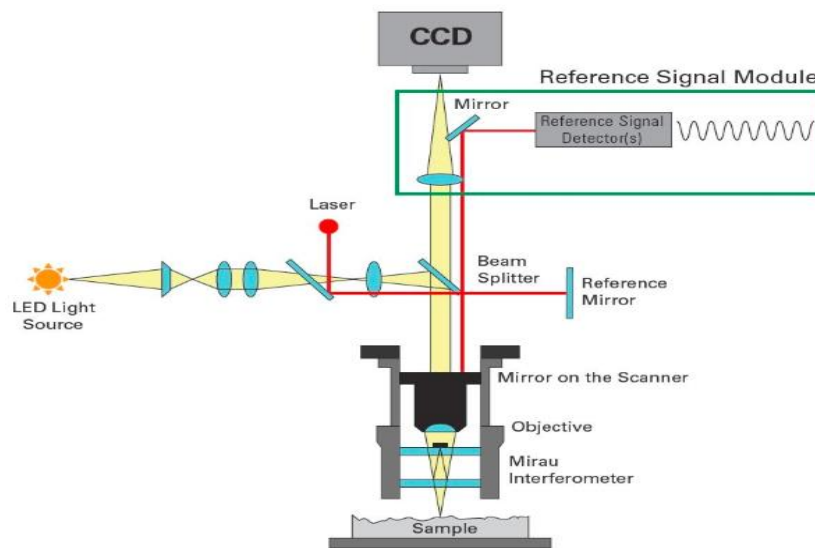


Figure 2-3 Schematic of a 3D optical profiler [35]

The 3D optical profiler (SENSOFAR, USA) was used in this thesis to measure the samples' surface roughness.

### 2.2.2 SEM/EDS

The resolution of microscope is limited by the wavelength of visible light. For large magnification images, light or particles with shorter wavelength is mandatory.

Electrons have shorter wavelengths; therefore in electron microscopy larger magnifications, up to two million times, become possible [36]. Based on electron microscopy, SEM was developed which is a widely used technique to study the surface morphology and compositional distribution. As Figure 2-4 shows, the tested sample is introduced into a vacuum chamber where a focused beam of electrons interacts with the sample. The primary electrons interact with the surface atoms producing several detectable signals, among which backscattered electrons, secondary electrons and X-rays are used the most for the analysis. Secondary electrons give information about the surface morphology. From backscattered electrons, the elements with high atomic number  $Z$  will appear lighter than the elements with a low  $Z$ . So, they can supply composition information. The number and energy of the X-rays emitted from a specimen can be measured by an EDS. As the energies of the X-rays are characteristic of the elements that emitting such X-rays. X-rays detection gives additional insight into the elemental composition of the surface.

In this thesis, JSM-6510LV (JEOL, Tokyo, Japan), JSM-6700F FEG-SEM (JEOL, Tokyo, Japan) and JSM-5601 (JEOL, Tokyo, Japan) were used to study the surface morphology and composition of the coating surfaces as well as wear tracks.

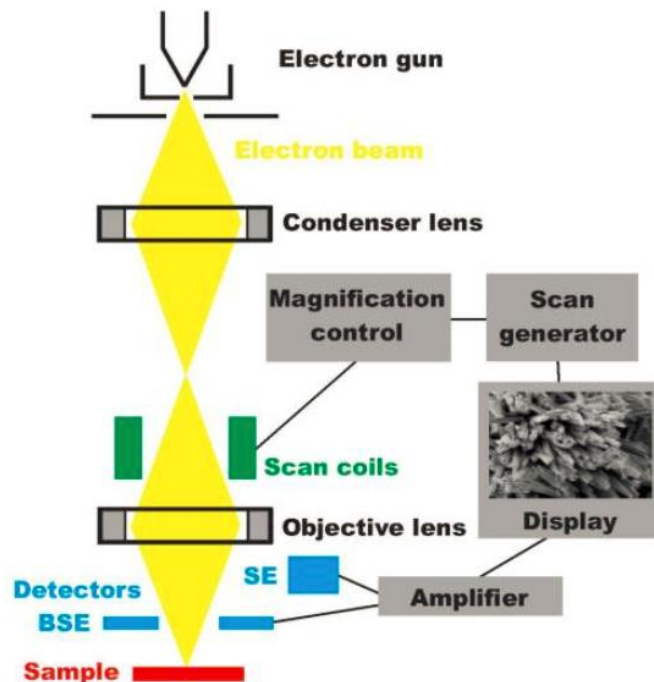


Figure 2-4 Schematic diagram of SEM system [37]

### 2.2.3 TEM

TEM is used to produce images from a sample by illuminating the sample with electrons beams within a high vacuum and detecting the electrons that are transmitted

through the sample. The TEM operates on the same basic principles as the light microscope but uses electrons instead of light. As the De Broglie wavelength of electrons is much smaller compared with visible light, the optimal resolution attainable for TEM images is significantly higher than optical microscopes, which reaches to 1nm [38].

TEM is a powerful tool for nanoparticle characterization and can be applied to study crystal structure and features in the structure like dislocations and grain boundaries. There are two modes in TEM, the imaging mode and the diffraction mode. In imaging mode, the darker areas of the image represent areas of the sample where fewer electrons are transmitted through, while the lighter areas of the image represent the areas of the sample where more electrons were transmitted through. The diffraction mode is a useful tool for doing a cell reconstruction and determining crystal orientation.

HRTEM images of the coating cross-sections were captured by using TECNAI G2 F20 S-TWIN (FEI, USA) instrument at an accelerating voltage of 200 kV equipped with EDS unit. Cross-sectional samples for TEM observations were prepared on Helios Nanolab 600i (FEI, Germany) focused ion beam system with Ga ions accelerating voltage of 30 kV for preliminary cutting and 5 kV for final milling.

#### **2.2.4 Micro-scratch tester**

The scratch test is a commonly used technique for assessment of thin films adhesive and cohesive properties against their substrates [39]. As shown in Figure 2-5, during a scratch test, a diamond indenter (Rockwell, Berkovich and cube-corner) is forwardly pulled straight ahead on the investigated surface at a constant velocity [40-42]. During the linear sliding of the indenter, a normal force is applied either in steps or more often continuously (usually linearly increased). During the test, the penetration depth and stylus position are recorded. In addition, the tangential force is acquired and the coefficient of friction (CoF) is calculated. The scratch tracks can be subsequently observed with SEM or optical microscopy to identify the coating failure mechanisms. Acoustic Emission (AE) sensor is also added to help determining the critical loads that cause coating failure.

In this thesis, the coating's adhesion properties were evaluated by using a CSEM<sup>®</sup> commercial micro-scratch tester. The scratch indenter is a diamond stylus that has a Rockwell C geometry with a 120° cone and a 200 µm radius spherical tip. Scratch tests were performed by applying a progressive load from 1 N to 50 N with a loading rate of 49 N/min. The indenter transverse speed was 4mm/min with a scratch length of 4 mm. For statistical analysis, three tests were performed on each sample.

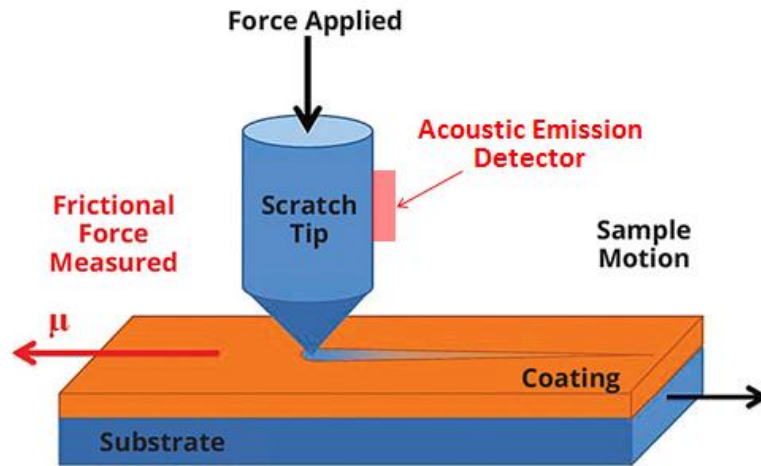


Figure 2-5 Schematic diagram of scratch test [43]

### 2.2.5 Nanoindentation tester

Nanoindentation testing has emerged as an important method for the evaluation of a material's mechanical properties, such as elastic modulus ( $E$ ) and indentation hardness ( $H_{IT}$ ). The technique is based on the continuous recording of applied force and resulting depth of penetration of an indenter throughout the whole loading and unloading cycle, when applied force is controlled [44]. During nanoindentation test, force and displacement are recorded as the indenter tip is being pressed into the test material's surface with a prescribed loading and unloading profile [45]. The typical load-displacement curve (P-h curve) recorded during a nanoindentation test is shown in Figure 2-6.

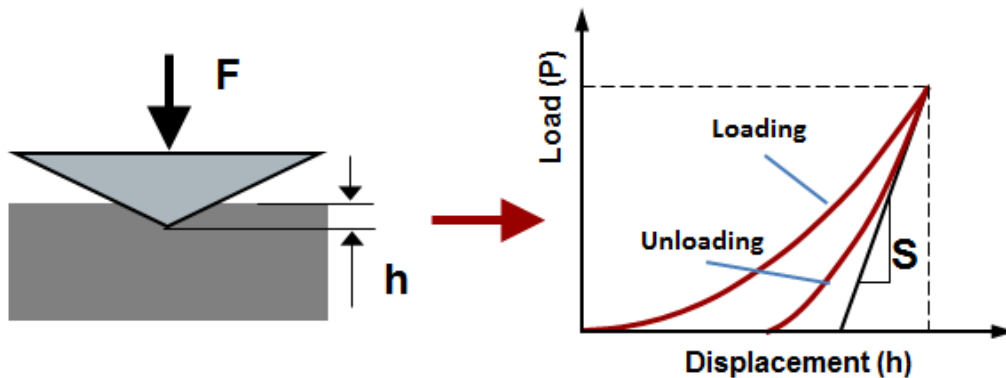


Figure 2-6 Schematic diagram of the nanoindentation test and typical P-h curves

The  $H_{IT}$  and  $E$  are calculated by the Oliver and Pharr method [46]:

$$H_{IT} = \frac{F}{A} \quad (2-5)$$

$$E_r = \frac{\sqrt{\pi}}{2} \frac{S}{\sqrt{A}} \quad (2-6)$$

$$\frac{1}{E_r} = \frac{(1-\nu^2)}{E} + \frac{(1-\nu_i^2)}{E_i} \quad (2-7)$$

where,  $F$  is the maximum test force,  $A$  is the projected area of contact of the indenter,  $S$  is the elastic unloading stiffness which is defined as the slope of the upper portion of the unloading curve during the initial stages of unloading,  $\nu$  is the Poisson's ratio of the tested material,  $\nu_i$  and  $E_i$  are the Poisson's ratio and elastic modulus of the diamond.

In this thesis, the elastic modulus and hardness of the coating were characterized at room temperature using a CSM<sup>®</sup> (CSEM, Switzerland) Ultra Nanoindentation Tester with a Berkovich indenter. The force and displacement resolution of the nanoindentation are 1 nN and 0.003 nm, respectively. The material's Vickers hardness (HV) can be calculated based on the indentation hardness ( $HV \approx H_{IT}/10.8$ ).

### 2.2.6 Microhardness tester

Hardness measurements were also performed on a Vickers microhardness tester (Model: HM-210, Mitutoyo, Japan), with a test force from 10 gf (0.098 N) to 1000 gf (9.8 N).

### 2.2.7 XRD

XRD technique is a non-destructive technique used for crystallographic structure study which provides information on structures, phases, preferred crystal orientations, etc.[47]. Crystalline substances act as three-dimensional diffraction gratings for X-ray whose wavelength is similar to the spacing of planes in a crystal lattice (Figure 2-7). The diffraction of the X-rays which are being focused on the sample at an incident angle  $\theta$  with respect to the lattice planes can occur only at certain angles that meet Bragg's equation as following [48, 49]:

$$n\lambda = 2d_{hkl} \cdot \sin \theta \quad (2-8)$$

where  $n$  is an integer corresponding to the order of the reflection,  $\lambda$  is the wavelength of X-ray used,  $d_{hkl}$  is the inter-planar distance in the crystal and  $\theta$  is the scattering angle.

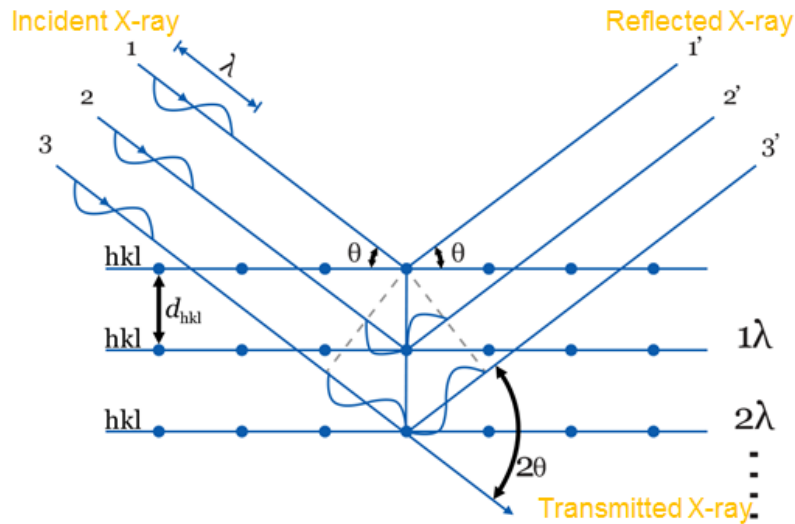


Figure 2-7 Diagram of Bragg's law

The diffracted X-rays are detected, processed and counted. The XRD pattern is obtained by plotting the intensity of diffraction peaks against the  $2\theta$  angle. Through analyzing the intensity and shape of the diffraction peaks, the crystallite size of the material can be obtained by using the Scherrer equation, which is expressed as [50-52]:

$$D = \frac{K \cdot \lambda}{\beta \cdot \cos \theta} \quad (2-9)$$

where  $\theta$  is the Bragg angle,  $\beta$  is the full-width at half-maximum (FWHM) of a diffraction line located at  $\theta$  (the peak broadening due to the facility itself has been removed),  $\lambda$  is the x-ray wavelength and  $K$  is the Scherrer constant.

In this thesis, coatings were characterized by using an X-ray diffractometer (XRD, BRUKER D4 ENDEAVOR, Germany) with Ni filter Cu  $K\alpha$  radiation ( $\lambda=1.541 \text{ \AA}$ , 40 kV, 40 mA). The X-ray diffraction data were collected from  $10^\circ$  to  $100^\circ$  in  $2\theta$ .

### 2.2.8 XPS

The XPS is a powerful technique for highly specific surface (3 nm-10 nm) elemental composition and chemical state characterizations. XPS spectra are obtained by using a beam of Al or Mg X-rays to bombard the material surface with a well-defined energy [53].

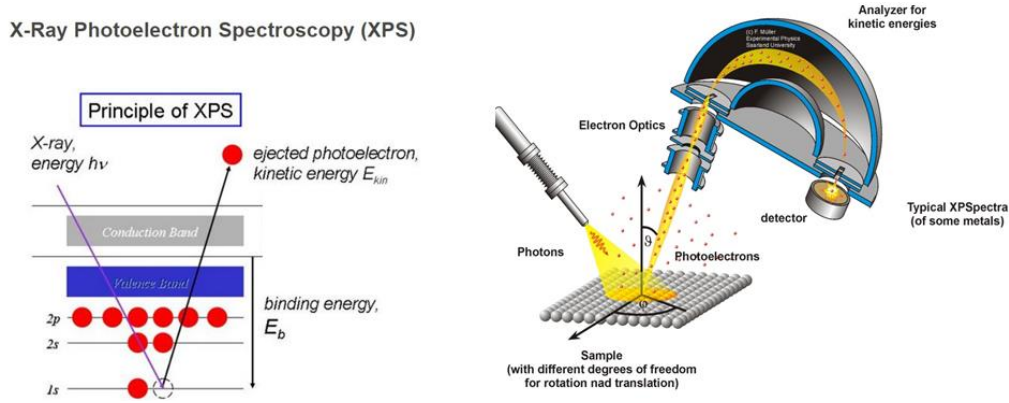


Figure 2-8 Schematic diagram of XPS principle and system [54]

As shown in Figure 2-8, the X-ray interacts with core electrons present around the nucleus of atoms contained in the material surface and a number of electrons escape from the surface with a specific kinetic energy  $E_k$ , which can be expressed as:

$$E_k = h\nu - E_b - \phi \quad (2-10)$$

where  $h\nu$  is the X-ray photon energy,  $E_b$  is the bonding energy of the electron and  $\phi$  is the energy that can extract the electron from the surface of the sample which depends on the spectrometer and the substrate.

The bonding energy of core electrons is an intrinsic material property. The electrons from different atoms, the same atom with different orbitals and the same orbital in different bonding states have specific binding energy values. As the energy of X-ray photon is known and by using an electron energy analyzer to measure the kinetic energy of the photoelectrons emitted, the bonding energy of the photoelectrons can be deduced from equation 2-10. Thus, by separating and characterizing the photoelectrons kinetic energy and their intensities, the atoms present in the material surface and their chemical states as well as their contents can be determined. Due to the short range of the photoelectrons that are excited from the solid, XPS is able to identify and quantify the elemental composition of the outer 10 nm or less of any solid surface.

The XPS system used in this thesis is Quantera SXM (ULVAC-PHI, Japan) with a base pressure of  $9 \times 10^{-7}$  Pa and Al  $K\alpha$  monochromatic X-ray source.

### 2.2.9 Raman spectroscopy

Raman spectroscopy allows for the detection and identification of molecules through their unique vibrational and rotational energy level structure. Raman spectroscopy allows direct detection of a molecule with no chemical alteration based on their

interaction with monochromatic light. When a beam of light is impinged upon a molecule, photons are absorbed by the material and scattered. Most of these scattered photons have the same wavelength (frequency) as the incident photons due to elastic scatter (Rayleigh scatter).

As Figure 2-9 shows, in Rayleigh scattering the molecules are excited to a higher energy level and then decay back to the same energy level. However, a small fraction of light (approximately 1 in  $10^7$  photons) is scattered at optical frequencies different from the frequency of the incident photons. Such scattering is called inelastic scattering or Raman scattering [55]. The photon's change in frequency is induced by the interaction of the light and molecular vibrations which provides chemical and structural information on the analyzed sample. It's worth mentioning that only the molecular vibrations that induce the polarizability change can interact with the photons.

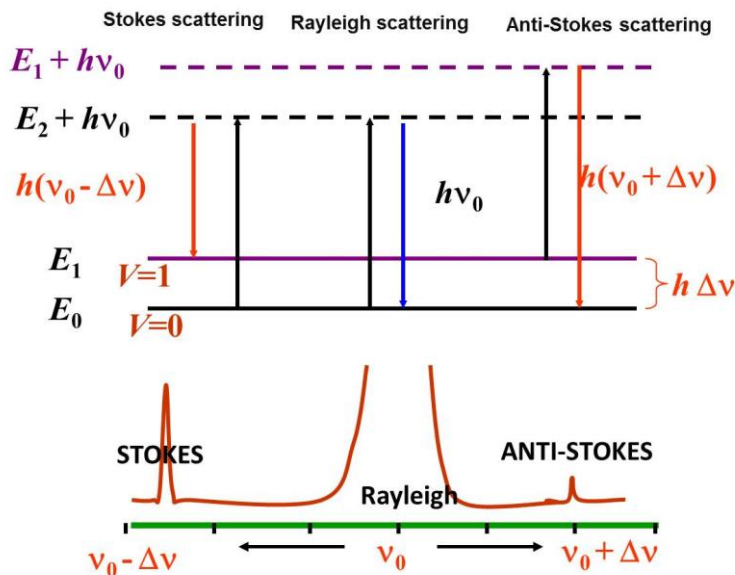


Figure 2-9 Energy level diagram for Raman scattering

In this thesis, the Raman spectrometer that was used is Horiba LabRAM HR800 system. Raman signal was excited by using a laser with wavelength of 532 nm and the Raman spectra were collected from  $100\text{--}2000\text{ cm}^{-1}$ . The measurements were performed at room temperature with a power of 12 mW.

## 2.3 Tribology of conductive contact

### 2.3.1 Electrical contact resistance

Engineering surface, even with careful polishing, are not really smooth surfaces in microscale scale, but present many asperities. When two engineering bodies come

into contact with an applied force, the contact between the two bodies occurs at the asperities firstly, as illustrated in Figure 2-10. For bulk metal materials, their surfaces are covered with oxidation layers or adsorbed gas layers, which are electrically insulating layers. Thus, the low resistivity conducting paths are generated only when the surface asperities of the contacting members penetrate oxidation layers and other contaminant films, generating metal-to-metal contact spots (*a-spots*, where *a* stands for asperity) [18].

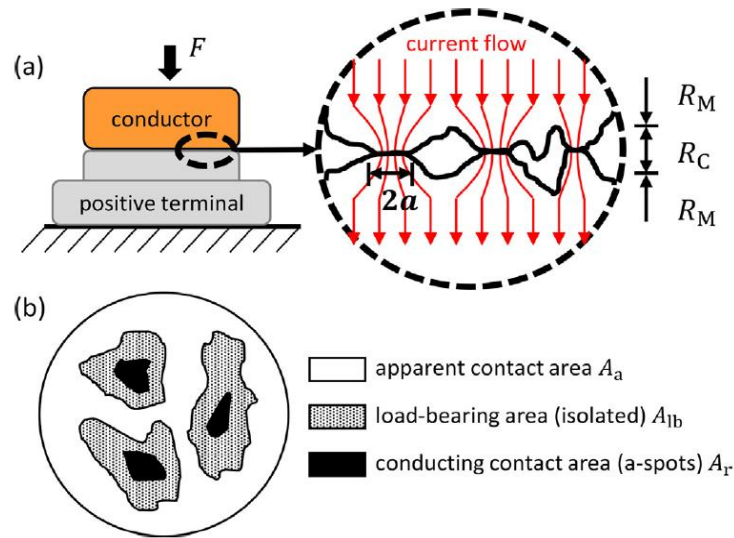


Figure 2-10 Schematic of current constriction and real contact area [56]

Due to the presence of such asperities and insulating layers, the real conducting contact area  $A_r$  between two surfaces is much lower than the apparent contact area  $A_a$ . Generally, the conducting contact area is less than 1% of the apparent contact area [57]. When current passes through a-spot to the bulk materials, the current lines are constricted and the length of the path is increased, resulting in an additional resistance called constriction resistance ( $R_c$ ). In addition, due to the presence of contaminating film with relatively high electrical resistivity, an additional resistance called film resistance ( $R_f$ ) is also generated. The total resistance  $R$  at the contact interface is the sum of the  $R_c$  and  $R_f$ :

$$R = R_c + R_f \quad (2-11)$$

Holm has shown that the constriction resistance for a single a-spot can be expressed as [18]:

$$R_c = (\rho_1 + \rho_2) / 4a \quad (2-12)$$

where  $\rho_1$  and  $\rho_2$  are the respective resistivities of the contacting metals and  $a$  is the

radius of the metal-to-metal contact area.

The above formula is valid only for single circular a-spot. However, for real electrical contacts, the contact takes place at a cluster of a-spots. Greenwood and Williamson proposed an expression of  $R_c$  in the simplest case of a large number  $n$  of circular a-spots located within a single cluster. The constriction resistance is expressed as [18]:

$$R_c = \rho \left\{ \frac{1}{2na} + \frac{1}{2\alpha} \right\} \quad (2-13)$$

where  $a$  is the average a-spot radius defined as  $\Sigma a_i/n$  ( $a_i$  is the radius of the  $i_{th}$  spot) and  $\alpha$  is the radius of the cluster sometimes defined as the Holm radius.

From equation (2-13),  $R_c$  (and thus  $R$  also) mainly depending on the contact area (which is affected by the applied contact force), the physical surface condition (surface roughness, contamination, etc.) and the mechanical properties of the contacting materials.

The expression (Equation 2-13) for constriction resistance was derived under the assumption of DC flow and based on the analytical solution to the Laplace equation. However, on ITER RF sliding contacts, the current will be an RF current with a frequency of 40-55 MHz. Under RF current conditions, current flows differ from DC case by the so-called skin-effect, which limits the penetration of the electromagnetic field to the center of the conductor. The parameter used to evaluate the skin effect is the skin depth  $\delta$ , expressed as:

$$\delta = \sqrt{\frac{\rho}{\pi f \mu}} \quad (2-14)$$

where  $f$  is the RF frequency,  $\mu$  is the magnetic permeability of free space and  $\rho$  is the resistivity of the conductor.

The RF current flows in a depth not higher than few times the skin depth, where four times the skin depth is generally considered as a rule of thumb since it represents 98% of the current density [58]. The skin-effect phenomenon affects the constriction resistance when the AC frequency is higher than 10 MHz, since the skin depth is comparable to the a-spot radius. This indicates that at 40-55 MHz, the constriction resistance should be very different from the value measured under DC cases. J. Lavers had studied the relationship between constriction resistance, constriction diameter and AC frequency by FEM [42]. Figure 2-11 shows that under RF condition, the  $R_c$  is

smaller than under DC condition.

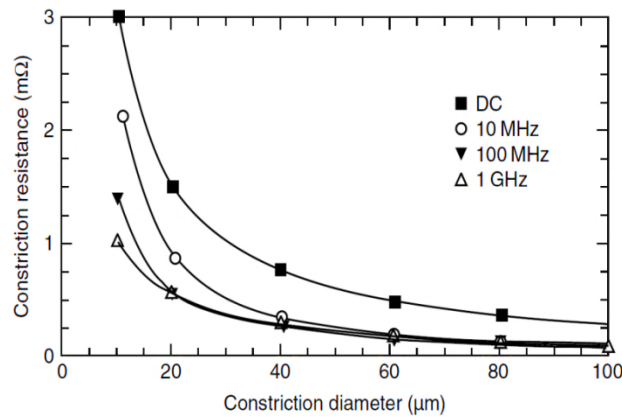


Figure 2-11 Dependence of constriction resistance on constriction diameter for current frequencies ranging from DC to 1 GHz AC [59]

However, in the FEM study, J. Lavers didn't take ohmic heating into consideration. More recently, Roland S. Timsit reported an opposite result, also originating from FEM study.

The Figure 2-12 shows that, when the frequency is lower than 1 MHz, the  $R_c$  is almost constant. For high frequencies, a  $R_c$  increase with the frequency was calculated. For the RF frequency range under consideration (45-60 MHz), the  $R_c$  can be 2 or 3 times higher than in the DC case. The rise in the resistance in Figure 2-12 is attributed to the increased ohmic heating in the constriction at the higher frequencies [60]. However, with the temperature increase, due to the creeping of the contact material, the contact area (constriction radius) could be increased accordingly, which could then decrease the  $R_c$ . The effect of temperature on the contact area was not considered in the Roland S. Timsit's recent study.

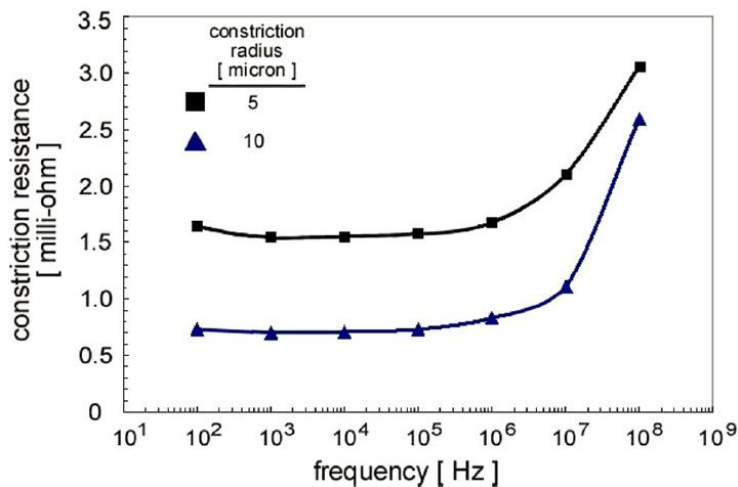


Figure 2-12 Contact resistances under different constriction radii and frequencies [60]

In this thesis, the  $R_c$  results between samples were measured under DC condition. In order to eliminate the temperature effects on the  $R_c$ , the  $R_c$  was measured under different temperatures with a maximum value of 200°C.

### **2.3.2 Friction and wear**

#### **2.3.2.1 Source of friction**

As Figure 2-10 shows, engineering surfaces presents peaks and valleys on the micrometer scale. When a normal contact force is applied on two contacting surfaces, the opposing asperities with maximum height come into contact. The contact asperities surface area increases with the contact force. Strong adhesive bonds can be generated between contacting surfaces when the surface contamination films are absent and if the pressure generated between contact spots is high enough [18, 61, 62]. When contacts are sliding in high vacuum and high temperature, the metallic pristine surfaces present high surface energy and are easier to generate a strong metallic bond. During sliding, an applied tangential load must generate a shearing force to break such strong bonds. Thus, friction is treated as a process of continuous formation and fracture of adhesive bonds [63].

Besides the strong adhesion at the contact areas, another source of friction is the elastic and plastic deformations occurring at the contact areas when harder counter surfaces being inserted into a relatively soft surface. When relative sliding happens, asperities on the harder surface generate ploughing effect to the soft surface and the ploughing resistance causes a force contributing to the frictional force. It's worth mentioning that, the ploughing effect is generally accompanied by adhesion effect.

#### **2.3.2.2 Wear**

During the relative movement between two contacting surfaces, material removal occurs from one or both of these surfaces, which is called wear. Wear phenomena are obviously affected by the sliding surface states, such as the roughness, the presence of adsorbed species and/or surface layers. Based on the underlying physical and chemical processes during the friction between two engineering bodies, the wear mechanisms can be classified as abrasion, adhesion, fatigue, corrosion, erosion, fretting, delamination, etc. [64-66]. The wear laws are generally based on the Archard's law, which is the wear volume divided by the applied load and the sliding distance [67].

##### *1) Adhesive wear*

In case of strong metallic bonding (cold welding) happening for clean, oxide-free

contacting asperities in a metal/metal contact [68], serious shear stresses are generated during relative sliding. Adhesive wear between metal contacts occurs when the adhesive strength at the interface is higher than the cohesive strength of the bulk material. As shown in Figure 2-13, a distinguishable feature of this form of wear is a transfer of material from one surface to another which occurs due to localized bonding between the contacting solid surfaces. Material is transferred from the cohesively weaker partner to the stronger one.

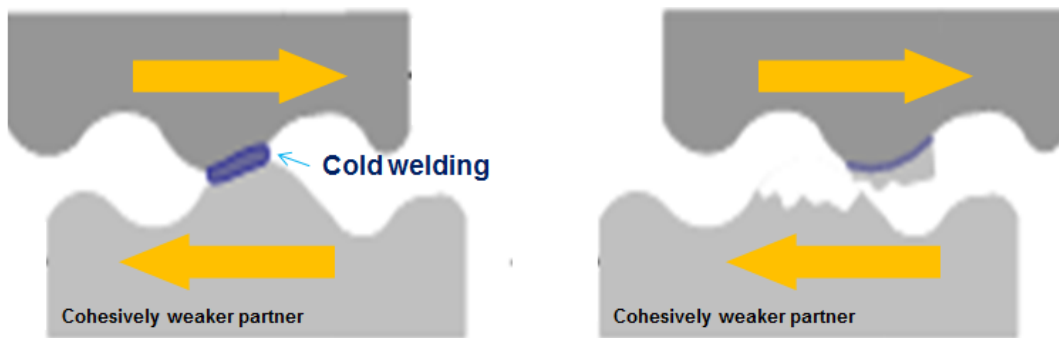


Figure 2-13 Illustration of adhesive wear [69]

The presence of oxides and other surface contamination films affects the adhesion between contacting metal surfaces and generally act as a natural protection layer against cold welding [70]. Under vacuum, such natural layers are removed by outgassing or wear during running-in and they are not rebuilt. As a result, severe adhesive wear occurs.

## 2) Abrasive wear

Abrasive wear happens between two surfaces of different hardnesses as explained in 2.3.2.1. Material from the relatively softer surface is ploughed with plastic material flowing or cut from the bulk material by the hard particles or hard protuberances from the counterpart (Figure 2-14). Abrasive wear is main source of wear, which contributes around 63% of the total cost of wear [71]. There are two main types of abrasive wear:

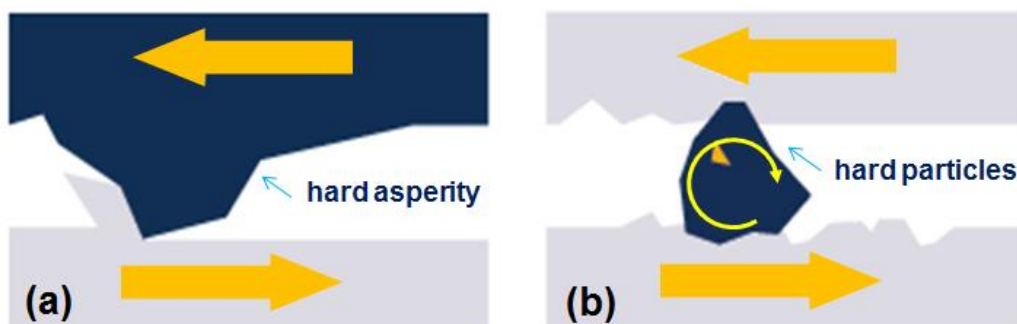


Figure 2-14 Illustration of two-body (a) and three-body (b) abrasive wear [72]

- Two-body abrasive wear

If there are only two parts involved in the wear process and the ploughing or cutting is due to the interference of hard asperities from one surface (or the wear debris fixed in the wear surface) to the other surface, this abrasive wear is called two-body abrasive wear.

- Three-body abrasive wear

When there are free hard particles existing between sliding surfaces, commonly occurring from wear debris generated during sliding, additional wear called three-body abrasive wear occurs and such free particles are called third bodies. The dimension of such particles is from 1  $\mu\text{m}$  to 10  $\mu\text{m}$  [67]. Besides the free particles, the static screens attached on the sliding surface, such as gases layers, oxidation layers and lubrication layers which have composition discontinuity with the sliding surface are also regarded as third bodies. Third bodies present between all the practical sliding surfaces and have an obvious effect on friction [73]. The existing of static screens minimize the adhesion phenomenon between sliding surfaces to avoid serious adhesive wear. During sliding, the free particles can roll and slide between the two contacting surfaces. Although the free particles can abrade the solid surfaces, the rolling movement takes around 90% of the time [71] and the free particles can generate mechanical load carrying phenomenon which protects the sliding surface from severe wear. The three-body abrasive wear has been proved relatively mild compared with two-body abrasive wear [74]. It is reported that the three-body abrasive wear is one order of magnitude lower than two-body abrasive wear [71].

### 2.3.2.3 Lubrication

For the ITER RF sliding contact, during reciprocating linear sliding, abrasive, adhesive and fatigue wears are the predominant wear phenomena. Applying a proper additional liquid or solid separation film between two metallic contact surfaces can reduce friction, wear and heat generation. In addition, fluid lubricants such as oil and grease can help to remove wear debris at the sliding interface, thus reducing the possibility of abrasive wear. However, oil and grease lubricants can pollute ITER high vacuum environment and are generally electrically insulating which are not compatible with electrical contact applications. Compared with fluid lubricants, solid lubricants have significant advantages for vacuum, electrical and high temperature application. Several inorganic materials have been proved with excellent lubrication performance, e.g.  $\text{MoS}_2$ ,  $\text{WS}_2$ , graphite and graphene [75, 76]. As shown in Figure 2-15, all these solid materials have similar crystal structures which are composed of layers held by Van der Waals interactions [77]. During sliding, due to the weak

strength of Van der Waals bonding, when a shear force is applied, these lamellas can slid one over the other, through which the low value of friction force can be achieved.

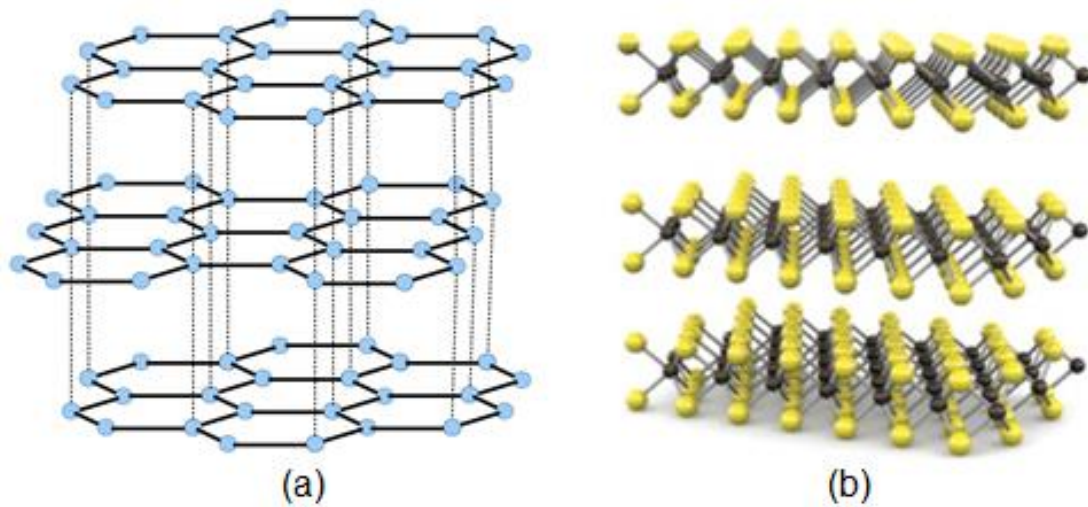


Figure 2-15 Crystal structure of: (a). graphite and (b). MoS<sub>2</sub> [78, 79]

Generally speaking, electrical conductivity of solid lubricants is lower than noble electrical functional coatings (e.g. silver and gold). Moreover, their thermal conductance is lower than noble metals. However, for ITER RF contacts that will sustain heavy current load and have significant heat deposition, dispersing solid lubricants in the metallic matrix which has good electrical and thermal properties could be a solution guarantying good lubricating performance as well as high current and heat conduction efficiency.

### 1) Amorphous carbon

Amorphous carbon (a-C) including diamond-like carbon (DLC) with  $sp^3$  dominant configuration and graphite-like carbon (GLC) containing a high content of  $sp^2$  bonds are widely researched as hardening or solid lubricate particles to achieve protective composite coatings through magnetron sputtering [80-82]. a-C lubricated TiC, WC sputtering coatings show higher wear performance and decrease the wear rate of TiC by a factor of ten [83, 84]. TiN/a-GLC and silver-doped DLC coatings were evaluated as biomaterials which show low coefficients of friction and excellent hardness [85, 86]. Me-DLC (Me: W, Mo, Nb and Ti) co-deposits were investigated and they showed good adhesion performance on their substrates and ultralow CoF of 0.03 [87]. Carbon lubricating materials fail to work properly with low friction and wear in inert, dry, or vacuum environments [88], but adding a-C in the coating can improve the coating's hardness performance to improve its wear performance. There is almost no literature to evaluate the performance of hard Au coatings composited with a-C nanoparticles and the results would be interesting for directing advanced function

coatings' development with integrated wear and electrical performance. In this thesis, Au-Ni/a-C composite coatings were developed by magnetron sputtering and their tribological performance was studied.

## 2) $MoS_2$ and $WS_2$

$MoS_2$  and  $WS_2$  are quite similar from crystal structure aspect. Based on cost considerations,  $MoS_2$  is more commonly used as solid lubricant compared with  $WS_2$  for many applications [89]. However,  $WS_2$  is one of the best solid lubricating materials known and it offers excellent dry lubricity unmatched to any other substance. Moreover,  $WS_2$  has better thermal stability and oxidation resistance at high temperature (650°C in atmosphere and 1316°C in vacuum) compared with  $MoS_2$  (400°C in atmosphere and 600°C -700°C in vacuum) [77, 90, 91]. The high lubricating performances and excellent chemical stability at high temperature make  $WS_2$  a good candidate as solid lubricant material for ITER RF sliding contacts. In this thesis, Au-Co/ $WS_2$  composite coatings were developed through electroplating method and their tribological performance was studied in chapter 5.

## 2.4 Tribological study tools

### 2.4.1 Tribometer configuration and parameters

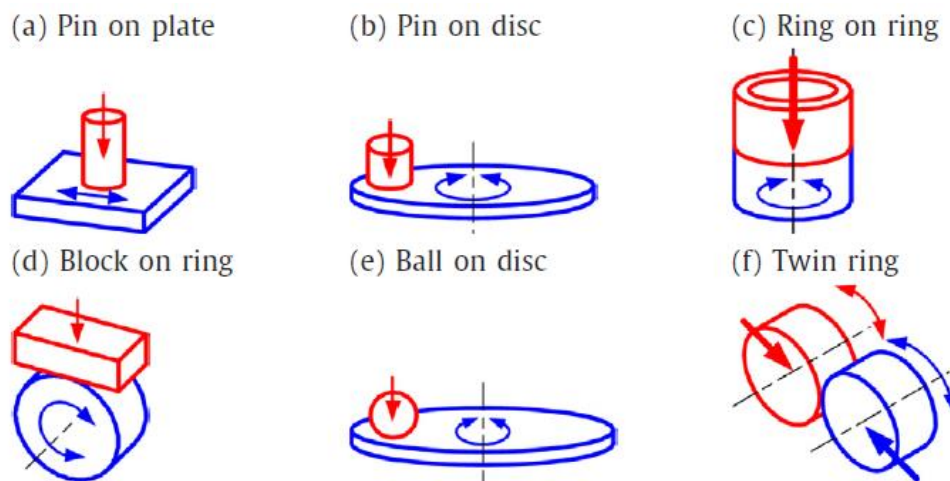


Figure 2-16 Main configurations of tribometers [92]

Tribological characterizations are aimed at determining friction and wear behaviors of the studied material pairs under relevant environmental and thermal conditions. For ITER, these conditions are: vacuum of  $10^{-3}$ - $10^{-4}$  Pa and operational temperature around 200°C. In order to get relevant results, tribometer parameters and motion type should be adapted to the real operational conditions. The categorization of tribometer machines is based on the character of the relative motion between the investigated

pair of materials. Broadly speaking, there are six main types of tribometers (Figure 2-16) [92]. The most commonly used on commercial tribometers to investigate wear and CoF are pin on plate, pin on disc and ball on disc tribometers.

For ITER ICRH RF contacts, during shimming or thermal induced movement, the RF contact fingers will be linearly sliding against the conductor reciprocally under low sliding speed. Therefore, the structure configuration of pin on plate with reciprocating motion is the most suitable for ITER RF sliding contact tribological study. The tip of the pin has a spherical surface to mimic the tip of the RF sliding contact louvers. CoF is an important parameter for ITER RF sliding contact since it constraints the working load of the remote handling system. Wear of functional coatings can induce the variation of  $R_c$ , which is another critical parameter for ITER RF sliding contact development. Therefore, performing contact resistance measurement during tribological tests is mandatory to assess the lifetime of the functional coating. Since no commercial tribometer can fully satisfy the requirements of tribological and electrical tests for ITER RF sliding contact, the development of a specific tribometer is therefore necessary.

The sliding movement of ITER RF sliding contact is a linear sliding at low speed (0.05 mm/s for thermal expansion, 1-5 mm/s for assembly) and the test duration of one tribological test is estimated to 10 hours. For a large quantity of test samples, especially during the coating parameter optimization period when a lot of parallel comparison tests between different coating groups are performed, the tribological tests is inconvenient to be performed under slow linear motion as there will be a high time-consuming. In this case, a vacuum tribometer with ball on disc configuration can be helpful to perform quick tribological experiments. During the coating study period, different coatings from different suppliers were tested under different conditions and on different tribometers. In order to compare all the coatings in parallel, comparison tests were performed on a commercial tribometer in  $N_2$  atmosphere.

#### **2.4.2 Ball on disc tribometers**

The vacuum tribometer used in the thesis for quick coating parameter selection was laboratory-made in the Lanzhou Institute of Chemical Physics (LICP), Chinese Academy of Sciences as Figure 2-17 shows. Ball on disc sliding configuration with dead loads loading system was applied and equipped with a molecular pumping set allowing the tribometer to be operated at  $10^{-4}$  Pa. The tribometer is not equipped with heating system and  $R_c$  measurements.

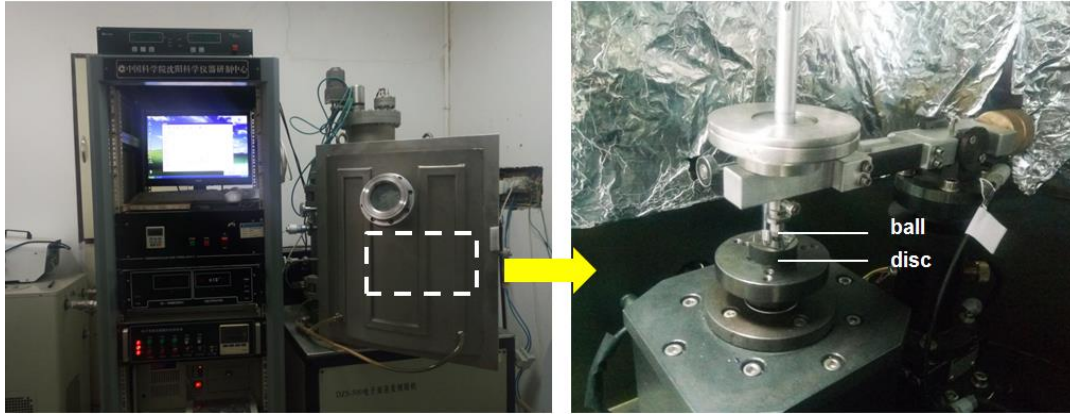


Figure 2-17 High vacuum tribometer

The  $N_2$  atmosphere tribometer that used for different coating comparison is a multifunctional tribometer (Rtec instrument, US) in Université Paul-Sabatier (UPS). Although  $N_2$  environment is not the realistic working condition of ITER RF sliding contacts, in order to avoid the effects of humidity on the tribological performance of Au-Ni/a-C composite coating (Chapter 5),  $N_2$  environment was selected to use.

#### 2.4.3 Pin on plate ITER RF contact specific tribometer

The ITER RF sliding contact support will be actively water cooled. The inlet temperature of the cooling water will be  $90^\circ\text{C}$  and its normal working temperature is estimated at around  $200^\circ\text{C}$  in  $10^{-4}$  Pa based on simulation. This tribometer must have heating capability to the test samples up to  $200^\circ\text{C}$  and must be equipped with a high vacuum pumping system. Slow reciprocating linear motion with sliding speed at mm/s scale is necessary. The normal contact force which is applied should be varied to study the effects of the normal contact force to the Rc and the wear phenomena. Since the time required to reach a high vacuum can be rather long (ten's of hours), a normal contact loading system which can adjust the normal contact force without breaking the high vacuum of the tribometer is an appreciated time-saving advantage. A multi-functional tribometer named: Heatable Vacuum Material Tribological & Electrical Study Testbed (HV-MTEST) was developed to carry out realistic tribological and electrical measurements between materials in ITER device [93]. In the following, the main engineering details related to HV-MTEST development are introduced.

##### 2.4.3.1 System design

###### 1) Overview

The design specifications of the HV-MTEST are summarized in Table 2-1.

Table 2-1 Design specifications of the HV-MTEST

Parameter	Value
Normal contact force	6 N-30 N
Sliding speed	0-10 mm/s
Stroke	±20 mm (Max)
Operating temperature	Room temperature-250°C (steady-state) 250°C-350°C (1 hour)
Vacuum	1 atm-10 <sup>-5</sup> Pa

The Figure 2-18 illustrates the HV-MTEST facility, which consists of six sub-systems, which will be described in the rest of this chapter: a CoF measurement system based on a full-bridge gauge circuit; a normal loading system; an high vacuum/baking system; a motor drive system that allows the reciprocating sliding; a data acquisition & controlling system and a Rc measurement system based on four-terminal method. The main novelties of the proposed multifunctional tribometer machine design lie in its ability to directly control the normal force by adding standard dead loads gradually from the outside of the vacuum vessel without breaking the vacuum, the realistic ITER ICRH RF contact working environment simulation and the precise static measurement of the Rc or dynamic simultaneous measurements of the CoF and Rc.

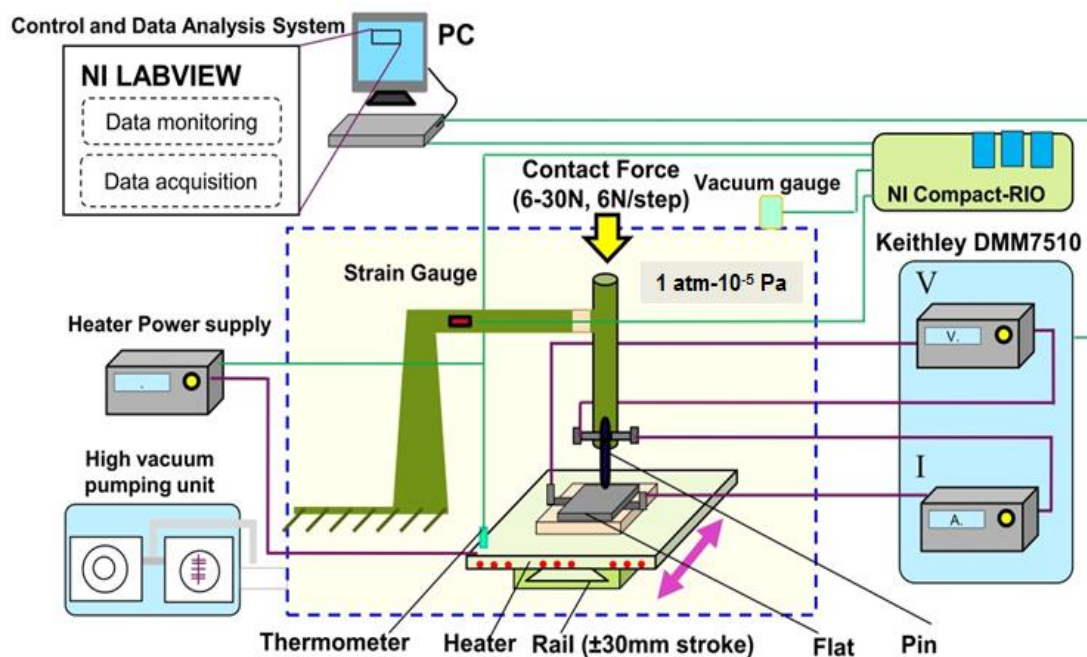


Figure 2-18 Scheme of the HV-MTEST facility

## 2) CoF measurement system

The instantaneous CoF (also denoted  $\mu$ ) is defined as the ratio of the friction force ( $F_f$ ) and the normal contact force ( $F_n$ ) which is expressed as:

$$\mu = \frac{F_f}{F_n} \quad (2-15)$$

Force sensors are the most important and critical elements for accurate tribological measurements which have to respond to some important criteria, like vacuum compatibility, accuracy and repeatability of the measurement [94]. The mandatory calibration procedure is performed in atmosphere condition before the tests, since calibration of the sensors under the same conditions as the real tests is impossible in vacuum conditions. However, due to the thermal and pressure effects during high temperature and high vacuum conditions, misalignment of the force measurement sensors could be generated. Typically, a calibrated force transducer or sensor that results in a measurable response when subjected to friction is commonly used to measure the friction force and such sensors include strain gauges, spring sensors [95], piezoelectric force sensor [92] and S2M load cell [96]. In order to handle the high temperature baking and high vacuum application requirements and minimize measurement errors, strain gauges with nickel-chromium alloy grid, encapsulated in fiberglass-reinforced epoxy phenolic and Teflon insulated connecting wires were selected which can be operated under 260° C steadily.

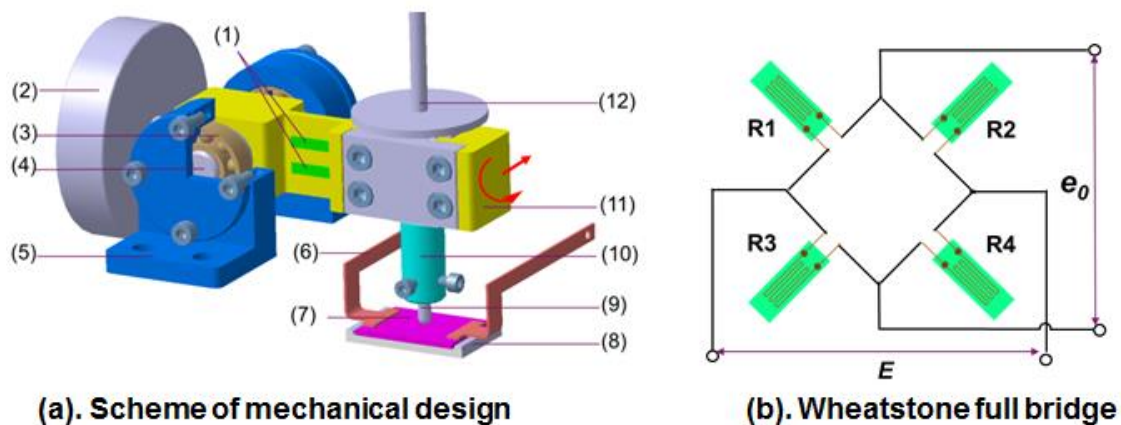


Figure 2-19: (a). Design of the CoF measurement system: (1). Strain gauges ( $\times 4$ ); (2). Counterweight; (3). Bearings ( $\times 2$ ); (4). Central shaft; (5). Beam support; (6). Electrodes ( $\times 2$ ); (7). Plate sample; (8). AlN ceramic plate; (9). Pin sample; (10). Pin sample holder; (11). Cantilever beam; (12). Loading support, (b). Wheatstone full bridge consists of four gauges

The Figure 2-19 describes the main component of the CoF measurement system,

which consists in a cantilever beam supported by two ball bearings and a central shaft. To avoid the self-loading by the gravity force of the cantilever beam on the test samples, a counterweight load is designed to keep its balance. The friction force is measured indirectly by measuring the bending strain caused by the bending moment. A necking part on the cantilever beam is designed to increase the sensitivity. In order to lower outgassing rate and make it high vacuum compatible, all the parts were made of stainless steel 304 with mechanical polishing and degreasing. Accurate measurement of small changes in electric resistance is critical in case of strain gauge application and Wheatstone bridge offers a good method for small strain (few  $\mu\epsilon$ ) measurement [97]. On HV-MTEST, four working gauges are used which are point welded on the two surfaces of the necking part of the cantilever beam symmetrically and then connected in a full-bridge Wheatstone circuit (Figure 2-19 (b)). The main advantage of using such a full bridge circuit is to: improve the sensitivity of the gauge system by amplifying the output voltage to four times than the quarter bridge. The resistance of the lead wire and the temperature induced resistance change can be compensated internally in the full bridge, which improves the accuracy of the system. The pin (with its holder) and the plate sample are insulated with other components by alumina ( $\text{Al}_2\text{O}_3$ ) ceramic plates.

### 3) $R_c$ measurement system

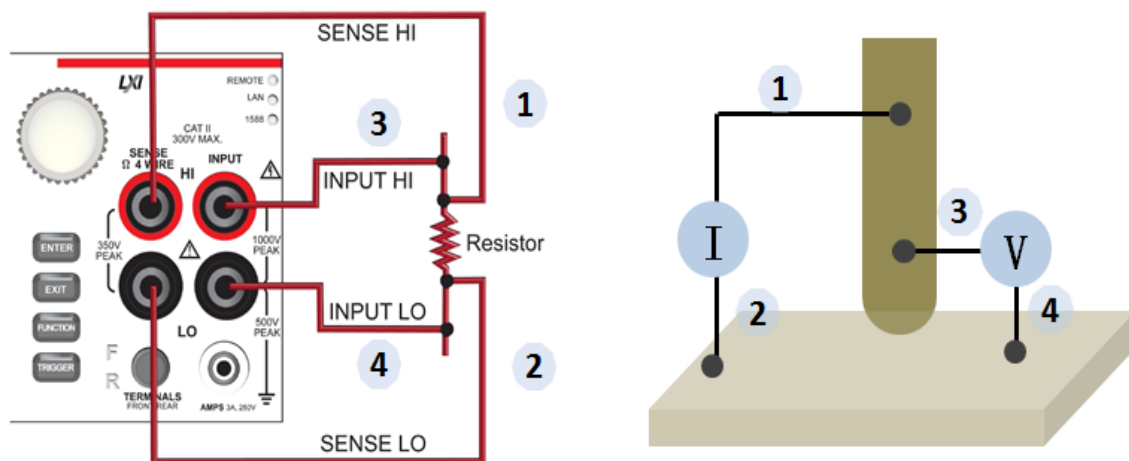


Figure 2-20 Keithley DMM7510 7½ four wire connection for the  $R_c$  measurement

The  $R_c$  measurement is performed by a four-terminal sensing method, which principle is to apply a small current on the electrical contact and measure the voltage drop to calculate  $R_c$  through Ohm's Law. As Figure 2-20 shows, a Keithley DMM7510 7½ precision multimeter is used as the measurement device. A 10 mA DC current is supplied by the multimeter to the electrical contact. It's worth mentioning that the  $R_c$  values aimed to be measured are very low (micro-ohm scale). In this case, the

thermoelectric effect [98] could not be neglected, as the bias voltage can amplify or diminish the voltage drop that happens due to the existing  $R_c$ . The Keithley DMM7510 7½ multimeter has a specific thermoelectric voltage compensation function which was used during the  $R_c$  measurement.

#### 4) *Loading system*

The loading system is designed to apply a constant and stable contact force between the pin and flat samples during sliding. Few techniques can be used to apply the contact force such as dead weight [94], springs [99], screw-drive module [92], etc. Except for the dead weight, almost all the other methods require preliminary calibration, for the system itself or the force transducers. As HV-MTEST is designed for high temperature application, unpredictable thermal effects on the sensors are difficult to eliminate. For this reason, dead weight loading is the most reliable, cheapest and simplest to implement and was chosen on HV-MTEST.

For ITER ICRH RF contact, the normal contact force is an important parameter which has strong effects on the  $R_c$ , CoF and wear rate. Therefore, it needs to be investigated carefully. For the classical tribometers working under ambient atmosphere, the change of contact force can be realized by adding or removing loads manually. However, on a vacuum tribometer like HV-MTEST, the load change is complicated due to the high vacuum test conditions. Indeed, breaking the high vacuum and changing the dead weight is time-consuming. To simplify the loading process, an innovative system was designed as shown in Figure 2-21, by which the normal contact force can be actuated from the outside of the vacuum vessel. Five load plates made of CuCrZr (6 N/ load plate) are connected in series by sixteen hocks and on each of the load plate, four lifting points are mounted to keep the balance of the plates horizontally. The whole load plate assembly is driven by a screw nut mechanism manually from the outside of the vacuum vessel with the vacuum insulation by a bellows. The loading process can be monitored from an observation window. With this flexible loading system, the contact force can be increased from 6 N to 30 N (with 6 N/step) conveniently without breaking the vacuum. This loading system has been patented [100].

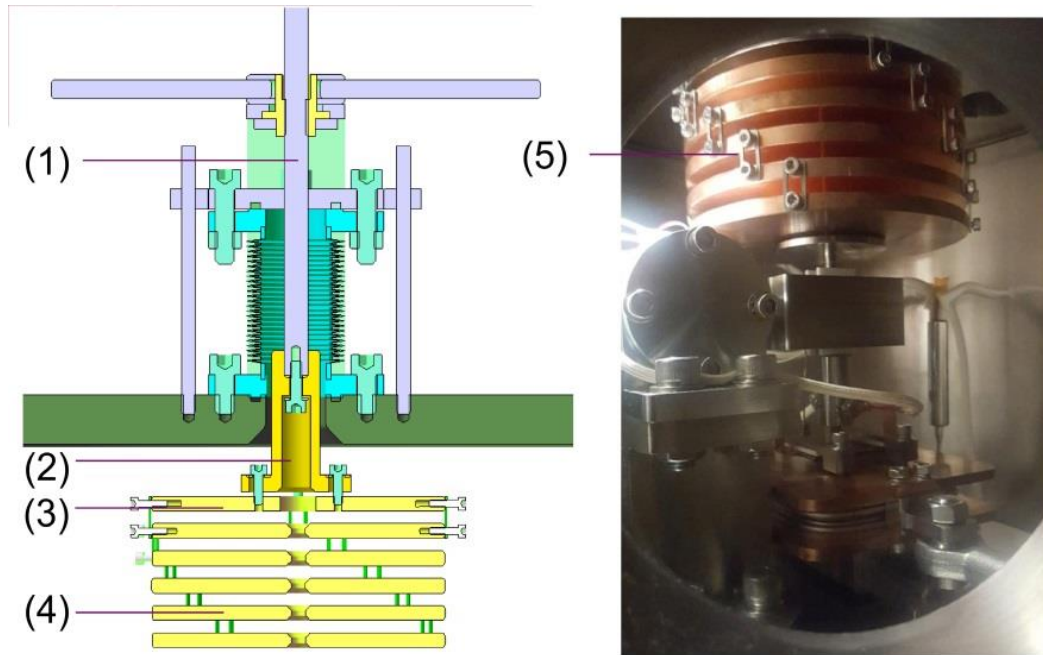


Figure 2-21 Loading system of the HV-MTEST: (1). Load lifting mechanism; (2).  $\text{Al}_2\text{O}_3$  insulation joint; (3). Dead load support; (4). Dead load plates ( $6\text{N} \times 5$ ); (5). Hocks ( $\times 16$ )

#### 5) *Vacuum and baking system*

As the HV-MTEST is designed for the operation under high vacuum level, therefore a high vacuum pumping set consisted of a turbo-molecular pump and a backing diaphragm pump was selected (Figure 2-22). Considering that the vibration of the pumping set during operation may induce the ground noise of the strain gauge measurement system, a bellows is installed between the pump set and the vacuum tank of the HV-MTEST even though it can abate the pumping efficiency of the pump set. Two heaters are installed, one is integrated on the sample holder plate to bake the samples to the expected test temperature and the other is attached around the outside of the vacuum vessel to accelerate the outgassing process and to improve the vacuum by heating the whole tank up to  $150^\circ\text{C}$ . The vacuum of the HV-MTEST could also be improved if needed by changing the gasket from fluoroelastomer to metallic seal.

#### 6) *Motor drive system*

The HV-MTEST uses a reciprocating sliding motion. Drive system main parts like the guide rods, motor, bearing and coupling are installed outside of the vacuum tank of the tribometer and the linear motion is transmitted to the vacuum chamber through a shaft sealed by bellows. An alternating current servo motor is used to serve the rotation. The motion transfer from the motor's rotation to the shaft's linear sliding is realized by a screw nut mechanism with two horizontal guide rods. To compensate for the axis misalignment between the motor and the central shaft, a flexible coupling is

installed. Even though most of the drive system parts needing oil lubrication is placed outside of the vacuum tank, a rail in the vacuum tank that makes the sample holder plate slide steadily is required. Therefore a high vacuum compatible and high precision ball linear guide (THK, Japan) is used.

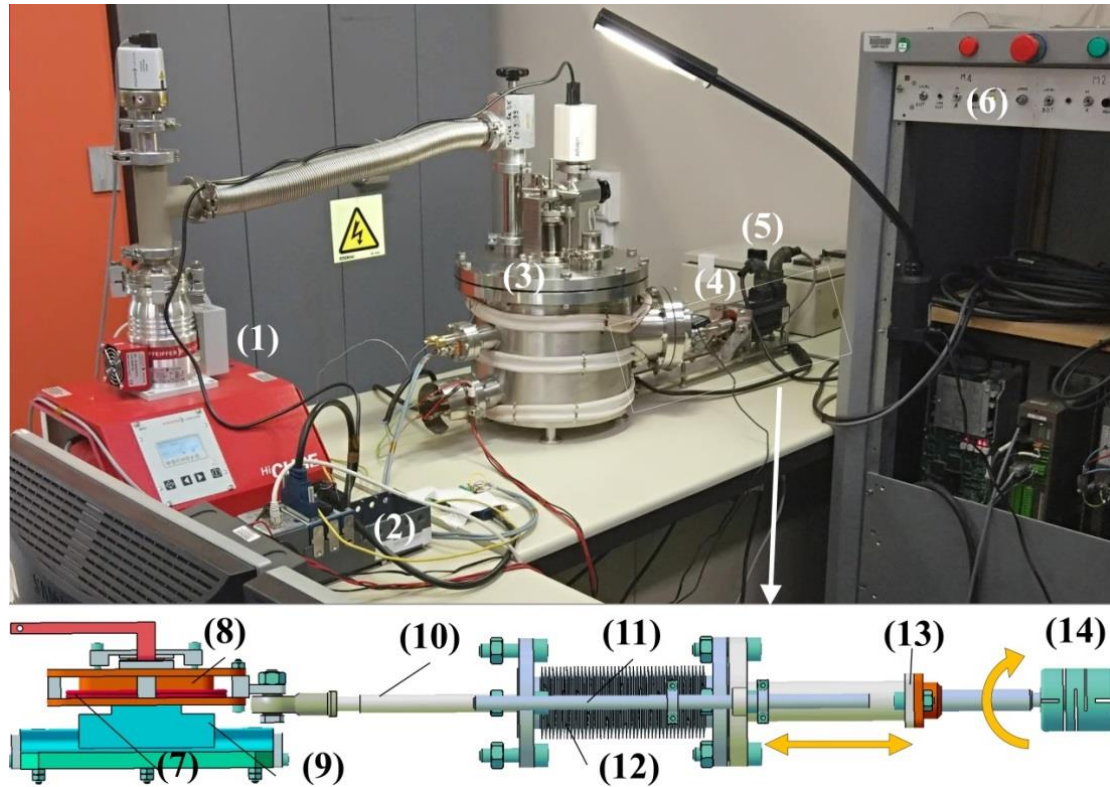


Figure 2-22 A photograph of the HV-MTEST assembly: (1). High vacuum pumping set; (2). NI cRIO-9002; (3). Vacuum tank with heaters; (4). Motor drive system; (5). Temperature regulator; (6). Motor controlling system; (7). Sample heater; (8). Sample holder plate; (9). Ball linear guide; (10). Central shaft; (11). Guide rods; (12). Bellows; (13). Screw nut mechanism; (14). Flexible coupling.

### 7) Data acquisition and controlling system

A National Instrument Compact-RIO which incorporates a real-time processor and a reconfigurable FPGA has been set up for the control and acquisition system [101]. A desktop computer equipped with LabVIEW is dedicated to the data acquisition and the monitoring. The NI Compact-RIO 9002 controller is connected with the PC through an Ethernet link.

The two channels of temperature signals are collected by the thermocouple input module NI 9211. The heaters can be controlled by the temperature regulator (PID controller) precisely with an error of  $\pm 0.5^{\circ}\text{C}$ . The signals of the strain gauge full bridge are acquired by a 24-bit full-bridge module (NI 9237) and the vacuum

gauge signal is acquired by a NI9201 module. The motor is governed by a TRIO-motion controller and is remotely programmed through a self-developed graphical user interface. Single or periodic sliding can be programmed at a velocity varying between 0 to 10 mm/s. The stroke of the plate is defined within (up to) +/- 20 mm.

#### **2.4.3.2 Modeling and simulations results**

Finite element method (FEM) has been used to model and optimize the structure's behavior under exact loads, so as to evaluate the structure's safety or functional performance. During the design of HV-MTEST, ANSYS Mechanical software was used to analyze the key components' mechanical behaviors under friction force, which include: static structural analysis (strain & stress distribution), structural dynamic analysis (natural frequencies and modes of vibration) and fatigue analysis.

##### *1) Structural static analysis and fatigue analysis*

The cantilever beam is the critical component for the CoF measurement, whose design has a strong effect on the sensitivity of the strain gauges. For sensitivity consideration, the thickness of the necking part should be as thin as possible: by applying a small force (friction force), the bending phenomenon of this part could be strong enough to generate a significant output on the Wheatstone bridge. Meanwhile, robust structure of the necking part should be guaranteed to avoid any plastic deformations. Besides the controlling the necking part thickness, designing a rigid supporting structure for the cantilever beam to avoid large elastic deformation on the supporting structure during the CoF measurement tests is another solution to improve the sensitivity of the measurement system. The concept of the CoF measurement is based on the direct measurement of the bending strain on the necking part caused by the friction force. However, except for the bending moment, there is also a torque applied on the cantilever beam (Figure 2-23). Actually, the final strain on the necking part is the combined effect of the bending moment and the torque. The concept of the Wheatstone full bridge measurement is based on the hypothesis that the four strain gauges would have the same elastic deformation. So, choosing an area on the necking part where strain is uniformly distributed for the gauge attachment is meaningful to improve the linear relationship between friction force and strain measured from the full bridge. The application of FEM analysis of the cantilever beam can help to solve the above problems.

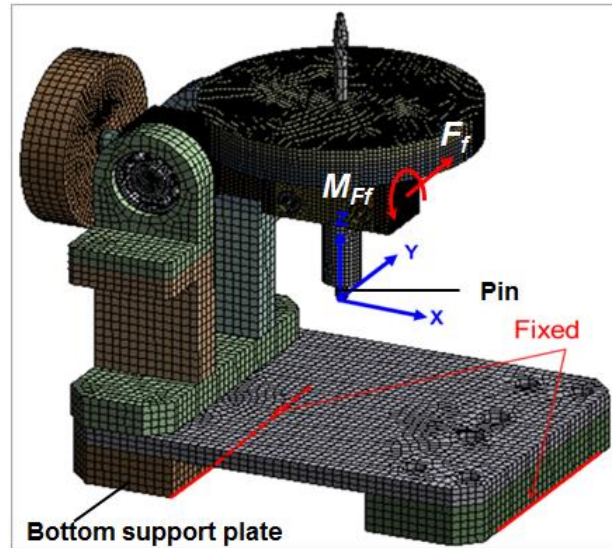


Figure 2-23 FEM and meshing of the HV-MTEST

- Model and mesh

A simplified model of the HV-MTEST main in-vessel components was created as shown in Figure 2-23. In this model, the thickness of the necking part was originally designed as 4mm. After meshing, there are 239999 elements and 1004926 nodes.

- Material properties

The structure is made of stainless steel 304. Considering the normal operating temperature of the test bed is around 200 °C, the material properties of stainless steel 304 at 200°C was used in the analysis (Table 2-2).

Table 2-2 Material properties of stainless steel 304 at 200 °C

Temperature	Density	Young's Modulus	Poisson's Ratio	Thermal expansion coefficient	Thermal conductivity
°C	kg/m <sup>3</sup>	GPa		10 <sup>-6</sup> /K	W/m·K
200	7858	185	0.3	16.6	16.98

- Boundary conditions

The maximum contact force of the HV-MTEST was 30 N and the maximum CoF between the test samples was assumed as 2 (including a safety margin), then the maximum friction force was calculated to 60 N. As shown in Figure 2-23, the friction force (60 N) was applied at the tip of the pin along Y direction. In reality, the bottom support plate is fixed by bolts, so in the analysis it was fixed without movement freedoms in X, Y and Z directions.

- Analysis results

The strain and stress distribution on the necking part and the cantilever beam support are shown in Figure 2-24. Under a friction force of 60 N, the maximum strain generated on the cantilever beam is 0.0463%, which occurs at the thickness transition. In the middle of the necking part, the strain is about 0.02%. The maximum strain is observed on the beam support and is only 0.00126% which shows that the support structure has good stiffness. Under 60 N, the maximum stress on the cantilever beam is about 92.4 MPa and such value is lower than the yield stress of the SS 304 under 350°C whose value is 103 MPa [102]. So, the structure can be operated under 350°C steadily without plastic deformation. It is also shown that, the relatively uniform distribution area of the strain on the necking part is the middle area, which indicates that the gauges should be welded as near as possible to the center of the necking part.

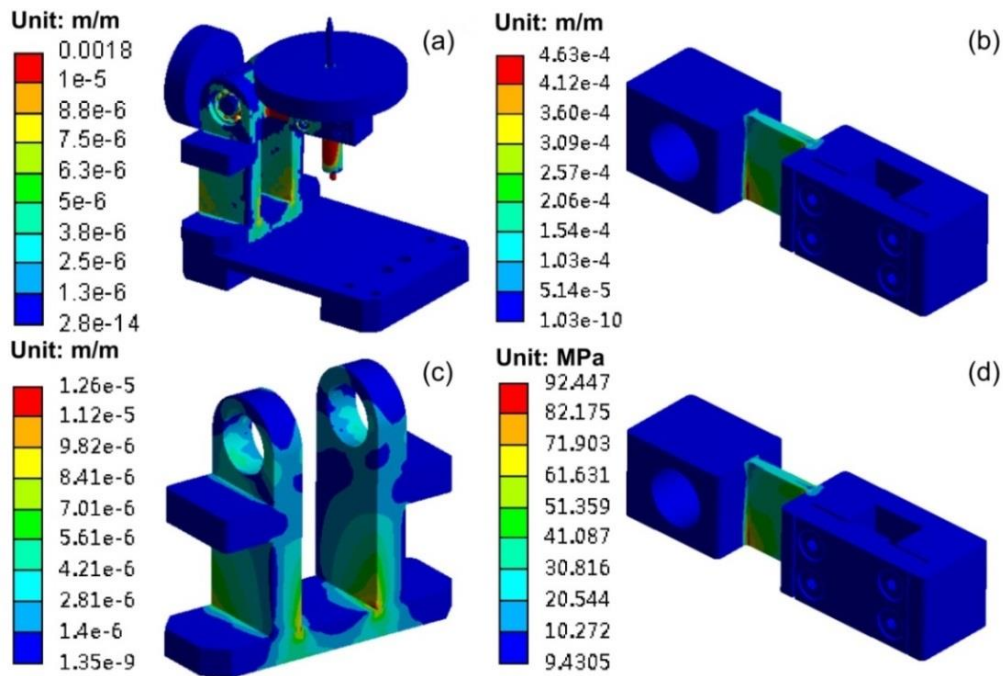


Figure 2-24 Structural analysis results under  $F_f=60$  N: (a). global strain distribution; (b). strain distribution on the cantilever beam; (c). strain distribution on the support; (d). stress distribution on the cantilever beam.

Although the static stress on the tribometer structure is less than the material's mechanical strength, rupture still may occur due to repeated application of stresses which induce fatigue failure [103]. For HV-MTEST, the critical component that subjects to fatigue failure is the cantilever beam on which a necking part was designed. The fatigue loading of the cantilever beam is the friction forces that are intended to be measured. The lifetime of HV-MTEST is specified to be higher than  $2 \times 10^5$  cycles, which indicates that the fatigue of the cantilever beam belongs to high-cycle fatigue

situation [104]. Under friction force of 60 N, the maximum strain on the cantilever beam is 0.0463%. By checking the strain-allowable cycles curve (Figure 2-25), the lifetime of the cantilever beam is higher than  $10^8$  cycles [105]. No fatigue failure is anticipated on the HV-MTEST facility.

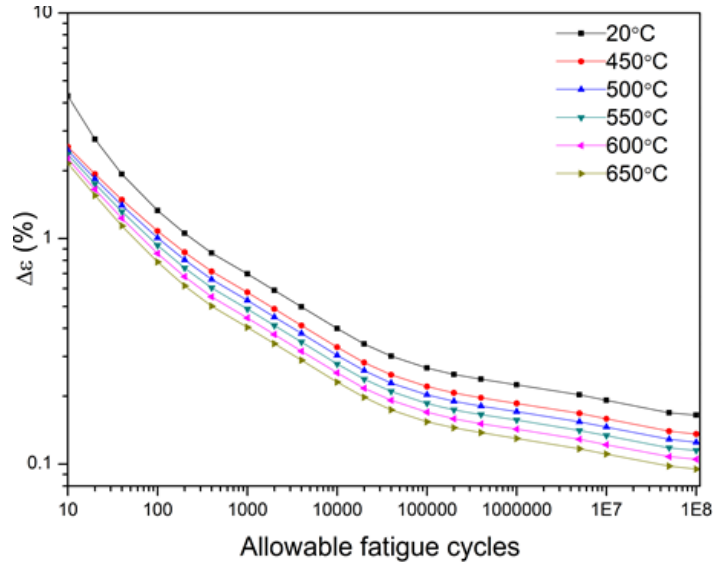


Figure 2-25 Allowable fatigue cycles (N) for 304 type stainless steel [102]

## 2) Dynamic analysis

During the sliding, periodic forces will be exerted on the bean structure, which can generate mechanical vibrations. When the force applied frequency is equal to the natural frequency of the system itself, the amplitude of vibration increases and such vibration not only has large effect on the measurement precision but also threatens the structural safety [106]. Therefore, the mechanical structure should have sufficiently high stiffness in order to increase the natural frequency and reduce the effect of low frequency oscillations. Modal analysis was performed to study the natural frequencies of the tribometer.

- Analysis model

As shown in Figure 2-26, a simplified model was created, which includes: three load plates (18 N) and the cantilever beam assembly.

- Material properties

Same material properties were used as in Table 2-2.

- Boundary conditions

Cylindrical support was applied on the cantilever beam support which can mimic the supporting of the bearings. On the tip of the pin sample, a frictionless support was

applied which can only give support for the gravity of the cantilever beam assembly without applying any other constraints on the model.

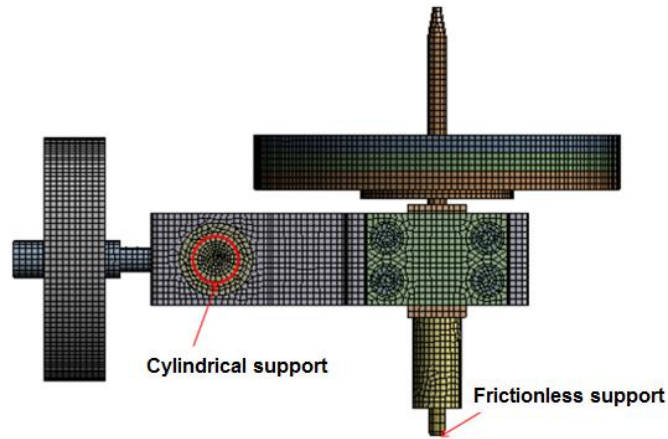


Figure 2-26 Model of modal analysis

- Analysis results

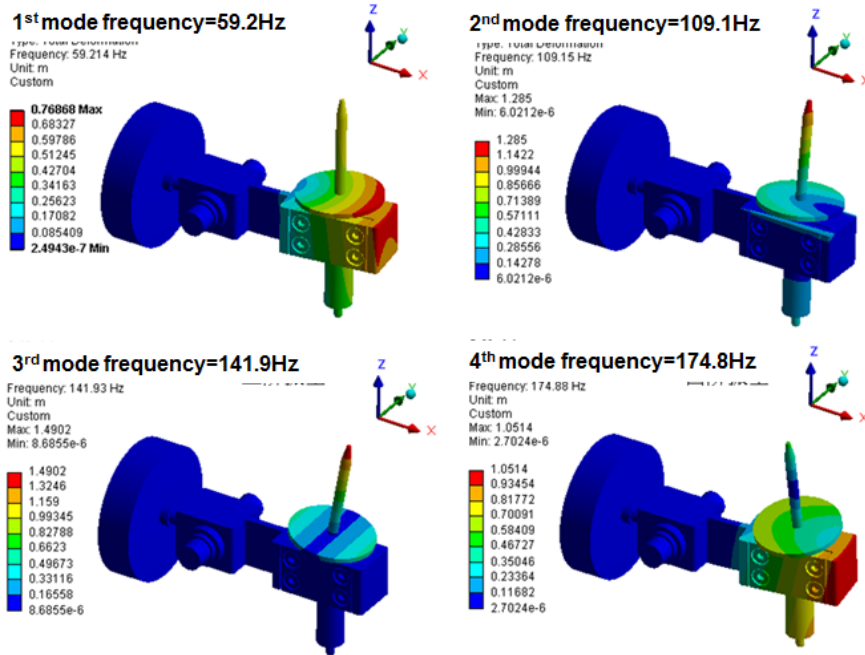


Figure 2-27 Deformation of each mode of natural vibration

The first four modes of natural frequency were calculated. Based on Figure 2-27, the first mode of vibration happens under the frequency of 59.2 Hz and the cantilever beam generates a bending behavior. The second mode of vibration happens under the frequency of 109.1 Hz and the cantilever beam generates a twisting behavior. The third mode of vibration occurs at 141.9 Hz and the deformation response is the twisting of the cantilever beam plus the swing of the loads. The fourth mode of

natural vibration happens at 174.8 Hz and the deformation of the system is similar to the 3<sup>rd</sup> mode. All the modes' natural frequencies are much higher than the excitation frequency from the drive system, so resonances are avoided during the operations of the HV-MTEST.

### 2.4.3.3 Calibration of the CoF measurement system

Since the friction force between samples can't be measured directly, it is deduced from the strain occurring on the cantilever beam. In order to find the corresponding relationship between the friction force and strain, the inherent relationship between the friction force and strain on the cantilever beam's necking part is investigated. Such relationship is determined by the configuration of the beam design.

#### 1) Theoretical calculation

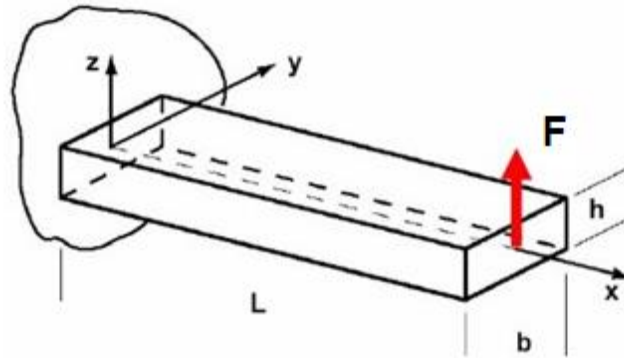


Figure 2-28 Sketch of the cantilever beam with force load

The Figure 2-28 shows a cantilever beam with a rectangle cross-section, whose bending strain can be theoretically calculated by the equation [107]:

$$\varepsilon = \frac{6FL}{bh^2E} \quad (2-16)$$

where  $F$  is the bending force applied on the cantilever beam,  $L$  is the distance between the strain gauge center to the load position (0.0385 m),  $b$  is the width of the cantilever beam (0.03 m),  $h$  is the thickness of the cantilever beam (0.004 m),  $E$  is Young's modulus of the SS304 (200 GPa). The theoretical bending strain corresponds to the bending force is plotted in Figure 2-29 (a).

#### 2) In situ calibration

Unlike the typical way to attach strain gauges, the high temperature strain gauges applied in this study were point welded on the cantilever beam at the edge areas instead of being glued entirely. Therefore, the difference between the strains that

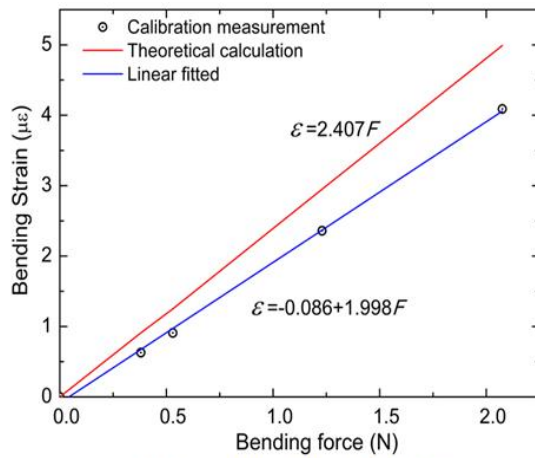
occur on the strain gauge and the cantilever beam is unavoidable. The strain of the cantilever beam is larger than the value that measured by strain gauge. So, several calibration procedures were performed after manufacturing and assembling to investigate the relationship between the friction force and the strain outputted from the grain gauges. The calibration system is shown in Figure 2-29 (b), in which the friction forces were simulated by applying a series of dead loads with different weight (0.38 N, 0.52 N, 1.23 N, 2.07 N) and the strain responses of the cantilever beam were recorded. After measurement, the least squares method was used to fit the expression of the strain  $\varepsilon$  corresponding to a friction force  $F_f$ :

$$\varepsilon = -0.086 + 1.998F_f \quad (\times 10^{-6}) \quad (2-17)$$

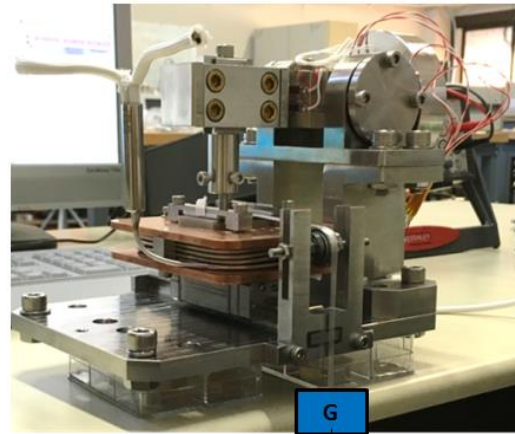
The friction force  $F_f$  which is applied to the pin during sliding can be calculated from the bending strain from:

$$F_f = 0.043 + 0.5\varepsilon \quad (\text{N}) \quad (2-18)$$

The calibration results show that, the HV-MTEST has good linearity property between the input of the friction force and the output of strain.



(a).  $F_f$ - $\varepsilon$  relation of the HV-MTEST



(b). Scheme of insitu calibration

Figure 2-29 Calibration of the HV-MTEST

As the strain gauges cannot be attached to the cantilever beam of the tribometer perfectly. Under the same bending force, the strain occurred on the cantilever beam (theoretical calculation) is a little bit larger than the strain measured by the strain gauges. However, the output (measured strain) has good linear relation with the friction force. Thus, once the calibration line obtained, the real-time  $F_f$  value can be deduced precisely based on the measured strain value.

#### 2.4.3.4 Precision Measurements

Before performing a test in HV-MTEST, few days are required to achieve ITER-like condition of vacuum and temperature. In order to mimic the ITER RF sliding contact's real sliding conditions, the tribological tests on HV-MTEST are performed under low sliding speeds (0.5-2 mm/s). Generally, the duration of one test is around 10 hours for 1000 cycles. Performing a new test requires to break the vacuum to change the sample. Therefore, it's not convenient to perform a large number of tests. This means that, the test bed developed should have good result reproducibility, in other words, it should have a high precision of measurement.

For measurement there are three general types of errors occur in lab measurements: random error, systematic error and gross errors. Gross errors are caused by the operator's carelessness or equipment broken, which should be avoided during any measurements.

Systematic errors are instrumental, methodological, or personal mistakes causing "lopsided" data, which is consistently deviated in one direction from the true value. Systematic errors can be identified and eliminated after careful inspection of the experimental methods, cross-calibration of instruments and examination of techniques. Systematic errors reveal the "accuracy" of the measurements [108].

Random errors are the components of measurement errors that vary in an unpredictable manner in replicated measurements [108]. Random errors characterize the reproducibility of measurements, and therefore, the "precision". Random errors are affected by the measuring techniques, sample properties, etc. The random error can only be minimized such as performing multiple experiments to do the average, but will never be avoided. A parameter that is typically used for quantifying random error is the standard deviation.

In order to evaluate the test bed's precision, four tests were performed under the same conditions (normal contact force: 6 N, sliding speed: 1mm/s, stroke:  $\pm 16$  mm, pressure: atmosphere, cycles: 40) between the CuCrZr pin and stainless steel 316L plate. The standard deviations of the CoF and Rc in each sliding cycle are calculated through:

$$\sigma_i = \sqrt{\frac{1}{3} \sum_{j=1}^4 (\mu_{j,i} - \bar{\mu}_i)^2} \quad (2-19)$$

where  $\mu_{j,i}$  is the result of the  $j^{\text{th}}$  measurement of the  $i^{\text{th}}$  sliding cycle and  $\bar{\mu}_i$  is the arithmetic mean of the four results.

### 1) Precision of CoF measurement

As shown in Figure 2-30, the CoF measurement results during the four tests have good reproducibility. From Figure 2-31, the standard deviation is quite stable in each cycle, with a maximum and minimum values of 0.022 and 0.002 respectively. Compared with high CoF values that are aiming to be measured, such error is very low. In a word, the HV-MTEST has a good reproducibility of CoF measurement and a high measurement precision.

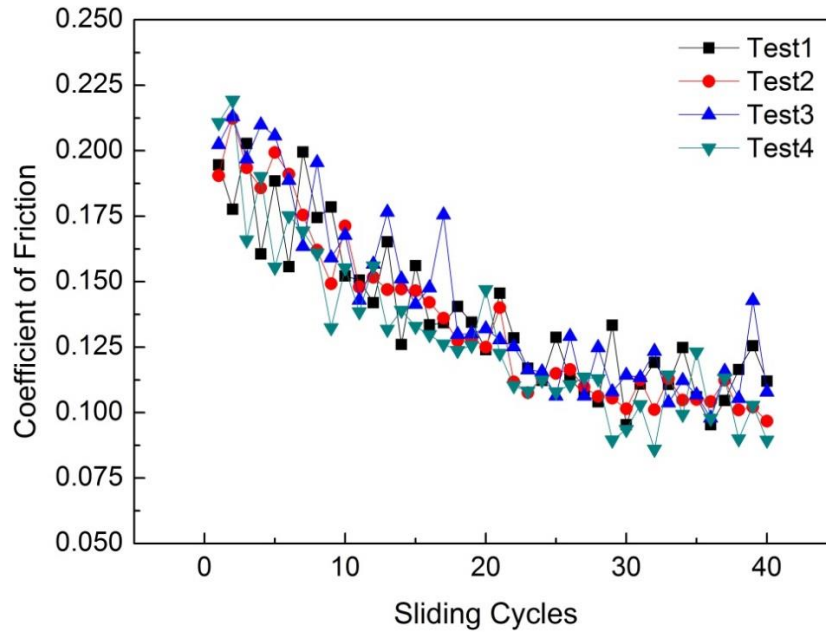


Figure 2-30 Results of CoF during 1-40 cycles <sup>[1]</sup>

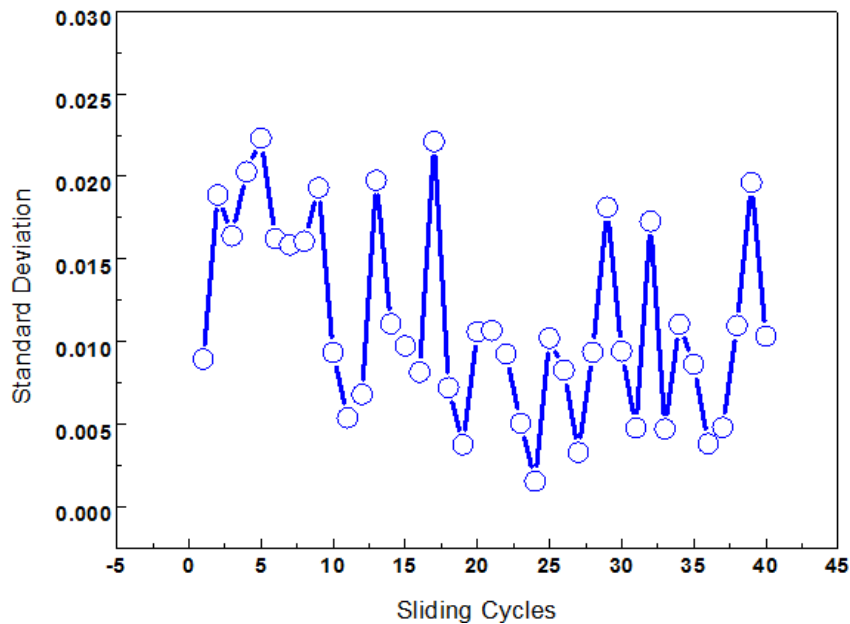
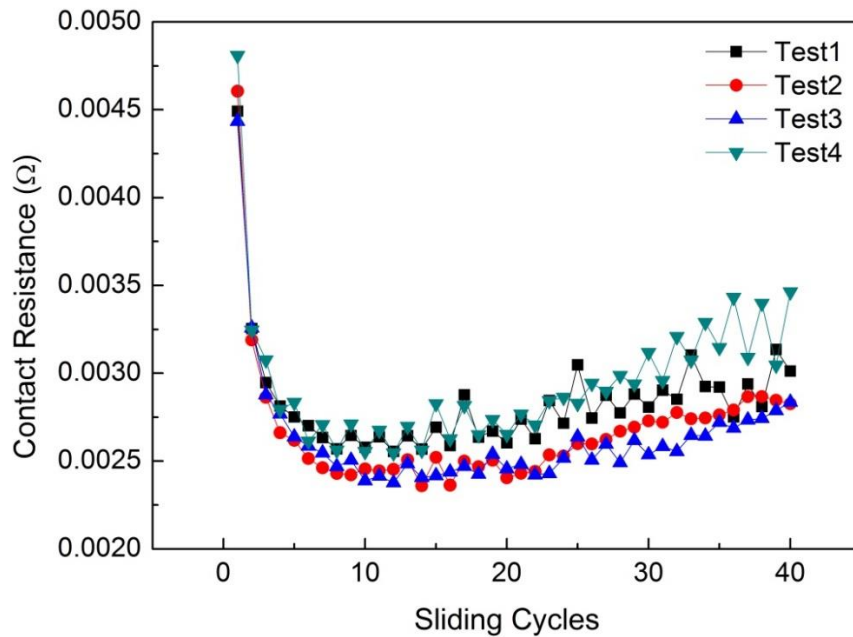
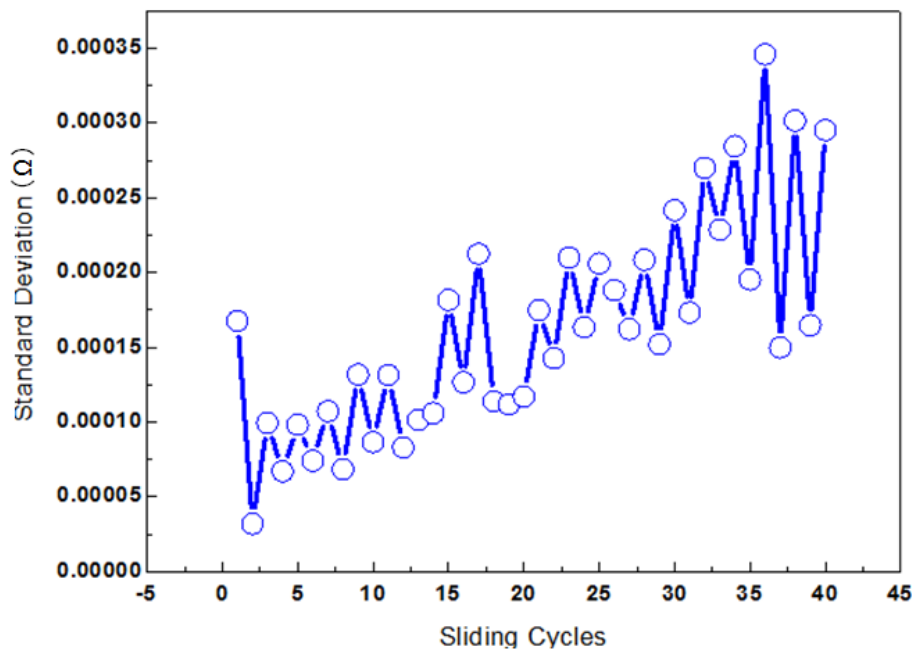


Figure 2-31 Standard deviation of CoF during 1-40 cycles

[1]. The plotting methods of CoF and Rc on HV-MTEST test bed are introduced in Appendix A

2) Precision of  $R_c$  measurementFigure 2-32 Results of  $R_c$  during 1-40 cyclesFigure 2-33 Standard deviation of  $R_c$  during 1-40 cycles

As Figure 2-32 and Figure 2-33 show, the four  $R_c$  tests results show similar  $R_c$  change tendency. In the beginning, the standard deviation was kept under a low value (0.1 m $\Omega$ ), however, after 15 cycles the standard deviation increased to 0.3 m $\Omega$ . The degradation of  $R_c$  measurement reproducibility with the sliding cycle number increase is due to the wear of test surfaces. The wear of the samples induced small mechanical vibration between the test samples. Although such vibration has no effects to the CoF

measurement, it can have obvious effects on the  $R_c$  measurements as our  $R_c$  measurement is in milliohm scale. However, the maximum standard deviation of  $R_c$  during the  $R_c$  measurements is below 10% of measured  $R_c$  value. Thus, from engineering aspects,  $R_c$  values measured from HV-MTEST test bed can give a good reference to the engineering design of the ITER RF sliding contact.

#### 2.4.4 Overview of tribological test parameters

Table 2-3 Tribological test conditions on different tribometers

Parameters	<b>RF sliding contact</b>	<b>CEA tribometer</b>	<b>LICP tribometer</b>	<b>UPS tribometer</b>
<i>Atmosphere</i>	$10^{-3}$ - $10^{-4}$ Pa vacuum	$10^{-3}$ - $10^{-4}$ Pa vacuum	$10^{-3}$ - $10^{-4}$ Pa vacuum	1 atm $N_2$
<i>Movement</i>	linear sliding	linear sliding	rotating	rotating
<i>Linear (equivalent) speed</i>	0.05 mm/s and 1-5 mm/s	1mm/s	84 mm/s	84 mm/s
<i>Max. contact pressure</i>	to be studied	896 MPa	970 MPa	970 MPa
<i>Sliding cycles</i>	30000	2000	8000	4000
<i>Total sliding length</i>	90 m	32 m	201 m	63 m
<i>Temperature</i>	175°C	200°C	25°C	25°C

As Table 2-3 shows, three tribometers were used in this thesis study, the CEA tribometer (HV-MTEST, introduced in section 2.4.3) can mimic ITER sliding RF contact relevant operational conditions and commercial electrical functional coatings: Au-Ni vs. Rh (section 4.3.2 and section 4.3.3), Ag vs. Rh (section 4.3.4 and section 4.3.5) were tested on it under ITER relevant conditions. During the developing of self-lubricating composite coatings, as there are many test samples (obtained from different coating parameters) with the constriction of sample size and test duration, it's inconvenient to use the HV-MTEST tribometer to perform the comparison tests in each coating group. So, a vacuum tribometer (LICP tribometer) with rotating movement in room temperature was applied to do the coating comparison tests in each coating group: Au-Ni/a-C composite coating group (section 5.1.2.5) and Au-Co/WS<sub>2</sub> composite coating group (section 5.2.2.4). Since the tribological tests of the commercial functional coatings and the developed composite coatings were tested

on different tribometer with different conditions, in order to compare them parallel, the best coatings from each group were selected and they were tested and compared on the UPS commercial tribometer under N<sub>2</sub> gas environment (Section 5.3).

## Chapter 3 Experimental study and failure analysis of Multi-Contact LA-CUT contact

### LA-CUT contact

ITER RF sliding contacts will be working in a complex environment, with high vacuum, high temperature and heavy RF current load. Although FEM method is widely used in engineering study to validate components' safety, the modeling and boundary conditions are generally simplified from their realistic ones. Thus, when there are multi-physics factors involved, the simulation results may have large difference with their real values. For ITER RF sliding contacts, the mechanical structure of the contact louvers are complex and the contact interfaces are generated through engineering bodies with rough surfaces. In finite element simulation, the boundary conditions such as Rc and thermal resistance are hard to model, in particular for RF currents and as a result, the analysis is not thoroughly believable. For this reason, ITER RF sliding contact development used 1:1 prototype tests on the dedicated testbed to investigate current carrying capability of the contact and FEM to help to understand the failure mechanism as well as to do the design optimization.

### 3.1 ITER RF sliding contact prototype design

Sliding electrical contacts have very distinctive characters to guarantee the electrical connection and mechanical sliding. Generally, sliding electrical contacts contain a large number of parallel louvers which can be compressed elastically. Improving the electrical contact performance and wear performance are the critical issues related with sliding electrical development and usually they are contradictory to each other. Especially for ITER RF sliding contacts, which are expected to be operated under high current load and have long lifetime, more attention should be paid to the mechanical design and material selection.

#### 3.1.1 RF sliding contact configuration selection

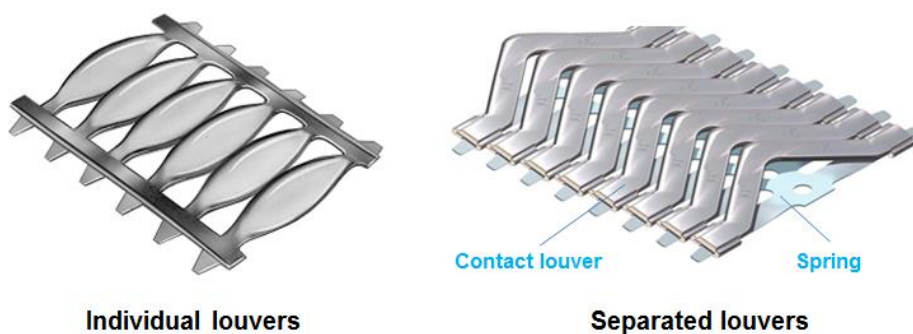


Figure 3-1 Commercial sliding electrical contact designs [19]

As introduced, the RF sliding contact should have compressive flexible contact

louvers to apply contact force. There are two kinds of louver designs which can realize this purpose: individual or separated louvers (Figure 3-1).

For individual louver sliding contact, the contact louvers are both the electrical current flowing media and the flexible mechanical support. The design is more compact compared with the separated louver configuration. In order to combine these two functions, the material used for this kind of contact should have good electrical, thermal and elastic properties. It's quite hard to find a material that can meet all the above properties. So, individual louver configuration is only suitable for low current sliding contact application which has low requirements on the material's electrical conductivity or mechanical performance. ITER RF sliding contact is a heavy load electrical contact, thus individual louver configuration is not suitable.

Separated louvers are the other sliding electrical contact configuration on which a functional division is realized between the contact louvers and the spring element. The main advantage of this configuration is that the louvers and the spring element can be manufactured with different materials. During design, the selection of the louver materials focuses on their electrical and thermal performances while for the spring element materials the focus is made on mechanical properties (e.g., fatigue strength and yield stress). Separated louvers sliding contact configuration (such as LA-CUT, from Stäubli Multi-Contact [19]) has been tested for ITER RF sliding contact development. With the LA-CUT product, there is no mechanical bonding between the contact strip and the conductor: the LA-CUT contact strip is inserted into a groove (Figure 3-2). Therefore, this type of sliding electrical contact can be replaced easily but at the price of a serious reduction of the heat transfer between the strip and the holding conductor.

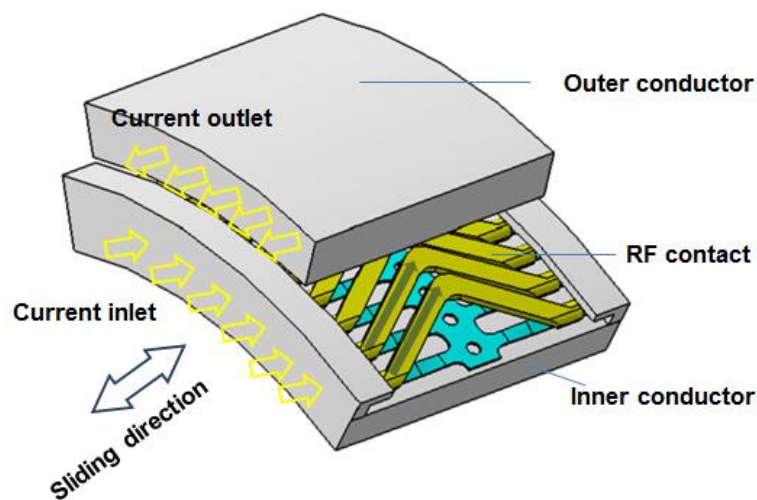


Figure 3-2 Schematic of LA-CUT sliding contact assembly

### 3.1.2 Base material selection for the RF contact

The Figure 3-2 shows an ITER RF sliding contact design where there are two primary materials: the base materials for the conductors and the base material for the contact louvers. For commercial LA-CUT contact, the contact louvers can be made of oxygen-free high conductivity (OFHC) copper which has high electrical conductivity and thermal conductivity. However, for ITER application, the mechanical properties of copper have to be improved to resist ITER 250°C (850 days cumulative) outgas baking and high temperature during operation, in which creeping issues can lead to failure[109].

Adding hetero-elements in a metal matrix to generate metal alloys can improve the microstructure of the pure metal and increases some of its material properties. For copper, common copper alloys are CuCrZr, CuBe, CuCr and CuNiBe. Their main mechanical and thermal properties are shown in Figure 3-3 and Figure 3-4. OFHC shows poor performance in yield stress under all temperatures. CuBe and CuNiBe have higher mechanical strength, around seven times higher than OFHC and have a higher thermal stability under mechanical strength under temperature up to 300°C. On the Large Hadron Collider (LHC) in CERN, RF contacts support a nominal beam current of 0.6 A and CuBe is used for the contact louvers' manufacturing [110, 111]. For ITER RF contacts which are expected to be operated under 2 kA, the relatively high resistivity and relatively low thermal conductivity of CuBe make it improper to use.

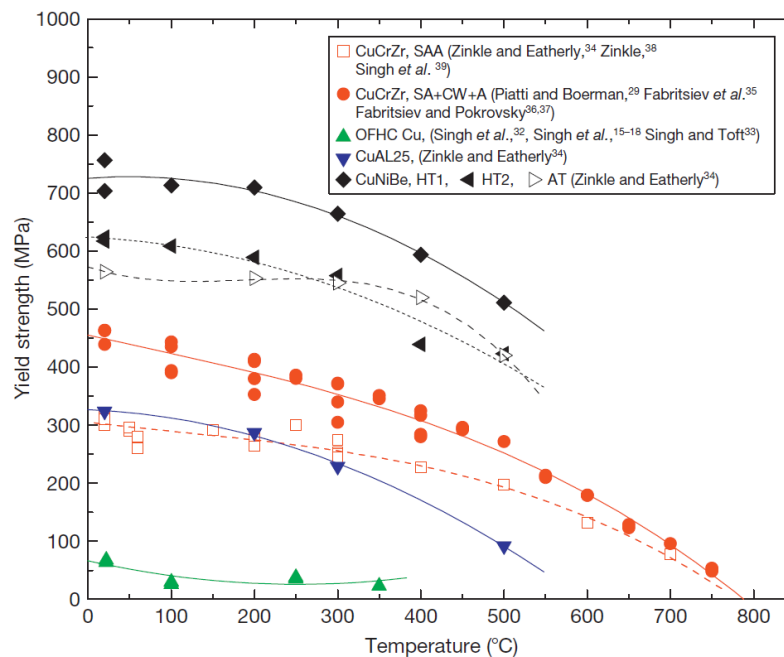


Figure 3-3 Yield stresses of copper alloys under different temperature [112]

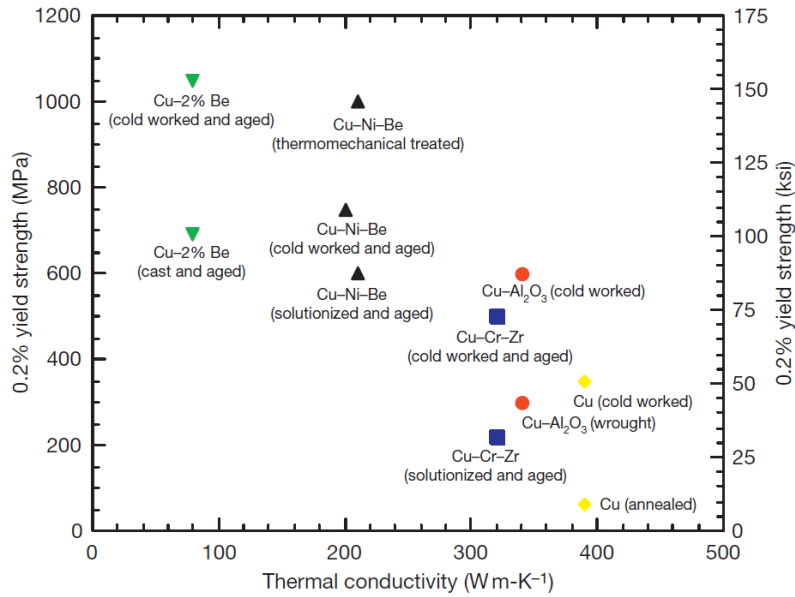


Figure 3-4 Yield stresses and thermal conductivities of copper alloys [112]

CuCrZr shows good mechanical performance even under high temperature at 250°C and its yield strength is about 5 times higher than OFHC. Moreover, the electrical conductivity and thermal conductivity of CuCrZr at room temperature are similar to OFHC, which are 77% IACS (International Annealed Copper Standard) [113, 114] and 80% IACS respectively. Consequently, they are suitable for high loading parts such as springs, which conduct electricity, contact wheel, etc [115]. CuCrZr alloy is widely used on fusion experimental devices as heat sink material [116-120], due to its excellent thermal conductivity, strength and fatigue resistance [121]. So, CuCrZr becomes an interesting material for ITER to manufacture the RF contact louvers. Like pure copper, Cu<sub>2</sub>O and/or CuO will form on the CuCrZr surface due to oxidation when exposed to atmosphere [121-124]. A functional coating to protect from oxidation and also to minimize contact resistance is then required. Gold or silver coating are generally selected to cover the surface of the contact louvers.

For the base material of ITER RF conductors, currently titanium is selected [17]. However, considering the large mass of the ITER ICRH antenna RF conductors, the application of titanium as base material is costly. Common structural base materials such as 316L and CuCrZr are also proposed. In this thesis study, the base materials of the RF conductor are focused on 316 L and CuCrZr.

### 3.2 RF tests of LA-CUT prototype

The RF contact prototype's investigation requires extensive tests at nominal RF current under high vacuum. Moreover, sliding tests should be performed during RF operation to ensure that the RF prototype tested can fulfill the sliding movement under high temperature and high vacuum as required. In order to mimic ITER

operational conditions for RF contact prototype tests, a dedicated test bench was developed in CEA [125, 126]. This testbed is a RF resonator (T-resonator) which operating conditions are:

- 2.25 kA at 62 MHz during quasi-continuous operation (20' -30')
- Vacuum pressure  $<10^{-3}$  Pa
- Water cooling from 20°C to 250°C
- Short displacements can be realized to mimic the relative thermal displacements of the ITER ICRH antenna, with or without RF application

### 3.2.1 T-Resonator Setup

The setup, illustrated in Figure 3-5, consists in a rigid coaxial resonator, made of two main branches approximately 2.2 meters long. Both branches are RF powered from a RF source feeding through a T-junction and are ended by adjustable short-circuits referred as trolleys hereafter. A vacuum feedthrough is located upstream of the T-junction, which allows the T-resonator to be vacuum pumped. Electric heating cables are wrapped around the outer conductors of the two branches for baking purposes.

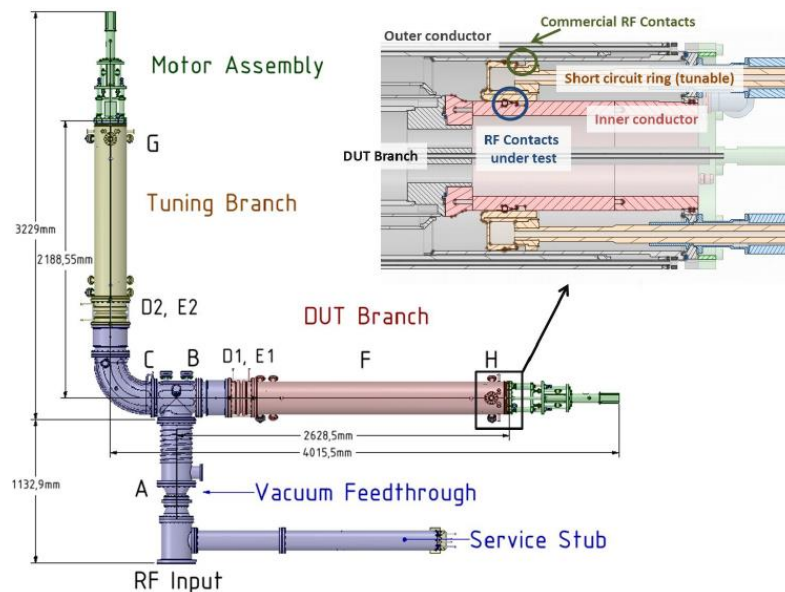


Figure 3-5 T-Resonator description[109]

In order to match the resonator, both short circuit lengths can be tuned by sliding the trolleys. In addition to tuning the short circuit lengths, the frequency of the RF source can also be adjusted to achieve matching of the T-resonator. Once the T-resonator is matched, a steady-state current generates at the short circuit area where the tested RF contact prototype is located. The value of the current is deduced through the voltage values measured by voltage probes [127].

### 3.2.2 RF Contact holder

#### 3.2.2.1 RF contact holder design

The contact holder is the component that supports the LA-CUT contact during the RF test on the T-resonator test bench. This holder has a similar dimension than the ITER ICRH antenna central conductor (Figure 3-6). The LA-CUT contact strip is installed in the dedicated groove on the contact holder which is made of 316L. Cooling channels are included in the holder to remove the RF heat losses during operation. Skin effect makes the majority of current flow through the skin surface, so a 100  $\mu\text{m}$  thick Cu is deposited on the surface of the RF contact holder to minimize Ohmic loss.

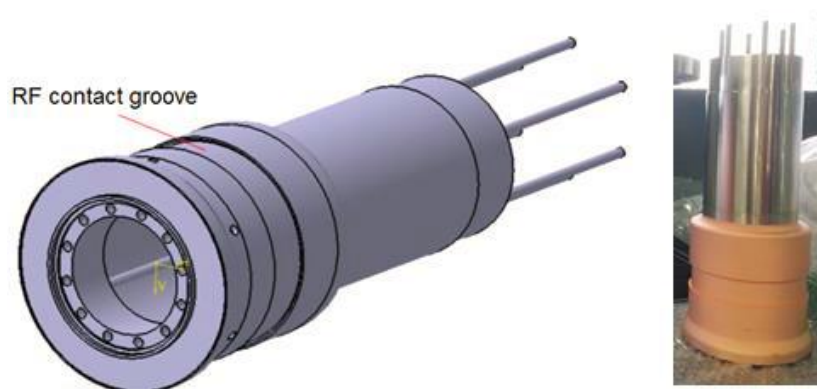


Figure 3-6 RF contact holder design

The LA-CUT RF contact prototype's current carrying capability is not only influenced by its own geometry, but also restricted by the cooling design of the RF contact holder. Design a reliable and sufficient cooling system for the RF contact holder is the prerequisite to achieve the performance of the RF contact itself. The cooling loop is designed as Figure 3-7 shows. According to ITER design specifications, the ITER inlet water temperature is 90°C [126].

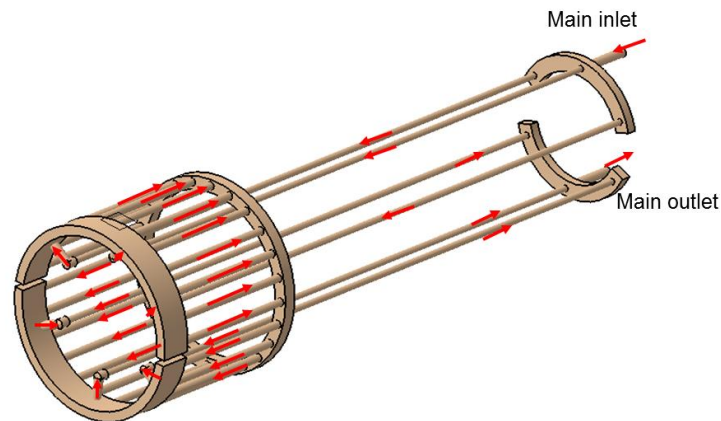


Figure 3-7 Water cooling loop design of the RF contact holder

### 3.2.2.2 Thermal-hydraulic analysis

The cooling performance of water depends on its flowing state. Compared with laminar flow, turbulent flow improves the thermal exchange between the coolant and the inner wall of the cooling pipe but induces higher pressure drops at the same time. Therefore, it's necessary to check the feasibility of the selected cooling parameters by using fluid and thermal simulation with ANSYS.

#### 1) Fluid analysis

- Model and mesh

The liquid domain was created by filling the cooling channels. Three inflations layers were created on the surface of the coolant model for analysis precision consideration (Figure 3-8).

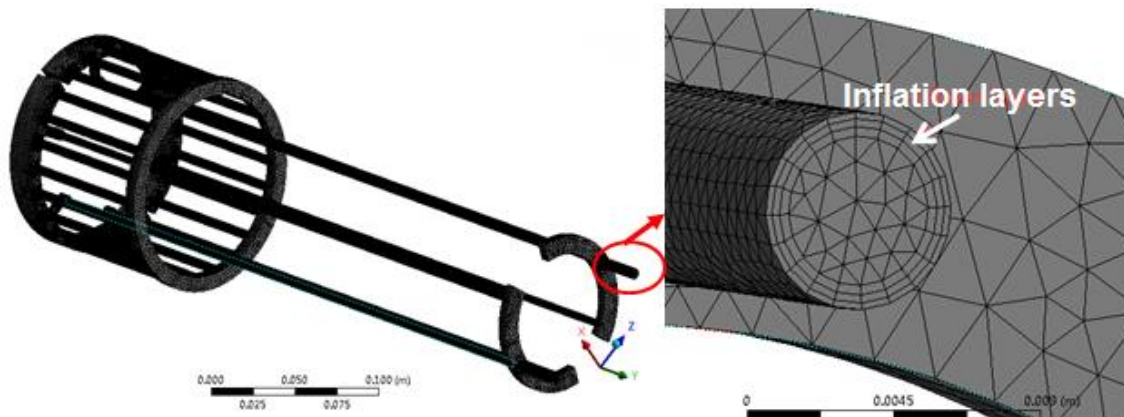


Figure 3-8 Fluid analysis model and mesh

- Material properties

The physical parameters of 90 °C water are summarized in Table 3-1.

Table 3-1 Physical properties of water at 90°C

Temperature [ °C ]	Density [ kg/m <sup>3</sup> ]	Specific Heat Capacity [ J/kg·K ]	Viscosity [ kg/m·s ]	Thermal Conductivity [ W/m·K ]
90	955.3	4187	$3.15 \times 10^{-4}$	0.66

- Boundary conditions

The following boundary conditions have been applied:

- At inlet, static pressure = 17 bar, temperature = 90°C.
- At outlet, mass flow rate= 0.3 kg/s (case1), 0.5 kg/s (case2)

- Analysis results

Two mass flow rates cases were studied and compared. The pressure and velocity distribution of cooling water under these two cases are shown in Figure 3-9.

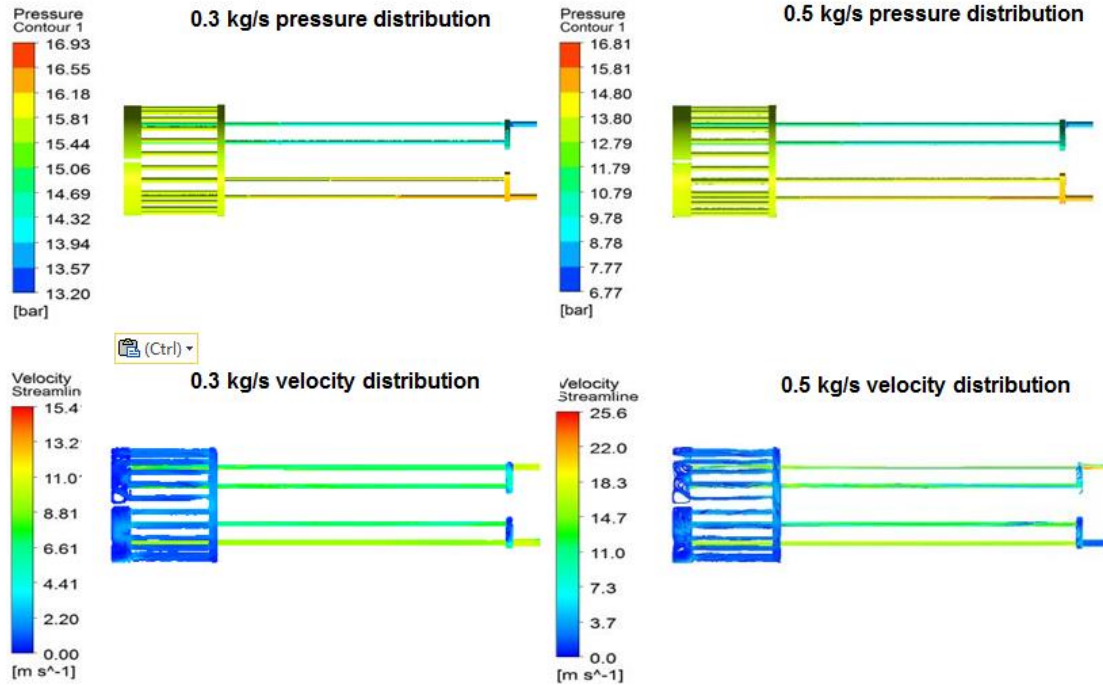


Figure 3-9 Fluid analysis results under mass flow rates of 0.3kg/s and 0.5kg/s

Under the mass flow rate of 0.3 kg/s, the pressure drop of the cooling system is 3.4 bar with a maximum flowing velocity of 15.4 m/s. When the mass flow rate increases to 0.5 kg/s, the pressure drop increases significantly to 8 bar. The large pressure drop is due to the long cooling pipes with small diameters which cause friction loss. Moreover, local diameter sudden changes in the cooling channel cause local pressure drops. According to the analysis results, increasing mass flow rate to improve cooling performance should be carefully evaluated to avoid high pressure drop.

The final temperature distribution on the RF contact holder is the final criteria for the cooling parameter selection. Thermal analysis was then carried out following the fluid analysis.

## 2) Thermal analysis

Ohmic losses are the main heat source for the RF contact holder, so calculating Ohmic losses is the first step for the thermal analysis. When the current flowing through conductors, the Ohmic loss  $P$  can be expressed as:

$$P = I^2 \cdot R = I^2 \cdot \frac{\rho \cdot l}{\pi [r^2 - (r - \delta)^2]} \quad (3-1)$$

where  $I$  is the value of the current (A),  $r$  is the radius of the conductor cross-section,  $\delta$  is the value of skin depth and  $\rho$  is the electrical resistivity of the conductor material (considering that the 100  $\mu\text{m}$  of copper coating are higher than one RF current's skin depth, copper electric resistivity is used, so here  $\rho = 1.68 \mu\Omega \cdot \text{cm}$ ),  $l$  is the length of the conductor.

As the skin depth is in micrometer scale, therefore, applying all the heat loads on the surface of the conductor will not cause large error. The heat loads were applied as heat fluxes which are calculated through:

$$q = \frac{P}{S} = I^2 \cdot \frac{\rho}{\pi [r^2 - (r - \delta)^2] \cdot 2\pi r} \quad (3-2)$$

where  $S$  is the outer surface area.

- Model and mesh

The thermal analysis model was created as shown in Figure 3-10.

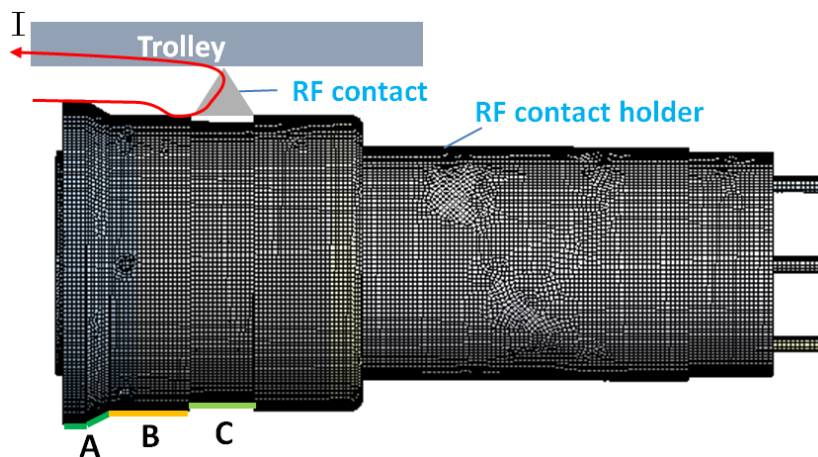


Figure 3-10 RF contact holder thermal analysis model

- Material properties

The base material of the RF contact holder is 316L, the material properties are summarized in Table 3-2.

Table 3-2 Material properties of 316L

Density	Young's Modulus	Poisson's Ratio	Thermal expansion coefficient	Thermal conductivity
$\text{kg/m}^3$	GPa		$10^{-6}/\text{K}$	$\text{W/m}\cdot\text{K}$
7858	200	0.3	15.3	14.28

- Boundary conditions

The boundary conditions include the heat fluxes calculated from Equation (3-2) and heat transfer coefficient (HTC) on the cooling channel surface calculated from the fluid analysis. The HTC results obtained from the fluid analysis were mapped to the nodes of the thermal analysis model directly and the heat fluxes of different surfaces are summarized in Table 3-3.

Table 3-3 Heat fluxes of different surfaces calculated through Equation (3-2)

Surface	Heat flux ( $\text{W/m}^2$ )
A	$9.24 \times 10^4$
B	$1.01 \times 10^5$
C	$1.06 \times 10^5$

- Analysis results

As Figure 3-11 shows, when the mass flow rate was increased from 0.3 kg/s to 0.5 kg/s, the maximum temperature on the RF contact holder only decreased by 4°C. For the two cases, the temperatures at the groove surface areas where the LA-CUT RF contact louvers installed are similar (~130°C). So, there is almost no cooling performance improvement if the mass flow rate is increased from 0.3 kg/s to 0.5 kg/s. The reason is that the temperature distribution on the RF contact holder is not only influenced by the coolant's parameters but also influenced by the thermal conductivity of the holder material. Due to the low thermal conductivity of the 316L, even though HTC increased under higher mass flow rate, heat loads cannot be transferred efficiently from the RF contact holder's surface to the cooling water. By balancing the cooling performance and pressure drop two factors, at last 0.3 kg/s was used during the RF tests.

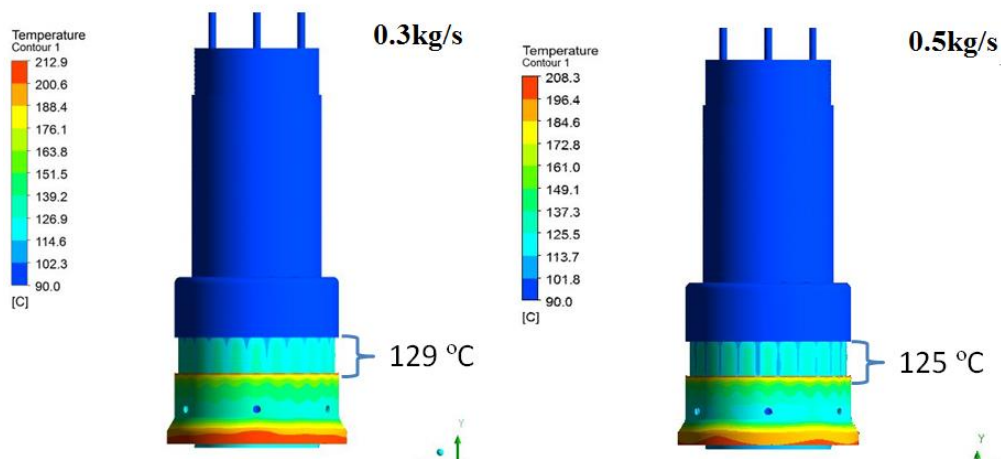


Figure 3-11 Temperature distribution on the RF contact holder

### 3.2.3 LA-CUT prototype RF test results

Figure 3-12 is the summary of the RF tests results. In this campaign, the target current (2.25 kA, @62 MHz) was achieved, but only for short pulse duration around 60s which is far less than required (1200 s). At 1.2 kA, steady-state (1200 s) RF operation has been obtained without any problem (Figure 3-13). An inspection of the contacts has been performed after having reached currents of 1.2 kA and didn't not show any visual damage. Dozens of shots have been performed at currents between 1.4 kA - 1.7 kA in steady-state regime (higher than 60 s and up to 1200 s) and difficulties to ramp-up the current were often found due to arcs. At last, the RF current has been increased up to a maximum of 1.9 kA during 300 s, but it was not possible to increase the current to larger values. After that, the T-resonator couldn't be operated, indicating that a failure happened on the LA-CUT RF contact.

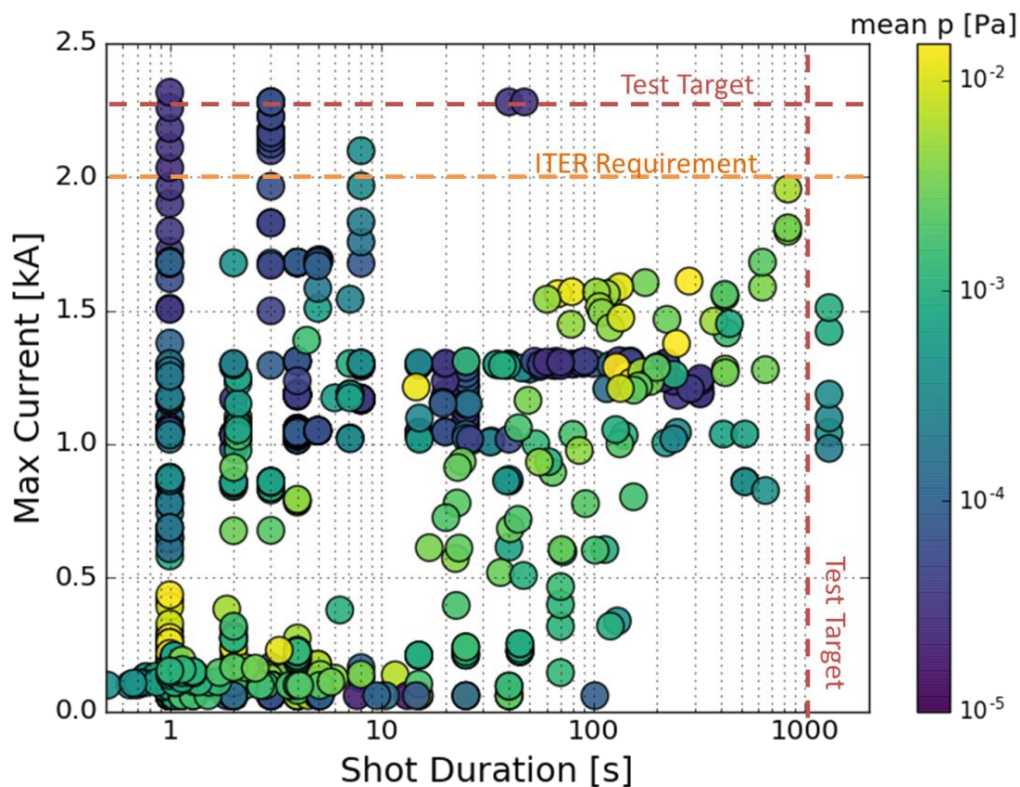


Figure 3-12 Maximum current achieved on the contact under test versus the total shot duration in seconds (in log scale). The marker colour corresponds to the average pressure during (and a few seconds after) the shot [127]

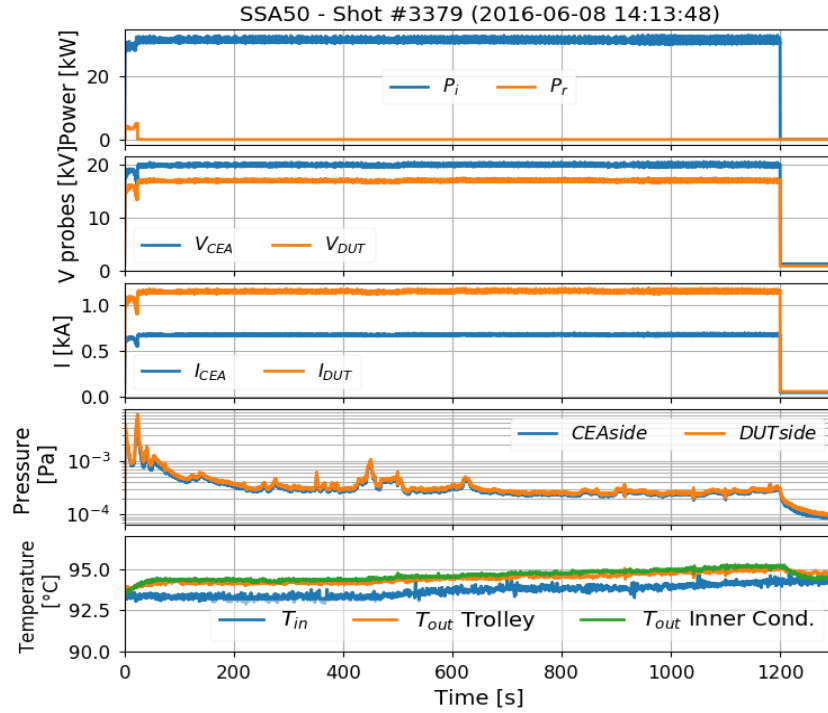


Figure 3-13 1.2 kA, 1200s operation

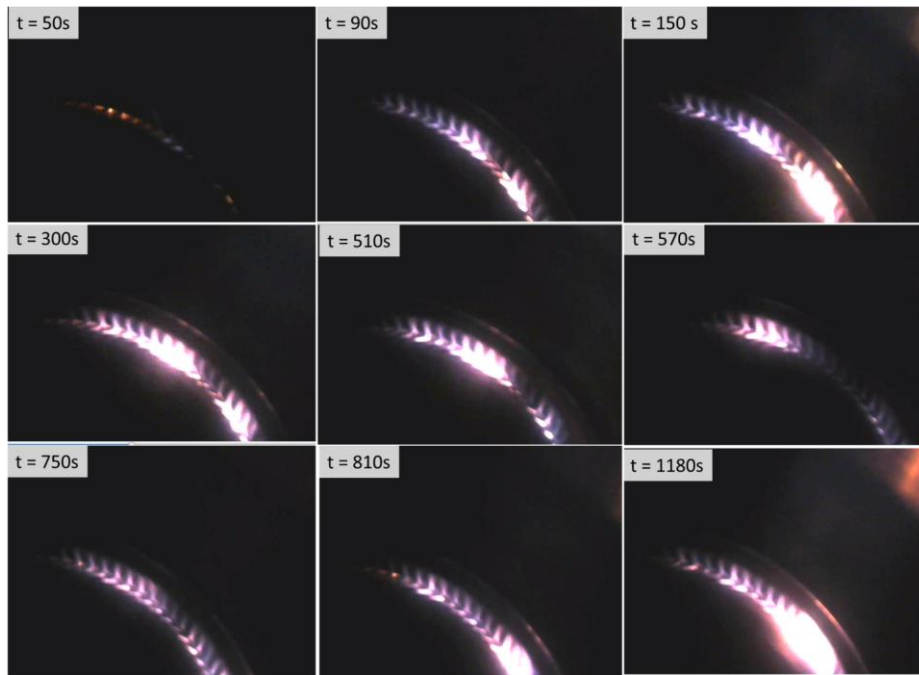


Figure 3-14 Status of the LA-CUT RF contact during 1.2 kA, 1200s operation

In this campaign, besides the RF current monitoring, a camera was installed at the rear of T-resonator to get a partial view of the LA-CUT RF contact through an observation window. Light emission was observed during these shots, starting after 60 to 120 s depending on the shot. Moreover, it was observed that the light emission changed both in brightness (increase or decrease) and locations during the shot duration as

illustrated in Figure 3-14.

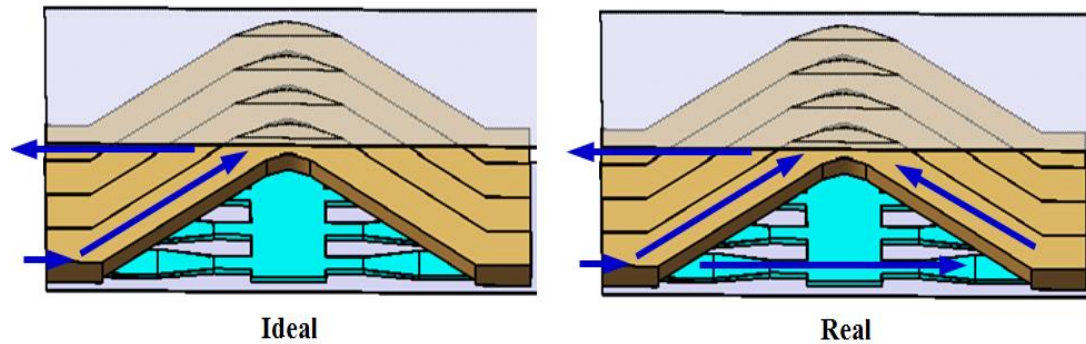


Figure 3-15 Illustration of current flowing in the LA-CUT RF contact during RF tests

One of the explanations of the light emission is that, during the RF tests, instead of flowing through the CuCrZr louvers, part of the current is flowing through the stainless steel spring whose electrical resistivity is more than 40 times higher than OFHC (Figure 3-15). As a result, the stainless steel spring plate was heated gradually till to few hundred degree of centigrade at which visible light generated. With the heating of the stainless steel spring (both the ohmic heating and baking), its magnetic permeability increased and the RF current can induce significant induction heating in the stainless steel spring. Considering the high frequency ( $\sim 62$  MHz) in the RF tests, induction heating could be a considerable heat load on the stainless steel spring. In any case, under high temperature, the mechanical properties of the spring were changed which caused the contact force release at the contact areas and induced instability of the current flowing in the whole LA-CUT RF contact due to the variation of the contact resistance. As a result, the light intensity and position changed during the RF operation. With the contact force release, some of the contacts between the LA-CUT louvers and the RF conductor were separated, which induced arcing phenomenon during the operation.

### 3.2.4 LA-CUT RF contact failure analysis

After 1.9 kA, 300 s shot, the RF contact had been severely damaged (Figure 3-16). In order to investigate the failure mechanism of the LA-CUT RF contact prototype, the RF contact holder together with the RF contact was disassembled from the T-resonator to perform the visual inspection and material analysis. As shown in Figure 3-16, almost all the RF contact strap was burned and the lower half circle of the RF contact was seriously melted. Especially the stainless steel spring on the RF contact was locally melted or changed from bright metal color to dark blue, which indicates that large current flowed through it during operation and heated the stainless steel part to a temperature higher than  $1000^{\circ}\text{C}$ . This phenomenon confirms the light emission

from the RF contact region as observed by the camera.

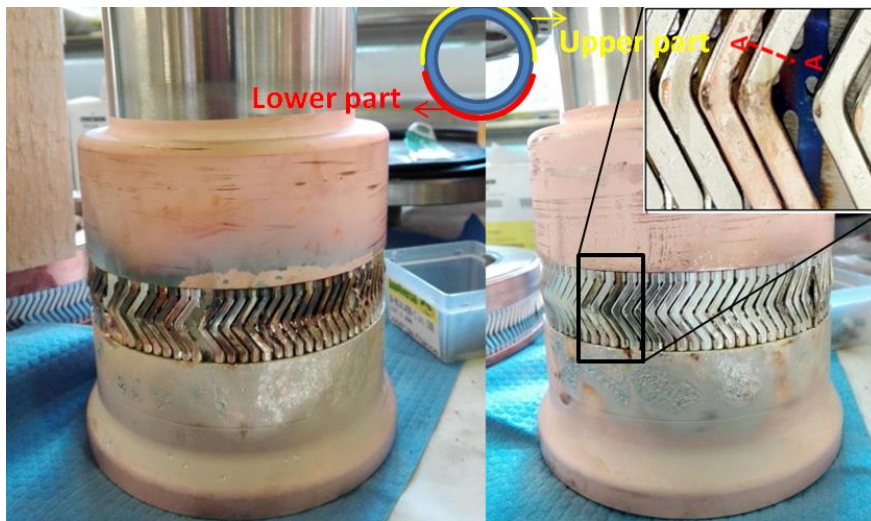


Figure 3-16 RF contact holder and RF contact after RF tests<sup>2</sup>

Burn traces on the whole LA-CUT RF contact strip is not uniform and compared with the upper half circle the lower one is much more severe. It indicates that, the current density in the lower part was higher than the upper one. A reason to cause such difference is a non-concentricity in the assembly of the RF contact holder. Gravity force made the electrical contact between the lower half circle of the RF contact more compressed to the outer conductor. As a result, the contact resistance at the lower contact area is smaller than that of the upper area. Current is prone to flow through the area where  $R_c$  is smaller. Based on the analysis, the assembly precision is also an important factor for the operation of the contact.

In order to decrease the  $R_c$  and protect the CuCrZr louvers from oxidation, a 30  $\mu\text{m}$  thick pure silver was deposited on the surface of the louvers by electroplating. After RF tests, the color of the louvers' surfaces turned from silver color to copper color. There are two explanations for this phenomenon: the diffusion between CuCrZr and silver coating and the silver sputtering from the louver' surfaces to their counterpart. Further analysis was performed by using SEM/EDS towards the cross-section of the louver.

<sup>2</sup> I would like to add that LA-CUT is a widely used and high-tech commercial electrical contact. It was not designed specifically for ITER application. In this thesis study, LA-CUT was selected to test under ITER relevant conditions. The failure presented in this figure doesn't present the quality of the LA-CUT product and the test results are significantly affected by the test conditions as well as the performance of the conductor that the LA-CUT was installed in. The test conditions were out of its manufacturing specifications.

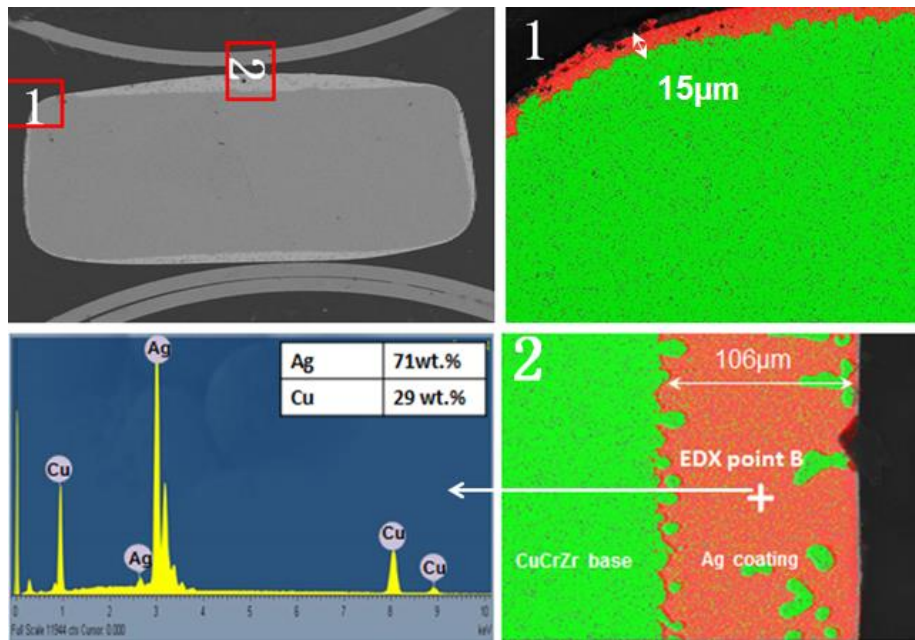


Figure 3-17 SEM/EDS analysis of a damaged CuCrZr louver after RF test

Figure 3-17 shows the cross section around the CuCrZr louver, where the thickness of the Ag coating is not uniform. In the central area, the thickness of Ag increased from 30  $\mu\text{m}$  to 106  $\mu\text{m}$ . In the four corners the Ag coating thicknesses decrease and in some local area Ag layer disappeared. The interface between Ag and CuCrZr blurred which indicates that serious diffusion occurred. In the 106  $\mu\text{m}$  thick Ag coating layer, Cu (Cu-riched) phase was observed which is another evidence of Ag-Cu interdiffusion. At the corners, the Ag layer is much thinner, which indicates that during operation the temperature at the corner area was higher; in other words, the RF current was prone to flow through the corners of the louver, which is known the effect of the RF current on thin conductors [128]. The serious diffusion of Cu into Ag can induce the increase of the coating layer's electrical resistivity [129, 130] and the decrease of corrosion resistance. The operating temperature on the RF contact should thus be minimized to achieve steady-state operation.

### 3.2.5 LA-CUT RF contact operating temperature study

As explained in the last section, high heat loads deposition due to Ohmic losses is the main reason that caused LA-CUT RF contact failure. High temperature changed both the mechanical structure and material composition of the RF contact louvers. Hence, in order to achieve steady-state operation, appropriate means should be applied to minimize the temperature on the RF contact louver. Decreasing the heat deposition and improving cooling performance are the two possible solutions. The factors that affect the operating temperature of the RF contact are the contact resistance  $R_c$  at the contact areas, the thermal conductivities of the RF conductor and RF contact louver

materials and the HTC at the cooled surfaces. In order to investigate the relationship of these factors with the operating temperature of the RF contact, simulations were performed.

### 3.2.5.1 Theoretical model

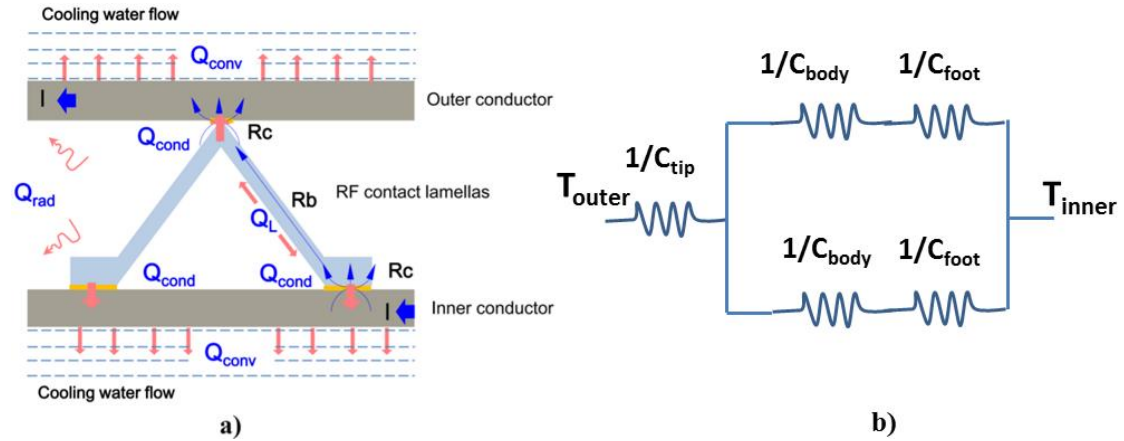


Figure 3-18 Sketch of the ITER RF contact analysis model: (a). thermal-hydraulic model. (b). heat transfer network diagram one RF contact louver

The Figure 3-18 (a) illustrates the ideal RF current flows from the inner conductor to the outer conductor through the LA-CUT RF contact louvers. Due to the existing of bulk resistance ( $R_b$ ) and contact resistance ( $R_c$ ), heat loads were generated. The operating environment of the LA-CUT RF contact is high vacuum, so thermal convection between the louvers to the surroundings can be ignored. If the RF contact works under normal conditions, the operating temperature of the RF contact louvers and the RF conductors are in the same order, so thermal radiation between the louvers and the environment can be neglected compared with thermal conductance. The heat loads are generated at the electrical contact interfaces and are transferred to the inner and outer RF conductors, which are actively water cooled.

The Figure 3-18 (b) depicts the heat transfer network diagram one RF contact louver.  $T_{outer}$  and  $T_{inner}$  are the temperatures of the outer and inner conductor respectively.  $C_{body}$ ,  $C_{foot}$  and  $C_{tip}$  are the thermal conductivity of the half louver, the foot contact and the tip contact. The rate of heat flow of one louver can be expressed as:

$$\Phi = (T_{outer} - T_{inner}) \cdot C_{total} \quad (3-3)$$

where  $C_{total}$  is the equivalent thermal conductivity of one RF contact louver, which can be calculated from:

$$C_{total} = \left( \frac{1/C_{body} + 1/C_{foot}}{2} + 1/C_{tip} \right)^{-1} \quad (3-4)$$

Since the base material of the LA-CUT louver is CuCrZr with a thin Ag coating, the body thermal conductance is much larger than the thermal conductance at the electrical contact area. Assuming that the thermal conductance values at the louver foot and tip areas are the same, then Equation (3-4) can be simplified as:

$$C_{total} = \left( \frac{3}{2C_{tip}} \right)^{-1} \quad (3-5)$$

In reference [131], the  $C_{total}$  has been measured through experiments to 0.016 W/K. So, according to Equation (3-5), the thermal conductance at the foot (tip) contact area is 0.024 W/K.

### 3.2.5.2 Finite element analysis model

A thermal analysis model was created in ANSYS as shown in Figure 3-19. From symmetry consideration, only four RF contact louvers and pieces of conductors were considered on a flat holder. For cooling point of view, the thicknesses of the conductor should be as thin as possible. However, the cooling channel on the conductors must have enough mechanical strength to sustain high cooling water pressure which in ITER can reach up to 60 bars. In the analysis model both the thicknesses of the inner and outer conductor cooling channel covers were 3.5 mm. The tip contact area per louver is 6 mm<sup>2</sup> and the foot contact area is 2.31 mm<sup>2</sup>.

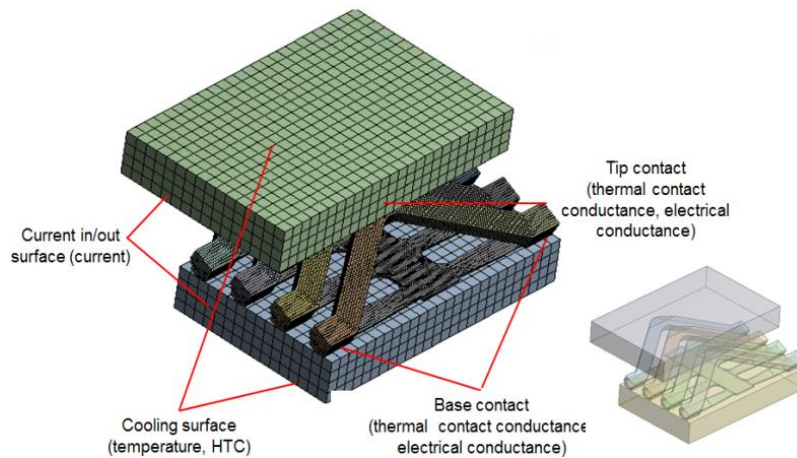


Figure 3-19 Thermal analysis model of LA-CUT RF contact

### 3.2.5.3 Analysis procedure and results

By assuming the  $R_c$  values at contact areas, the Ohmic losses were calculated under DC of 19.6 A/ louver (corresponding to 2.25 kA with 115 louvers, as in the case of the worst ITER antenna case). The Ohmic loss on the louver body was also taken into account: the calculated Ohmic losses were applied on the related surfaces on the model. Active cooling was simulated by applying HTC at the cooling channel surfaces of the inner and outer RF conductors. Through static thermal analysis, the operating temperature distributions on the RF contact louvers under different  $R_c$  values ( $R_c=1\text{ m}\Omega$ ,  $2\text{ m}\Omega$ ,  $4\text{ m}\Omega$ ,  $7\text{ m}\Omega$ ) were studied. By changing the HTC values, the effects of increasing cooling parameter to minimize operating temperature were evaluated. Finally, the influence of changing RF conductors' base material from 316L to CuCrZr was studied.

1) *The effects of  $R_c$  to the operating temperature*

- Boundary conditions
  - Heat transfer coefficient of the louver tip:  $4057\text{ W/ m}^2\cdot\text{K}$
  - Heat transfer coefficient of the louver foot:  $10570\text{ W/ m}^2\cdot\text{K}$
  - Heat transfer coefficient of the cooling surfaces on the inner and outer RF conductors and temperatures:  $6300\text{W/ m}^2\cdot\text{K}$  (cooling water velocity:  $0.5\text{ m/s}$ ),  $90\text{ }^\circ\text{C}$
  - Heat fluxes under 19.6A/ louver: as shown in Figure 3-20.

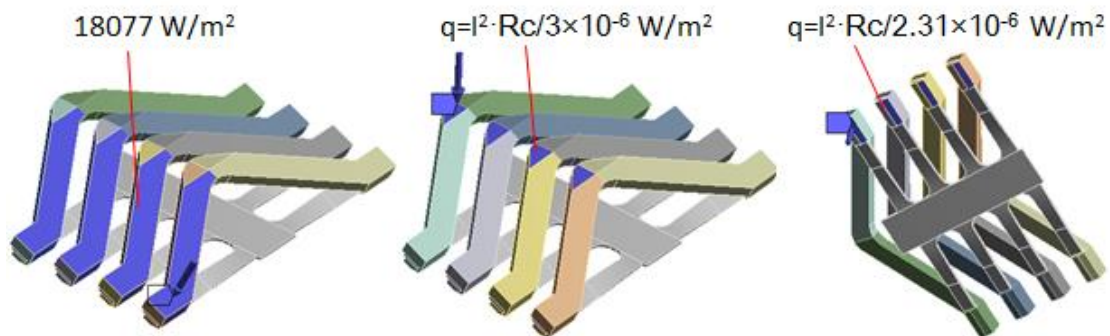


Figure 3-20 Heat fluxes on the louvers

- Results

The maximum and minimum temperatures on the RF contact louvers under different  $R_c$  are shown in Figure 3-21.

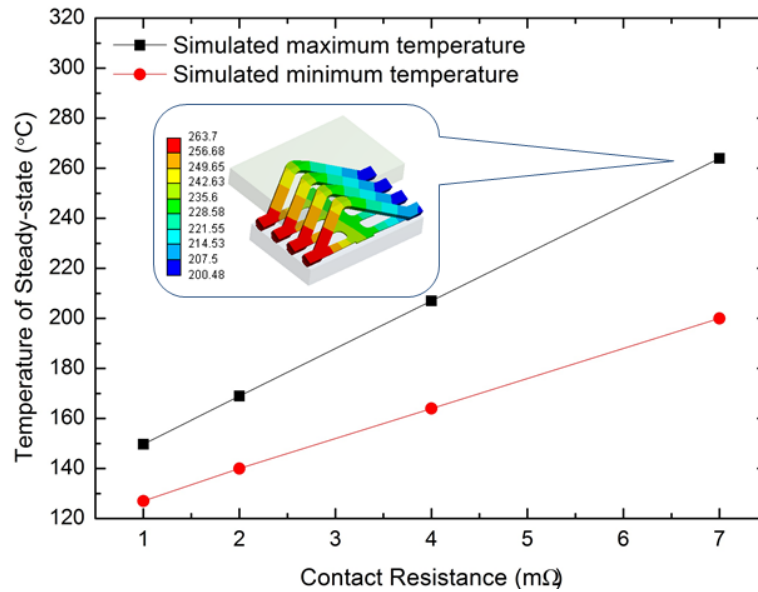


Figure 3-21 Rc-T relation

The maximum and minimum temperatures on the RF contact louvers linearly increased with the increase of  $R_c$ . When  $R_c$  is 6.5 mΩ, the maximum temperature reaches to 250°C, which is the steady-state operating limit for CuCrZr. Thus, for ITER RF sliding contacts, 6.5 mΩ is the design limit of the  $R_c$ .

## 2) The effects of cooling parameter to the operating temperature

In addition to controlling the heat loads, another method to minimize the operating temperature is to improve the cooling efficiency. From Figure 3-21, when  $R_c$  is 7 mΩ, the maximum temperature of the RF contact is 263.7°C. Keeping all the other conditions without change and only increasing the HTC on the RF contact cooling surfaces to 12175 W/m<sup>2</sup>·K (cooling water velocity: 1 m/s) and 19000 W/m<sup>2</sup>·K (cooling water velocity: 2 m/s), the new temperature distributions on the RF contact were obtained (Figure 3-22).

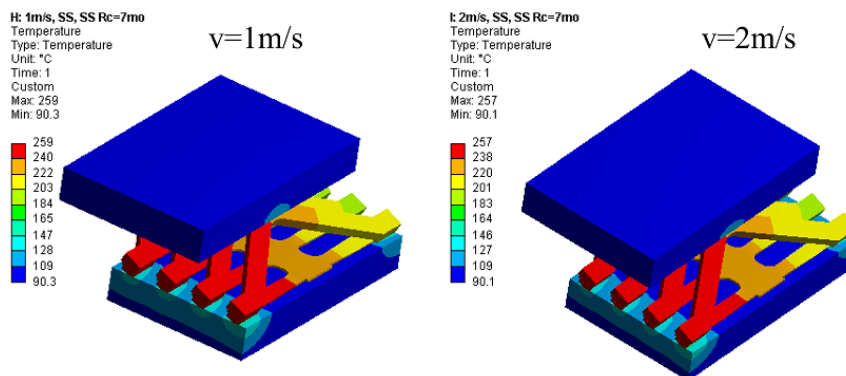


Figure 3-22 Temperature distribution on the RF contact under cooling water velocity of 1 m/s and 2 m/s

When the cooling water velocity was increased to 1 m/s, to maximum temperature decreased by 4°C and the difference decreased to only 2°C when cooling water velocity was increased from 1 m/s to 2 m/s. According to the analysis results, the increasing of water speed can't decrease the operating temperature of the RF contact efficiently. As is explained in section 3.2.2.2, the cooling efficiency is restricted by the low thermal conductivity of the RF conductor base material (316L in this case).

Compared with 316L, CuCrZr has excellent thermal conductivity and similar mechanical strength (Table 3-4). So, CuCrZr can be a good candidate to replace 316L as the base material of the RF conductor, which is investigated in the next section.

Table 3-4 Material properties of CuCrZr

Density	Young's Modulus	Poisson's Ratio	Thermal expansion coefficient	Thermal conductivity
kg/m <sup>3</sup>	GPa		10 <sup>-6</sup> /K	W/m·K
8900	127.5	0.33	16.72	318

### 3) The effects of cooling parameter to the operating temperature

ITER plasma operation is pulsed operation. Although from the previous static thermal analysis, maximum contact resistance of 6.5 mΩ is required to keep the contact to temperature lower than 250°C. If the time required for the temperature to exceed 250°C is longer than the expected pulse duration (1200 s) the RF contact can still be operated safely. Transient thermal analysis was performed to study this point.

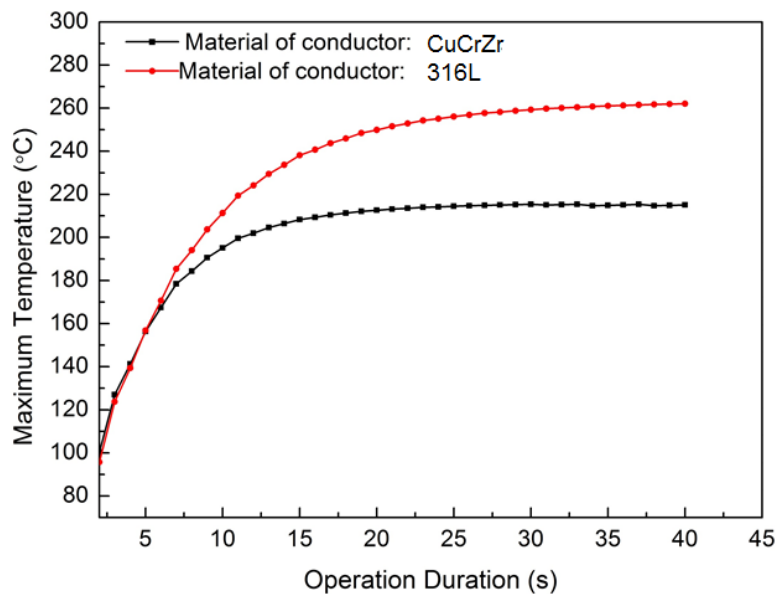


Figure 3-23 Transient temperature on the RF contact with different RF conductor base materials ( $R_c=7$  mΩ,  $v=0.5$  m/s)

The Figure 3-23 has been calculated with a  $7 \text{ m}\Omega$   $R_c$  and a cooling water velocity of  $0.5 \text{ m/s}$ . The temperature on the RF contact increases from  $90^\circ\text{C}$  to around  $260^\circ\text{C}$  in  $40 \text{ s}$  and reaches steady-state after that.  $40 \text{ s}$  is far less than  $1200 \text{ s}$ , which means that pulsed operation can't improve the operating safety of the RF contact. After replacing 316L to CuCrZr, the time reached steady-state decreased to  $20 \text{ s}$ . At the same time, the maximum temperature decreased by  $60^\circ\text{C}$  to  $200^\circ\text{C}$ .

### **3.3 Discussion**

LA-CUT configuration was selected in the latest RF test campaign. Aiming to improve the RF contact louver's structure stability under high temperature application, the base material of the louver was changed from pure copper to CuCrZr. In this campaign,  $1.2 \text{ kA}$ ,  $1200 \text{ s}$  operation was achieved, but burn failure occurred at last. By visual observation, burn trace was observed on the stainless steel spring and the heat loads may have two sources: the ohmic losses generated by the RF current and the eddy current. Applying insulating coating between the CuCrZr louver and the stainless steel could be helpful for avoiding the RF current flowing through the stainless steel part. Solutions should also be found out to prevent the magnetic permeability of the spring material from increasing.

Based on the analysis results, using CuCrZr to manufacture the RF conductor is the best option to decrease the operating temperature of the LA-CUT RF contact. Therefore, in the following coating performance studies, CuCrZr was selected as one of the candidates for the base material.



## **Chapter 4 Thermal stability, electrical and tribological characterization of coatings**

In chapter 3, the RF test of LA-CUT contact prototype was performed and through the characterization of the damaged louvers, serious metal interdiffusion between Cu and Ag was confirmed. Such metal diffusion was caused by the high temperature ( $>250^{\circ}\text{C}$ ) of the louvers during RF operation. Generally, metal diffusion changes the coating's original electrical and chemical properties, which should be avoided. Before operation in ITER, RF contacts will be subjected to long periods of high temperature ( $250^{\circ}\text{C}$ ) baking to attain high vacuum. Even if the operating temperature of the RF contact can be minimized to below  $250^{\circ}\text{C}$ , long time baking process could still induce serious diffusion on the RF contact. Therefore, diffusion characterizations after a long time of high temperature baking should be performed. Through FE simulations,  $R_c$  was found to be an important parameter for RF contact which is affected by the contact material, contact force and contact surface state (e.g., wear state). In this chapter, the diffusion phenomena between coatings to their substrates and between contacting coatings and the tribological/electrical performances of these coatings were studied.

### **4.1 Materials and samples preparation**

#### **4.1.1 Material selection**

Two kinds of base materials and coating materials are respectively foreseen for the ITER ICRH antenna. For the RF contact louvers, the selected material is CuCrZr, which is material that has both good mechanical, thermal and electrical performance. For the RF conductor, 316L is a commonly used material and CuCrZr can be another interesting base material whose efficiency to minimize the operational temperature of the RF contact louvers was demonstrated in Chapter 3. The electrical functional coatings that can be applied to the above materials should have the following properties:

- High thermal and electrical conductivity;
- Low CoF and wear rate under high vacuum ( $<10^{-3}$  Pa) and high temperature ( $\sim 200^{\circ}\text{C}$ );
- High corrosion resistance and high chemical stability.

On electrical contact industry, Au, Ag and Rh are commonly used, which are also interesting for the ITER ICRH RF contact application. The summary of the material selection (base + coating) for the following coating characterization study is shown in Figure 4-1.

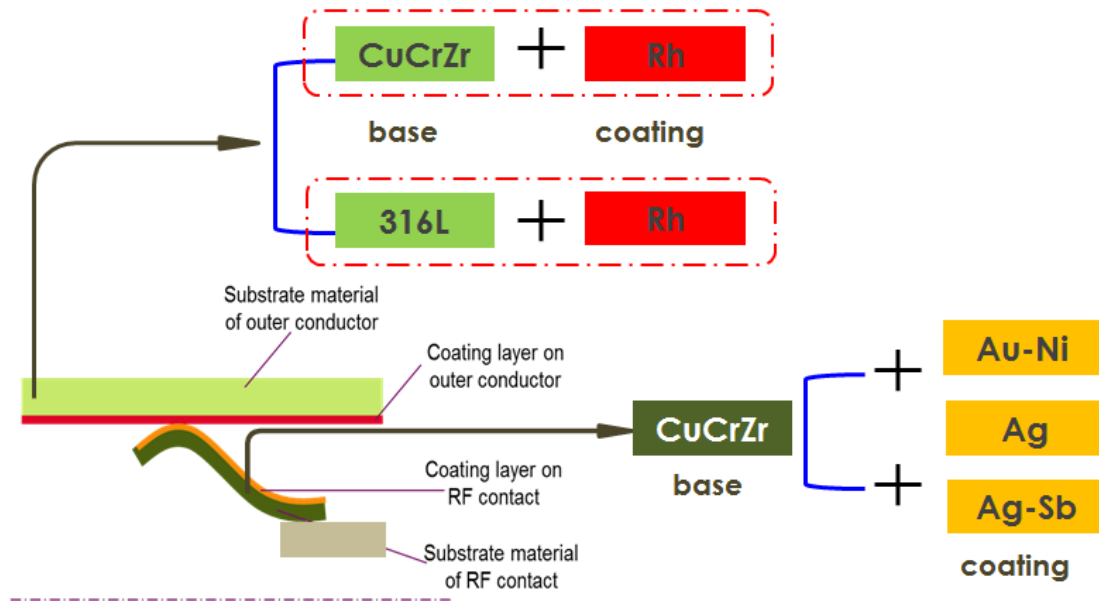


Figure 4-1 Overview of material selection for coating characterizations

#### 4.1.1.1 Au and Au alloys

Pure Au is one of the most chemically stable precious metals. It exhibits an electrical resistivity of  $2.32 \mu\Omega\cdot\text{cm}$ , close to the one of Silver. In its pure form, it's not very suitable for use as a contact material in electromechanical devices because of its tendency to stick and cold-weld at even low contact forces [132]. Moreover, the hardness value about 70 HV induces too low wear resistance to be used as sliding contact material. These factors limit the use of pure Au as an electrical functional coating.

Adding Co or Ni to harden the electroplated Au layer is commonly used in the electronics industry [133, 134]. The atom content of Co is usually about 0.3–1.6 at.% [135]. Other researchers' results showed that the contact resistance is related with the cobalt content: a cobalt content lower than 0.3% is generally recommended. Since ITER is a nuclear reactor, the RF contact will be exposed to neutron radiation. Cobalt has large activation cross-section and thus can be activated easily. It has a long radioactive half-life, which reaches to 5.3 years. ITER requires that the Co content of the materials used on plasma facing components should be lower than 0.2 wt.% [114]. Alloying Ni into Au matrix has a similar function as Co and there is no limitation of Ni content in Au-Ni coating. In the following coating characterizations study, Au-Ni coating was selected as one of the coatings on CuCrZr RF contact louvers.

#### 4.1.1.2 Ag and Ag alloys

Ag is another well-used contact material. Pure Ag has the highest electrical and thermal conductivity of all metals (resistivity:  $1.67 \mu\Omega\text{cm}$ ) and is also resistant against oxidation. Electroplated Ag is an excellent functional coating which has good fretting and electrical performance at temperatures less than  $160^\circ\text{C}$  [136]. Recrystallization at temperatures higher than  $100^\circ\text{C}$  can degrade the original Ag coating's mechanical properties (e.g., hardness), which could induce wear, cold welding and material migration during sliding. Alloying with Cu, Pt, Pd, Ni and W can improve the Ag coating's mechanical properties as well as tarnishing resistance. Ag-Sb, which is also called hard silver, is much harder than Ag and its wear resistance is 10 to 12 times higher than Ag when Sb content is around 2 wt.% [137]. Besides Au-Ni, hardened silver (Ag-Sb) was selected as another RF contact coating in the following study.

#### **4.1.1.3 Rhodium**

With high resistance to tarnishing and high hardness properties, Rh becomes extremely useful as electrical contact material. However, as it's difficult to be fabricated, generally Rh is only used as plating material in light-duty electrical contacts where reliability is of the most important thing [138]. In our situation, we have two components which require to be coated: the RF contacts and the RF outer conductors. During operation, the sliding RF contacts will contact with the RF outer conductor directly and slide against it frequently. Due to mechanical sliding, abrasion is inevitable. For the ITER ICRH antenna, the expected design lifetime is few years and after installation the possibility to change or repair the RF outer conductor is low. Nevertheless, the RF contact can be changed if serious abrasion occurred in the coating layer. So, for maintenance feasibility consideration, the hard Rh coating (few microns only) will be plated on the surface of RF outer conductor to enhance its wear resistance. Relatively soft materials (e.g., Au-Ni or Ag-Sb) will be plated on the surfaces of the RF contact to improve its electrical contact performance.

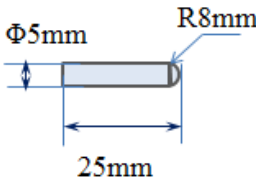
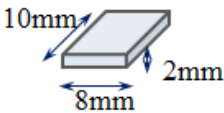
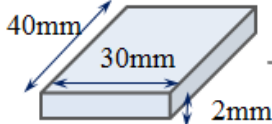
#### **4.1.2 Sample manufacturing**

Table 4-1 shows the three kinds of coating samples that were manufactured with two base materials: small CuCrZr and 316L plates ( $10 \text{ mm} \times 8 \text{ mm} \times 2 \text{ mm}$ ) with surface roughness  $S_a$  (arithmetic mean height) of  $0.58 \mu\text{m}$  and  $0.44 \mu\text{m}$ , respectively; large CuCrZr and 316L plates ( $40 \text{ mm} \times 30 \text{ mm} \times 2 \text{ mm}$ ) with surface roughness ( $S_a$ ) of  $0.77 \mu\text{m}$  and  $0.45 \mu\text{m}$ , respectively; CuCrZr pin samples with a length of 25 mm, diameter of 5 mm and a curved tip surface with a radius of 8 mm with surface roughness of  $2.1 \mu\text{m}$ . The coating methods of all the coating samples were electroplating.

The pure Ag coating samples were manufactured by JianYi Diangong<sup>®</sup>, Liuzhou,

China and Ag-Sb coating samples were manufactured by Multi-Contact<sup>®</sup>. The Au-Ni coating samples and Rh coating samples were manufactured by Radiall<sup>®</sup> and CERN, respectively. Based on Appendix B, metal interdiffusion can easily happen between Au and Cu [139]. Therefore, a Ni interlayer was applied on CuCrZr substrates before depositing Au-Ni coatings. When Rh coating samples were manufactured in CERN, the interlayer material's selection was only focused on the minimization of coating stress and the protection of the Rh electroplating bath (with high acidity that can corrode the CuCrZr substrate) from contamination. So, a 0.5  $\mu\text{m}$  Au (an inert material) interlayer was applied on CuCrZr substrates and a 3  $\mu\text{m}$  Ni/0.5  $\mu\text{m}$  Au interlayer was applied on 316L substrates. However, as Au can readily diffuse with Cu, applying an Au interlayer on CuCrZr substrate is not a good idea.

Table 4-1 List of sample shapes and coatings applied

Sample shape	3D drawing	Base material	Coating (s)
<b>Pin</b> (tribological study)		CuCrZr	34 $\mu\text{m}$ Ag
			14 $\mu\text{m}$ Au-Ni+ 5 $\mu\text{m}$ Ni
<b>Small plate</b> (thermal aging and diffusion study)		CuCrZr	4 $\mu\text{m}$ Au-Ni+ 4 $\mu\text{m}$ Ni
			15 $\mu\text{m}$ Ag-Sb
		316L	3 $\mu\text{m}$ Rh+ 0.5 $\mu\text{m}$ Au
<b>Large plate</b> (tribological study)		CuCrZr	3 $\mu\text{m}$ Rh+ 0.5 $\mu\text{m}$ Au
		316L	4.5 $\mu\text{m}$ Rh+ 3 $\mu\text{m}$ Ni+ 0.5 $\mu\text{m}$ Au

### 4.1.3 Characterizations and sample preparation

#### 4.1.3.1 Thermal aging process

In order to simulate the ITER baking process, thermal aging treatment was performed on the assembled and free coating samples under ITER-specific baking conditions (i.e., high-vacuum and high-temperature conditions of  $10^{-6}$  Pa and  $250^{\circ}\text{C}$ , respectively). These samples were heated from room temperature to  $250^{\circ}\text{C}$  at a heating rate of  $1.3^{\circ}\text{C}/\text{min}$  and then aged at  $250^{\circ}\text{C}$  for 500 h. The samples were subsequently cooled down to room temperature at a rate of  $0.16^{\circ}\text{C}/\text{min}$  under

vacuum (Figure 4-2). Due to the technical problems of the baking oven, at 200 h, the temperature of the sample increased to 300°C (around two hours).

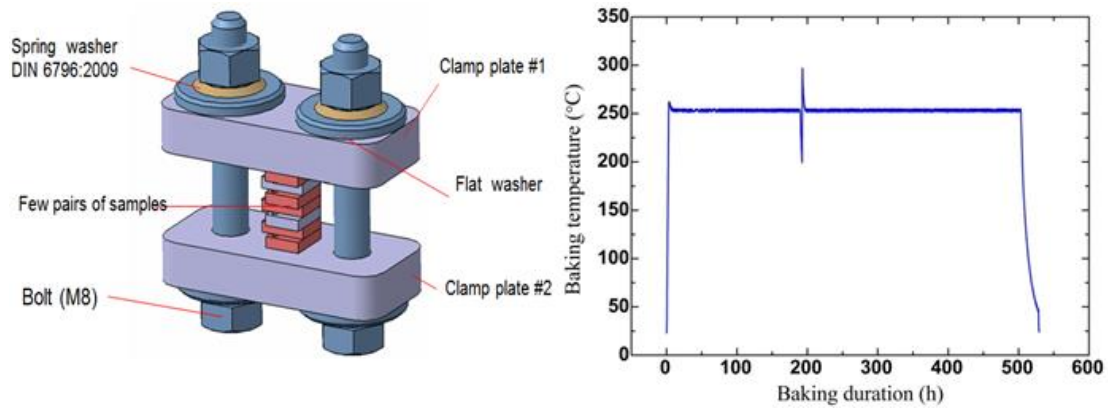


Figure 4-2 Clamping system and baking process of diffusion test

#### 4.1.3.2 Tests planning

Three tests were performed which include: thermal aging test, diffusion test and electrical/tribological test.

##### 1) Thermal aging test

After 250°C, 500 h thermal aging, the changes of different coatings' mechanical, electrical and crystal properties (hardness, wear resistivity, surface quality, crystallite size, lattice constant, etc.) were checked.

##### 2) Diffusion test

For diffusion tests, the metal diffusion phenomena were investigated between the functional coatings to their substrates as well as the diffusion between two functional coatings (assembled by mechanical force) after 250°C, 500h high temperature baking.

The diffusion test between two coatings (coating on RF contact louver and coating on RF conductor) was carried out by assembling the two small plates with a specially designed clamping system (Figure 4-2). By adjusting the pre-tightening force of the bolts, a 200 MPa mechanical pressure was applied on the coating surfaces to mimic the real contact between the two coatings after the RF contact being assembled.

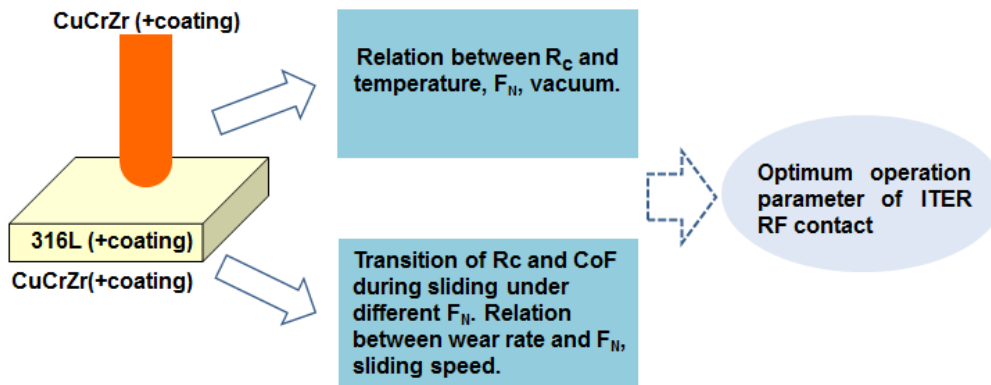
3) *Electrical/tribological test*

Figure 4-3 Procedure of electrical/ tribological tests

The workflow of the tribological/electrical experiments is shown in Figure 4-3. Different thermal aged sample pairs (pin vs. large plate) were evaluated on the home-made multifunctional tribometer HV-MTEST. The test sample pairs are listed as follows:

- Pin: CuCrZr (no coating), plate: 316L (no coating);
- Pin: Au-Ni on CuCrZr, plate: Rh on 316L;
- Pin: Au-Ni on CuCrZr, plate: Rh on CuCrZr;
- Pin: Ag on CuCrZr, plate: Rh on 316L;
- Pin: Ag on CuCrZr, plate: Rh on CuCrZr.

## 4.2 Characterization results of thermal stability

Coatings' properties change due to thermal treatment, diffusion phenomena between coatings and their substrates and between two coatings, are evaluated in the following subsections.

### 4.2.1 Coating properties changes and diffusion with substrate

#### 4.2.1.1 Au-Ni on CuCrZr

##### 1) *Surface morphology*

The microstructure of the surface of the original Au-Ni coating was observed under  $\times 50000$  magnification, as shown in Figure 4-4. A grain structure with cauliflower-like nodules was observed, with an average grain size of around 20 nm. No coating defects such as cracks and pores were observed in the SEM image of the coating. After

thermal aging, no noticeable increase in the grain size was observed in the SEM image. However, numerous pores (number density:  $1.7/\mu\text{m}^2$ ) with an average diameter of 48 nm were formed on the surface of the coating. During the long period of thermal aging, recovery, recrystallization and grain growth occurred in the Au-Ni coating. Boundary migration occurred simultaneously and these pores were probably formed among the grain boundaries owing to discontinuities of boundary movement [140, 141]. As these pores were extremely small in size, they did not have any obvious effect on the electrical and tribological performances of the coating.

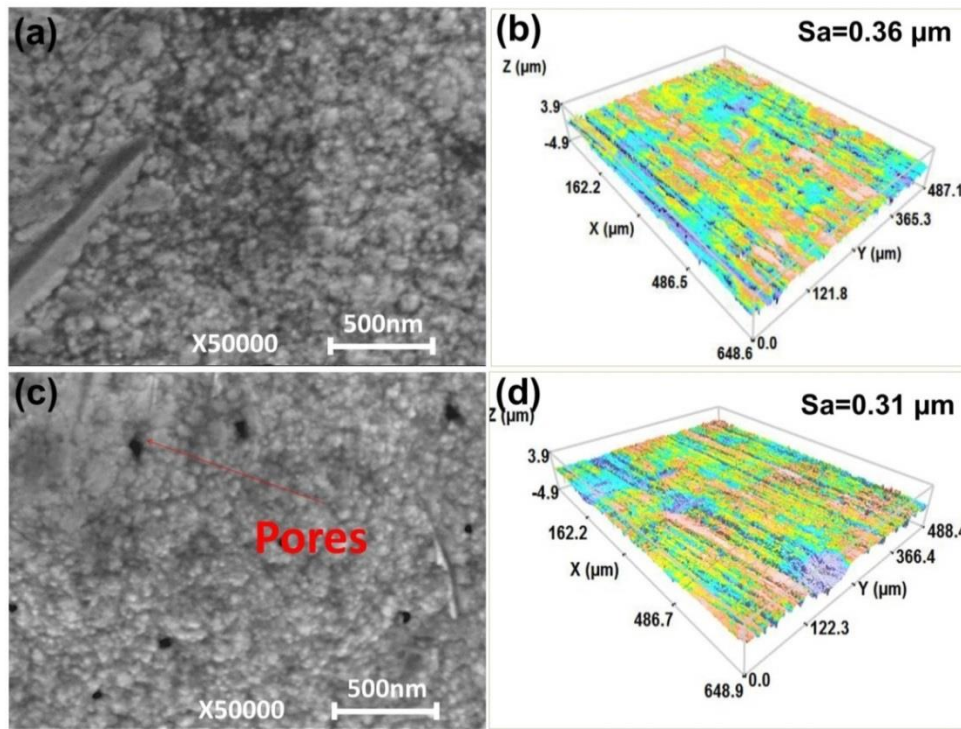


Figure 4-4 Observation results of surface morphology of coating surfaces: (a) SEM image of the surface of the original coating, (b) 3D interferometric image of the surface of the original coating, (c) SEM image of the surface of the thermally aged coating, (d) 3D interferometric image of the surface of the thermally aged coating

The surface topography of the Au-Ni coating on the CuCrZr substrate was also studied. The  $S_a$  value of the original coating was about  $0.36 \mu\text{m}$ , which indicated that the original Au-Ni coating was smooth. After thermal aging, there was no apparent change in the surface roughness of the coating and  $S_a$  of the thermally aged coating was  $0.31 \mu\text{m}$ .

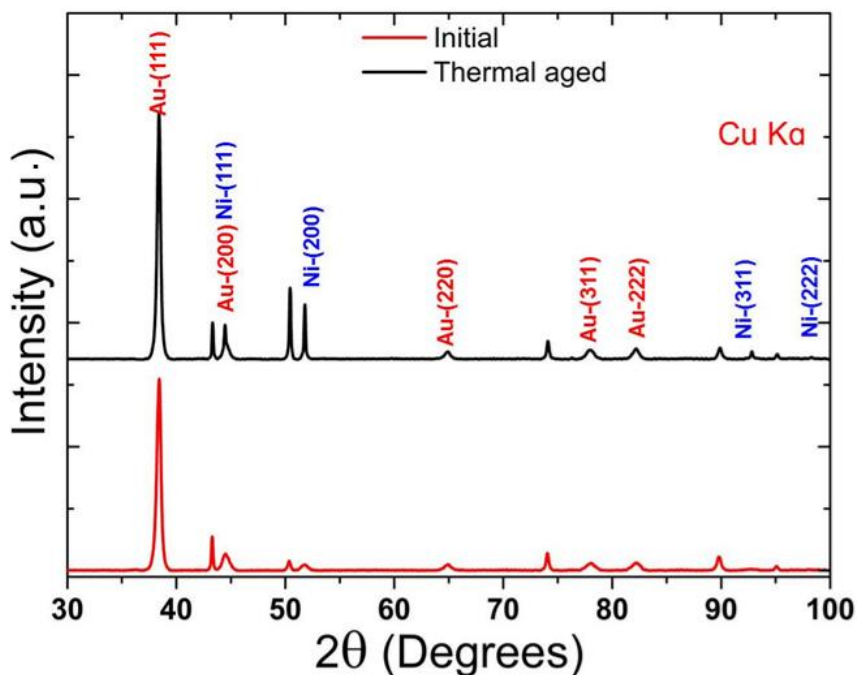
## 2) Crystal structure

The crystallite size of a coating is closely related to the coating's mechanical properties, e.g., its hardness, which would affect the wear performance of the coating.

The grain sizes of the Au-Ni coating before and after thermal aging were studied by XRD.

As shown in Figure 4-5, before thermal aging, peaks of the Au, Cu and Ni phases are present in the XRD pattern. The Ni peaks originate from the Ni interlayer of the Au-Ni coating and the Cu peaks originate from the substrate. From the (111) peak and according to the Scherrer equation [51], the crystallite size is determined to be about 20.1 nm, with a lattice constant of 0.4058 nm. The right shift of the Au peaks and the smaller lattice constant than that of pure Au were caused by the co-deposition of the Ni element (which has a smaller atomic diameter), into the Au layer; the higher the substitution of Au by Ni, the smaller the Au lattice becomes. The Au (111) peak shifted by  $0.03^\circ$  in the low- $\theta$  direction, which may have been caused by the diffusion of Cu atoms (whose atomic radius is larger than that of Ni) into the Au-Ni layer.

In comparison to the XRD pattern of the initial sample, after thermal aging, the FWHM of the Au peaks did not decrease noticeably, which means that the Au-Ni coating remained fairly unchanged during thermal aging, without severe grain coarsening. The crystallite size was calculated from the Au (111) peak to be about 24.4 nm. The lattice constant of the Au-Ni coating after thermal aging was 0.4062 nm. Grain coarsening did not have any significant effect on the hardness of the coating. The crystallite size of the Ni interlayer was calculated from the Ni (200) peak. Obvious grain coarsening of the Ni interlayer was observed, which indicates that after the long-term thermal aging, the crystallite size of the Ni interlayer increased from 14.4 nm to more than 100 nm.



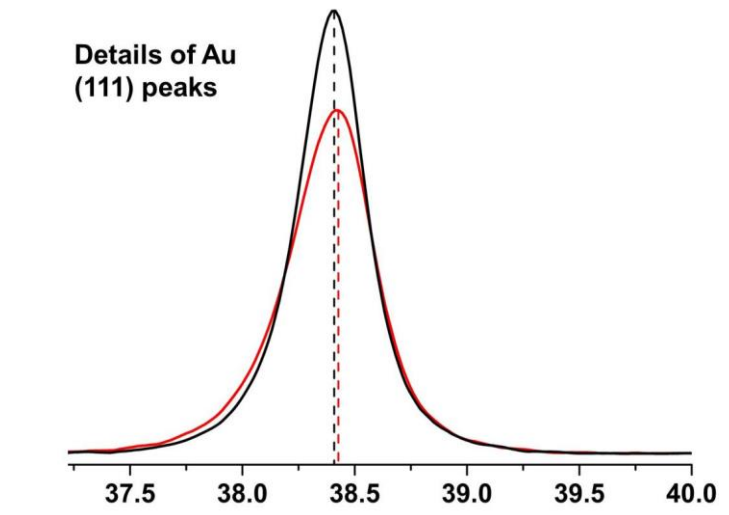


Figure 4-5 XRD pattern of Au-Ni coating on CuCrZr (original and thermally aged)

### 3) Hardness and elastic modulus

Nanoindentation tests were conducted to evaluate the Au-Ni coating's hardness and elastic modulus. The CuCrZr substrate and Ni interlayer may influence the measured mechanical properties, especially the elastic modulus, during the indentation of the Au-Ni coatings; therefore, the penetration depth should be kept smaller than 1/10th of the thickness of the Au-Ni coatings [142]. In view of this requirement of the penetration depth, a peak load of 7 mN was applied. In all cases, under the peak load of 7 mN, the loading rate and unloading rate were set to the same value of 14 mN/min. During the nanoindentation tests, when the loads reached 7 mN, the maximum loads were maintained for 60 s to observe the creep of the coatings. The Vickers hardness of the coatings was calculated using the obtained indentation hardness ( $HV \approx H_{IT}/10.8$ ). The Poisson's ratio of the Au-Ni coatings was assumed to be 0.3. In order to enhance the reproducibility of the measured results, on each sample, measurements were performed 10 times at different selected positions.

From the load–displacement curves in Figure 4-6, it can be seen that the results of the 10 measurements on the original coating, especially during loading, were more homogenous than those on the thermally aged coating. It has been reported that differences in surface roughness lead to dispersion of loading curves [143]. However, in this study, the original and thermally aged coatings had similar surface roughness values. Thus, the large dispersion of the load–displacement curves for the thermally aged coating was caused by other factors. Physical (thickness) and chemical (composition) changes that occurred in the Au-Ni coating after thermal aging may be the possible explanations of this dispersion. In addition to the large scattering of the residual indentation depths for the thermally aged coating as obtained from its load–displacement curves, another obvious difference from the original coating was

observed: a decreased residual indentation depth. A smaller imprint depth indicates that the hardness of the thermally aged coating increased. In addition, during the load hold period, the thermally aged coating showed better creep resistance than the original coating because of the smaller creep deformation of the former. The elastic modulus and hardness of the original Au-Ni coating were calculated to be  $133.3 \pm 4.6$  GPa and  $267.7 \pm 19.0$  HV, respectively. These values changed to  $135 \pm 8.0$  GPa and  $371.2 \pm 36.1$  HV, respectively, after thermal aging.

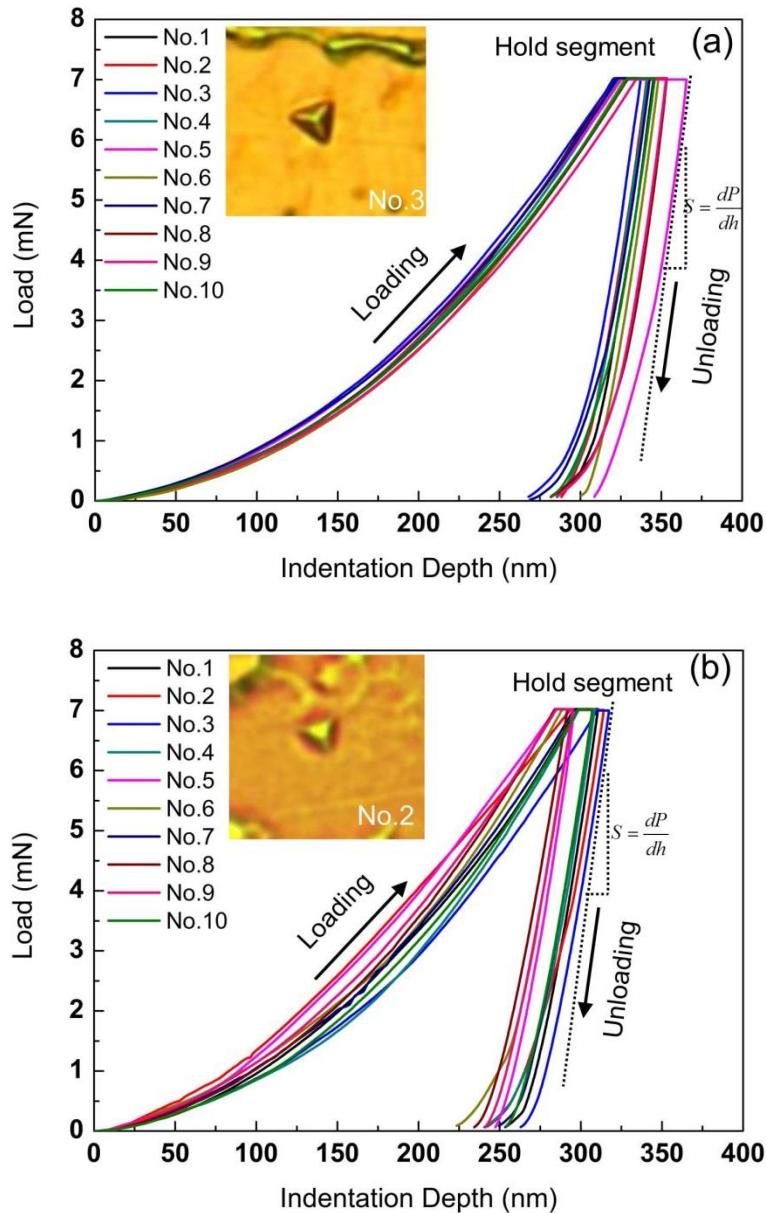


Figure 4-6 Nanoindentation load–displacement curves of Au-Ni coatings: (a) original coating, (b) thermally aged coating

#### 4) Diffusion

Changes in the material properties and coating heterogeneity on the thermally aged

Au-Ni coating were observed by the nanoindentation tests. The reasons for the occurrence of these phenomena were investigated by SEM-EDS. Specifically, EDS area mapping and EDS line were performed at the coating interface on the cross-sections of the mechanical polished samples. Further, the phenomenon of material interpenetration between different coating layers due to diffusion was observed. Quantitative EDS point analyses were performed to determine the coating compositions.

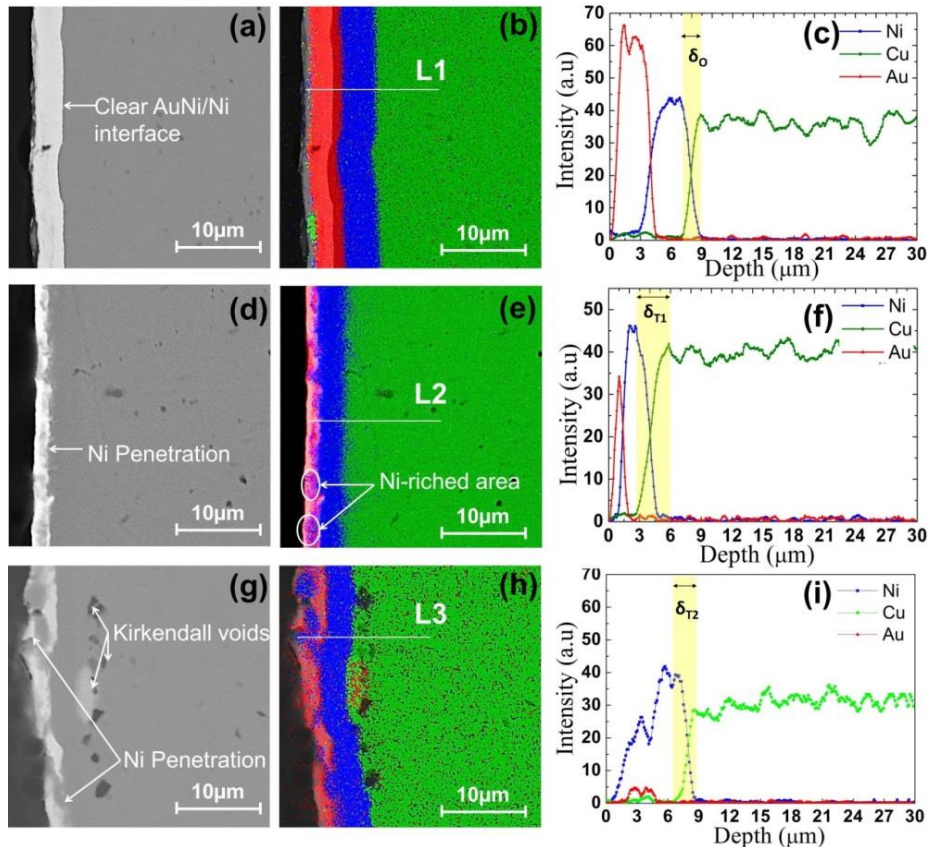


Figure 4-7 Results of SEM-EDS mapping and line scan at coating interfaces: (a, d, g) SEM images of original coating, thermally aged coating at position 1 and thermally aged coating at position 2; (b, e, h) EDS mapping images of original coating, thermally aged coating at position 1 and thermally aged coating at position 2; (c, f, i) element profiles along lines 1, 2 and 3

As shown in Figure 4-7, in the case of the original coating, the interfaces between Au-Ni/Ni and CuCrZr/Ni substrate were clearly observed with high contrast and no obvious broad transition layers between the coating layers and their alloy substrate were observed. The element depth profiles showed the presence of a small amount of Cu, in addition to Ni, in the Au-Ni coating. The original thickness of the Au-Ni coating was about 3.5  $\mu\text{m}$  and as mentioned earlier a 4.3- $\mu\text{m}$ -thick Ni interlayer was applied. Indeed, after thermal aging, considerable diffusion occurred at the CuCrZr/Ni interface and the Ni/Au-Ni interface. Obvious penetration of Ni into the Au-Ni layer

was observed at different locations, which caused blurring of the bonding interface and a decrease in the thickness of the Au-Ni coating. Through statistical analysis, the remaining thicknesses of the Au-Ni and Ni layers were determined to be  $1.84 \pm 0.46 \mu\text{m}$  and  $3.04 \pm 0.42 \mu\text{m}$ , respectively.

The considerable diffusion of Ni into the Au-Ni layer can be explained as follows: during the thermal aging at  $250^\circ\text{C}$  for 500 h, the migration of the Ni atoms from the Ni interlayer to the Au-Ni layer was accelerated and the oversaturated Ni soluted in the Au matrix and precipitated from this matrix to form a Ni-rich phase. In some areas, the Au-Ni layer had already disappeared and subsequently appeared on the top surface. Interdiffusion between the Ni interlayer and the CuCrZr substrate was also observed and many voids (Kirkendall voids [144]) were formed because of this interdiffusion (Figure 4-7 (g) and Figure 4-7(h)). The occurrence of this phenomenon was also reflected in the element depth profiles, which showed a broadening of the transition layers of Ni and Cu after thermal aging.

The obvious diffusion of Ni into the Au-Ni layer could be one of the reasons for the increase in the hardness of the Au-Ni coating after thermal aging via two hardening mechanisms: solid-solution hardening and precipitation hardening [145, 146]. Moreover, the thickness of the Au-Ni layer decreased in several local areas after the thermal aging process; therefore, the increase in the hardness of the Au-Ni layer after thermal aging was probably due to the effects caused by the Ni interlayer (the indenter tip was pressed into the Ni interlayer or near to the Ni interlayer), which has similar hardness values than the values measured, as reported previously [147].

Quantitative EDS point analyses were performed and the diffusion phenomenon was studied via analysis of the chemical compositions of the coating surfaces (Figure 4-8). Before thermal aging, the composition was 2.09 wt.% Ni, 1.59 wt.% Cu and 96.32 wt.% Au. The 2.09 wt.% Ni that alloyed into the coating increased the hardness of the Au matrix significantly. After thermal aging in high vacuum, the Ni content on the coating surface increased to 3.24 wt.% owing to metal diffusion. At a local position (position C in Figure 4-8 (e)), a sharp increase in the Cu content from 1.59 wt.% to 46.35 wt.% was observed, which indicated that the CuCrZr substrate had invaded into the Au-Ni coating and became exposed to the surroundings without the protection of the coating. Exposure of the Cu present on the Au-Ni coating surface can degrade the corrosion resistance of the RF contacts when they are exposed to air during assembly and maintenance. Direct contact between Cu and Au can result in the formation of intermetallic compounds. Consequently, the electrical and tribological performances of the Au-Ni coating are degraded after thermal aging.

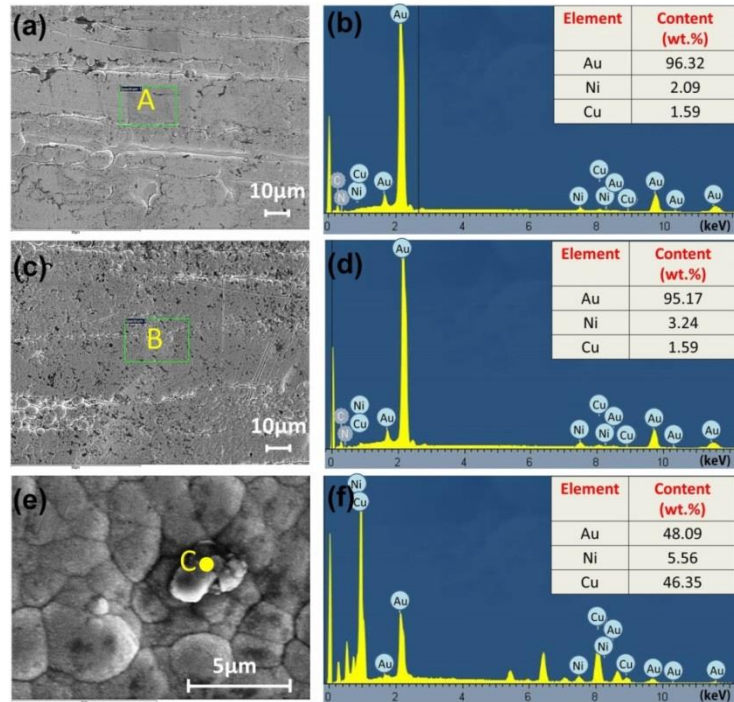


Figure 4-8 SEM/EDS analyses of Au-Ni coating: (a, c, e) SEM images of surfaces of original Au-Ni coating, thermally aged Au-Ni coating ( $\times 1000$ ) and thermally aged Au-Ni coating ( $\times 8000$ ), respectively; (b, d, f) EDS spectra of area A, area B and point C in, respectively

### 5) Adhesion

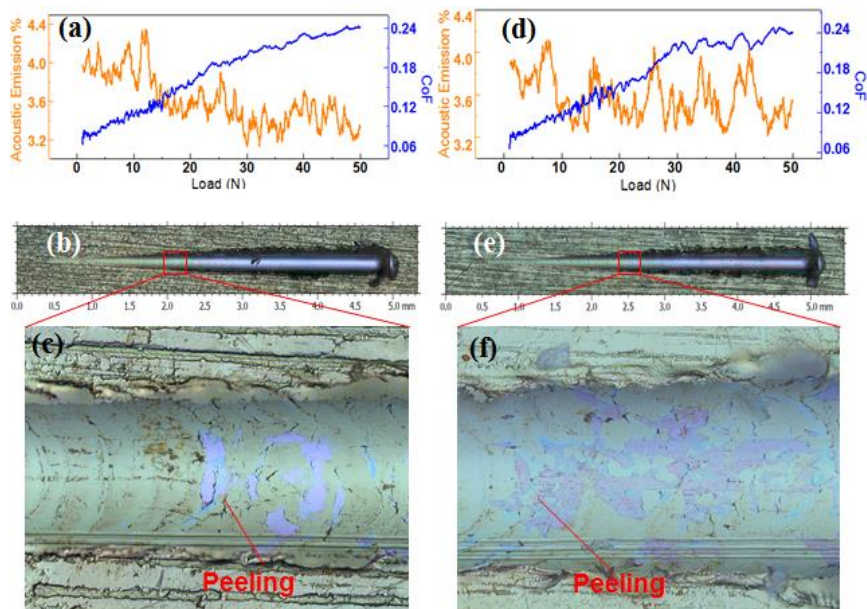


Figure 4-9 Scratch tests results of Au-Ni coating on CuCrZr substrates: (a, d) Acoustic emission and CoF signals of original and thermally aged samples, (b, e) Optical microscope images of scratch tracks of original and thermally aged samples, (c, f) SEM micrographs of cracks on the scratch tracks of original and thermally aged samples

As wear protective coating, the wear performance of Au-Ni determines its lifetime. Adhesion performance of coating reveals its wear resistance. Three scratch tests were performed on the original sample and thermally aged sample respectively. There were no apparent transitions observed on the acoustic and CoF signals, which meant no cracking phenomenon occurred during scratch tests (Figure 4-9). The critical load of the original Au-Ni coating was  $15.8 \pm 2.6$  N and the thermally aged one was  $17.1 \pm 0.72$  N. With lower coating thickness and diffusion voids, the critical load of the Au-Ni coating after thermal aging still increased. The increase of critical loads after thermal aging was probably caused by the hardness increase of the Au-Ni coating.

#### 4.2.1.2 Ag-Sb on CuCrZr

##### 1) Surface morphology

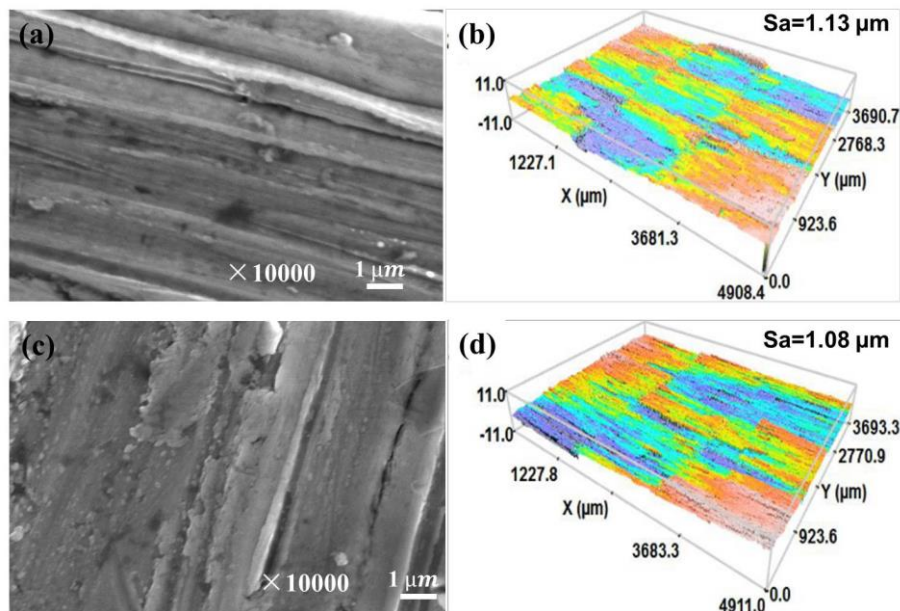


Figure 4-10 Coating surface morphology: (a, b) SEM image and 3D interferometric image of the original coating surface, (c, d) SEM image and 3D interferometric image of the thermally aged coating

Figure 4-10 shows the surface morphology of the Ag-Sb coating on CuCrZr. There are no obvious coating defects observed. After thermal aging, no noticeable change happened on the Ag-Sb coating surface. The surface roughnesses of the Ag-Sb coating before and after thermal aging are  $1.13 \mu\text{m}$  and  $1.08 \mu\text{m}$  respectively.

##### 2) Crystal structure

As shown in Figure 4-11, only Ag peaks were observed on the original coating. Although Sb was co-deposited into the Ag coating, as the Sb atom's radius ( $141 \text{ pm}$ )

is similar to Ag atom's radius (144 pm) and the Sb content (1.1 at.%) is low, the lattice structure of Ag was not obviously changed. The crystallite size of the Ag-Sb coating was 24 nm (from (111) peak) with a lattice constant of 0.4091 nm. After thermal aging, the remarkable change was the sharpening (with smaller FWHM) of all the Ag peaks which was caused by the significant grain coarsening. With the growing of grain size, more peaks were observed and peak intensities increased. Based on the peak positions, before and after thermal aging, there was no compositional change in the coating observed. After thermal aging, the grain size of the coating grew significantly which was higher than 100 nm. Even though the Scherrer equation can only be applied when the crystallite sizes are lower than 100 nm, the crystallite size of Ag-Sb coating was still calculated based on the peak (111) to evaluate the effect of thermal aging. After 250°C, 500 h thermal aging, the crystallite size of Ag-Sb increased nearly 8 times to 199 nm. The grain size growing would obviously impair the hardness of Ag-Sb coating.

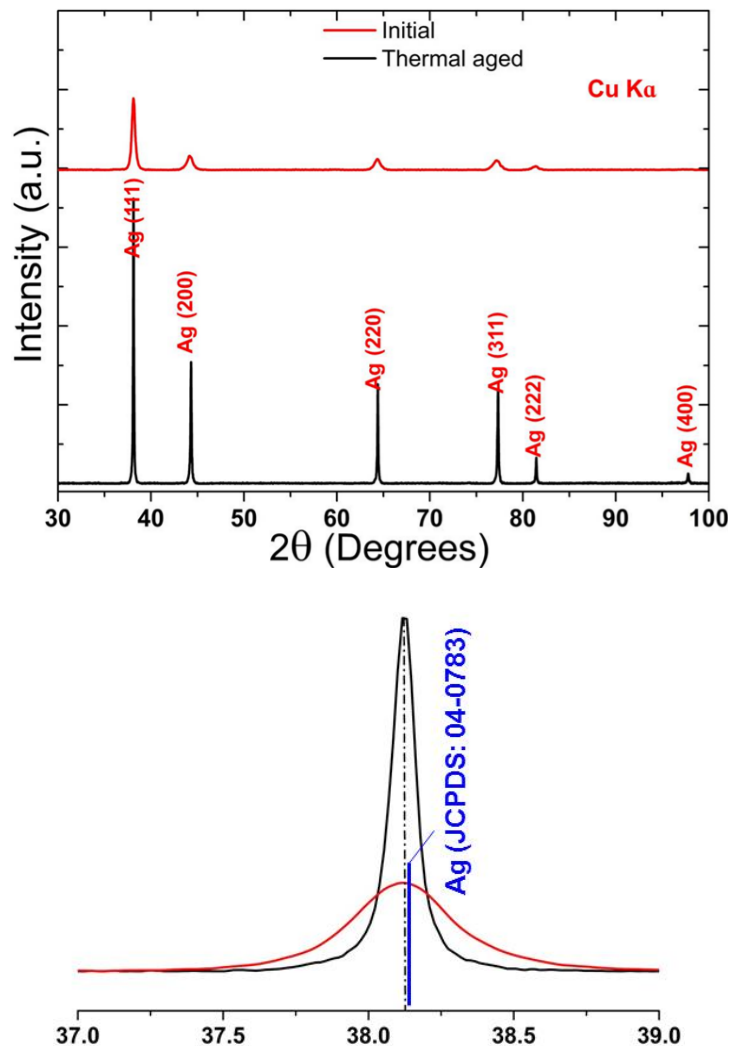


Figure 4-11 XRD pattern of Ag-Sb coating on CuCrZr (original and thermally aged)

### 3) Hardness

The hardness of Ag-Sb coating was measured by using microhardmeter with test force of 10 gf. Five measurements were performed both on the original and thermally aged samples respectively. The measurement results are shown in Table 4-2.

Table 4-2 Hardness measurement results of Ag-Sb coating on CuCrZr

Sample	Test No.1	Test No.2	Test No.3	Test No.4	Test No.5
<b>Original</b>	188.3	195.8	190.8	201	198.4
<b>Thermally aged</b>	63.1	63.6	69.9	66.5	66.5

The average hardness of the original coating is 194.8 HV0.01. The alloying of Sb improved the hardness of the Ag coating significantly compared with conventional Ag coating whose hardness is around 100 HV. However, after thermal aging, the average hardness of Ag-Sb coating decreased to 65.9 HV0.01. The hardness degradation of Ag-Sb coating was caused by the significant grain coarsening during thermal aging. After 500 h, 250°C thermal aging treatment, the hardness of Ag-Sb coating was similar to the hardness of pure Ag after heat treatment reported by other researchers [148]. Thus, for ITER ICRH RF contact application, there will be no advantages of applying Ag-Sb alloy coating instead of pure Ag to improve its wear resistance.

### 4) Diffusion

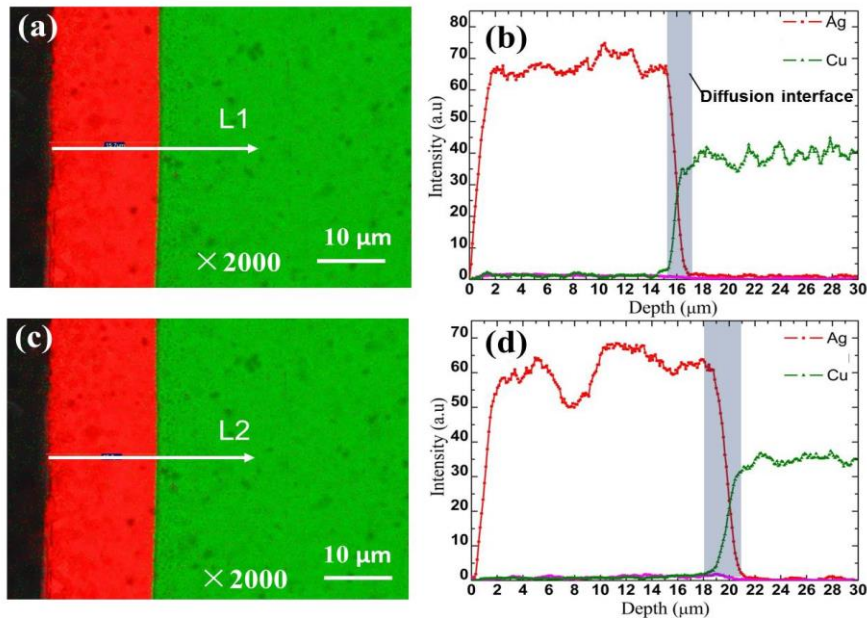


Figure 4-12 Results of SEM-EDS mapping and line scan at coating interfaces: (a,c) EDS mapping images of the original coating and the thermally aged coating, (b, d) Element profiles along lines 1 and 2

Based on the Ag-Cu binary phase diagram, below 300°C, the solubility between Ag and Cu is very low. As shown in Figure 4-12, although there was no diffusion barrier applied between Ag-Sb and CuCrZr, the coating interface was very clear. After thermal aging, the coating interface had a slight increase (around 1  $\mu\text{m}$ ). However, the coating interface was still bright and there were no voids generated.

#### 4.2.1.3 Rh on CuCrZr

##### 1) Surface morphology

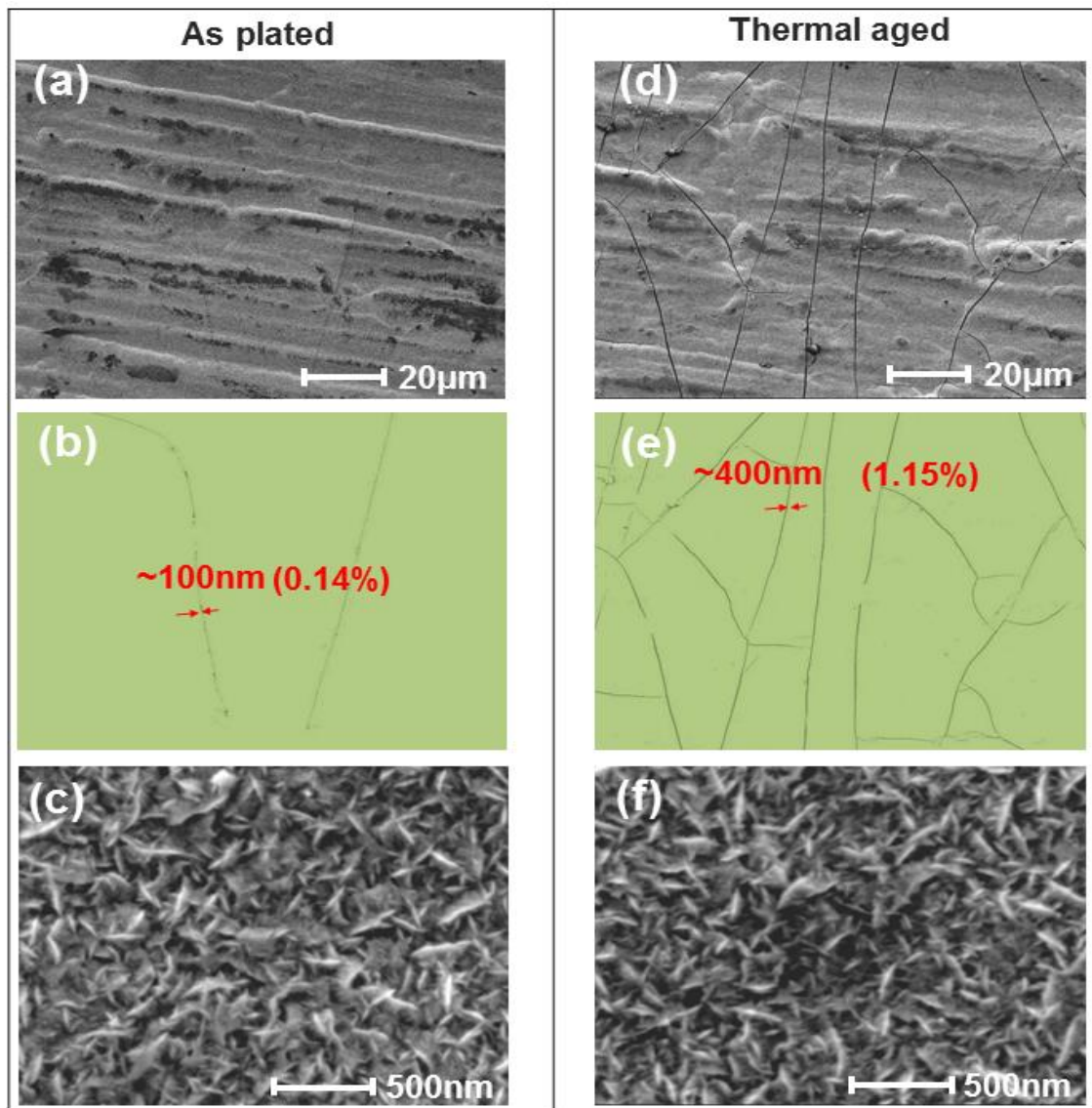


Figure 4-13 Surface morphology of the Rh coating on CuCrZr substrate: (a, d) SEM images of original coating and thermally aged coating ( $\times 1,000$ ), (b, e) Cracks on the original coating and thermally aged coating processed by Image J, (c, f) SEM images of original coating and thermally aged coating ( $\times 50,000$ )

As shown in Figure 4-13, on the Rh coating's SEM view under magnification of  $\times 1000$ , columnar ridges were observed on the surface of Rh coating and the coating was very dense without pores. Very few narrow cracks were observed, which were mainly induced by the chemically generated internal stresses which usually arise during the coating's fabrication process and highly correlated with the processing conditions [136, 149, 150]. Actually, one of the most serious disadvantages of electroplating is the presence of high internal stresses that can lead to cracking in the coating [18]. In order to quantify the cracks, two parameters were used which include the crack width and crack area proportion. The cracking susceptibility was evaluated by the proportion of cracks area per surface area of coating which can be processed and calculated through Image J software [151]. After thermal aging, the number of cracks on the Rh coating increased significantly and the crack width enlarged. The area proportion of cracks increased from 0.14% to 1.15% with crack width increasing from 100 nm to 400 nm. Moreover, the cracks have obvious parallel distribution characteristic.

The explanation of crack generation and propagation during thermal aging treatment is the tensile thermal stresses' relaxation. As illustrated in Figure 4-14, after plating, the coating is assumed to be low-stress coating or coating without stress. While during baking, due to the large difference of coefficient of thermal expansion (CTE) between Rh and CuCrZr substrate (Table 4-3), Rh coating acted as a constraint to CuCrZr for thermal expansion and as a result, high tensile stress is generated in the Rh coating [152, 153]. When the thermal stress in the coating is higher than the coating's strength, cracking or fracture occurs. Especially for the materials which have low ductility in property such as Rh, their deposits are inherently brittle because they contain cracks that readily lead to fracture. The initial cracks in the Rh coating are unstable and they can spread rapidly without causing obvious plastic deformation. The directions of crack generation are almost perpendicular to the direction of the applied tensile stress caused by the thermal stresses, which include the crack propagation tendencies to the top surface of the Rh coating and parallel to the coating surface. With the cracks generation and propagation, the thermal stresses in the coating assembly are released. Applying a relative soft interlayer whose CTE is between Rh and CuCrZr is a practical solution to minimize the thermal stress in the Rh layer [154, 155]. So, in addition to avoiding Rh bath contamination due to its corrosion to the CuCrZr substrate, the 0.5  $\mu\text{m}$  thick Au layer is applied between the Rh coating and CuCrZr substrate to release coating stress.

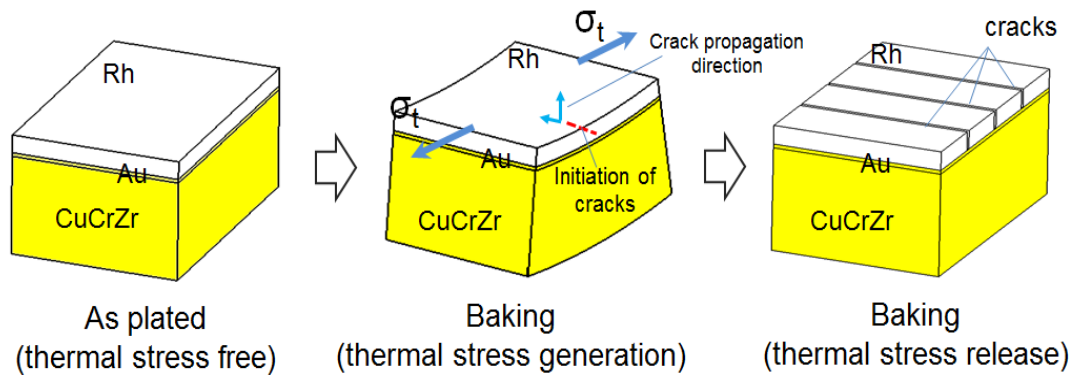


Figure 4-14 Failure mechanism of the Rh coating during baking

Table 4-3 Main material properties of Rh, CuCrZr and Au at room temperature

Property	Material		
	Rh	CuCrZr	Au
CTE ( $\times 10^{-6}/\text{K}$ )	8.2	16.7	14.2
Young's Modulus (GPa)	372	127.5	76.6
Poisson's Ratio	0.26	0.33	0.42

Under a magnification of  $\times 50000$ , dense acicular grains, with an averaged size of 200 nm in length and 50 nm in width were observed. After 250 °C, 500 h thermal aging, the acicular morphology of the Rh coating was not changed and the average size of the acicular structures was similar with the initial coating. The fine-grained deposit structure of Rh increases the tendency of crack generation since the plastic deformation that occurs primarily by dislocation motion can be significantly impeded by the abundance of grain boundaries.

In addition to the cracking phenomenon, thermal aging changes the surface roughness of the Rh coating. After thermal aging, the surface roughness (Sa) increases from  $0.44 \pm 0.02 \mu\text{m}$  to  $0.65 \pm 0.08 \mu\text{m}$ , which may be induced by the diffusion at the coating interface.

## 2) Crystal structure

The crystallite size of the Rh coating before thermal aging is about 7.5 nm, with a lattice constant of 0.3787 nm. Cu (Cu alloy) peaks are observed in the pattern due to the X-ray penetration into the base material of the Rh coating (Figure 4-15). Compared with the initial sample, after thermal aging, the phenomenon of the Rh pattern peaks shifting to high  $\theta$  direction weakened, which is caused by the diffusion of Au layer into the Rh layer (after thermal aging, the content of Cu in Rh increased significantly which raised the solid solubility of Au in Rh). The melting point of Rh is 1966°C, so 500 hours of thermal aging at 250°C would not influence the crystallite

size of the Rh coating too much. The crystallite size grows to 11.3 nm during thermal aging with a lattice constant about 0.3802 nm. No Au peaks found from the XRD pattern which means that the thin Au layer had diffused into Cu base and no Au or Au-based alloy exist. The diffusion aspect is discussed in section 4).

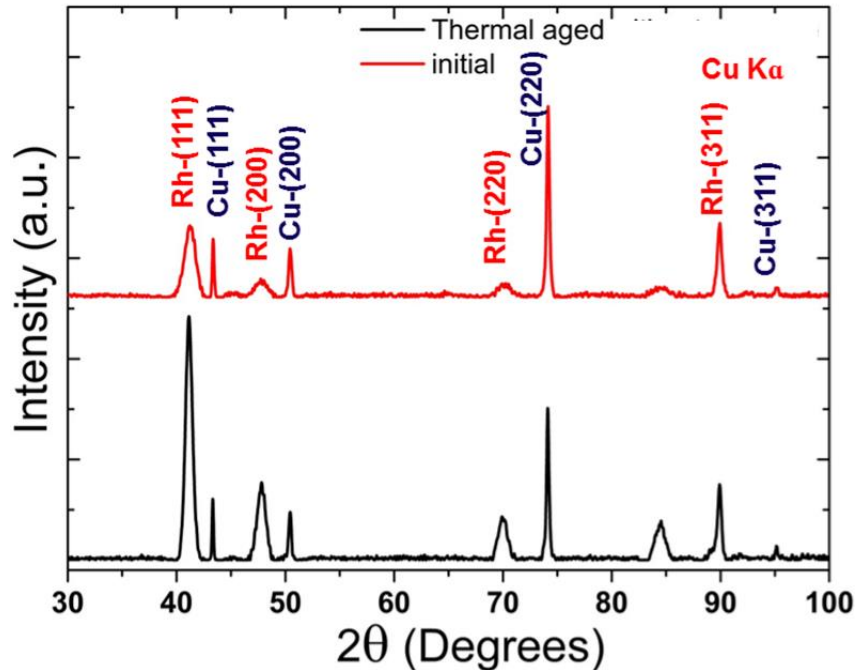


Figure 4-15 XRD patterns of Rh coatings on CuCrZr substrates (original and thermally aged)

### 3) Hardness

The reason that Rh is widely applied as wear protective coating is due to its extremely high hardness characteristic. Through crystal structure characterization, the diffusion of Cu into Rh layer was observed and the crystallite size increase of Rh was validated. There are two factors that affect the hardness of the Rh coating after thermal aging: (i) crystallite coarsening that could decrease the Rh coating's hardness and (ii) the solid-solution hardening effect due to Rh-Cu interdiffusion that could increase the Rh coating's hardness. The hardness of Rh coating was measured by using microhardmeter with test force of 20 gf. As shown in Figure 4-16, the hardness of the Rh coating after thermal aging is  $421.8 \pm 22.3$  which is obviously higher than the hardness  $375.5 \pm 16.4$  of the original Rh coating. Cracks were observed around the impressions both on the original and thermal aged Rh coatings, which were mainly caused by the large gap of hardness between Rh and CuCrZr. The hardness of CuCrZr substrates before and after thermal aging was measured and their hardness was around 154 without change. Therefore, based on these results, the hardness increase after thermal aging indicates that the solid-solution hardening effect of Cu diffused into Rh crystal lattice was the dominant factor to affect the hardness of the Rh coating.

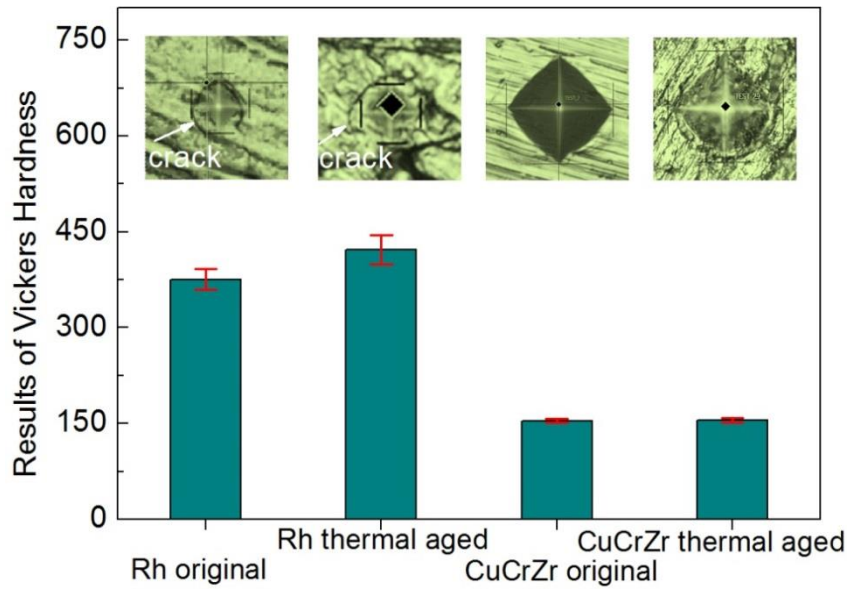


Figure 4-16 Measurement of Vickers hardness of Rh coating and CuCrZr substrate

#### 4) Diffusion

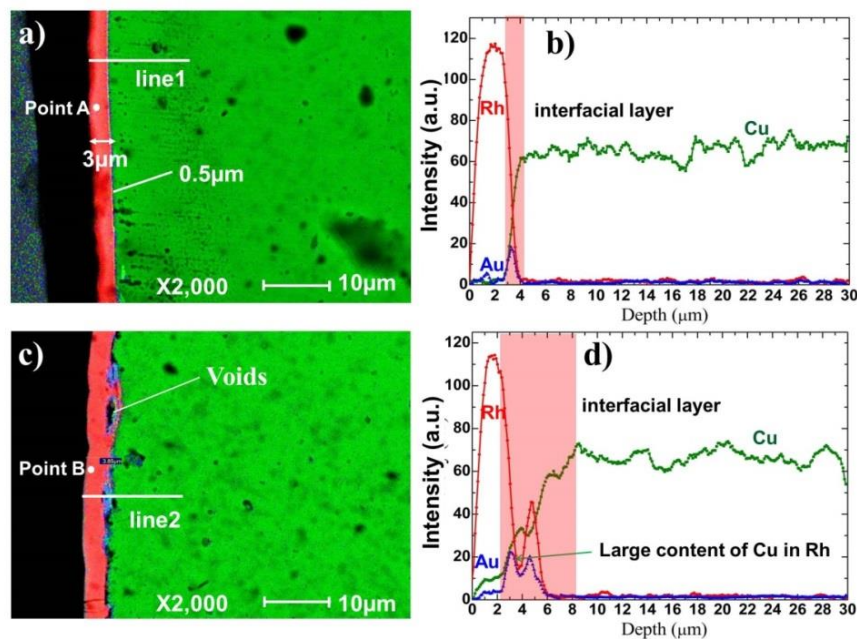


Figure 4-17 Mapping and depth profile of the Rh coating on CuCrZr substrate: (a) EDS mapping of original sample section, (b) Elements profiles along line1, (c) EDS mapping of thermally aged sample section, (d). Elements profiles along line2

The EDS mapping of the Rh coating on CuCrZr substrate as plated is shown in Figure 4-17 (a). On this sample, the Rh layer and CuCrZr substrate have a clear coating interface without any pores observed. About 0.5  $\mu\text{m}$  of Au interlayer was applied to improve adhesion performance of Rh on CuCrZr. The thickness of the Rh layer is about 3  $\mu\text{m}$ . Figure 4-17 (b) is the elements' depth profiles along line 1, good bonding

interfaces can be proved by the abrupt changes of curves at the coating interfaces. As shown in Figure 4-17 (c), after thermal aging, serious diffusion happened at the Rh and CuCrZr interface and voids generated. The diffusion both happened between Au/Cu and Rh/Cu. Due to the large amount of Cu that diffused into Rh layer and the voids' generation, at some positions the thickness of the Rh layer increased from 3  $\mu\text{m}$  to about 4  $\mu\text{m}$  and the surface roughness of Rh coating increased. Based on the elements profiles (Figure 4-17 (d)), thickness increase of the Rh layer was observed and serious diffusion of Cu into Rh was proved. The Cu atoms that diffused into the Rh layer had also increased the solid solubility of Au in the Rh layer. The significant diffusion phenomenon proves that solid-solution hardening induced the hardness increase of Rh coating after thermal aging. For tribological point of view, the hardness increase can improve the Rh coating's wear resistance. As Cu/Ni interface is more stable than Au/Cu interface, replacing Au interlayer by Ni could be a solution to minimize the diffusion issue.

In order to quantify the Cu diffusion into Rh, EDS point (point A and point B in Figure 4-17) analyses were performed and the diffusion phenomenon was studied through analyzing the chemical compositions of the Rh coating. Before thermal aging, the compositions in the Rh coating were: Cu–2.67 wt.%, Rh–97.33 wt.%. However, after thermal aging, the Cu content increased significantly to 12.89 wt.%.

### 5) Adhesion

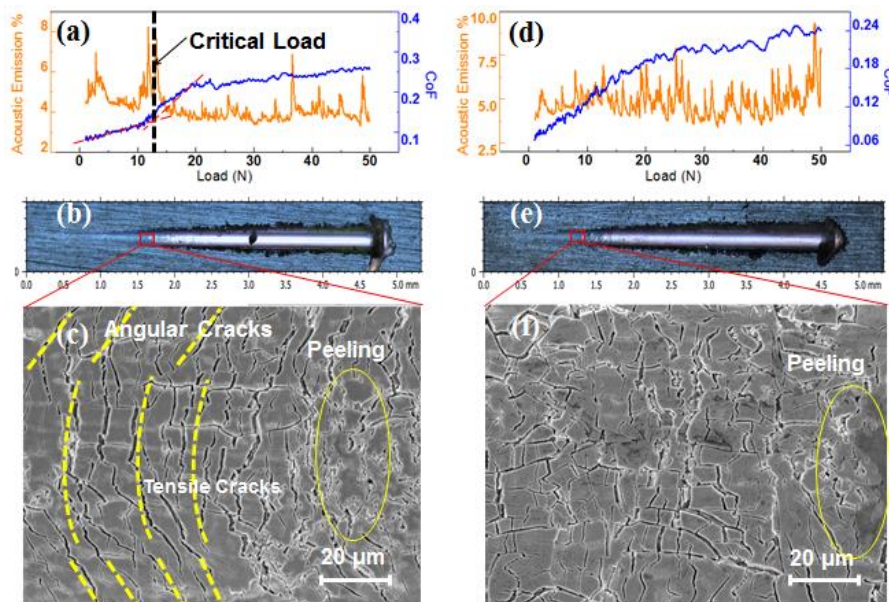


Figure 4-18 Scratch tests results of Rh coating on CuCrZr substrates: (a, d) Acoustic emission and CoF signals of original and thermally aged samples, (b, e) Optical microscope images of scratch tracks of original and thermally aged samples, (c, f) SEM micrographs of cracks on the scratch tracks of original and thermally aged samples

The voids generated at the coating interface due to diffusion may degrade the attachment performance of Rh coating on CuCrZr substrate. Consequently, the wear resistance of the Rh coating would be deteriorated. Scratch tests were performed to evaluate the effects of thermal aging on Rh adhesion and the results are shown in Figure 4-18.

The failure of Rh coating on CuCrZr substrate during scratch tests presents a typical mechanical behavior of a hard and brittle coating film deposited on the soft substrate, whose main failure phenomenon is coating cracking through the whole thickness. For the original Rh coating on CuCrZr, with the increase of the test load, angular cracking occurred and then tensile cracking was observed. At around 13 N, obvious transitions on the signals of acoustic emission and CoF happened. Based on SEM observation, the dense tensile cracks turned to massive Rh delamination at that time. Based on statistical analysis, the critical load of original coating on CuCrZr substrate is  $13.0 \pm 1.4$  N. However, for the samples that baked at 250°C for 500 h, there are no obvious transition points on the acoustic emission and CoF curves. Through SEM microscopic observations, on the scratch track, there were no regular cracks generated. Mesh cracking generated at the beginning of the scratch test and its critical load is  $9.6 \pm 0.7$  N. The degeneration of the Rh coating's adhesion performance is caused by two reasons: the cracks generated during thermal aging and a large number of holes existing at coating interface due to Kirkendall effect. The exiting of holes and original cracks impairs the supporting of the base material (CuCrZr) to the Rh coating. Therefore, cracks generated faster without any direction of orientation and peeling happened earlier.

#### **4.2.1.4 Rh on 316L**

##### *1) Surface morphology*

As shown in Figure 4-19, cracks were observed on the surface of the coating and the crack width was uniform (about 100 nm). These cracks were mainly induced by the chemically generated stresses which occurred during the coating's electroplating process [136, 149, 150]. The proportion of the cracks is about 0.55%. By observing under high magnification, the Rh coating surface consists of dense acicular grains, with the averaged size of 200 nm in length and 50 nm in width.

After the thermal aging process, the most significant change of the coating surface is the increase in the proportion of cracks, which increased from 0.55% to 4.56%. Two main factors cause the increase of the cracking proportion which is the crack width enlarging of original cracks and the generation of new cracks. The crack width of the original cracks turned from 100 nm to nearly 2  $\mu\text{m}$  due to the tensile thermal stress

relaxation in the Rh coating, whose mechanism had been explained in the last section.

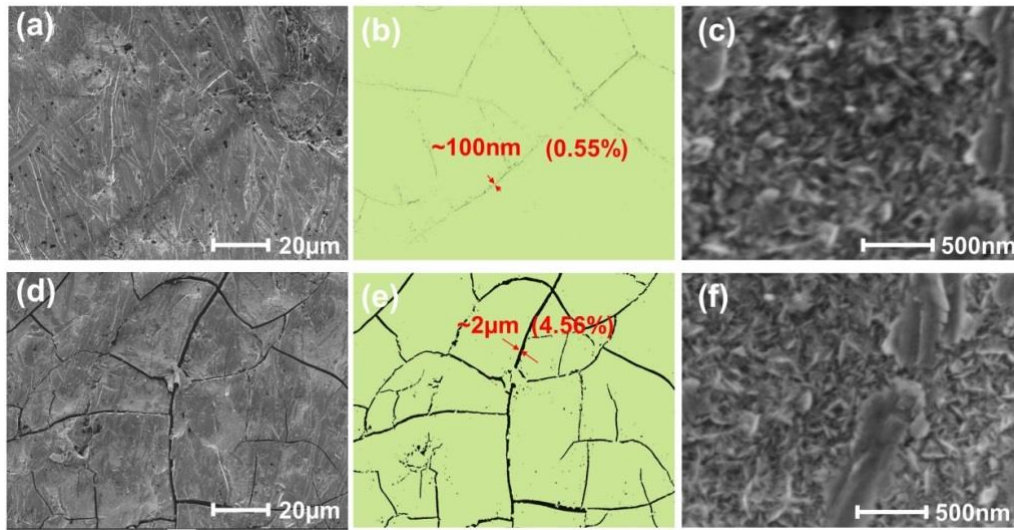


Figure 4-19 Surface morphology of the Rh coating on 316L substrate: (a, d) SEM images of original coating and thermally aged coating ( $\times 1,000$ ), (b, e) Cracks on the original coating and thermally aged coating processed by Image J, (c, f) SEM images of original coating and thermally aged coating ( $\times 50,000$ )

## 2) Crystal structure

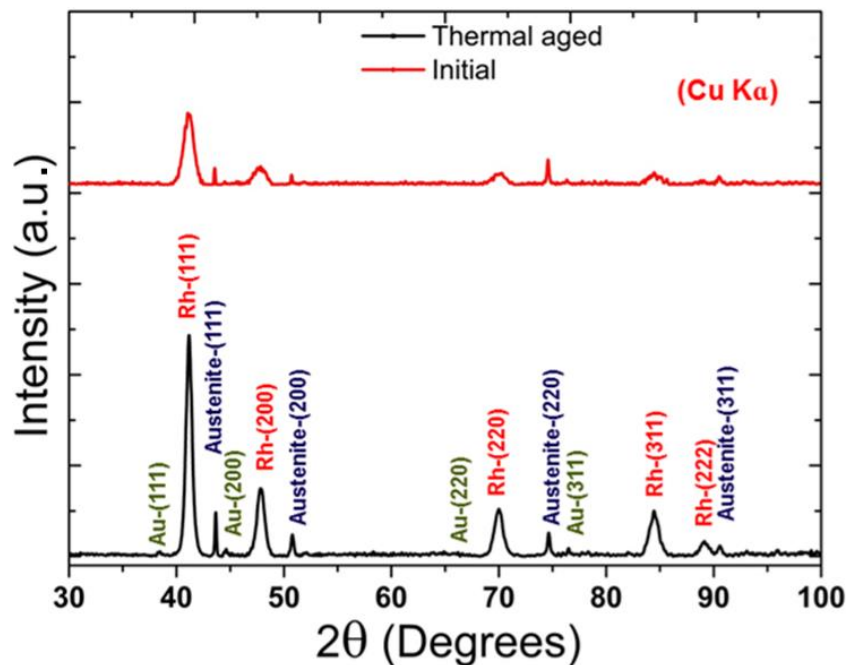


Figure 4-20 XRD patterns of Rh coatings on 316L substrates (original and thermally aged)

The crystallite size of the Rh coating before thermal aging is about 7 nm, with a lattice constant of 0.3795 nm. In Figure 4-20, austenite peaks were found in the

pattern due to the cracks on the Rh coating surface as well as the X-ray penetration. For the same reason, a small amount of Au was found as it acts as the interlayer between Rh and 316L. The crystallite size grew to 15 nm during thermal aging with a lattice constant of about 0.3795 nm. The peak intensity increased after thermal aging is due to the reduction of the microstructural defects and the consequent improvement of the film crystallinity [156].

### 3) *Hardness*

The hardness of Rh coating on 316L was measured under a test force of 30 gf. The measurement results are shown in Table 4-4.

Table 4-4 Hardness measurement results of Rh coating on 316L

Sample	Test No.1	Test No.2	Test No.3	Test No.4	Test No.5
<b>Original</b>	572.3	511.2	611.1	636.3	626.1
<b>Thermally aged</b>	667.7	691.6	640.6	667.7	627.7

The averaged hardness of the Rh coating on 316L is 591 HV0.03. After thermal aging, the hardness of the Rh coating increased to 659 HV0.03. The reason that caused the hardness increase could be the diffusion of Fe and Ni atoms into the Rh layer which generated solid strengthening effect.

### 4) *Diffusion*

The EDS mapping of Rh on 316L as plated that is shown in Figure 4-21 (a) indicates that a 4.27  $\mu\text{m}$  thick Rh with a 2.4  $\mu\text{m}$  thick Ni interlayer and a 500 nm thick Au strike were electroplated on the 316L substrate. After thermal aging, the material interfaces are still clear without obvious diffusion happened. The enlarging of cracks in the Rh layer was observed and these cracks initiated in the Rh layer at the beginning and extended into the Ni interlayer. This crack propagation phenomenon indicates that the attachment performance of Rh on Ni is good. Although cracks grew after thermal aging, no peeling phenomenon of Rh from its substrate observed. Based on the binary phase diagrams, for Rh-Au there is nearly no solid solubility over the entire range of composition and for Au-Ni their solid solubility is very low when the temperature is lower than 200°C. The good stability of Rh/Au and Au/Ni coating interfaces was confirmed through the elements depth profiles shown in Figure 4-21 (c) and Figure 4-21 (d). The Ni/316L interface was modified due to thermal aging and the interfacial layer enlarged by 1  $\mu\text{m}$ .

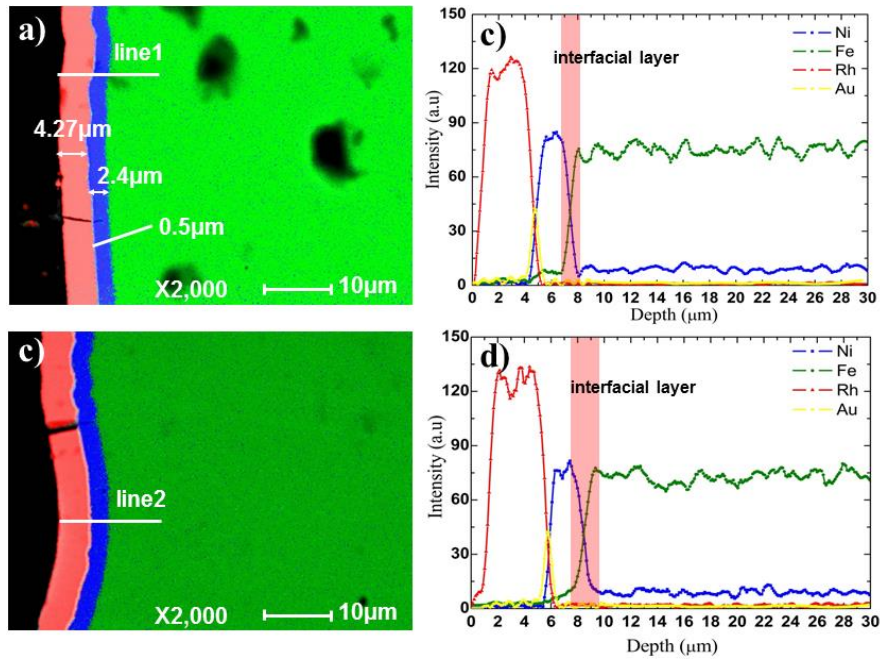


Figure 4-21 Mapping and depth profile of the Rh coating on 316L substrate: (a) EDS mapping of original sample section, (b) Elements profiles along line1, (c) EDS mapping of thermally aged sample section, (d). Elements profiles along line2

### 5) Adhesion

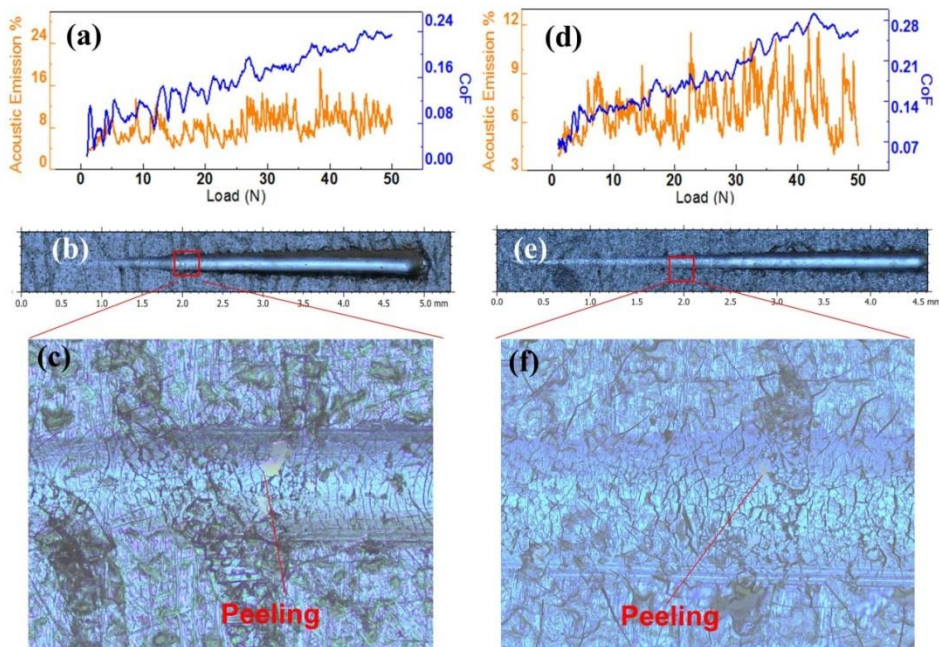


Figure 4-22 Scratch tests results of Rh coating on 316L substrates: (a, d) Acoustic emission and CoF signals of original and thermally aged samples, (b, e) Optical microscope images of scratch tracks of original and thermally aged samples, (c, f) SEM micrographs of cracks on the scratch tracks of original and thermally aged samples

Before thermal aging, the critical load of the Rh coating is  $13.8 \pm 6.6$  N. The large data dispersion was caused by the existing of large amount of cracks in the Rh coating, which increased the randomness of Rh coating delamination. After thermal aging, the critical load decreases to  $11.3 \pm 3.5$  N. There is no obvious adherence performance degradation of the Rh coating observed after thermal ageing, which is an interesting result for the ITER application.

#### **4.2.2 Diffusion between coatings**

In section 4.2.1, thermal aging effects on the four coatings (Au-Ni on CuCrZr, Ag-Sb on CuCrZr, Rh on CuCrZr and Rh on 316L) were studied separately. In ITER, the RF contact louver will be contacting with the surface of an RF conductor by applying an additional force. So, the above four coating samples can generate four kinds of assembly combinations:

1. Au-Ni on CuCrZr vs. Rh on 316L,
2. Au-Ni on CuCrZr vs. Rh on CuCrZr,
3. Ag-Sb on CuCrZr vs. Rh on 316L,
4. Ag-Sb on CuCrZr vs. Rh on CuCrZr.

During 250°C thermal aging, diffusion between the two coatings can generate cold welding. When mechanical sliding starts between these two cold welded coatings, tearing or delamination may occur on the coatings. Thus, it's necessary to evaluate the diffusion phenomena between the above coating assemblies beforehand.

##### **4.2.2.1 Au-Ni on CuCrZr vs. Rh on 316L**

As shown in Figure 4-23, the surface morphologies of the Rh and Au-Ni surfaces are similar to their morphologies after thermal aging without assembling. No coating delamination happened and no obvious diffusion has been observed between the two surfaces. Based on the Au-Rh binary phase diagram (Appendix B), Au and Rh are immiscible in almost the entire composition range. In other words, metal diffusion between Au and Rh pair is very low and the effects caused by the Au/Rh diffusion on the electrical contact performance can be ignored.

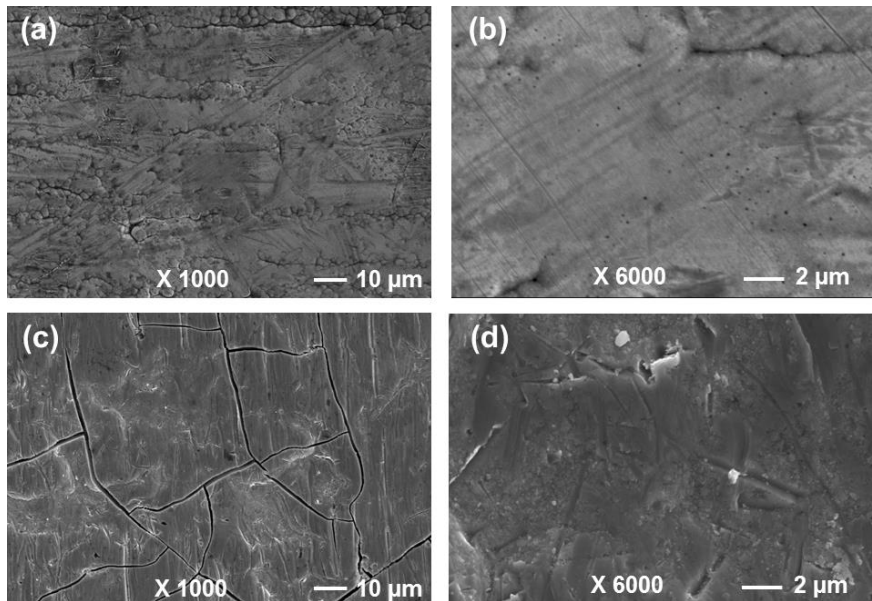


Figure 4-23 SEM images of Au-Ni (on CuCrZr) surface and Rh (on 316L) surface: (a) Au-Ni surface  $\times 1,000$ , (b) Au-Ni surface  $\times 10,000$ , (c) Rh surface  $\times 1,000$ , (d) Rh surface  $\times 10,000$

#### 4.2.2.2 Au-Ni on CuCrZr vs. Rh on CuCrZr

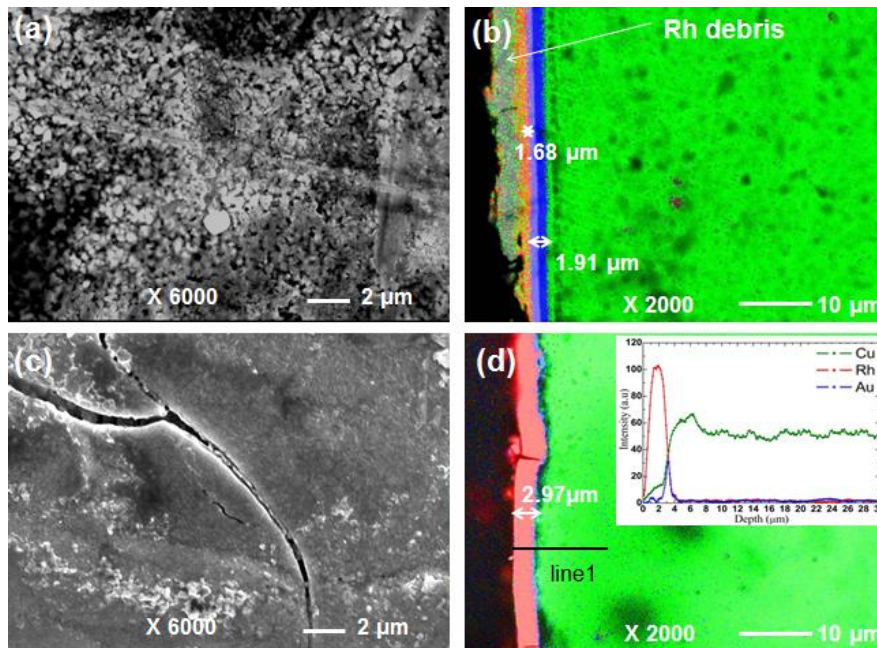


Figure 4-24 SEM and EDS mapping of Au-Ni (on CuCrZr) and Rh (on CuCrZr): (a) SEM image of Au-Ni surface, (b) EDS mapping of Au-Ni cross-sectional surface, (c) SEM image of Rh surface, (d) EDS mapping of Rh cross-sectional surface

When the thermal aging process had finished, the two samples had been cold welded together, indicating that serious diffusion happened between the two coatings. On the Au-Ni surface (Figure 4-24 (a)), the original dense coating turned to be porous with material loss. As shown in Figure 4-24 (b), at some positions, large pieces of Rh

debris were attached on the Au-Ni surface due to cold welding. In ITER, such attachment and peeling are very harmful to the RF conductor, as its functional coating can be removed fast.

In the previous section, Rh-Au has been proved without diffusion after 250°C, 500 h thermal aging. Therefore, the serious diffusion here should not be caused by Rh-Au diffusion. By making a cross-section of the Rh coating and doing an element scanning from the Rh coating surface to the CuCrZr substrate, large amount of Cu was observed in the Rh coating. Thus, the cold welding didn't happen between Rh and Au but occurred between Au and Cu (from the CuCrZr substrate of Rh). The diffusion of Cu into the Au-Ni layer can degrade the Au-Ni coating's electrical conductivity due to the occurrence of intermetallic compounds.

#### 4.2.2.3 Ag-Sb on CuCrZr vs. Rh on 316L

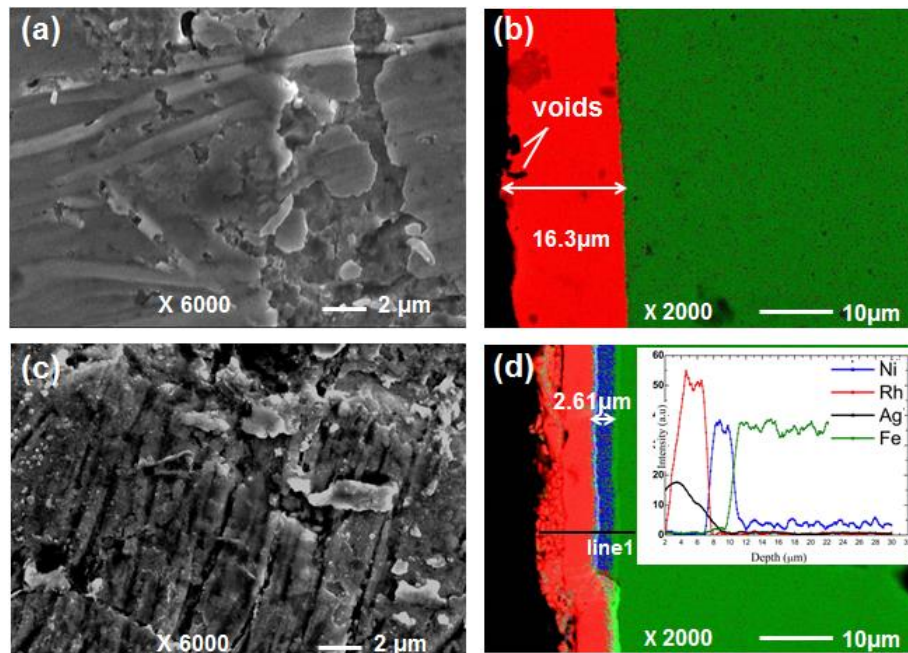


Figure 4-25 SEM and EDS mapping of Ag-Sb (on CuCrZr) and Rh (on 316L): (a) SEM image of Ag-Sb surface, (b) EDS mapping of Ag-Sb cross-sectional surface, (c) SEM image of Rh surface, (d) EDS mapping of Rh cross-sectional surface

From the Ag-Rh binary phase diagram, the solid solubility of Rh in Ag under 250°C is very low. However, the solid solubility of Ag in Rh under the same temperature is about 10 wt.%. So, during the diffusion test, diffusion between Ag and Rh happened and cold welding between the two coatings' surfaces occurred. As shown in Figure 4-25, when the two samples were disassembled, debris of Ag-Sb remained attached on the Rh surface. Because the diffusion rate of Ag into Rh was much higher than Rh

into Ag, Kirkendall voids generated on the Ag-Sb surface. There was no delamination of Rh from 316L substrate observed, which indicates that the adhesion performance of Rh is high. Cold welding and pores on the Ag-Sb surface can impair its wear resistivity and applying thicker Ag-Sb coating could prolong its lifetime.

#### 4.2.2.4 Ag-Sb on CuCrZr vs. Rh on CuCrZr

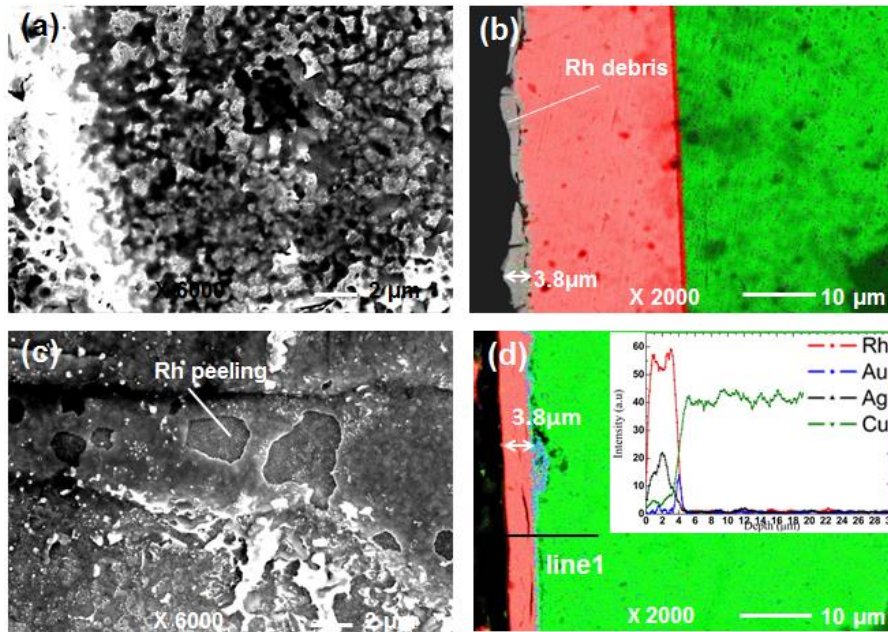


Figure 4-26 SEM and EDS mapping of Ag-Sb (on CuCrZr) and Rh (on CuCrZr): (a) SEM image of Ag-Sb surface, (b) EDS mapping of Ag-Sb cross-sectional surface, (c) SEM image of Rh surface, (d) EDS mapping of Rh cross-sectional surface

Due to the diffusion of Ag into Rh, a similar phenomenon occurred on the surfaces of the Ag-Sb as introduced in section 4.2.2.3. The only difference is that Rh debris with thickness around 3  $\mu\text{m}$  was observed on the Ag-Sb surface (Figure 4-26). Rh peeling was also observed from the SEM image of the Rh surface. As the Rh sample mimicked the RF conductor which is a large part with low maintainability, the peeling of Rh is not acceptable.

### 4.2.3 Discussion

Four kinds of commercial coatings were intensely studied, which include: Au-Ni on CuCrZr, Ag-Sb on CuCrZr, Rh on CuCrZr and Rh on 316L. The first two were used to mimic the RF contact louver and the other two were used to mimic the RF conductor.

- Au-Ni coating showed good performance in grain size stability. However, severe invasion of Ni into the 3.5- $\mu\text{m}$ -thick Au-Ni layer was caused by metal

interdiffusion. Moreover, the Cu phase was observed in some areas on the top surface of the Au-Ni coating. This diffusion phenomenon may degrade the performance of the Au-Ni coating, e.g., its oxidation resistance and wear resistance. Increasing the thickness of the Au-Ni coating or applying a more effective diffusion barrier between Au-Ni and CuCrZr substrate are possible solutions to improve Au-Ni coating's performances. For the aspect of diffusion resistance between the Rh coating of the opposite RF conductor, Au-Ni is a perfect candidate.

- Ag-Sb showed good diffusion resistance with CuCrZr substrate, which is very important for ITER ICRH RF contact application. However, during the thermal aging process, significant grain coarsening occurred and its hardness decreased more than 60%. The advantage of alloying Sb in Ag to increase Ag coating hardness was totally lost. Based on this fact, it's unnecessary to replace pure Ag by Ag-Sb for ITER application. Cold welding will occur at the Ag/Rh interface, so a thick Ag layer is suggested to be used to guarantee its lifetime.
- CuCrZr is a good RF conductor base material candidate and applying an Au interlayer can help to minimize thermal stresses in the Rh coating. However, considering the long duration baking process, Au is not a proper interlayer as it can diffuse with CuCrZr easily. An interlayer of Ni+Au could be the solution to improve the thermal stability of the coating system.
- Rh on 316L with an interlayer of Ni showed good performance. Although cracks generated in the Rh layer due to thermal stress releasing, good adhesion performance of Rh coating on 316L was validated. This coating solution is very promising for ITER RF conductor application.

### **4.3 Electrical/tribological characterizations under ITER relevant conditions**

#### **4.3.1 CuCrZr vs. 316L**

This pair was used as the reference. No coating has been applied to the base materials. The roughness values ( $S_a$ ) of the pin and plate were 2.1  $\mu\text{m}$  and 0.45  $\mu\text{m}$  respectively. Ultrasonic cleaning in ethanol was performed towards all the samples before the electrical/tribological measurements to remove the organic pollutions.

##### **4.3.1.1 Static contact resistance**

The effects of vacuum condition, operation temperature and normal contact force to the  $R_c$  were studied on HV-MTEST. Generally, when a normal contact force is

applied, the equilibrium of elastic and plastic deformation between the asperities on the contacting surfaces can be achieved in a short time and the value of  $R_c$  turns to static quickly. However, for the CuCrZr/SS316L pair, during the static contact resistance measurements, after the loads being applied, the value of  $R_c$  varied continually and without achieving a steady-state regime. The reason for the  $R_c$  instability was probably caused by the oxidation on the surface of CuCrZr pin, which behaved like insulation layers between two electrical contact surfaces. The oxidation phenomenon of CuCrZr had been well researched and the oxidations are  $\text{Cu}_2\text{O}$  and  $\text{CuO}$  [122, 157]. As shown in Figure 4-27, at room temperature, the high vacuum condition ( $\sim 10^{-4}$  Pa) decreases the contact resistance. Under the same contact forces, the  $R_c$  under high vacuum was about 50 m $\Omega$  lower than those measured under in air. This phenomenon was caused by the release of gases and hydrocarbons physically absorbed on the pin tip.

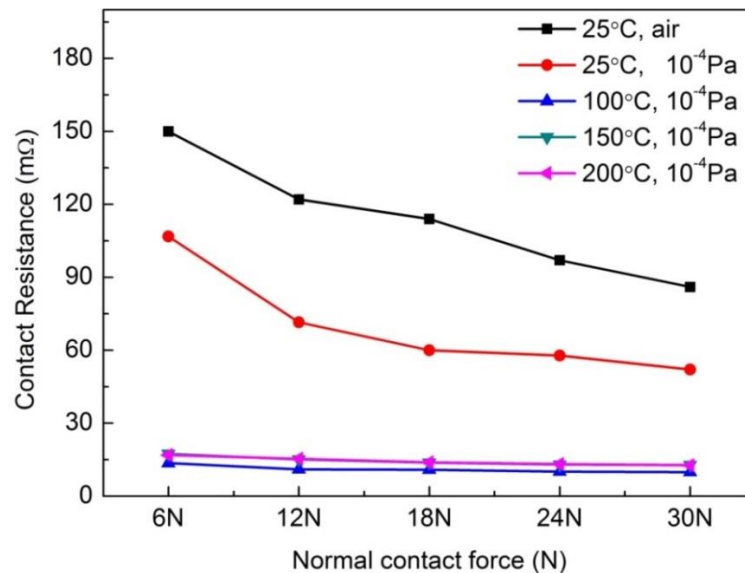


Figure 4-27  $R_c$  measurement results of the CuCrZr/ 316L pair under different contact force and temperature

Increasing contact force can enlarge the real contact area and break the copper oxidation layers, which decreases the  $R_c$ . However, the obvious effect of the normal contact force on the  $R_c$  was only observed when the operating temperatures were lower than 100°C and its effect weakened after 18 N. Under 6 N, when the operation temperature was higher than 100°C, the  $R_c$  decreased by one order of magnitude and stabilized at around 15 m $\Omega$ . This sharp decrease of  $R_c$  was mainly due to the decomposition of the hydrocarbons under high temperature and the obvious improvement of contact quality caused by plastic deformation of the contact materials under high temperature. Beyond 100°C, the  $R_c$  was neither sensitive to the increase of

temperature nor normal contact force. In addition to the effects such as pollution removal and contact area enlarging, increasing the operating temperature can increase the resistivity of the contact materials as well. As a result, under the same normal contact forces, the  $R_c$  at 150°C and 200°C were slightly higher than those at 100°C.

The lowest  $R_c$  measured is 15 m $\Omega$ , which is higher than the limit established in section 3.2.5.3 of 6.5 m $\Omega$ . Therefore, it is mandatory to apply coatings to minimize the  $R_c$  in these conditions.

#### 4.3.1.2 Evolution of $R_c$ and CoF during sliding cycles

CoF is most often a function of three main influencing parameters: temperature, slip speed and normal force [92, 158]. Although for the ITER ICRH RF contact, the operating temperature under nominal conditions is hard to predict since it is a combination of the RF contact's mechanical structure, cooling design and thermal deposition. For the material's performance study, an operation temperature of 200°C was used as an estimated value. Based on the results from the last section, at 200°C the  $R_c$  was not sensitive to the normal contact force and after 18 N, there almost no change for the  $R_c$ . So, 18 N was selected as the maximum  $F_n$  in the sliding test to guarantee the electrical contact's stability.

In order to understand the friction and wear phenomena, 2000 cycles of sliding test under the conditions:  $F_n=18$  N, sliding speed of 1 mm/s ( $\pm 16$  mm stroke), vacuum around  $7 \times 10^{-4}$  Pa and temperature of 200 °C was performed. The transient results of the  $R_c$  and CoF are shown in Figure 4-28.

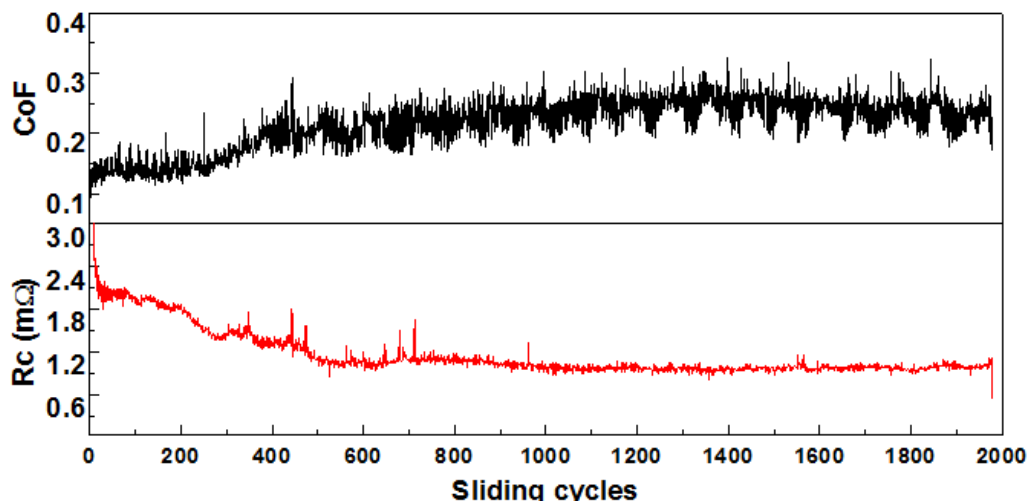


Figure 4-28 Evolution of the  $R_c$  and CoF for the CuCrZr/ 316L pair under 2000 cycles of sliding test at  $F_n=18$  N, 1 mm/s, 200 °C,  $7 \times 10^{-4}$  Pa

At the beginning of the sliding, the contact surface was smooth so the CoF was about

0.1. Before 200 cycles, the CoF only slightly changed from 0.12 to 0.15. After 220 cycles, the CoF started to change faster and the CoF reached 0.25 at nearly 700 cycles. The maximum value of CoF occurred at around 1400 cycles and reached 0.3. A reverse trend was observed for the Rc. Because of the oxidation layers, when the 18N contact force applied, the Rc was near to 20 mΩ, but when the sliding started and after four cycles, the Rc decreased sharply to 4.2 mΩ. A good correlation between the CoF and the Rc was found during the cycles between 200 to 700. Even though during that time the contact surfaces started to be severely worn, the plow phenomenon between the rough surfaces increased the possibility of contact between asperities. At last, the Rc was kept at around 1 mΩ.

#### 4.3.1.3 Wear surface morphology

As shown in Figure 4-29. Series abrasive wear was observed both on the pin and plate samples. On the tip of the pin, a flat surface with a radius about 1 mm has been generated and the pin had a 0.0014 g mass loss due to wear. The wear rate is  $2.73 \times 10^{-4} \text{ mm}^3/\text{N}\cdot\text{m}$ . The width of the wear track on the 316L plate is about 1.6 mm, with a surface roughness around 1 μm. On the plate, two large grooves with a maximum depth of 10 μm have been generated due to plowing and cutting processes by the CuCrZr pin. The mass loss of the plate is about 0.0015 g and the wear rate is  $3.28 \times 10^{-4} \text{ mm}^3/\text{N}\cdot\text{m}$ .

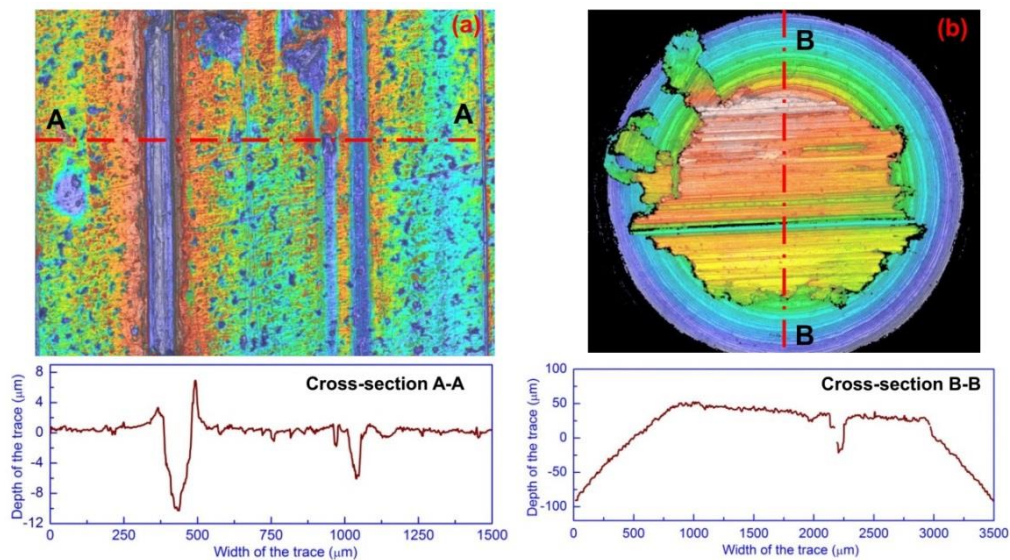


Figure 4-29 3D morphologies and depth profiles of the worn samples: (a) 316L plate sample, (b) CuCrZr pin sample

The serious abrasion wear on the plate mimicking the RF conductors showed that the wear resistivity of 316L against CuCrZr under ITER application conditions was poor. As the RF conductors are large components with low maintainability, 316L is

unsuitable to be directly applied as the contact material against the RF contact louvers that are made of CuCrZr. A protective coating is thus necessary.

### 4.3.2 Au-Ni on CuCrZr vs. Rh on 316L

On the CuCrZr pin, a 14.2  $\mu\text{m}$  Au-Ni layer with 5  $\mu\text{m}$  Ni interlayer was applied. The surface roughness of the Au-Ni coating is 2.14  $\mu\text{m}$  ( $S_a$ ). The thickness of the Rh coating is 4.18  $\mu\text{m}$  with a 2.4  $\mu\text{m}$  Ni interlayer. The roughness of the Rh surface is  $S_a=1.95 \mu\text{m}$ .

#### 4.3.2.1 Static contact resistance

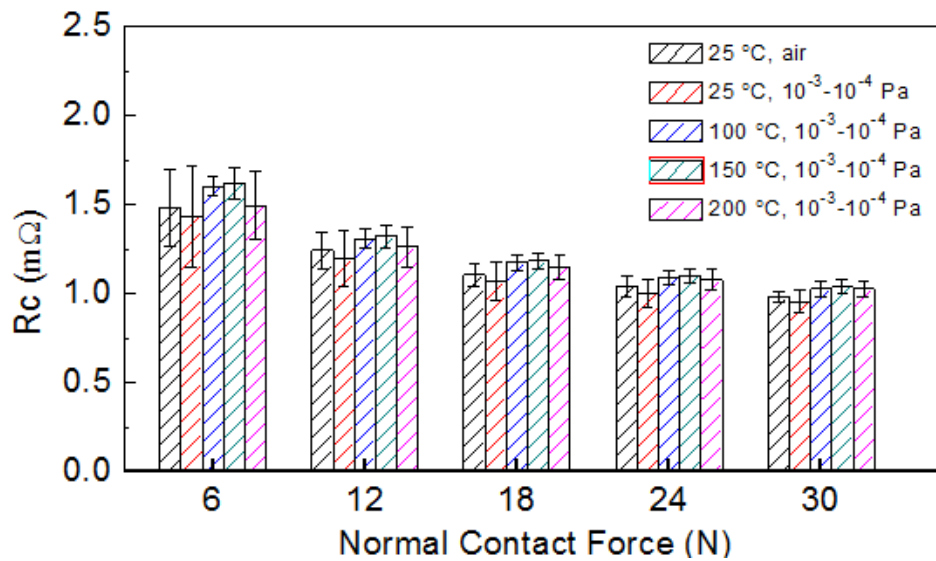


Figure 4-30 Rc measurement results of the Au-Ni on CuCrZr/ Rh on 316L pair under different contact force, temperature and atmosphere conditions

The resistances in the vacuum environment were smaller than those measured under atmosphere (Figure 4-30). However, the differences are much smaller compared with the reference pair, which indicates that the surfaces were less oxidized after the application of functional coatings. The Rc decreases with the  $F_n$  increase and after 18 N the Rc is almost stable without obvious change. The Rc initially increases with an increase in the test temperature and it reaches a threshold value between the operating temperatures of 150°C and 200°C, beyond which the relation between the Rc and the test temperature changes. The effects of increasing temperature on the Rc can be explained by two different mechanisms: the increase in the resistivity of the coating materials and the creeping of the coating materials. Compared with the creeping effect which increases the contact area, resistivity increase is the predominant factor that affects the Rc under a temperature lower than 150°C. However, under a temperature higher than 150°C, the coating materials creeping turns into the dominating factor.

The measured  $R_c$  are close to  $1.5 \text{ m}\Omega$  even under low normal contact force of  $6 \text{ N}$ . Thus, for  $R_c$  aspect, the feasibility of applying Au-Ni and Rh as electrical function coatings was validated.

#### 4.3.2.2 Evolution of $R_c$ and CoF during sliding cycles

2000 cycles of sliding test under the conditions:  $F_n=18 \text{ N}$ , sliding speed of  $1 \text{ mm/s}$  ( $\pm 16 \text{ mm}$  stroke), vacuum around  $1.5 \times 10^{-3} \text{ Pa}$  and temperature of  $200^\circ\text{C}$  was performed. Figure 4-31 shows the evolution of CoF and  $R_c$  during 2000 cycles of sliding test. In the beginning, the CoF is around 0.2. Before 200 cycles, the CoF increases gradually from 0.2 to 0.3. Between 200 cycle and 1200 cycles, large variation of CoF and  $R_c$  was observed, which indicates that wear phenomenon in this period is more severe than after 1200 cycles. The  $R_c$  of this sample pair is around  $0.5 \text{ m}\Omega$  and although its maximum value reaches  $1 \text{ m}\Omega$  in some cycles, the  $R_c$  was still lower than the design requirement of  $6.5 \text{ m}\Omega$ .

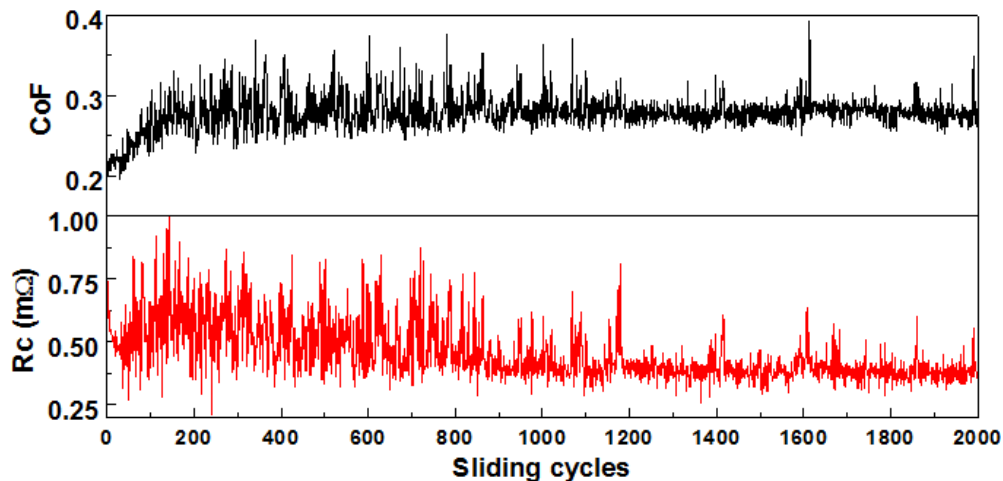


Figure 4-31 Evolution of the  $R_c$  and CoF for the Au-Ni on CuCrZr/ Rh on 316L pair under 2000 cycles of sliding test at  $F_n=18 \text{ N}$ ,  $1 \text{ mm/s}$ ,  $200^\circ\text{C}$ ,  $1.5 \times 10^{-3} \text{ Pa}$

#### 4.3.2.3 Wear surface morphology

As shown in Figure 4-32, after 2000 cycles sliding test, discontinuous wear grooves occurred on the Rh on 316L sample. The depths of these grooves are around  $4 \mu\text{m}$ , which are in the same range of Rh coating thickness. So, such wear grooves are actually caused by Rh coating delamination during sliding tests. After calculation, the wear rate of Rh on 316L sample is  $9.79 \times 10^{-5} \text{ mm}^3/\text{N}\cdot\text{m}$ . On the tip of the pin, a large volume of material was worn. Au-Ni coating was fully removed due to abrasive wear with a wear rate of  $1.48 \times 10^{-3} \text{ mm}^3/\text{N}\cdot\text{m}$ . The roughness ( $S_a$ ) of the wear surface on the pin is  $1.4 \mu\text{m}$ .

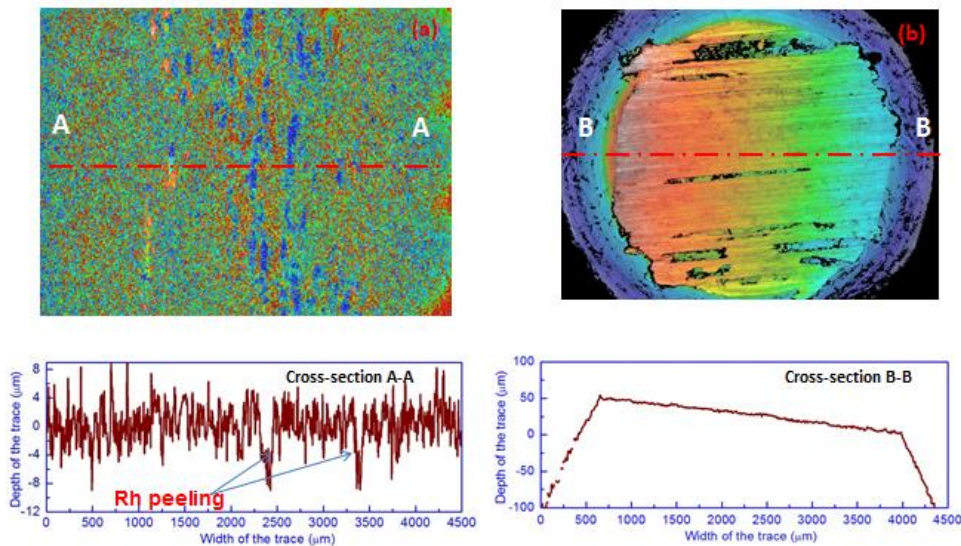


Figure 4-32 3D morphologies and depth profiles of the worn samples: (a) Rh on 316L plate sample, (b) Au-Ni on CuCrZr pin sample

Both abrasive and adhesive wear occurred between the Rh and Au-Ni coatings during sliding and abrasive wear is the predominating factor. The asperities on the Rh coating surface embedded into the Au-Ni coating and caused plowing and cutting phenomena, which is called two-body abrasion [159]. Flake-like [160, 161] wear debris with an average size of 0.5 mm was generated (Figure 4-33). These flakes were piled up at the edge of the wear surface on the Au-Ni pin sample due to cutting from Rh asperities and detached as loose wear debris, which generated three-body wear after that. With the wear of the Au-Ni surface, the contact surface area increased and contact pressure decreased accordingly. As a result, wear on the Au-Ni turned to mild. This is the reason that after 1200 cycles, the variations of CoF became smaller.

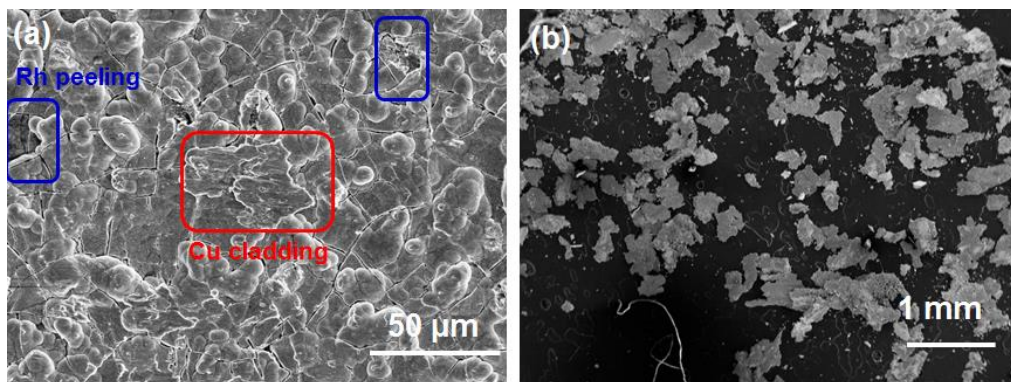


Figure 4-33 SEM images of wear track and wear debris: (a) wear track of Rh on 316L, (b) wear debris

On the Rh surface, in some areas, Cu cladding and Rh delamination were observed. Compared with the reference plate (316L without Rh coating), the wear rate of the

plate sample decreases by 2/3. This means that applying Rh on 316L substrate can protect the 316L base material from wear efficiently. So, if the ITER RF conductors facing sliding louvers are made of 316L, a Rh coating is worth to be applied to improve their lifetimes.

### 4.3.3 Au-Ni on CuCrZr vs. Rh on CuCrZr

The Rc between Au-Ni on CuCrZr pin and Rh on 316L plate was studied in the last section. Even under 6 N, the Rc is around 1.5 mΩ which is lower than the design limit (6.5 mΩ) obtained from simulation (section 3.2.5.3). For the contacting pair of Au-Ni on CuCrZr vs. Rh on CuCrZr, the Rc should be lower than the value measured from Au-Ni on CuCrZr vs. Rh on 316L under the same condition. Therefore, for the electrical performance aspect, Au-Ni on CuCrZr vs. Rh on CuCrZr will be satisfactory for the ITER RF contact application too. The only doubt concerns their tribological performance.

#### 4.3.3.1 Evolution of Rc and CoF during sliding cycles

Serious metal diffusion between the Rh coating and its substrate CuCrZr was observed in section 4.2.1.3. Kirkendall voids generated under Rh coating deteriorate the Rh coating's wear resistance. In order to evaluate the tribological performance of the Au-Ni on CuCrZr vs. Rh on CuCrZr pair, sliding test was performed under the same conditions as the pair of Au-Ni on CuCrZr vs. Rh on 316L introduced in section 4.3.2.2. The evolutions of CoF and Rc are shown in Figure 4-34.

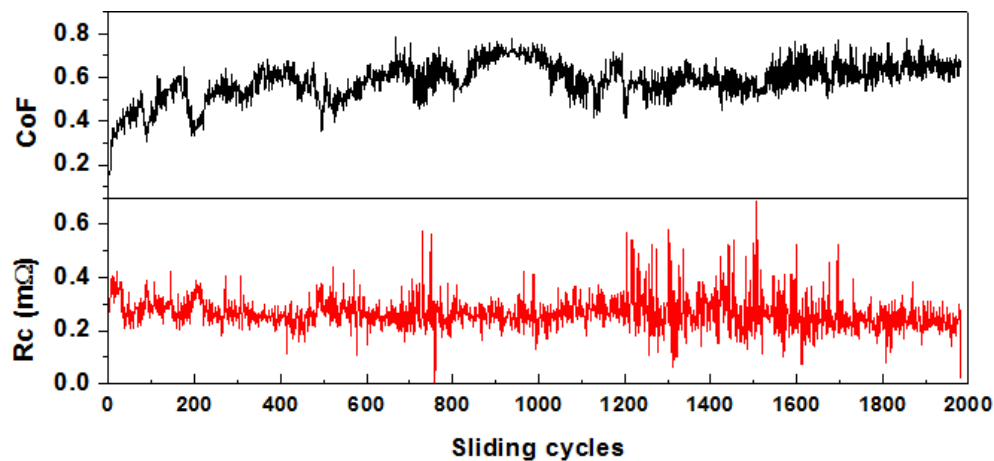


Figure 4-34 Evolution of the Rc and CoF for the Au-Ni on CuCrZr/ Rh on CuCrZr pair under 2000 cycles of sliding test at  $F_n=18$  N, 1 mm/s, 200 °C,  $9.9 \times 10^{-4}$  Pa

When the sliding started, the CoF was around 0.2 and it increased after a few cycles. At around 1000 cycles, the CoF reached a maximum value of 0.8. For the Rc, it stabilized at around 0.3 mΩ.

### 4.3.3.2 Wear surface morphology

Serious wear occurred on the plate sample and a wear track with 2.5 mm width and 0.13 mm depth was generated (Figure 4-35). The wear rate of the plate is  $1.11 \times 10^{-3} \text{ mm}^3/\text{N}\cdot\text{m}$ , which is more than ten times higher than the Rh on 316L plate. On the contrary, surface transfer film (CuCrZr) was observed on the Au-Ni.

The wear mechanism between the pin and plate is illustrated in Figure 4-36. Due to the existing diffusion voids under Rh layer, when the pin and plate got into contact and contact pressure is applied, brittle fractures occurred in the Rh coating as it was insufficiently supported by the substrate. During sliding, adhesion between Rh and Au-Ni layers generated shear stresses under the Rh coating and when the shear stress was higher than the bond strength of the Rh coating, delamination happened. Hard Rh debris remained in the Au-Ni/CuCrZr interface and caused three-body abrasive wear to the Au-Ni surface and CuCrZr surface.

With the delamination of Rh coating, Au-Ni coating surface directly contacted with CuCrZr surface, which induced more severe adhesion. Prow formation occurred between the pin tip (Au-Ni) and the plate sample (CuCrZr) and material transfer from the CuCrZr plate to the pin tip occurred. Due to work hardening effect, the transfer film (CuCrZr) on the pin tip was harder than the plate and wore the plate sample by continuous plastic shearing and cutting. During the sliding, prows that attached on the pin tip were lost as loose debris. For ITER RF contact application, this prow formation process will continue indefinitely with the reciprocating sliding of the RF contact louvers against the RF conductor. Serious damage of the RF conductor will happen which is not acceptable for ITER operation.

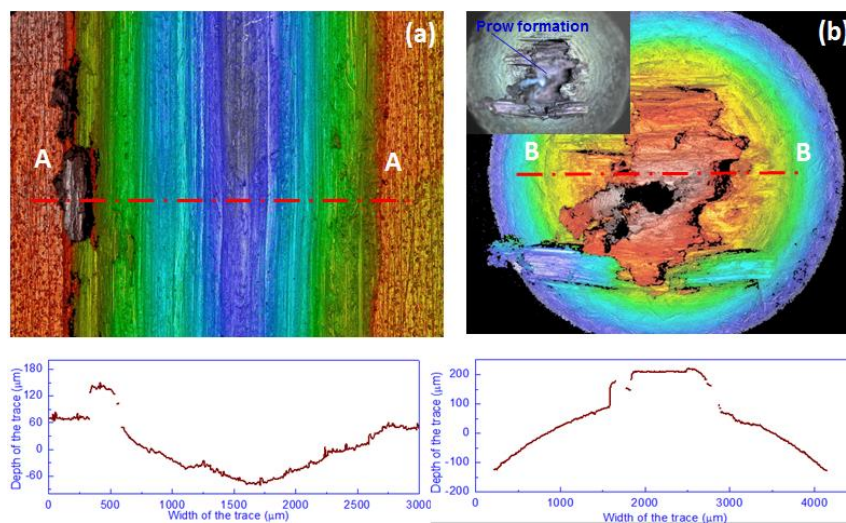


Figure 4-35 3D morphologies and depth profiles of the worn samples: (a) Rh on CuCrZr plate sample, (b) Au-Ni on CuCrZr pin sample

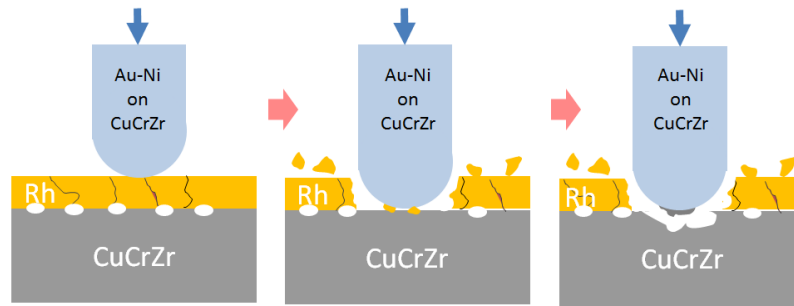


Figure 4-36 Wear mechanisms of Au-Ni on CuCrZr vs. Rh on CuCrZr pair

#### 4.3.4 Ag on CuCrZr vs. Rh on 316L

The surface roughness of the Ag coating on the pin sample is  $S_a=1.5 \mu\text{m}$ .

##### 4.3.4.1 Static contact resistance

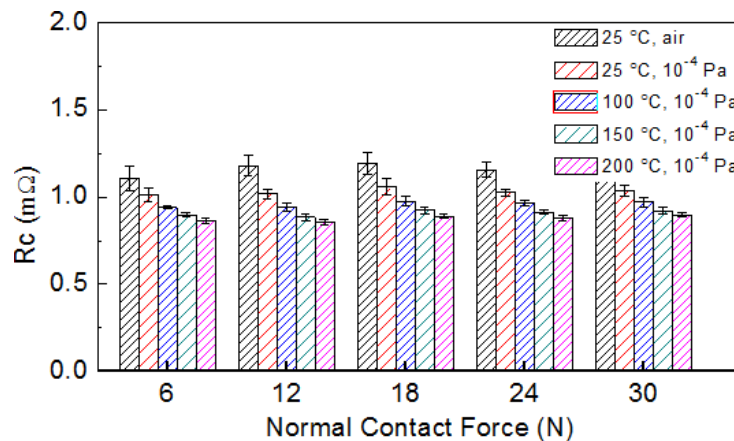


Figure 4-37  $R_c$  measurement results of the Ag on CuCrZr/ Rh on 316L pair under different contact force and temperature

As shown in Figure 4-37,  $R_c$  didn't change obviously with the increase of the  $F_n$ . The explanation is that, after thermal aging (500 h, 250°C), the hardness of the Ag coating decreased to 60 HV. The asperities on the Ag coating surface were easily deformed even under 6 N. Under 6 N, the contact area had saturated and there were no obvious effects on  $R_c$  by applying higher normal contact forces. However, the effects of operating temperature on the  $R_c$  was observed. Unlike Au-Ni coating, with operation temperature increase, the mechanical strength degradation of Ag which induced larger contact area dominated the  $R_c$  variation. As the  $R_c$  values are around 1 mΩ, the feasibility of applying Ag and Rh coatings on the RF contact louvers and RF conductor respectively to minimize the  $R_c$  was approved.

##### 4.3.4.2 Evolution of $R_c$ and CoF during sliding cycles

From the static contact resistance study, it seems that 6 N is already enough to

minimize the Rc. However, in order to compare with the above pairs, 18 N was kept to perform the sliding test. 2000 cycles of sliding test under a sliding speed of 1 mm/s ( $\pm 16$  mm stroke), vacuum around  $1.9 \times 10^{-3}$  Pa and temperature of  $200^\circ\text{C}$  was performed. In the beginning, both abrasive wear and adhesive wear happened and the CoF was around 0.3. Due to the adhesive wear of Ag, Ag transferred from the pin tip to the Rh surface and generated Ag transfer film. The Ag transfer film covered the asperities on the Rh surface and as a result, the abrasive wear was reduced. With the reduction of abrasive wear and the lubricating from Ag (low shear layer), after around 100 cycles, the CoF decreased to 0.2.

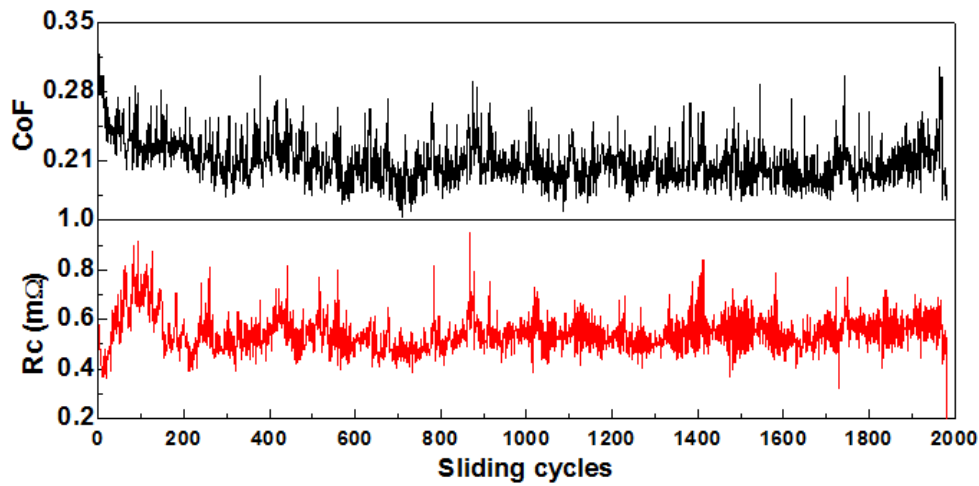


Figure 4-38 Evolution of the Rc and CoF for the Ag on CuCrZr/ Rh on 316L pair under 2000 cycles of sliding test at  $F_n=18$  N, 1 mm/s,  $200^\circ\text{C}$ ,  $1.9 \times 10^{-3}$  Pa

#### 4.3.4.3 Wear surface morphology

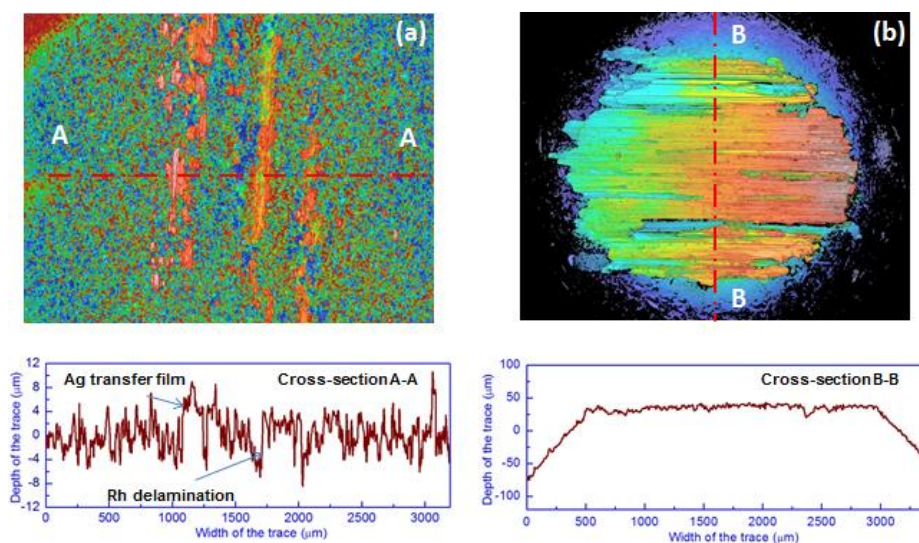


Figure 4-39 3D morphologies and depth profiles of the worn samples: (a) Rh on 316L plate sample, (b) Ag on CuCrZr pin sample

Obvious Ag transfer was observed on the Rh surface (Figure 4-39). At some local positions Rh delamination happened. Due to the Ag attachment on the Rh surface, after sliding test, the weight of the plate sample increased. Serious wear occurred on the pin sample with a wear rate of  $2.8 \times 10^{-4} \text{ mm}^3/\text{N}\cdot\text{m}$ .

### 4.3.5 Ag on CuCrZr vs. Rh on CuCrZr

#### 4.3.5.1 Evolution of Rc and CoF during sliding cycles

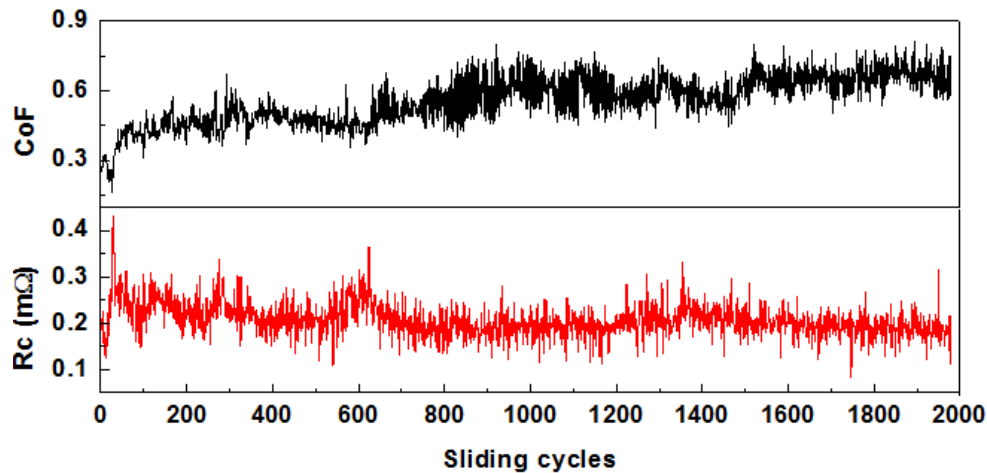


Figure 4-40 Evolution of the Rc and CoF for the Ag on CuCrZr/ Rh on CuCrZr pair under 2000 cycles of sliding test at  $F_n=18 \text{ N}$ ,  $1 \text{ mm/s}$ ,  $200 \text{ }^\circ\text{C}$ ,  $1.4 \times 10^{-3} \text{ Pa}$

As shown in Figure 4-40, the CoF started at 0.3 and sharply increased to 0.45 after 50 cycles. The sharp increase of the CoF was caused by the broken Rh coating. At around 600 cycles, another sharp increase of CoF was occurred, which was probably due to the prow formation. The Rc stabilized at 0.25 mΩ.

#### 4.3.5.2 Wear surface morphology

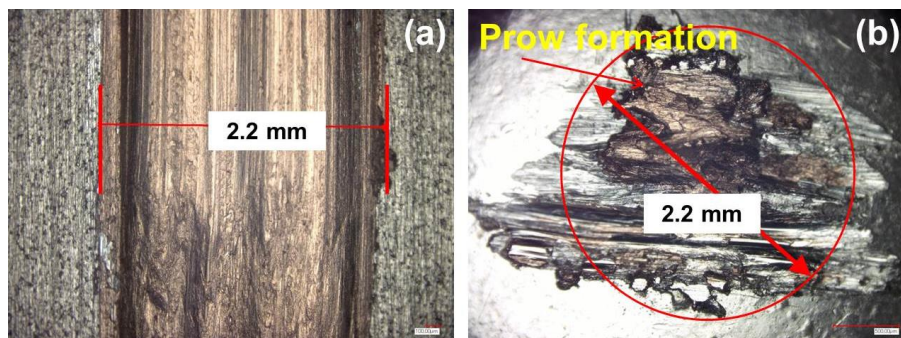


Figure 4-41 Optical microscope images of the worn samples: (a) Rh on CuCrZr plate sample, (b) Ag on CuCrZr pin sample

As shown in Figure 4-41, the wear phenomenon between Rh on CuCrZr and Ag on

CuCrZr is similar to the sample pair of Rh on CuCrZr vs. Au-Ni on CuCrZr. Serious adhesive wear (prow formation) occurred. A 2.2 mm wide groove generated on the plate sample and the wear rate was  $1.13 \times 10^{-3} \text{ mm}^3/\text{N}\cdot\text{m}$ . Again, such a high wear rate on the plate sample (mimic RF conductor) is not acceptable for the ITER application.

#### 4.3.6 Discussion

There are two base material candidates for the RF conductor (plate sample) manufacturing: 316L and CuCrZr. For the RF contact louvers (pin sample), CuCrZr is the only interesting option, due to its high thermal conductivity and high stiffness.

➤ For the Rc aspect:

- The static Rc between bared 316L and CuCrZr without coating is measured to be higher than 15 mΩ, which is higher than the ITER design limit (6.5 mΩ). Although during sliding, the transient Rc is around 1 mΩ, the high static Rc is a threat for the ITER RF sliding contact, especially at the beginning of the operation (no sliding occurs). So for ITER application, this material solution without coatings applied is not recommended.
- If functional coatings are applied on the RF conductor (Rh coating on 316L substrate or Rh coating on CuCrZr substrate) and RF contact louvers (Au-Ni coating on CuCrZr substrate or Ag coating on CuCrZr substrate), both the static Rc and transient Rc are lower than the ITER design limit.

➤ For the friction and wear aspect:

- If no coatings are applied on the RF conductor (made of 316L) and RF contact louvers (made of CuCrZr), serious abrasive wear happened both on the RF conductor and the RF contact louvers. Serious wear on the RF conductor will be problematic for ITER application. So, applying functional coating to the 316L RF conductor is mandatory.
- By applying a thin (around 4 μm) Rh coating on the RF conductor made of 316L, the RF conductor can be efficiently protected from serious wear and its lifetime can be prolonged accordingly.
- A bare pair RF conductor (made of CuCrZr) vs. RF contact louvers (made of CuCrZr) was not studied: it's a general knowledge that for parts that have relative movement, it should be avoided to use the same material to manufacture them as serious adhesive wear can happen between them. Under high vacuum, adhesive wear between two identical materials is even more serious.
- If the RF conductor is made CuCrZr, even though Rh coating was applied, due to

the serious diffusion between Rh and Cu interface, the adhesion of Rh was poor and delamination of Rh occurred during the sliding versus the RF contact louvers. After losing the Rh coating's protection, sliding will happen between two parts made of CuCrZr. As explained, sliding between the same materials should be avoided.

- So, for the electrical/tribological aspect, 316L is more suitable as ITER RF conductor's base material. Rh coating is necessary to be applied on the surface of the 316L surface. If one wants to use a Rh coating on a CuCrZr base material, since it has a higher thermal conductivity than 316L, a more efficient interlayer than Au should be developed. Using Ni as the interlayer is an interesting option which would require assessment.
- Aiming to minimize the CoF and wear rate on the RF contact louvers, which are made of CuCrZr with Au-Ni or Ag coating, applying of solid lubricants in the Au or Ag matrices is interesting to be investigated.

## Chapter 5 Self-lubricating coating development

As introduced in chapter 4, under high vacuum and high temperature, adhesive wear plays an important role in the wear of the coating. Solid lubricants which have lamellar or layered structures like graphene, amorphous carbon (a-C), molybdenum disulphide ( $\text{MoS}_2$ ) or tungsten disulphide ( $\text{WS}_2$ ) (cf. section 2.3.2.3) could reduce shear resistance and therefore lead to a decrease in the energy dissipation by friction dissipation. The layers of such lamellar lubricants have shown ability to slide over each other repeatedly with low damage [62], while presenting relatively free movement between each other and reduced shear resistance. The lubricating of the solid lubricants can minimize the adhesive wear efficiently [162]. In this chapter, the deposition of two composite coatings, Au-Ni/a-C and Au-Co/ $\text{WS}_2$  by magnetron sputtering and electroplating respectively is detailed. The coatings properties and tribological performance in vacuum and in  $\text{N}_2$  atmosphere were then evaluated and discussed.

### 5.1 Au-Ni/a-C deposition and coating characterizations

#### 5.1.1 Magnetron sputtering process of Au-Ni/a-C

The Au-Ni/a-C nanocomposite coatings were deposited on CuCrZr substrates and p-type silicon (100) wafers. J450 magnetron co-sputtering system was used in this study with three targets (Au-99.99%, Ni-99.995%, graphite-99.999%) procured from ZNXC Technology Co., Ltd. The target to substrate distances of Au, Ni and graphite targets are 6.5 cm, 8.5 cm and 5.5 cm respectively. Before the deposition process, the silicon and CuCrZr substrates were ultrasonically cleaned for 10 min in acetone and then by 10 min cleaning in ethanol. For the CuCrZr plates, acid etching was performed for 30 s in 10 wt.%  $\text{H}_2\text{SO}_4$  to remove passivation layers. The machine chamber was pumped to the base vacuum of  $9 \times 10^{-4}$  Pa by using a turbomolecular pump set. The substrates were negatively biased plasma cleaned at 500 V in 2.5 Pa pure Ar atmosphere for 10 min. Before the coating deposition, the targets were pre-sputtered to clean both the target surface and the chamber for 10 min. The coating deposition consisted of two steps. Firstly, pure Ni interlayer as diffusion barrier was deposited using a current of 1 A (390 V) at a pressure of 0.8 Pa with 40 standard cubic centimeters per minute Ar flow for 120 min. Then, the Au-Ni/a-C nanocomposite layer was deposited at 0.6 Pa, with Au target current of 0.35 A (400 V) and Ni target current of 0.14 A (290 V). The sputtering of the graphite target was achieved by using an RF power supply (13.56 MHz) and four powers (100 W, 200 W, 300 W and 400 W) were selected to obtain Au-Ni/a-C composite coatings with different C content. The coating times of Au-Ni/a-C layers were kept constant to

55 min to control their total thickness.

## 5.1.2 Coating characterizations

### 5.1.2.1 Surface morphology

As shown in Figure 5-1, the composite coatings show fish scale-like morphologies, which indicate that the coatings have columnar structures [163]. Under all the sputtering powers, the coatings present dense structures and no obvious coating defects such as pores and cracks observed. Based on the cross-sectional image of coating, a 3.1  $\mu\text{m}$  Au-Ni/a-C composite coating with a 4.2  $\mu\text{m}$  thick Ni diffusion barrier was achieved. High quality junctions between two coating layers and coating to CuCrZr substrate were also validated. However, with the increase of sputtering power from 100 W to 400 W, there are more micron-sized nodules generated and embedded into the composite coating. The origin of the nodular structures is probably due to the inhomogeneous coating growth caused by the landing of foreign microparticles on the coating surface, which came from the graphite target or the mechanical structure of the magnetron sputtering machine [164, 165]. Generally, the presence of nodules is accompanied by voids in their surroundings; therefore, the bonding between these nodules and the coating matrix is weak. For tribological aspect, such defect may impair the coating's wear resistance.

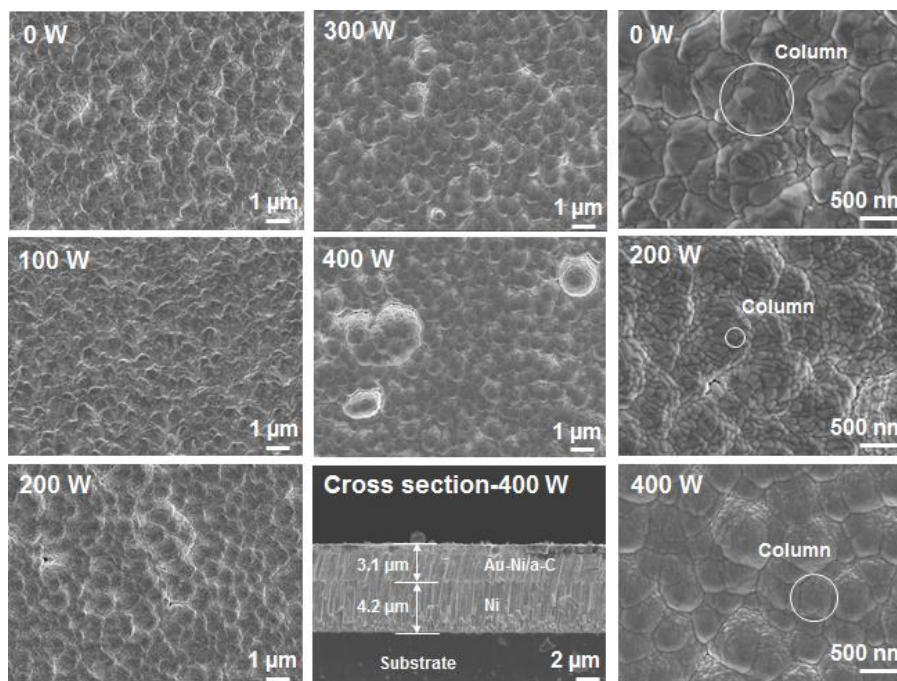


Figure 5-1 SEM images of the Au-Ni and Au-Ni/a-C coatings

By checking under higher magnification, with the increase in sputtering power of graphite target from 0 W to 200 W, the column's diameter decreased from around

1  $\mu\text{m}$  to 0.25  $\mu\text{m}$ . After 200 W, an opposite trend of column diameter change with the sputtering power increase was observed. The coating surface roughness (arithmetical mean height) decreases slightly with the sputtering power increase (0 W: 0.48  $\mu\text{m}$ , 400 W: 0.29  $\mu\text{m}$ ).

### 5.1.2.2 Coating composition and crystal structure

Au and Ni have the same face-centered cubic (fcc) crystal structure. However, the Au-Ni binary phase diagram (Appendix B) exhibits a wide miscibility gap between Au and Ni at low temperature and in equilibrium state, i.e., continuous Au-Ni solid solution can only be achieved at low Ni content [166]. Au-Ni solid solutions with high Ni contents can be achieved by PVD methods. Au-Ni alloy with Ni content reaching up to 20 at.% was reported in [167]. Nevertheless, such solid solutions are in metastable state and phase separation can happen if they are thermally aged. Phase separation can cause precipitation hardening effect which can increase the coating's hardness and the coating's electrical conductivity can also be improved [167]. However, the Ni-riched precipitations on the coating surface are less resistant to corrosion in the air and the insulation oxidations are very harmful to the electrical contact performance.

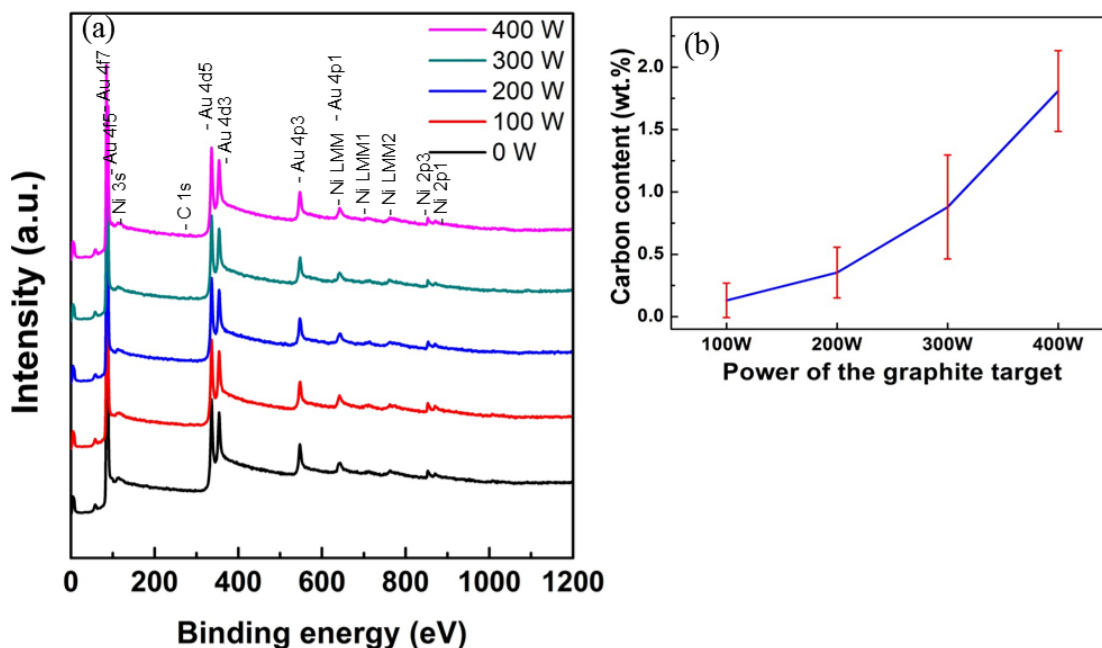


Figure 5-2 XPS spectra (a) and carbon content relation with different sputtering power of the graphite target (b)

The XPS spectra of the coatings are shown in Figure 5-2. In the Au-Ni/a-C coating system, the content of Ni which is achieved is 2 wt.% which is a low value that can avoid phase separation during the coating application on electrical contact, especially under high temperature working condition. The C content in the composite coating

increases with the increase of the sputtering power of the graphite target. Under 400 W, the C in the composite coating is around 2 wt.%.

Figure 5-3 shows the XRD patterns for the composite coatings. From 0 W to 400 W, bright and sharp XRD peaks were observed which indicates that all the deposited coatings have good crystallinity. With a clear preferential growth orientation of (111), other crystal planes like (200), (220) and (311) were also observed in all the coatings with different C contents. All the above crystal planes belong to the Au-Ni fcc phase. It's interesting to note that, near the fcc-(111) peak, there is another peak with  $2\theta$  around  $37.7^\circ$  appears which doesn't belong to the fcc phase. Fcc structure is the solid phase of Au in the equilibrium state. However, under some particular conditions such as high temperature and high pressure, Au atoms in fcc structure were observed to be transferred from fcc stacking to hexagonal close-packed (hcp) stacking [168]. Since Au-Ni is Au matrixed solid solution whose structure is also fcc, the metastable state of hcp structure should also exist. The peak presents at  $2\theta=37.7^\circ$  has a good coincidence with the hcp-(100) peak of Au reported in [168] and the peak presents at  $2\theta=38.6^\circ$  which coincides with fcc-(111) belongs to hcp-(002) [169]. Based on the XRD patterns, the generation of hcp phase can be suppressed by the implantation of the C in the Au-Ni matrix.

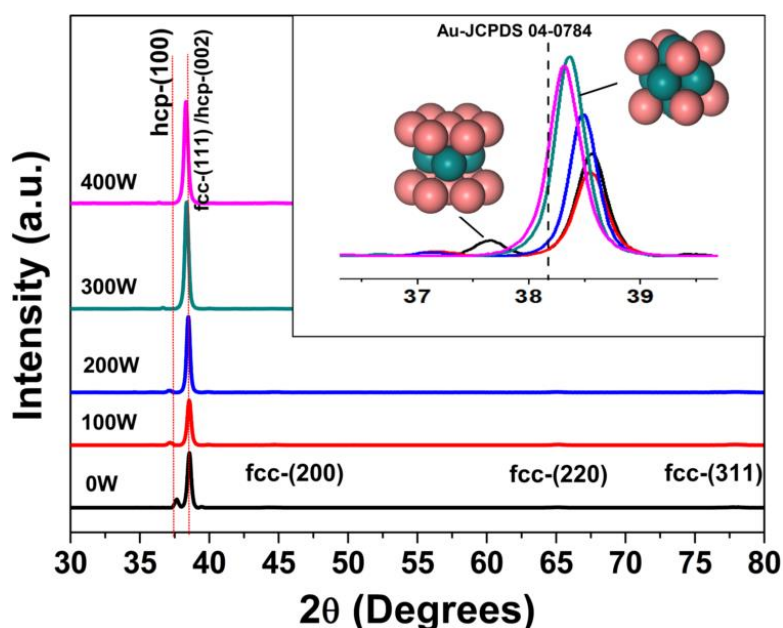


Figure 5-3 XRD patterns of the Au-Ni and Au-Ni/a-C composite coatings

Although fcc and hcp Au-Ni solid solution phases coexist in the coatings, no Ni peaks appear, which indicates that with a Ni content of 2 wt.%, the Ni atoms were uniformly distributed in the Au matrix and no phase separation happened. Compared with the (111) peak position of standard pure Au (JCPDS: 04-0784), the Au-Ni and Au-Ni/a-C

composite coatings have apparent  $2\theta$  shifting to higher angles due to the substitution of Au atoms by Ni atoms (with smaller atom radius than Au), which is another confirmation of Au-Ni alloy formation. The crystallite size of Au-Ni coating was calculated by using Scherrer equation according to the FWHM value of the (111) peak [51]. The crystallite size of the Au-Ni coating without C content is 28 nm. Moreover, the C sputtering power has no significant effect on the crystallite size of the Au-Ni/a-C composite system. However, with the C content increase, the (111) peaks shift to low  $2\theta$  direction, which is probably caused by the residual coating stress.

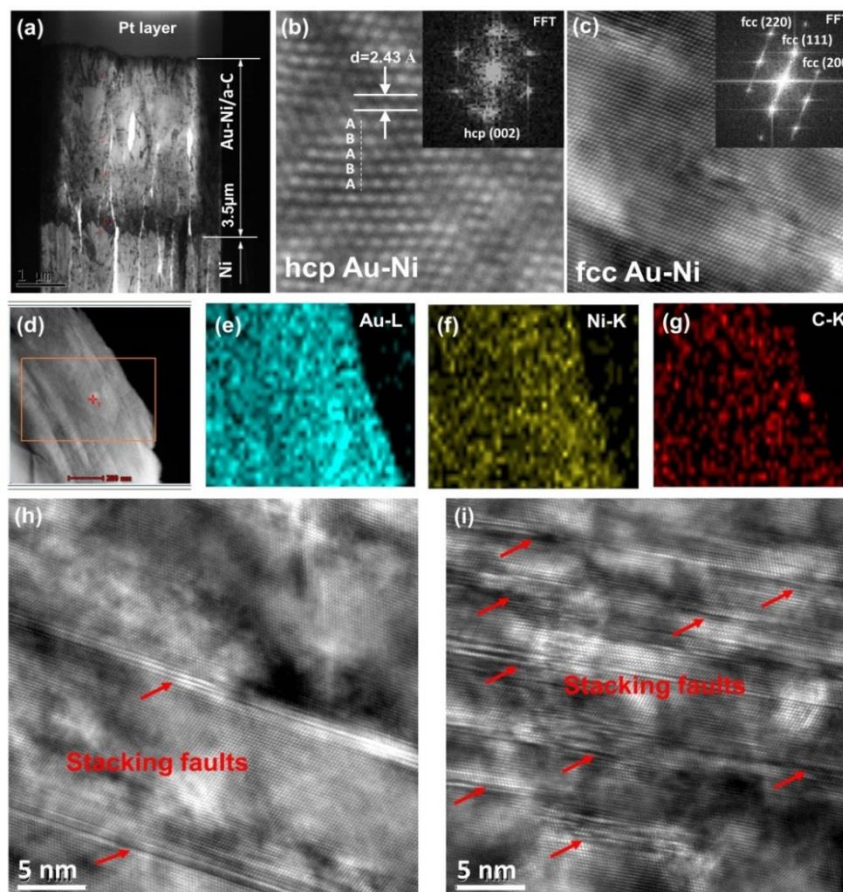


Figure 5-4 TEM and EDS mapping images of the Au-Ni/a-C coatings: (a). TEM image shows the whole Au-Ni/a-C thickness of 400 W sample, (b). HRTEM of Au-Ni hcp structure and the corresponding FFT pattern of 400 W sample, (c). HRTEM of the Au-Ni fcc structure and the corresponding FFT pattern of 400 W sample, (d). The selected EDS mapping area on the 400 W sample, (e, f, g). EDS mapping of Au, Ni and C in the square-marked area shown in (d), (g). HRTEM image shows stacking faults of 100 W sample, (i). HRTEM image shows stacking faults of 400 W sample.

TEM observation verified the co-existence of hcp and fcc structure phases in the Au-Ni and Au-Ni/a-C coatings (Figure 5-4). Crystal planes with an averaged interplanar spacing of 0.243 nm and ABAB stacking sequence have a good agreement

and can be identified as the (002) of Au-Ni hcp phase [170]. The STEM-EDS mapping images reveal that the Au, Ni and C are uniformly distributed in the composite coatings. The sputtering power of graphite target has a significant effect on the stacking faults generation in the composite coatings. The high density of crystal defects in coating could help to improve the coating's hardness.

To have a deeper understanding of the C nanostructure in the composite coatings, Raman analyses were performed and the results are shown in Figure 5-5. Under 100 W, the content of carbon is too low to generate enough (or large) carbon clusters, and as a result no distinct carbon peaks were observed from the Raman spectrum. In addition to generating small carbon clusters, some of the carbon atoms could be alloyed in the Au-Ni lattice. With the increase of RF power on graphite target, three phenomena were observed from the Raman spectra: the rise of D and G peak intensities, the decrease of  $I_D/I_G$  ratio and the G peak position shifting. From 200 W to 400 W, the two apparent peaks with broad peak character is another evidence besides XPS results which indicates that the nature of the carbon composite deposited is amorphous carbon. Although amorphous carbon is the mixing of  $sp^2$ -bonded atoms and  $sp^3$ -bonded atoms [80, 171], the D and G peaks are due to  $sp^2$  bonds only. The D peaks that indicate the non-crystallinity of the carbon clusters are located at around  $1370\text{ cm}^{-1}$ - $1396\text{ cm}^{-1}$ , which is due to the breathing modes ( $A_{1g}$ ) of  $sp^2$  bonds [172-174]. The G peaks are located at around  $1567\text{ cm}^{-1}$ - $1595\text{ cm}^{-1}$ , which is due to the bond stretching motion ( $E_{2g}$ ) between  $sp^2$  atoms in chains and rings [175].

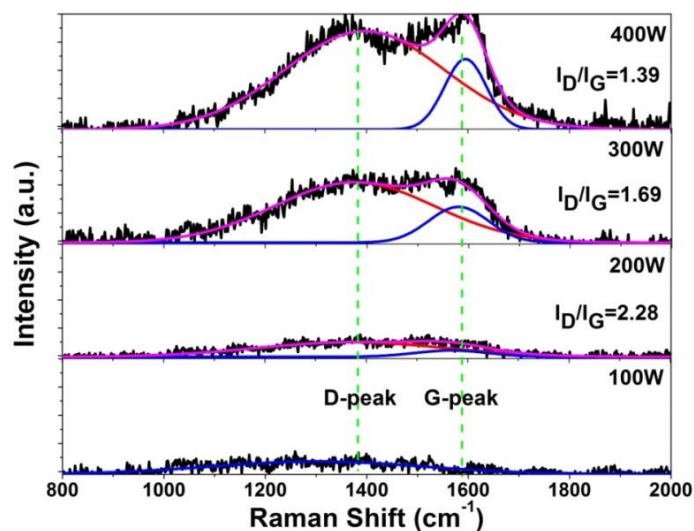


Figure 5-5 Raman spectra of the Au-Ni/a-C composite coating under different sputtering powers of the graphite target

The  $I_D/I_G$  ratio had been applied to characterize the  $sp^2/sp^3$  ratio in the a-C structure and it's useful to evaluate the degree of disorder of the carbon clusters [173, 176]. The

decrease of  $I_D/I_G$  ratio means that in the amorphous carbon clusters, the fraction of  $sp^2$  bonds increases with the power increase of the graphite target, i.e., the carbon clusters turn from high disordered structure to more graphitic-like structure. The structural transition of carbon clusters can also be observed from the G peak position increase from  $1567\text{ cm}^{-1}$ - $1595\text{ cm}^{-1}$  [175].

### 5.1.2.3 Mechanical performance

The occurrence of residual stresses is a typical feature of magnetron sputtered functional coating, which plays an important role in affecting the coating's performance. Generally, tensile residual stresses impair the durability of the coating by inducing cracking and compressive stresses can cause coating peel-off [177]. High stresses are prone to occur in the coating interface zone and such stresses can be accumulated with the coating thickness increases. Achieving a low internal stress system is therefore critical for the Au-Ni/a-C composite coating, whose total thickness with the Ni interlayer reaches up to  $7\text{ }\mu\text{m}$ . With the presence of stresses in the coating, bending occurs and the bending can be measured by 3D profiler. The residual stresses in the composite coatings were calculated from the curvature changes of the Si substrates after deposition with the following Stoney equation [178]:

$$\sigma_f = \frac{E_s}{6(1-\nu_s)} \cdot \frac{t_s^2}{t_c} \cdot \left( \frac{1}{R} - \frac{1}{R_o} \right) \quad (5-1)$$

where  $E_s$ ,  $\nu_s$  are the elastic modulus and Poisson's ratio of the substrate (Si wafer),  $t_s$  and  $t_c$  are the thicknesses of the substrate and the coating,  $R$  and  $R_o$  are the curvature radii of Si wafers before and after deposition.

The residual stress results are shown in Figure 5-6. After deposition, upward bending occurred on the Si wafer substrates, which indicates that tensile stress generated in the Au-Ni and Au-Ni/a-C coatings. For the Au-Ni coating, 140 MPa of residual stress is the sum of the intrinsic stress and thermal stress. The thermal stress can be well estimated from the following equation [179]:

$$\sigma_T = \frac{E_c E_s t_s}{(1-\nu_c)(E_s t_s + E_c t_c)} \cdot (\alpha_c - \alpha_s) \cdot (T_d - T_r) \quad (5-2)$$

where  $E_s$ ,  $t_s$  and  $\alpha_s$  are the elastic modulus, thickness and CTE of the Si substrate;  $E_c$ ,  $t_c$ ,  $\nu_c$  and  $\alpha_c$  are the elastic modulus, thickness, Poisson's ratio and CTE of the coating;  $T_d$  and  $T_r$  are the sample temperature and room temperature.

Due to the large CTE difference between Au ( $14.4\text{ }\mu\text{m/m}\cdot^\circ\text{C}$  @  $25\text{ }^\circ\text{C}$ ) and Si wafer

( $2.49 \mu\text{m}/\text{m}\cdot^\circ\text{C}$  @  $25^\circ\text{C}$ ) and relative high temperature on the coating samples caused by plasma radiation and second electron bombardment, the thermal stress (tensile stress) in the Au-Ni coating is estimated to be around 100 MPa. Therefore, the intrinsic stress in the Au-Ni coating is very likely to be tensile stress too. However, with C atoms implantation (100 W), a noticeable decrease of residual stress by 40 MPa is calculated. This phenomenon can be explained from the fact that when C atoms have been added in the Au-Ni coating, the intrinsic stress changed from tensile stress to compressive stress and the tensile thermal stress was offset partly by the compressive intrinsic stress. With RF power increase from 100 W to 400 W, residual stress increases accordingly, which is probably due to the temperature rise of the sample after deposition with higher sputtering power.

It worth mentioning, however, that the residual stresses in the coatings were evaluated based on the Si substrates. For real application, as the target substrate is CuCrZr whose CTE ( $16.7\mu\text{m}/\text{m}\cdot^\circ\text{C}$ ) is similar to Au, the residual stress in the composite coating should be lower than that obtained from the Si substrate and the type of the residual stresses is compressive stress. Thus, the Au-Ni/a-C coatings on CuCrZr substrates were achieved with low residual stresses.

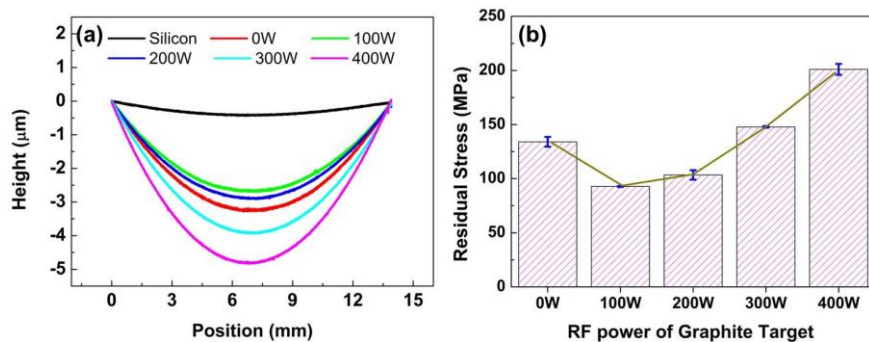


Figure 5-6 Results of coating residual stress measurement on Si (100) wafer: (a). The curvature of Si substrates, (b). Residual stresses of Au-Ni/a-C under different graphite sputtering powers

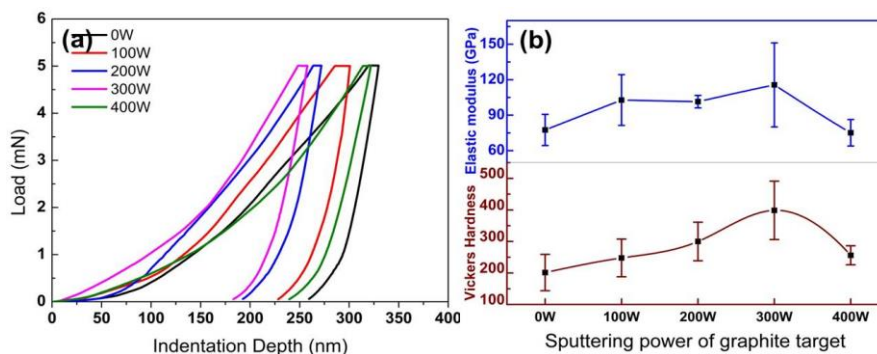


Figure 5-7 Nanoindentation measurement results: (a). Load–displacement curves, (b). Vickers hardness and elastic modulus

The purpose of compounding C in the Au-Ni coating is to improve its wear performance. In addition to providing solid lubrication function, increasing the Au-Ni matrix's hardness is another purpose of C atom implantation for wear prevention. As shown in Figure 5-7, under a peak load of 5 mN, the averaged Vickers hardness of Au-Ni alloy coating is 200. From the XRD and TEM observation, the presence of Au-Ni hcp phase was confirmed, which can generate additional precipitation hardening effect on the coating [180]. However, the magnetron sputtered Au-Ni coating is still softer than the electroplated Au-Ni (fcc structure and Ni content 2 wt.%) coating whose hardness was reported as 267.7 HV [181].

C atoms play an important role in improving the hardness of the Au-Ni coating as all Au-Ni/a-C coatings with different C contents were observed harder than the Au-Ni reference coating. From 100 W to 300 W, the residual indentation depth of the composite coating reduces with the C content increase and the hardness of Au-Ni/a-C composite coating with graphite sputtering power of 300 W reaches to 400 HV. However, the tendency of coating hardness variation is reversed when the sputtering power is higher than 300 W. Based on the Raman results, embedding in Au-Ni crystal lattice and accumulating as a-C clusters are the two forms of C atoms in the composite coating. As impurity atoms, the C atoms that are interstitially doped in the Au-Ni crystal lattice can induce lattice strains, as a result, significant solid solution strengthening effect is induced in the Au-Ni coating. In addition, as proved by TEM observation, the crystal defects induced by the embedding of C clusters benefit to the hardness improvement too. After reaching a plateau, the hardness of Au-Ni/a-C composite coating decreases with further C content increase. This phenomenon could be explained by the volume increase of soft a-C clusters in the coating [182]. Similar variation tendency of elastic modulus as hardness was observed too. In Au-Ni/a-C coatings, the residual stresses are compressive stresses which compress the interatomic distance and increase the stiffness of the interatomic bonding accordingly [183]. Therefore, compared with Au-Ni coating, the elastic modulus of Au-Ni/a-C (300 W) increases from 77 GPa to 115 GPa. Again, the sudden decrease of the elastic modulus of the 400 W coating is due to the high volume content of a-C phase.

Besides residual stress and hardness, adhesion performance of Au-Ni/a-C coating on CuCrZr substrate is also an important factor for coating durability. As shown in Figure 5-8, based on the SEM observation of the scratch tracks, all the Au-Ni and Au-Ni/a-C coatings show typical ductile failure mode without occurrence of chipping phenomenon [41]. Three typical stages happened on the scratch track on the 200 W, 300W and 400 W coatings, which include small plastic deformation stage, transverse cracking (tensile cracking) stage and buckling & spallation stage. For the coatings without C and with low C (100 W), no transverse cracking stages are observed, which

indicates that the cohesive strength of the Au-Ni/a-C coating decreases with C content increase, i.e., C constituent impairs the toughness of the composite coating. However, all the coatings show high adhesive strength on CuCrZr substrates and no obvious difference of adhesive strength between them were observed. The critical loads of the coatings are around 30 N.

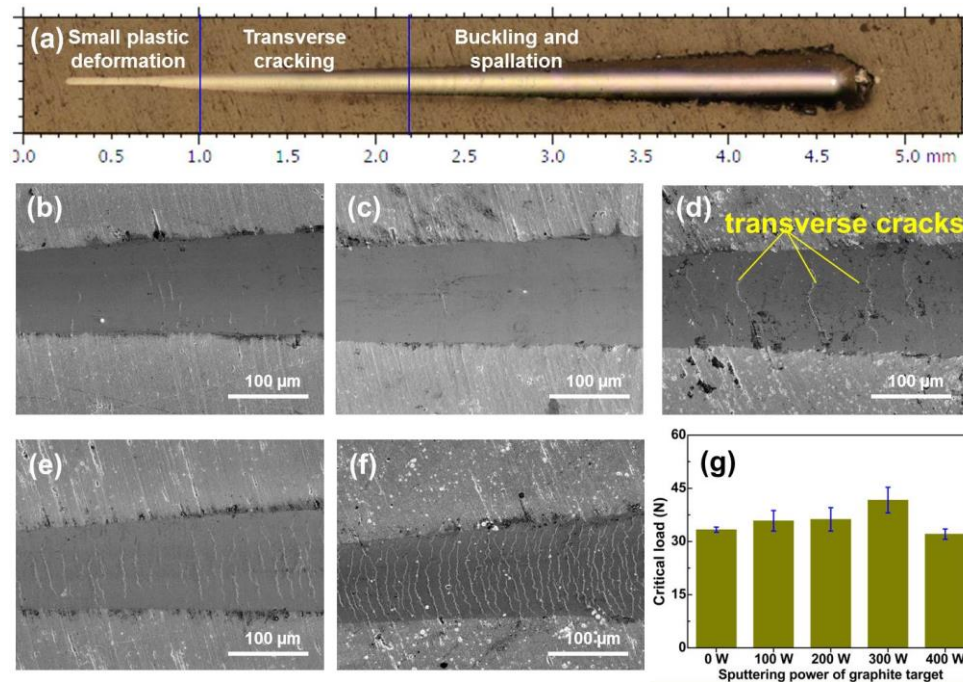


Figure 5-8 Scratch test results: (a). Optical microscope image of the full scratch track on the 400 W sample, (b-f). SEM images of scratch tracks from 0 W to 400 W, (g). Critical loads of coatings

#### 5.1.2.4 Electrical performance

The electrical resistivity of coating is measured by four-point probe measurement. For the electrical resistivity, a sudden increase by  $1.7 \mu\Omega/\text{cm}$  happened on the 100 W Au-Ni/a-C coating compared with the Au-Ni reference (Figure 5-9). Based on Raman analysis, in the 100 W Au-Ni/a-C coating, C atoms are mainly alloyed in the Au-Ni lattice. The lattice distortion caused by the C atoms embedding could be the reason that caused the sudden increase of the electrical resistivity. With higher C contents, the a-C nano-clusters generated have a small effect on the coating's electrical resistivity. The Au-Ni/a-C composite coatings developed have electrical resistivities around  $8.2 \mu\Omega/\text{cm}$ , which can be compared to the electrical resistivity of the magnetron sputtered pure Au coating ( $3.2 \mu\Omega/\text{cm}$ ).

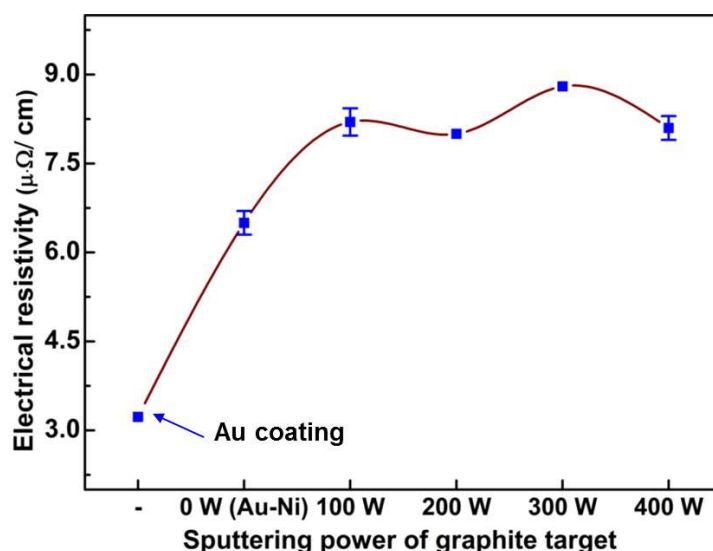
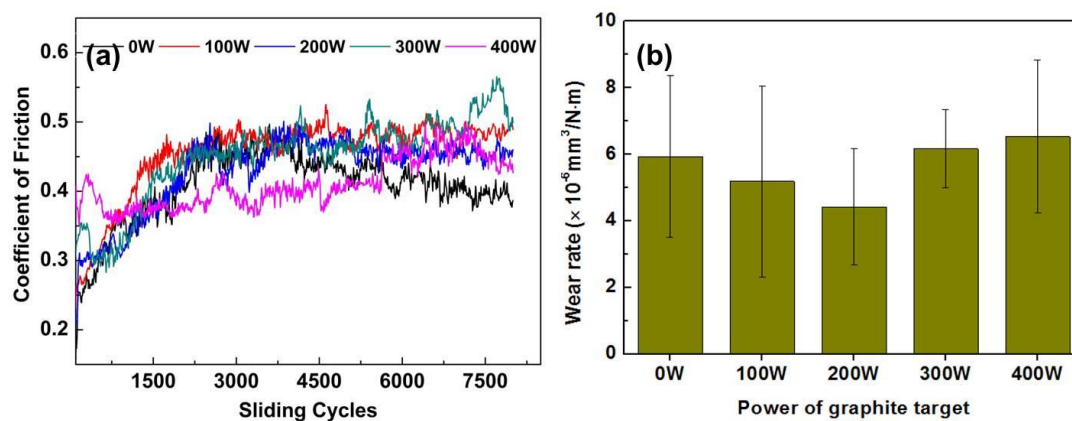


Figure 5-9 Electrical resistivities of Au-Ni and Au-Ni/a-C coatings

### 5.1.2.5 Tribological performance

Coatings' tribological performance was evaluated on a ball-on-disc tribometer equipped with high vacuum pumping system against GCr15 ball ( $\varnothing=3$  mm). 8000 cycles' rotary sliding tests were performed under  $10^{-3}$  Pa with a linear speed of 8.4 cm/s and a normal contact force of 2 N.

Figure 5-10 Tribological performance of the Au-Ni and Au-Ni/a-C coatings: (a,b). CoF and wear rate under atmosphere, (c,d). CoF and wear rate under  $10^{-3}$  Pa vacuum.

As lubricating efficiency of a-C is low in high vacuum condition, not surprisingly the CoFs of all the coatings are similar (Figure 5-10). The 400 W coating sample still had a slight self-lubricating function before 5500 cycles with CoF of 0.4. However, in vacuum, the smallest wear rate is  $4.5 \times 10^{-6} \text{ mm}^3/\text{N}\cdot\text{m}$ , which happened on the 200 W sample. In this case, lubricating is not the main factor that determines the wear rate and the combined effects of coating's hardness, residual stress and toughness on wear rate are more important.

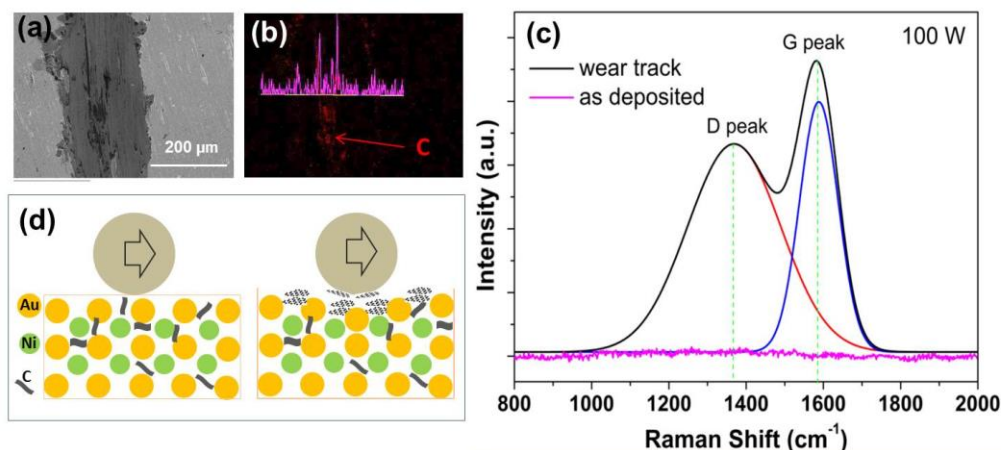


Figure 5-11 Wear track characterizations of 100 W Au-Ni/a-C coating: (a). SEM image of wear track, (b). EDS mapping of C in the position of (a), (c). Raman spectra in the wear track, (d).

Schematic diagram of C lubricant film generation

Aiming to understand the lubricating mechanism of the Au-Ni/a-C coating, the 100 W sample was selected and wear track characterizations were carried out. As shown in Figure 5-11 (b), C accumulation in the wear track was verified through EDS mapping after the sliding. Compared with the Raman spectrum of 100 W coating as deposited, two pronounced peaks which correspond to D and G peaks were observed at  $1369\text{ cm}^{-1}$  and  $1588\text{ cm}^{-1}$ , respectively. The  $I_D/I_G$  ratio is calculated as 0.83. All these evidences indicate that agglomeration of  $sp^2$ -bond rich C happened during sliding, i.e., graphitic carbon tribo-layer transferred and covered the wear track. As the schematic diagram shows in Figure 5-11(d), originally C atoms were uniformly distributed in the Au-Ni/a-C coating as free atoms in Au-Ni lattice or in a-C nanocrystallite with high content of  $sp^3$  bonds. During the sliding, accompanied with wear, C clusters accumulated and possibly transferred between the ball and the coating. The pressure due to the normal contact force and the annealing due to friction could induce the graphitization process at local contact areas [184]. The graphitic layer which has developed between the two wear surfaces helped to reduce CoF. With higher C content in the original coating, the graphitization process is more significant and as a result, the CoF lowered.

### 5.1.3 Summary

By regulating the sputtering power of a graphite target, Au-Ni/a-C coatings with different C content were deposited by magnetron sputtering. Under 400 W, the C content in the composite coating reaches 2 wt.%. The coating's hardness improvement of compounding C in Au-Ni matrix was measured. The Au-Ni/a-C coating deposited under 300 W has the largest hardness, elastic modulus and critical load, which are 400 HV, 115 GPa and 41.7 N, respectively. Because the tribological tests were

conducted in vacuum, the lubricating function of a-C is not very efficient. Only the 400 W sample shows a little lower CoF compared with the Au-Ni coating without a-C. The wear rate of coating is determined by its mechanical properties (hardness, residual stress) as well as lubricating performance. 200 W sample shows the lowest wear rate, however, compared with Au-Ni coating without C, the advantages of compounding C inside to minimize the wear rate are not obvious.

For application in the ITER environment, another important performance required is the coating thermal stability under 250°C baking. Compounding a-C in Au-Ni matrix may improve the coating's thermal stability, which needs to be further investigated. If this point is proved, Au-Ni/a-C will still be a good candidate for ITER ICRH RF sliding contact application.

## 5.2 Au-Co/WS<sub>2</sub> deposition and coating characterizations

Co is not a material recommended for nuclear application, as it has unfavorable activation characteristics under neutron irradiation [185]. For ITER application, 0.2 wt.% is the Co content limit of the structural materials. For Au coating, alloying 0.2 wt.% Co inside can still improve the mechanical performance of the Au coating significantly. Au-Co commercial bath is easier to acquire. In this section Au-Co is selected as the coating matrix for the WS<sub>2</sub> lubricant. The electroplating process is firstly developed and qualified, then the tribological performance of the composite coating is assessed.

### 5.2.1 Electroplating process of Au-Co/WS<sub>2</sub>

#### 5.2.1.1 Ni interlayer plating

##### 1) Electrolyte preparation

The nickel sulfamate solution is commonly used to achieve good Ni plating layer with low stress and moderate hardness [186, 187]. Thus, in this study, the diffusion layer between the Au-Co/WS<sub>2</sub> and CuCrZr substrate was electroplated from sulfamate electrolyte. The details of the Ni plating electrolyte are shown in Table 5-1.

Table 5-1 Details of Ni electrolyte

Bath composition	Concentration	Electrodeposition condition
Ni(SO <sub>3</sub> NH <sub>2</sub> ) <sub>2</sub> ·4H <sub>2</sub> O	300 g/L	Tem: 45°C
NiCl <sub>2</sub> ·6H <sub>2</sub> O	30 g/L	PH: 3.8
H <sub>3</sub> BO <sub>3</sub>	30 g/L	
Butyndiol	0.06g/L	

## 2) *Electroplating setup*

As Figure 5-12 shows, the electrodeposition and electrochemical analyses were performed on an electrochemical potentiostat (Gamry Interface 1000, Gamry Instruments, USA). A double layer three-electrode cell was used with a solution volume of 125 mL and the solution was maintained at 45 °C by water heating system during the plating and electrochemical analysis. The CuCrZr plates worked as cathode and the counter electrode was a platinum-coated titanium mesh with surface area around 12 cm<sup>2</sup>. A platinum-wire was used as reference electrode.

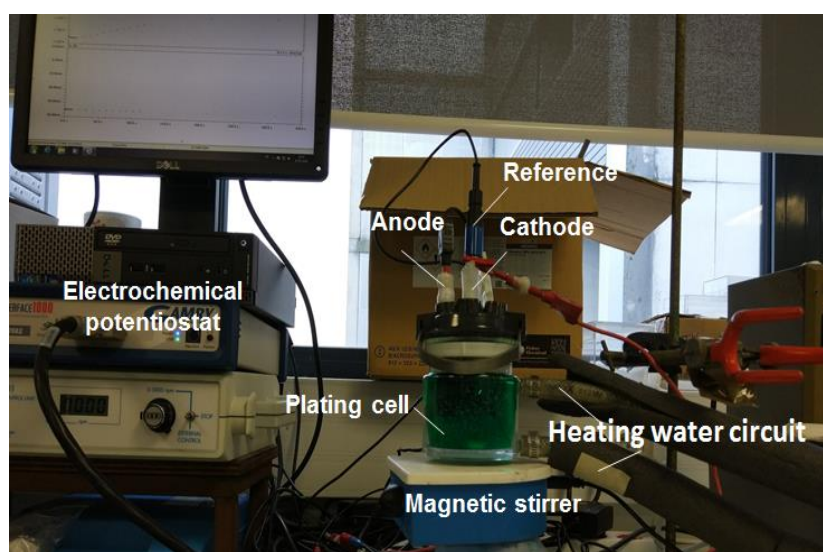


Figure 5-12 Photo of electrodeposition setup

## 3) *Linear sweep voltammetry study and galvanostatic electrodepositions*

Before the deposition, all the substrates were pretreated by a degreasing process with 5 min sonication in acetone and 5 min sonication in ethanol. After the degreasing process, an activating treatment was performed with 30s immersion in 10% H<sub>2</sub>SO<sub>4</sub>, followed by a quick deionized water rinse and the electroplating was started immediately.

Linear sweep voltammetry (LSV) measurement was conducted and the potential (versus Pt-wire) was scanned between 0 V and -2 V at a scan rate of 5 mV/s and magnetic stir speed of 300 rpm. Figure 5-13 shows the polarization curve measurement results of the Ni sulfamate electrolyte. It shows that the electrolyte can be used under a wide current density range from 1 A/dm<sup>2</sup> to 15 A/dm<sup>2</sup>. Applying a higher current density can achieve higher coating rate; however, the Ni coating generally shows large crystallite size and low hardness if the current density is too large [188]. Ni coatings under current densities of 2 A/dm<sup>2</sup>, 3 A/dm<sup>2</sup>, 4 A/dm<sup>2</sup>, 5 A/dm<sup>2</sup> were deposited and characterized. The coatings' thicknesses were controlled at

4  $\mu\text{m}$  by regulating the coating time calculated from the Faraday's Law (equation 2-4).

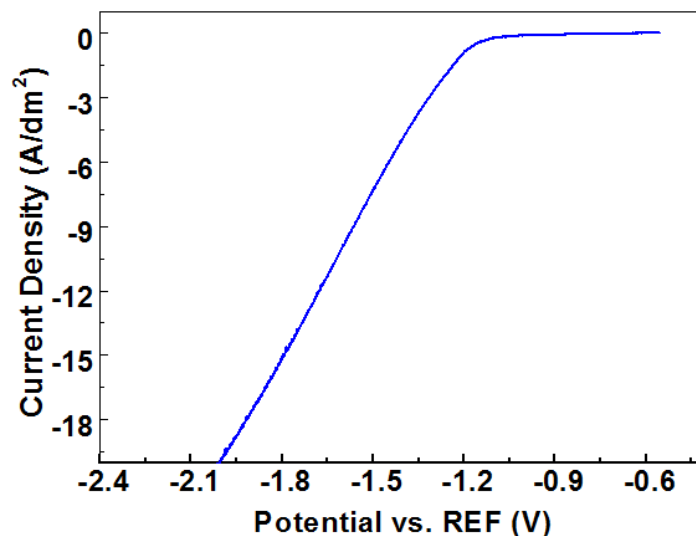


Figure 5-13 Polarization curve for the Ni sulfamate electrolyte

#### 4) Ni coating characterizations

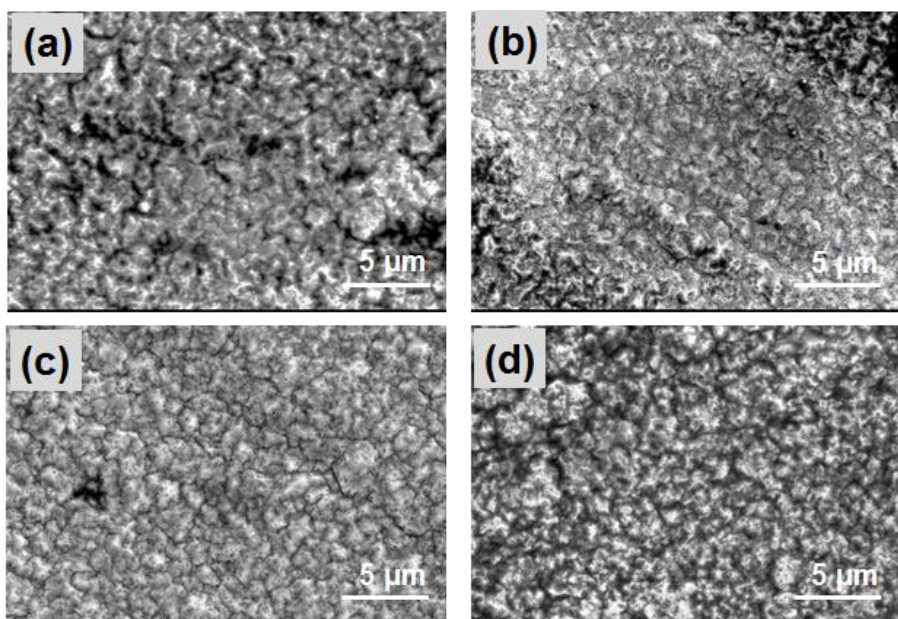


Figure 5-14 SEM images of Ni coatings plated under different current densities: (a). 2 A/dm<sup>2</sup>, (b). 3 A/dm<sup>2</sup>, (c). 4 A/dm<sup>2</sup>, (d). 5 A/dm<sup>2</sup>

Based on the SEM morphology study shown in Figure 5-14, all the Ni coatings deposited under current densities of 2A/dm<sup>2</sup>, 3A/dm<sup>2</sup>, 4A/dm<sup>2</sup>, 5A/dm<sup>2</sup> exhibit a pyramidal-like morphology. All the coatings show compact structure without obvious coating defects observed.

The Ni coatings' crystal structures are studied by using XRD and the results are shown in Figure 5-15. All the coatings show (200) preferred orientation, which is similar to the results reported in [188]. The crystallite sizes of the Ni coatings were calculated based on (002) peaks and the results are shown in Figure 5-16. With the current density increases from 2 A/dm<sup>2</sup> to 5 A/dm<sup>2</sup>, a slight crystallite size increase is observed from 33 nm to 36.5 nm.

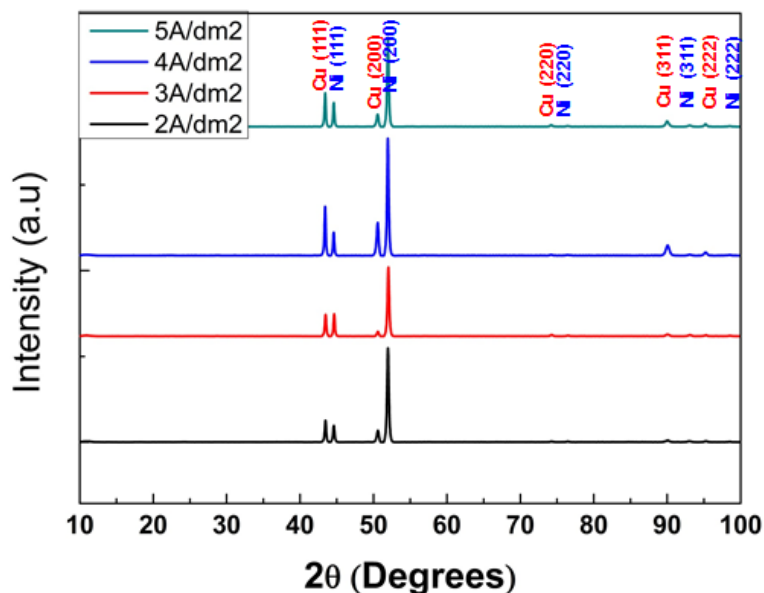


Figure 5-15 XRD patterns of the Ni coatings

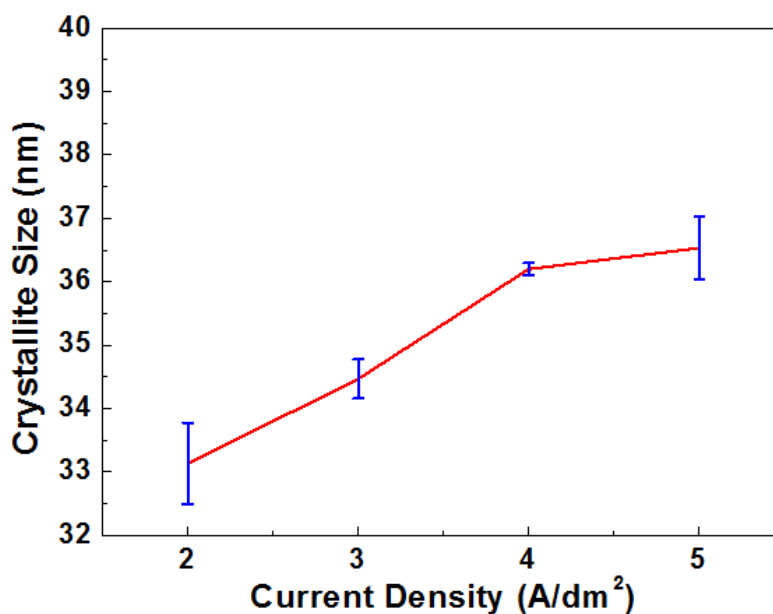


Figure 5-16 Crystallite sizes of the Ni coatings

In order to evaluate the adhesion performance of the Ni coating, a sample electroplated under 3 A/dm<sup>2</sup> was selected to perform the scratch test. As shown in Figure 5-17, the critical load of the Ni coating is 31 N. Based on the EDS mapping,

although there is large plastic deformation of coating and substrate occurring in the scratch track, the Ni layer is still attached on the substrate closely without delamination. All these evidences indicate that the Ni layer deposited on the CuCrZr substrate has good adhesion performance.

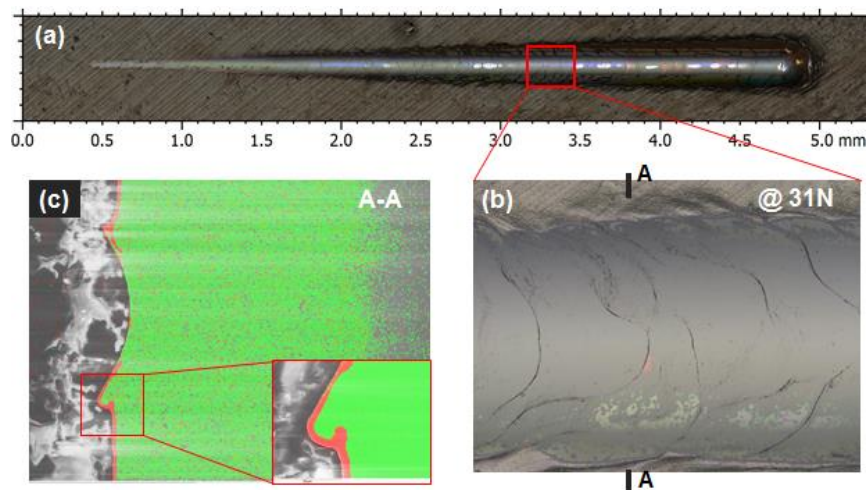


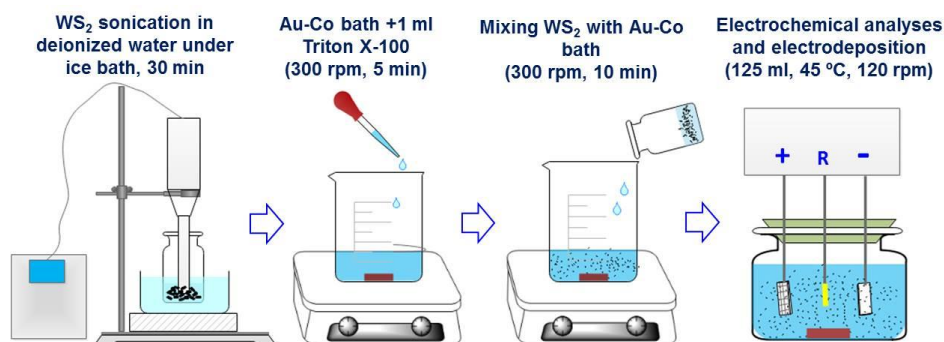
Figure 5-17 Adhesion performance of Ni ( $3 \text{ A/dm}^2$ ): (a). Scratch track, (b). Details picture of the first delamination area, (c). EDS mapping of the A-A cross-section

### 5.2.1.2 Au-Co/WS<sub>2</sub> plating

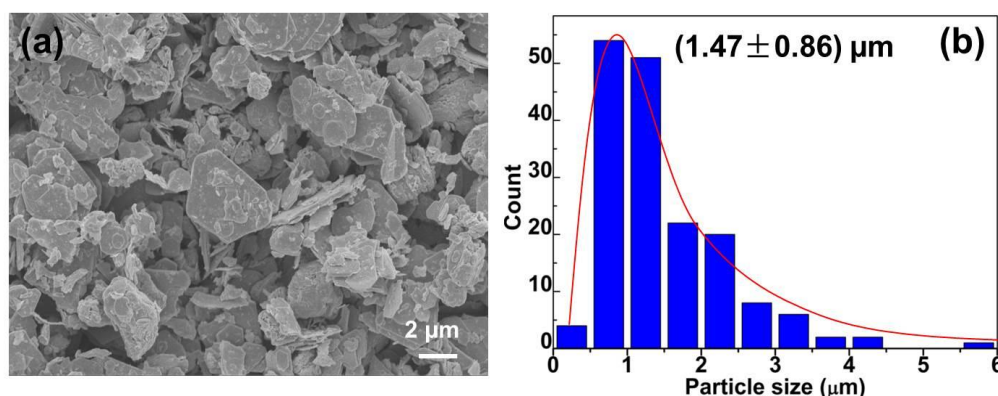
#### 1) Electrolyte and substrate preparation

The Au-Co electroplating is based on commercial aqueous cyanide electrolyte from COVENTYA<sup>®</sup> containing 4 g/L KAu(CN)<sub>4</sub>, CoSO<sub>4</sub>, H<sub>3</sub>PO<sub>4</sub> and H<sub>2</sub>SO<sub>4</sub>. The PH of the electrolyte was maintained at 0.6.

Particle concentration and degree of dispersion have a significant effect on the property of the composite coating. WS<sub>2</sub> (0001) surface is made of chemical saturated sulfur atoms. Thus WS<sub>2</sub> particles are very hydrophobic [189] and large agglomerates are easily generated when they are mixed with the aqueous Au plating bath. Magnetic stirring is often used for particle dispersion; however, magnetic stirring has been suspected not to be efficient for WS<sub>2</sub> dispersion [190]. Composite deposition assisted by ultrasonication during electroplating was also reported [191]. Even though the efficiency of ultrasonication is high, the drawbacks of this method are the limit of electrolyte volume and the heating of the electrolyte. Applying surfactant is a practical solution for industrial composite coating production. As a non-ionic surfactant, Triton X-100 has high chemical stability in acid and alkaline electrolytes [192] and it can be used as a wetting agent in KAu(CN)<sub>4</sub> electrolyte [193]. The feasibility of applying Triton X-100 for Au matrix WS<sub>2</sub> composite coating deposition is further investigated.

Figure 5-18 Sketch of Au-Co/WS<sub>2</sub> electrolyte preparing flow

Like Figure 5-18 shows, Triton X-100 ( $C_{14}H_{22}O(C_2H_4O)_n$ ,  $n \approx 10$ ) (Acros Organics) was added into the Au-Co electrolyte to a concentration of 8 ml/L with 300 rpm magnetic stirring for 5 min. WS<sub>2</sub> powder (2  $\mu\text{m}$ ,  $\geq 99\%$ , Sigma-Aldrich) was mechanically exfoliated in deionized water by using a probe sonicator (Vibra Cell 75042, 20 kHz, 500 W, 30% power with 2 s on / 2 s off pulses) for 30 min (the WS<sub>2</sub> particles after sonication are shown in Figure 5-19). Then, the exfoliated WS<sub>2</sub> solution was poured into the Au-Co electrolyte with 8 ml/L Triton X-100 surfactant slowly and agitated with magnetic stirring. By regulating the weight of the WS<sub>2</sub>, three Au-Co electrolytes with 8 ml/L Triton X-100 and different WS<sub>2</sub> concentration (2 g/L, 4 g/L, 8 g/L) were prepared. Besides, three electrolytes (pure Au-Co electrolyte, Au-Co electrolyte with 8 ml/L Triton X-100, Au-Co electrolyte with 2 g/L WS<sub>2</sub>) were also prepared as references for coating comparison or for WS<sub>2</sub> particle stability study.

Figure 5-19 SEM and particle size (diameter) distribution of WS<sub>2</sub> after sonication

Before the deposition, all the substrates were pretreated by a degreasing process with 5 min sonication in ethanol and 5 min sonication in acetone. After the degreasing process, an activating treatment was performed on the Ni surface with 1 min immersion in 20% HCl and 3 min immersion in 25% H<sub>2</sub>SO<sub>4</sub>, followed by a quick deionized water rinse and the electroplating was started immediately.

2) *WS<sub>2</sub> stability in electrolyte*

In order to evaluate the dispersion state of WS<sub>2</sub> particles in the electrolyte and investigate the mechanism and process of particle aggregation, Turbiscan LAB (Formulation, France) was used [194]. During the measurements, specific transparent glass tubes with different electrolytes of 4 cm high were installed in the machine uprightly and they were scanned by a laser source from the bottom to the top. Signal of backscattered (BS) light was detected as a function of time and position along the axis of the tube. The first scanned BS profile was regarded as the reference and after that in each scan, the BS profiles were recorded in delta mode ( $\Delta BS = BS_{scan} - BS_{ref}$ ). From the  $\Delta BS\%$  profile [195], the particles' movement behavior can be recognized. Turbiscan stability index (TSI) can be used to evaluate the dispersion stability, which is defined by the following equation [196]:

$$TSI = \sum_i \frac{\sum_h |scan_i(h) - scan_{i-1}(h)|}{H} \quad (5-3)$$

where,  $h$  and  $H$  are the selected height and the total height of the electrolyte sample respectively. The smaller the  $TSI$  is, the more stable of the electrolyte is.

In this study, three electrolytes (Table 5-2) were selected to carry out the WS<sub>2</sub> particle stability study. All the electrolytes were magnetically stirred under the speed of 300 rpm for 5 min, then installed in Turbiscan and measured immediately. The electrolyte samples were scanned in every 30 s for 1 h and the tests were carried out at room temperature (25°C).

Table 5-2 Electrolytes for the WS<sub>2</sub> particle stability measurement

<b>Au-Co electrolyte</b>	<b>WS<sub>2</sub> concentration</b>	<b>Triton X-100 concentration</b>	<b>Heating condition</b>
A	2 g/L	-	-
B	2 g/L	8 ml/L	-
C	2 g/L	8 ml/L	45°C, 40 min

The Figure 5-20 (a) shows that for the electrolyte A without Triton X-100 surfactant, at the bottom (0 mm-0.5 mm) there is a peak with  $\Delta BS\%$  in positive values appears, which indicates the sedimentation of the WS<sub>2</sub> particles. At the top of the tube (38.5 mm-40 mm) there is also a positive peak observed, which reflects the existence of a floating layer, i.e., creaming occurred. The Au-Co electrolyte shows poor wettability to WS<sub>2</sub> particles and the large surface tension is the reason that induces the creaming of the WS<sub>2</sub> particle. In the middle of the tube, the  $\Delta BS\%$  profiles show large

fluctuation which is dominated by the flocculation and creaming mechanisms. The floating layer can also be observed visually as shown in Figure 5-20 (e). In Figure 5-20 (b), with 8 ml/L Triton X-100 in the electrolyte, the creaming phenomenon is suppressed as the adsorption of Triton X-100 molecules on the  $WS_2$  particle surfaces improved their wettability and decreased the surface tension [197]. Although sedimentation and flocculation are also observed in the electrolyte with Triton X-100, the TSI values of electrolyte B is only half of the electrolyte A (Figure 5-21), in which the capability of Triton X-100 to improve the Au-Co/ $WS_2$  electrolyte stability is verified. Based on the visual observation (Figure 5-20 (e)) and TSI curves (Figure 5-21), the electrolyte B shows high stability before 5 min. As the optimum deposition temperature of the Au-Co electrolyte is  $45^\circ C$ , the stability study of  $WS_2$  particle in the  $45^\circ C$  electrolyte is necessary. Compared with electrolyte B, the electrolyte C shows higher instability with higher speed of flocculation and higher tendency of creaming (Figure 5-20 (c)). Based on the TSI curve of electrolyte C, something happened in the electrolyte after two minutes since the measurement started.

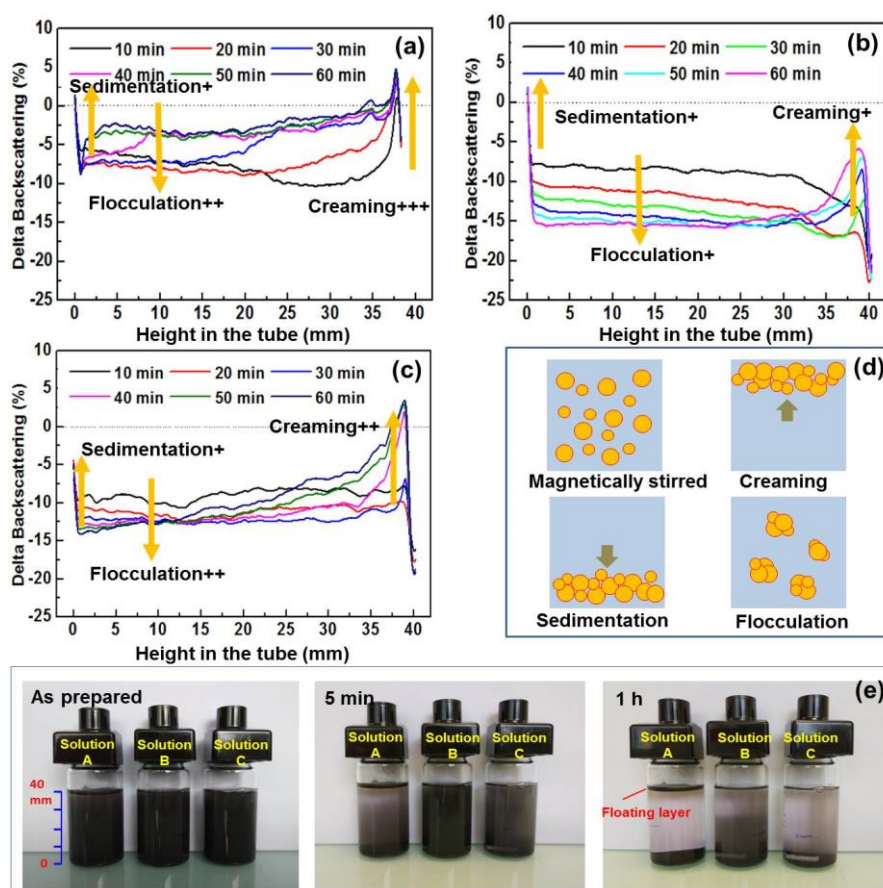


Figure 5-20 Results of  $WS_2$  particle stability measurements: (a).  $\Delta BS\%$  profiles of electrolyte A shown in Table 5-2, (b).  $\Delta BS\%$  profiles of electrolyte B, (c).  $\Delta BS\%$  profiles of electrolyte C (d).

Schematic of  $WS_2$  particle behavior in electrolytes, (e). Evolution of the three electrolytes according to the waiting time

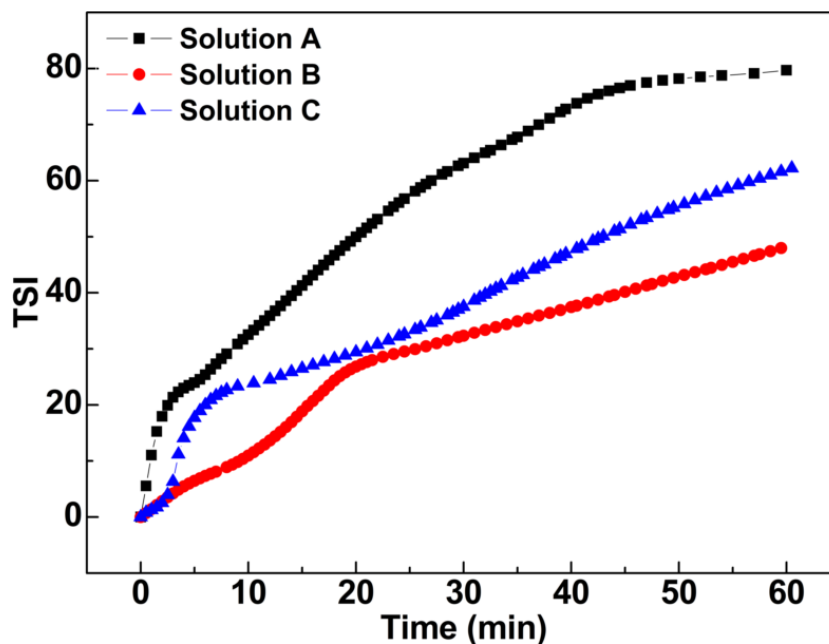


Figure 5-21 Changes of TSI of different electrolytes over time

### 3) Linear sweep voltammetry study and galvanostatic electrodepositions

The cathodic polarization curves measured in different electrolytes are shown in Figure 5-22. Without adding Triton X-100 surfactant and  $WS_2$  particles, the Au-Co electrolyte shows a wide working range of current density from  $1 A/dm^2$  to  $20 A/dm^2$ . With 8 ml/L Triton X-100 being added in the Au-Co electrolyte, the cathodic potentials shifted negatively and the slope of the curve decreased. This indicates that the presence of Triton X-100 in the electrolyte can affect the Au-Co deposition process, which may be own to the adsorption of Triton X-100 molecules on the coating surface and work as an inhibitor [198-200]. Compared with Au-Co electrolyte with Triton X-100, adding of 0.5 g (4 g/L)  $WS_2$  particles shifts the potential of the cathode to more negative values. The decrease of reduction potential is attributed to the adsorption of  $WS_2$  particles on the coating surface which decreased the active surface area and decreased the ionic transport rate in the diffusion layer accordingly. When current densities are higher than  $7 A/dm^2$ , significant fluctuation has been observed. The fluctuation is supposed to be caused by the violent hydrogen evolution on the cathode as  $H_2$  bubbles can insulate the cathode with the electrolyte or remove the  $WS_2$  particles attached on the coating surface. From the  $WS_2$  particle stability study introduced in the last section, the electrolyte which contains Triton X-100 surfactant was proved to be unstable after being heated at  $45^\circ C$  for 40 min. After keeping this electrolyte at  $45^\circ C$  for about 40 min and measuring the polarization curve again, an obvious potential transition to positive side compared with the fresh electrolyte was observed. Especially, when the current density is lower than  $7 A/dm^2$  the polarization curve of the deteriorated electrolyte is almost the same as the pure

Au-Co electrolyte and the violent hydrogen evolution phenomenon was postponed in comparison with the fresh Au-Co electrolyte with Triton X-100 and WS<sub>2</sub> particles. These evidences indicate that the property of Au-Co electrolyte with Triton X-100 and WS<sub>2</sub> particles changed with time. According to the polarization curve measurements, 5 A/dm<sup>2</sup> has been selected as the current density for the galvanostatic chronopotentiometry study and for the Au-Co/WS<sub>2</sub> coating deposition too.

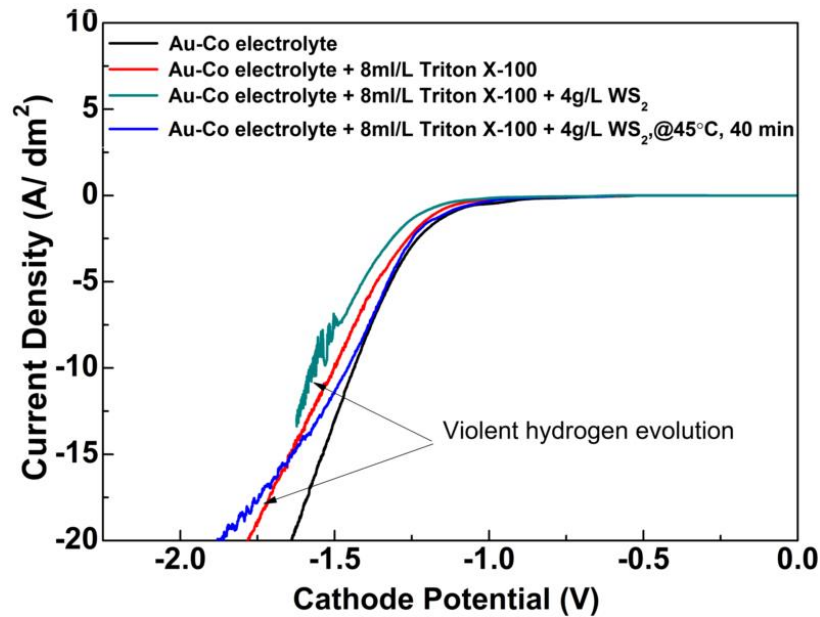


Figure 5-22 Cathodic polarization curves from different electrolytes

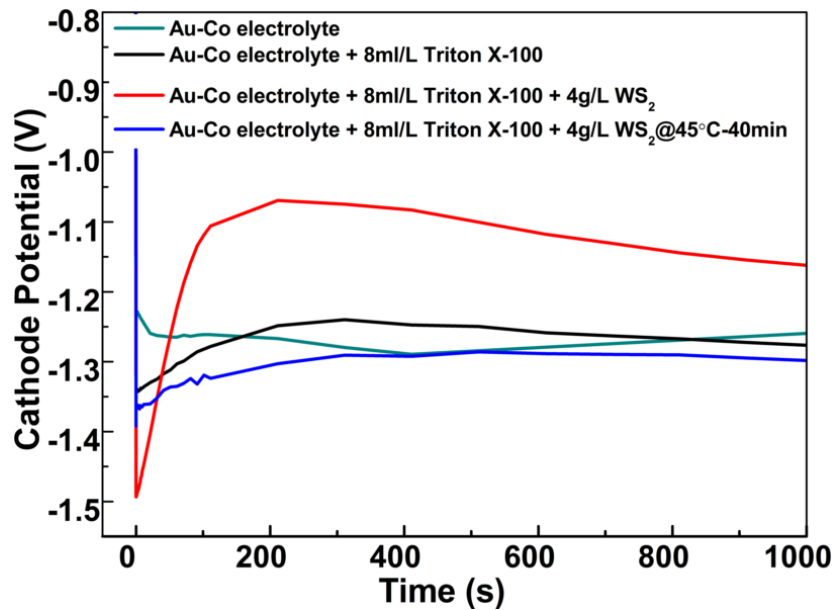


Figure 5-23 The potential-time (E-t) curves obtained at  $J=5 \text{ A/dm}^2$  from the electrolyte of Au-Co and Au-Co with Triton X-100 and WS<sub>2</sub> particles.

Figure 5-23 shows the E-t curves measured under constant current density ( $5 \text{ A/dm}^2$ ) during electrodeposition in different electrolytes. For the Au-Co electrolyte, the cathodic potential reached steady-state after a short nucleation stage and the cathodic potential is about -1.3 V. For the fresh prepared Au-Co electrolyte with 8 ml/L Triton X-100 and 4 g/L  $\text{WS}_2$ , a very different E-t behavior is observed. When the current is applied, the cathodic potential is -1.49 V which agrees with the result shown in Figure 5-22, then it decreased to -1.1 V gradually in around 200 s, followed by a slight increase process. The remarkable decrease of cathodic potential indicates that the dominant cathodic reaction happened easier than the  $[\text{Au}(\text{CN})_4]^-$  ion reduction, i.e., the cathodic reaction happened needs a lower overpotential than the reduction of  $[\text{Au}(\text{CN})_4]^-$ . Hydrogen evolution was probably the dominated reaction at -1.1 V. The  $[\text{Au}(\text{CN})_4]^-$  reduction (whose onset potential is -1 V shown in Figure 5-22) was suppressed as the ion density in the double layer was very low due to the effect of Triton X-100 and  $\text{WS}_2$  particles adsorbed on the active coating surface. As there is no effect coming from  $\text{WS}_2$  particles, the Au-Co electrolyte with 8 ml/L Triton X-100 shows a similar shape, but with a moderate change for the E-t curve in comparison to the electrolyte with  $\text{WS}_2$ . As referred in the polarization curve measurement section, the degradation of electrolyte with Triton X-100 and  $\text{WS}_2$  particles was also approved during the chronopotentiometric study. The electrolyte maintained at  $45^\circ\text{C}$  for 40 min presents a similar E-t behavior as the Au-Co electrolyte.

Together with  $\text{WS}_2$  stability measurement results, the property change of Au-Co electrolytes with Triton X-100 surfactant at  $45^\circ\text{C}$  for 40 min is illustrated in Figure 5-24. Triton X-100 molecule has a hydrophobic tail and a hydrophilic head. When Triton X-100 is dissolved into the aqueous electrolyte, the hydrophobic tail of the surfactant can orient toward the  $\text{WS}_2$  particle surface and the surface of electrodes while the hydrophilic head associates with water for dissolution [201, 202]. The adsorption of Triton X-100 molecules on the  $\text{WS}_2$  particle surfaces prevent the  $\text{WS}_2$  particles from agglomeration by overcoming the van der Waals attractions [203]. With magnetic stirring,  $\text{WS}_2$  and Triton X-100 surfactant present in the electrolyte as micelles uniformly. As a nonionic surfactant, Triton X-100 has a certain temperature (cloud point) in its aqueous solution above which, phase separation occurs [204]. Studies show that the aqueous Triton X-100 solution with a concentration of 1% (v/v) has a cloud point around  $65^\circ\text{C}$  [205]. However, in the Au-Co base electrolyte, there are many foreign ions existing and such ions decreased the cloud point of Triton X-100 surfactant to a value not higher than  $45^\circ\text{C}$ . By keeping the Au-Co electrolyte with 8 ml/L Triton X-100 and  $\text{WS}_2$  particles at a temperature of  $45^\circ\text{C}$  for 40 min, the well-dispersed Triton X-100 micelles (with  $\text{WS}_2$  particles inside) separated as droplets. When the magnetic stirring stopped, sedimentation of Triton X-100 phase which is

rich in  $WS_2$  particles was observed at the bottom of the cell. This mechanism can explain the abnormal phenomena of  $WS_2$  particles' stability and electrochemical performance of the electrolyte heated at  $45^\circ C$  for 40 min.

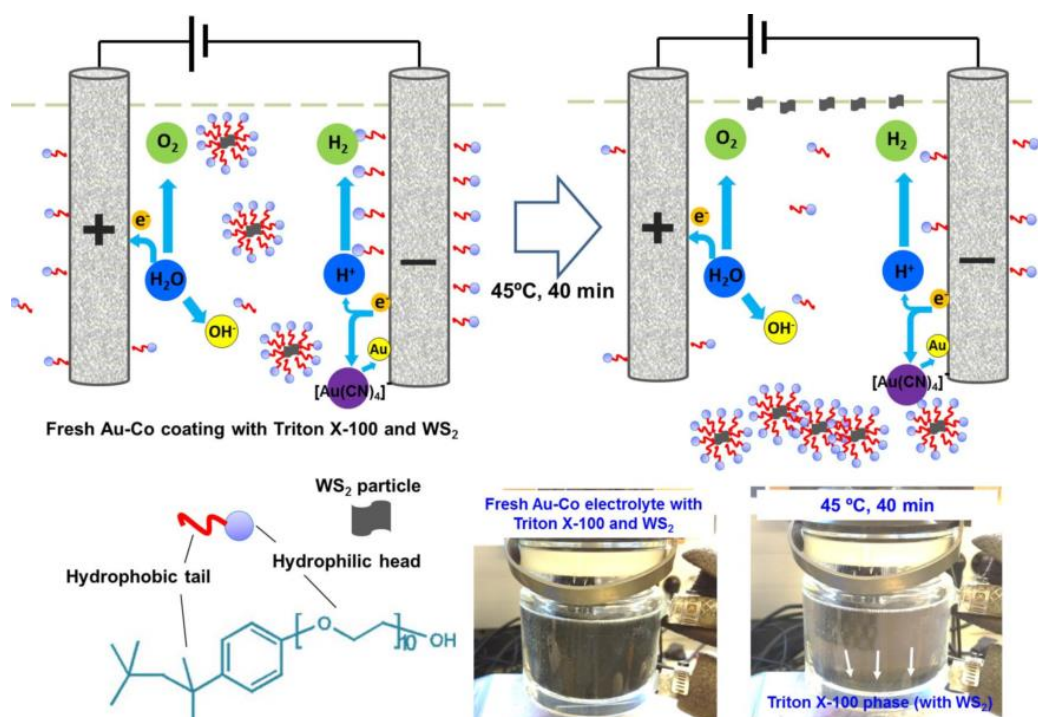


Figure 5-24 Schematic illustration of Triton X-100 surfactant assembly on  $WS_2$  particles

## 5.2.2 Coating characterizations

### 5.2.2.1 Coating composition

The compositions of Co and  $WS_2$  particles in the Au-Co or Au-Co/ $WS_2$  composite coating are important as they can minimize the coatings' wear rate by increasing the hardness and decreasing CoF, respectively. As shown in Figure 5-25, under a current density of  $5 \text{ A/dm}^2$ , 0.19 wt.% Co in the alloy coating with coating rate of  $0.28 \text{ } \mu\text{m/min}$  was achieved by using the Au-Co electrolyte. The Au-Co coating's hardness is about 250 HV0.01 [206]. With the presence of Triton X-100 (8 ml/L), the coating rate decreased obviously by 50 %, which was caused by the low concentration of  $Co^{2+}$  and  $[Au(CN)_4]^-$  in the electric double layer. When Triton X-100 was added, the cathodic potential shifted to more negative values (Figure 5-22) and promoted the reduction of Au (III), which can explain the decrease of Co content in the Au-Co from 0.19 wt.% to 0.12 wt.%. Due to the Co content decrease, which weakened the solid solution strengthening effect, the Au-Co coating's hardness decreased to 223 HV0.01. For the fresh Au-Co electrolyte with Triton X-100 and  $WS_2$  particles, hydrogen evaluation turned to be the main cathodic reaction due to the low transportation rate of  $Co^{2+}$  and  $[Au(CN)_4]^-$  ions. As a result, the cathodic efficiency is very low. The coating

rate of the Au-Co/WS<sub>2</sub> electrolyte decreases with the WS<sub>2</sub> concentration increase. Another obvious effect of mixing WS<sub>2</sub> particles in the electrolytes is the depressing of Co in the composites coatings, which is also due to the enhancement of cathodic polarization. When the WS<sub>2</sub> concentration is higher than 4 g/L, the Co contents are too low to be measured by EDS technique. As explained in the previous section, due to phase separation, the WS<sub>2</sub> concentration in the electrolyte and the electrolyte's viscosity decreased and as a result there are no WS<sub>2</sub> particles compounded inside in the Au-Co coating.

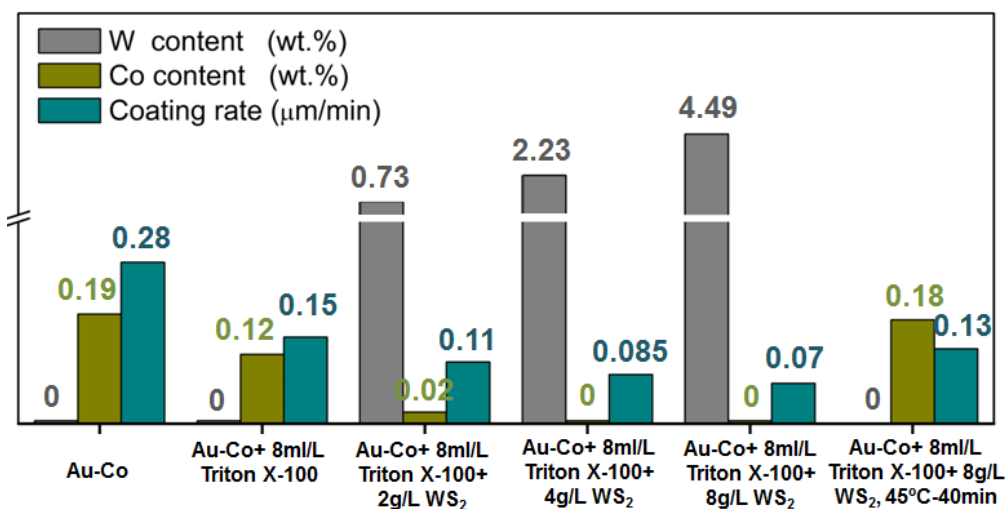


Figure 5-25 W, Co contents and coating rate of different electrolytes under a current density of 5 A/dm<sup>2</sup>

### 5.2.2.2 Coating morphology and topography

As Figure 5-26 (a) shows, the electrodeposited Au-Co coating exhibits a smooth surface with a spherical nodular structure. With Triton X-100 in the electrolyte, the grain size tends to decrease, a phenomenon which was also observed in the Pt-Rh co-deposition with the presence of Triton X-100 [207]. With Triton X-100, the surface roughness (Sa) of Au-Co coating decreased from 0.47 μm to 0.37 μm (Figure 5-27). The enhancement of cathodic polarization after adding Triton X-100 surfactant could be the reason that caused the grain refining effect on the coating. With WS<sub>2</sub> particles being added and concentration increased from 2 g/L to 8 g/L in the electrolyte, the coating surface tends to coarsen with the appearance of more irregular shape nodules (Figure 5-26 (c) to (e)). As shown in Figure 5-27, the coating roughness of Au-Co/WS<sub>2</sub> composite coatings with WS<sub>2</sub> particle concentration of 2 g/L, 4 g/L and 8 g/L are 0.51 μm, 0.63 μm and 0.67 μm respectively. Such protruding structures on the coating surfaces were proved by EDS to be WS<sub>2</sub> clusters embedded into the coatings.

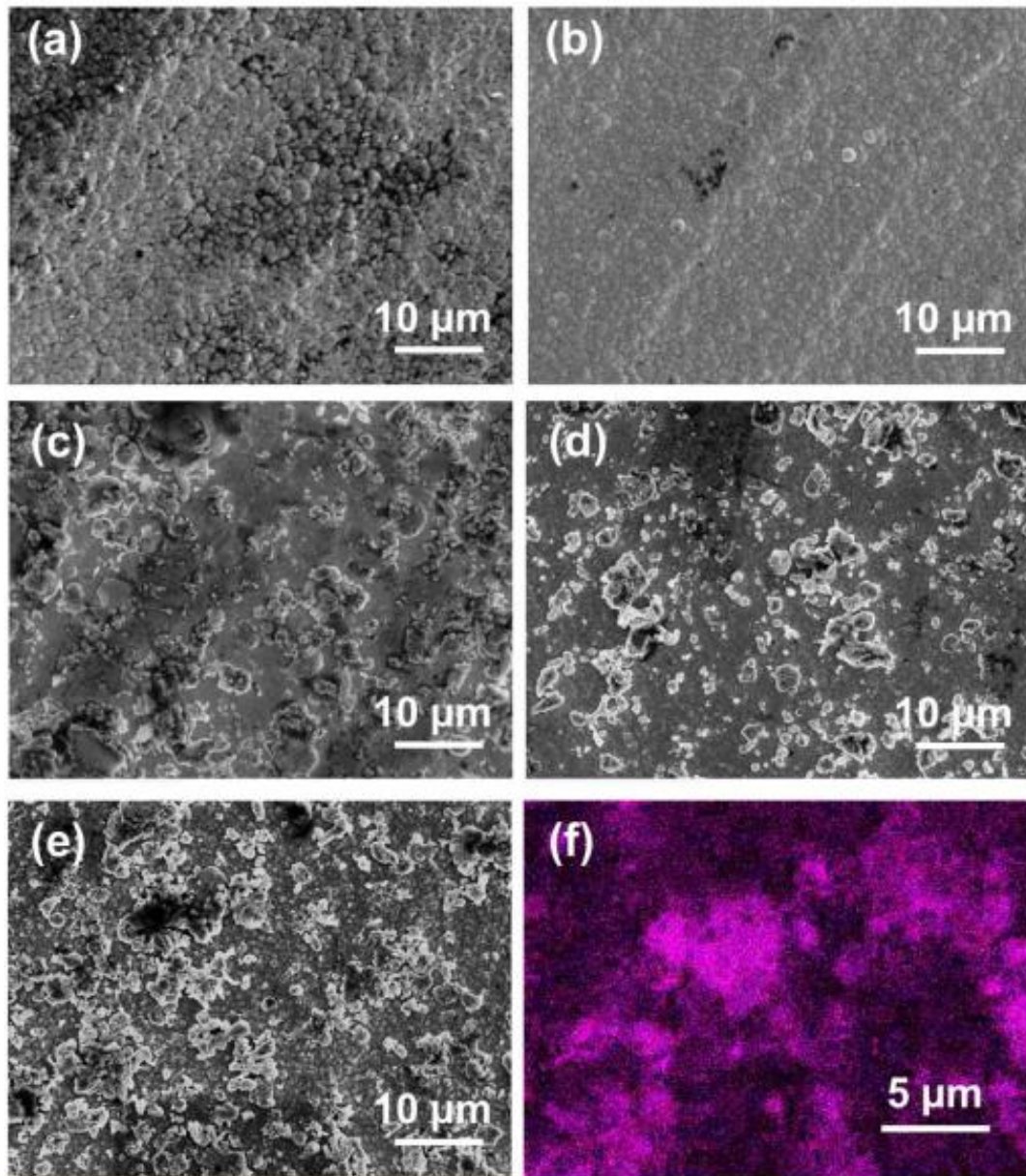


Figure 5-26 SEM and EDS images of the electroplated coatings from different electrolytes: (a). Au-Co, (b). Au-Co with 8 ml/L Triton X-100, (c). Au-Co with 8 ml/L Triton X-100 and 2g/L  $WS_2$ , (d). Au-Co with 8 ml/L Triton X-100 and 4g/L  $WS_2$ , (e). Au-Co with 8 ml/L Triton X-100 and 8g/L  $WS_2$ , (f). EDS mapping of W element on the Au-Co/ $WS_2$  coating from electrolyte with 8g/L  $WS_2$

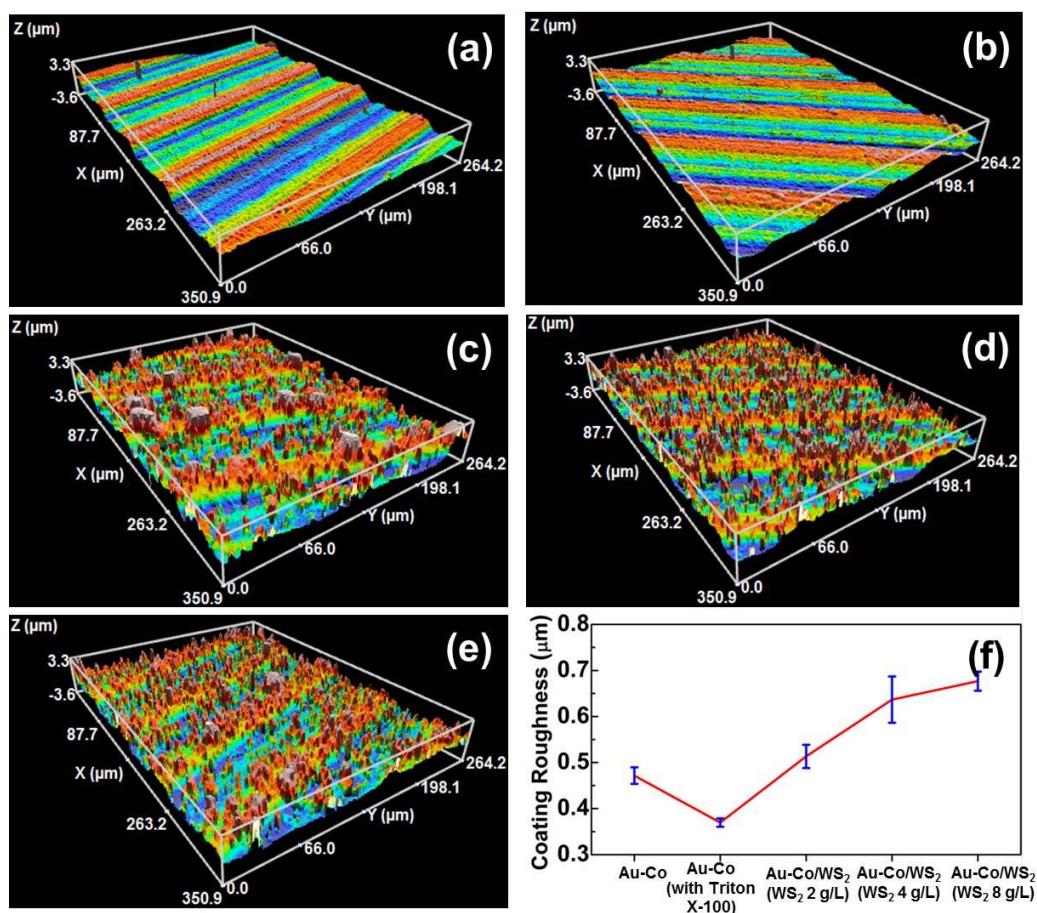


Figure 5-27 3-D surface topography measurements of coatings deposited from different electrolytes: (a). Au-Co, (b). Au-Co with 8 ml/L Triton X-100, (c). Au-Co with 8 ml/L Triton X-100 and 2 g/L WS<sub>2</sub>, (d). Au-Co with 8 ml/L Triton X-100 and 4 g/L WS<sub>2</sub>, (e). Au-Co with 8 ml/L Triton X-100 and 8 g/L WS<sub>2</sub>, (f). Results summary of coating roughness (arithmetic mean height)

Cross-sectional SEM images of Au-Co/WS<sub>2</sub> composite coating deposited from electrolyte with 8 g/L WS<sub>2</sub> are shown in Figure 5-28 (a) to Figure 5-28 (c). The results indicate that the Au-Co/WS<sub>2</sub> composite coating has good bonding interface with Ni interlayer and the Au-Co matrix coating has a dense structure. The WS<sub>2</sub> particles used in the composite coating deposition were exfoliated beforehand by probe sonication aiming for increasing their adsorption on the cathode surface so as to increase WS<sub>2</sub> content in the composite coating. The effectiveness of exfoliation was proved from the cross-sectional observation. The WS<sub>2</sub> particles in the composite coating show clearly a preferential orientation which is parallel to the coating surface. The thicknesses of the WS<sub>2</sub> particles are around 100 nm-150 nm. As WS<sub>2</sub> particles are semiconductors [208], during deposition, Au-Co nucleation not only occurred on Au-Co surface (initially Ni surface) but also on WS<sub>2</sub> particle surfaces. So, Au-Co growth followed the shape of the WS<sub>2</sub> particles; hence, WS<sub>2</sub> flakes were embedded into the Au-Co matrix compactly.

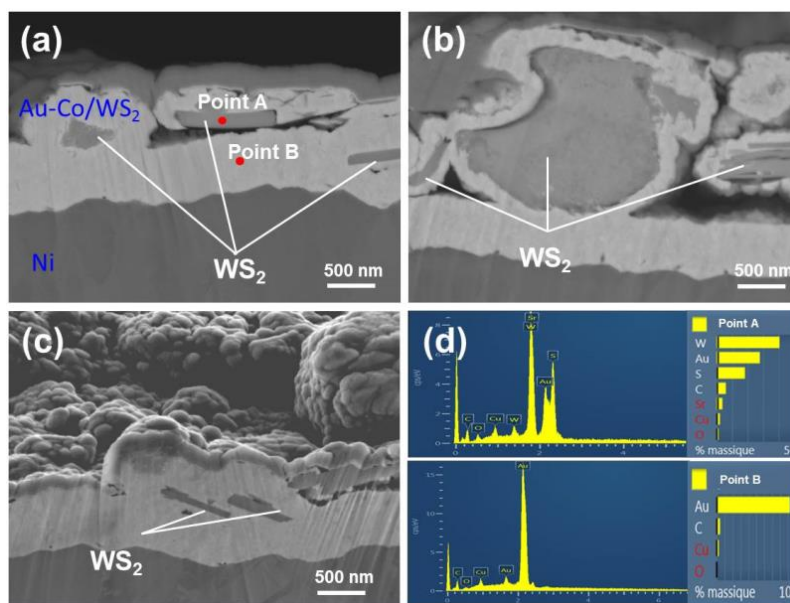


Figure 5-28 Cross-sectional SEM and EDS images of Au-Co/WS<sub>2</sub> coating deposited from electrolyte with 8 g/L WS<sub>2</sub>: (a). SEM image of position 1, (b). SEM image of position 2, (c). SEM image of position 3, (d). EDS point analyses at point A and B positions shown in (a).

### 5.2.2.3 Crystal structure

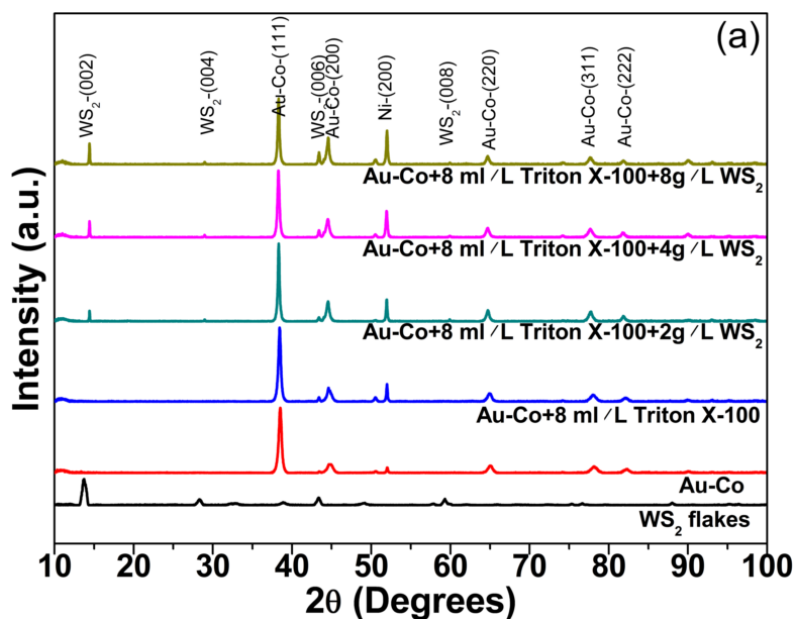


Figure 5-29 XRD patterns of the coatings

The influence of Triton X-100 and WS<sub>2</sub> particles on the coatings' crystal structure was investigated by XRD. Figure 5-29 shows that the WS<sub>2</sub> particles used for the composite coating study have crystal planes of (002), (004), (100), (101), (103), (006), (105), (110), (008), (112), (118), etc. All the above planes belong to hexagonal WS<sub>2</sub> [209]. However, in the Au-Co/WS<sub>2</sub> composite coatings, only (002), (004), (006) and (008) diffraction peaks of WS<sub>2</sub> are observed at 2θ of 14.3°, 28.9°, 44° and 59.9° respectively.

Here, only the {002} family of crystal planes were observed, which is another evidence showing that the WS<sub>2</sub> particles are regularly distributed in the coating (with {002} planes parallel to the coating surface). With the increase of WS<sub>2</sub> concentration, the intensities of WS<sub>2</sub> peaks increase accordingly. Crystallite sizes of Au-Co and Au-Co/WS<sub>2</sub> coatings were calculated through the Scherrer equation [51] from Au-Co (111) peaks and the results are shown in Figure 5-30. Grain size refinement of the matrix coating was reported with WS<sub>2</sub> particle added in the electrolyte [210], however here we found the crystallite size of the Au-Co matrix increases with the adding of WS<sub>2</sub> particles and the presence of Triton X-100. The reason for the crystallite size increase could be probably due to the inhabitation of Triton X-100 molecules which decreased the Au-Co nucleation. The Co content decrease could be another reason that caused Au-Co crystallite increase.

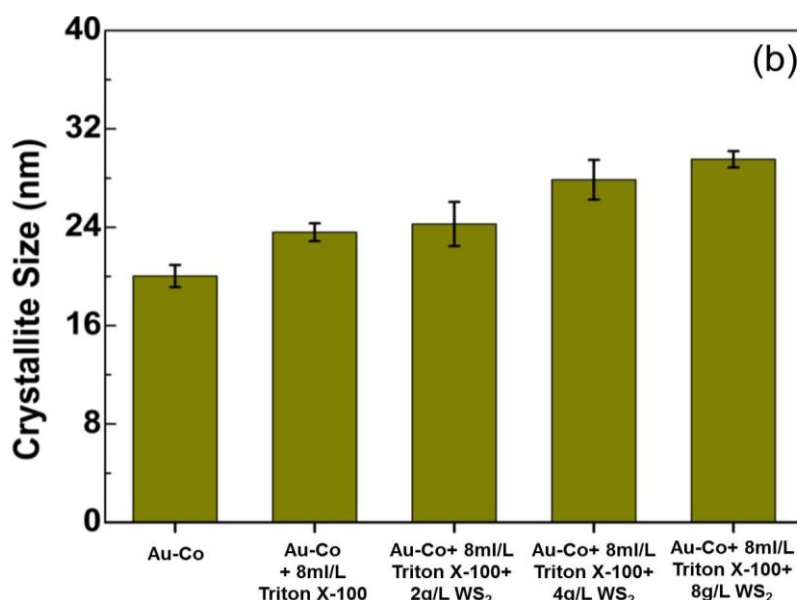


Figure 5-30 Crystallite size calculated from Au-Co (111) peaks

#### 5.2.2.4 Tribological performance

Coatings' tribological performance was evaluated on a ball-on-disc tribometer equipped with high vacuum pumping system against 316L ball ( $\varnothing=3$  mm). 8000 cycles' rotary sliding tests were performed under  $10^{-3}$  Pa with a linear speed of 6.3 cm/s and a normal contact force of 2 N.

As shown in Figure 5-31, for the Au-Co coating obtained from Au-Co electrolyte, the CoF started at 0.15 and increased slowly to 0.3 during the 8000 cycles sliding. With 8 ml/L Triton X-100 being added, the Au-Co coating obtained showed worse tribological performance and its maximum CoF reached 0.4. Based on the coating compositional study and crystallite size study, with the presence of Triton X-100 in the electrolyte, the Co content in the Au-Co alloy coating was suppressed and the

coating crystallite size increased. All these factors impair the hardness of the Au-Co coating and therefore induce a higher CoF. At the contrary, Au-Co/WS<sub>2</sub> composite coatings show very different CoFs compared with Au-Co coatings. For the Au-Co/WS<sub>2</sub> coating which was obtained from the electrolyte with 2 g/L WS<sub>2</sub>, there are three obvious transition periods observed on the CoF curve, which are induced by the transfer of WS<sub>2</sub> on the ball surface. At last, the CoF stabilized at 0.15. The CoFs of Au-Co/WS<sub>2</sub> coatings obtained from electrolytes with 4 g/L and 8 g/L WS<sub>2</sub> give similar CoF of around 0.05, which is a good results.

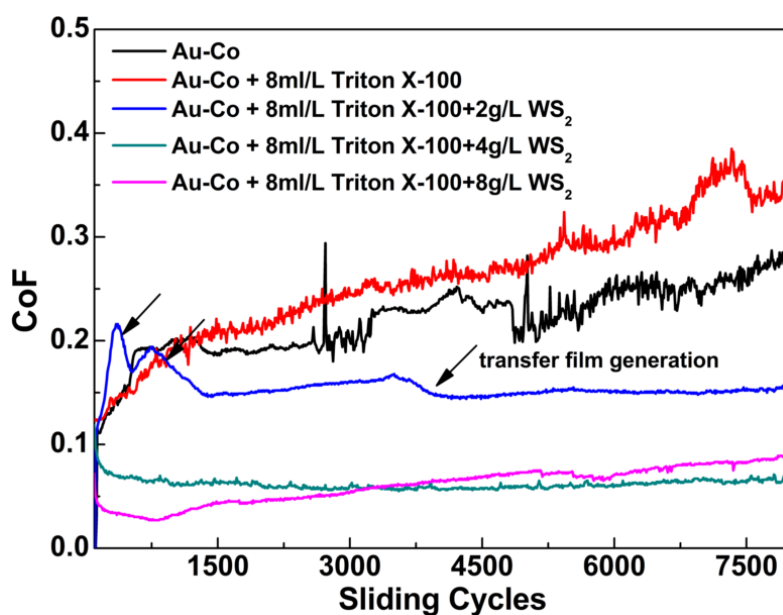


Figure 5-31 Coefficients of friction of Au-Co and Au-Co/WS<sub>2</sub> coatings

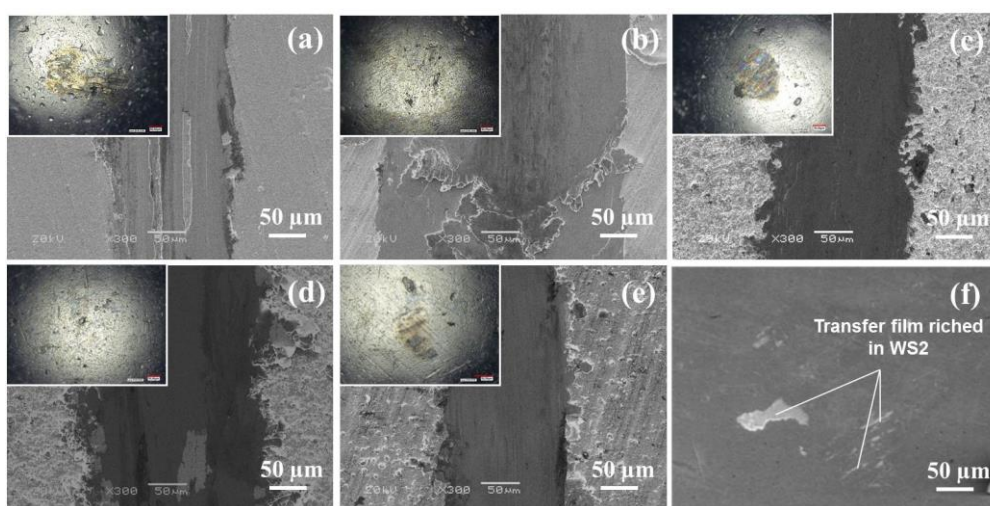


Figure 5-32 Worn surface morphologies of different coatings and their counterpart balls: (a). Au-Co, (b). Au-Co with 8 ml/L Triton X-100, (c). Au-Co with 8 ml/L Triton X-100 and 2 g/L WS<sub>2</sub>, (d). Au-Co with 8 ml/L Triton X-100 and 4 g/L WS<sub>2</sub>, (e). Au-Co with 8 ml/L Triton X-100 and 8 g/L WS<sub>2</sub>, (f). Transfer film of Au and WS<sub>2</sub> on the worn surface of the ball shown in (c)

As Figure 5-32 shows, during the tribological tests, the wear mainly occurred on the Au-Co and Au-Co/WS<sub>2</sub> coatings without obvious wear on the 316L balls. Adding Triton X-100 in the Au-Co electrolyte degraded the wear performance of the Au-Co coating significantly: the depth of wear track increased from 2 μm to 4 μm (Figure 5-33 (a)). This degradation is due to the decrease of Co content in the Au-Co coating which decreases the coating's hardness accordingly. As Figure 5-33 (b) shows, the wear rate of Au-Co (without Triton X-100 in the electrolyte) coating is  $2.3 \times 10^{-5} \text{ mm}^3/\text{N}\cdot\text{m}$ . With Triton X-100 being added, the wear rate increased to  $3.5 \times 10^{-5} \text{ mm}^3/\text{N}\cdot\text{m}$ . When WS<sub>2</sub> is contained in the coating, Au film with WS<sub>2</sub> is transferred from the coating to the ball surface during adhesive wear (Figure 5-32 (f)).

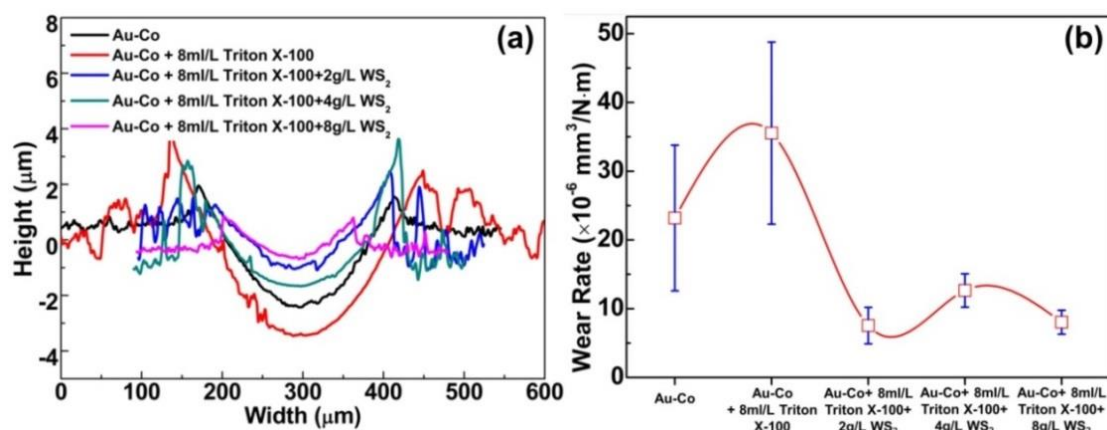


Figure 5-33 2-D profiles of wear tracks and wear rates of different coatings

SEM observations were carried out on the wear track of the Au-Co/WS<sub>2</sub> coating to understand the lubricating mechanisms. As shown in Figure 5-34, relative smooth wear track was observed after the tribological test. A 300 nm tribolayer was generated on the surface of the coating layer, which is the mixing of Au and WS<sub>2</sub> fine flakes (Figure 5-35). The configuration of WS<sub>2</sub> in the tribolayer is very different from the original WS<sub>2</sub> particles imbedded in the Au-Co/WS<sub>2</sub> coating. It can be inferred that, during sliding, with the wear of the coating matrix, the ball got into contact with the WS<sub>2</sub> particle and sheared the WS<sub>2</sub> into small flakes. The wear debris of Au-Co matrix mixed with the WS<sub>2</sub> flakes and generated a WS<sub>2</sub>-rich tribolayer on the coating surface in the wear track. This tribolayer transferred between the ball surface and the coating surface by shearing the weak interlayer bonding in WS<sub>2</sub>. As a result, the sliding was lubricated and a low CoF obtained. Due to the presence of this tribolayer, the coating was protected from further wear, thus the wear rate of the composite coating was minimized efficiently. With WS<sub>2</sub> lubricating, the wear depths and wear rate are minimized efficiently. The Au-Co/WS<sub>2</sub> composite coating has wear rate of  $8 \times 10^{-6} \text{ mm}^3/\text{N}\cdot\text{m}$ , which is only 1/3 of the Au-Co coating's wear rate.

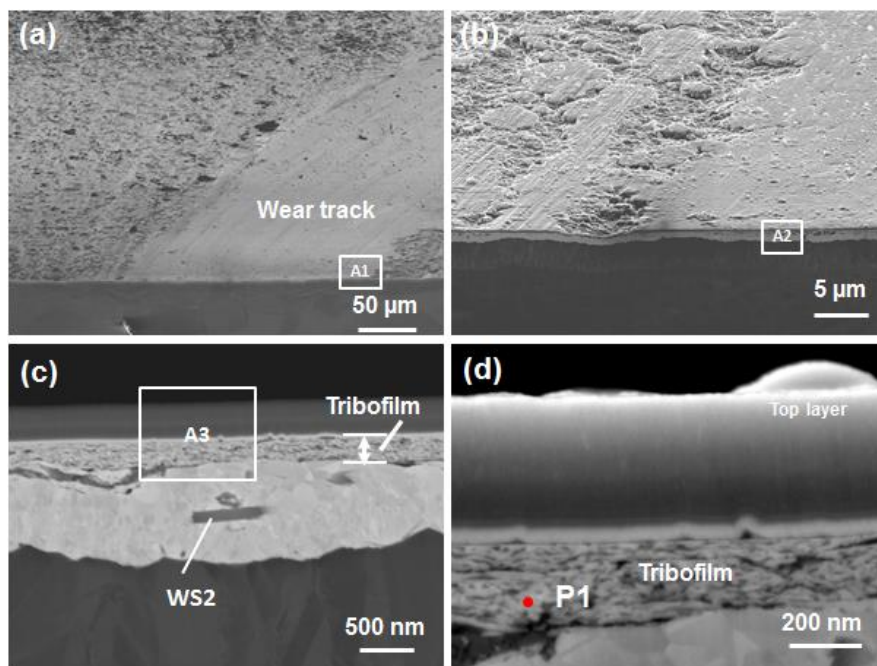


Figure 5-34 SEM images in the wear track of Au-Co/WS<sub>2</sub> (from electrolyte with 8g/L WS<sub>2</sub>): (a). Overview of wear track, (b, c, d). Detail views in the area of A1, A2 and A3. (There is a 300 nm thick top layer observed, which is generated during the cross-sectional sample preparation by using cross-polisher. The provement is shown in Appendix C.)

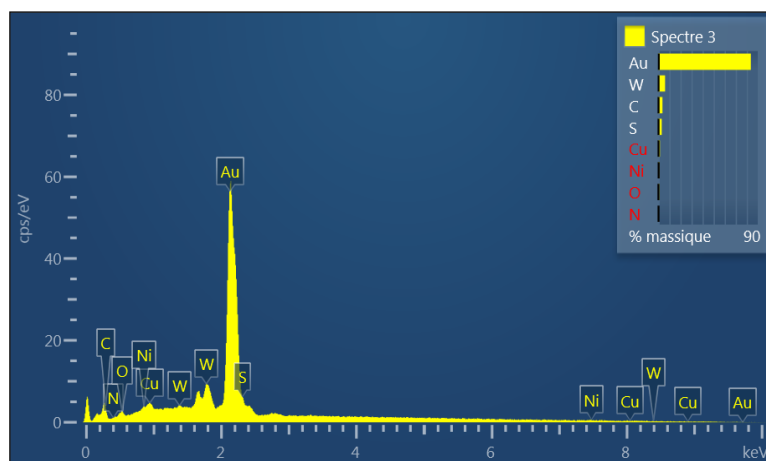


Figure 5-35 EDS results at point P1 shown in Figure 5-34 (d)

### 5.2.2.5 Summary

The feasibility of achieving WS<sub>2</sub> composite coatings with Au alloy matrix was investigated in this section. Au-Co commercial electrolyte was used to carry out the study, even though Co is a limited element for nuclear application. To improve the WS<sub>2</sub> particles dispersion in the Au-Co electrolyte, non-ionic surfactant Triton X-100 was applied and its function in improving the electrolyte stability was proved. With the assistance of Triton X-100, Au-Co/WS<sub>2</sub> composite coatings with different WS<sub>2</sub>

contents were successfully deposited. Interestingly, by adding Triton X-100 and  $WS_2$  particles in the electrolyte, the Co content in the Au-Co/ $WS_2$  composite coating is significantly suppressed to zero. With  $WS_2$  flakes compounded, the Au-Co/ $WS_2$  coatings present much lower CoFs compared with Au-Co coating and the minimum CoF is around 0.05. The Au-Co/ $WS_2$  coatings' wear rates are also proved to be significantly lower than the Au-Co coating. So,  $WS_2$  was proved to be a very efficient solid lubricant under ITER relevant environment. Actually, in the Au-Co/ $WS_2$  composite coating, the Co content is much lower than the ITER requirement (0.2 wt.%), which is a good point for ITER application.

### 5.3 Tribological performance comparison of different coatings

The tribological performance of the developed Au-Ni/a-C and Au-Co/ $WS_2$  coatings were evaluated in the vacuum tribometer with different test parameters due to the constraint of the sample size. So, the test results obtained can't be compared directly. In order to compare the tribological performance of the two self-lubricating coatings with the commercial Au-Ni coating, tribological tests with the same parameters were performed on a commercial tribometer with ball-on-disk configuration in  $N_2$  atmosphere (to mimic vacuum condition as near as possible). The ball is made of 100Cr6 with a 6 mm diameter. 8000 cycles' rotary sliding tests were performed in  $N_2$  atmosphere with a linear speed of 8.4 cm/s and a normal contact force of 8 N.

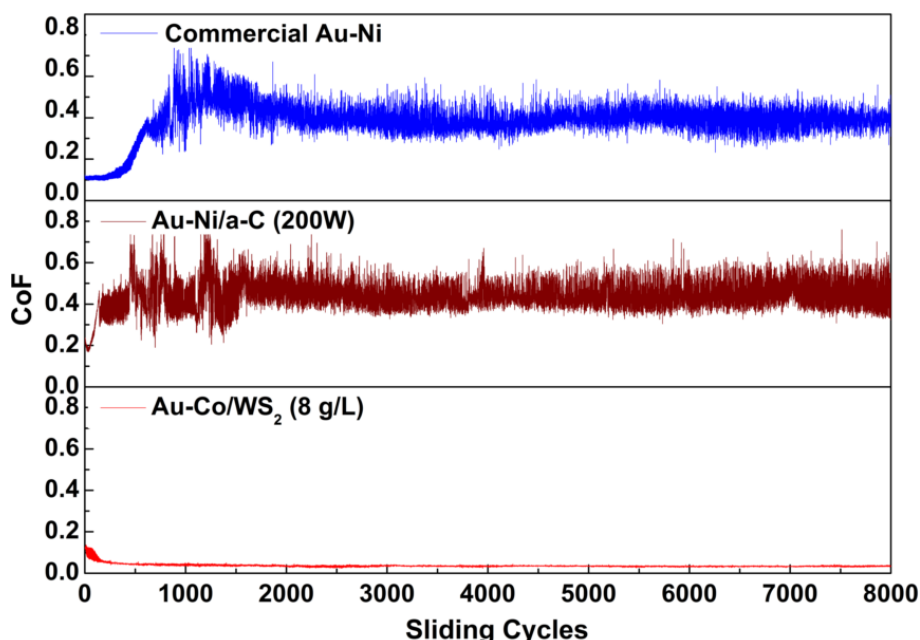


Figure 5-36 CoF of different coatings in  $N_2$  atmosphere

As Figure 5-36 shows, for the Au-Ni/a-C (200 W) coating, the CoF started at 0.2 and increased fast after ~200 cycles to 0.4. For the commercial Au-Ni coating, similar phenomenon is observed but the transition time of the CoF is delayed to 500 cycles.

The Au-Co/WS<sub>2</sub> (deposited from electrolyte with 8 g/L WS<sub>2</sub>) showed the best tribological performance with a constant CoF around 0.04.

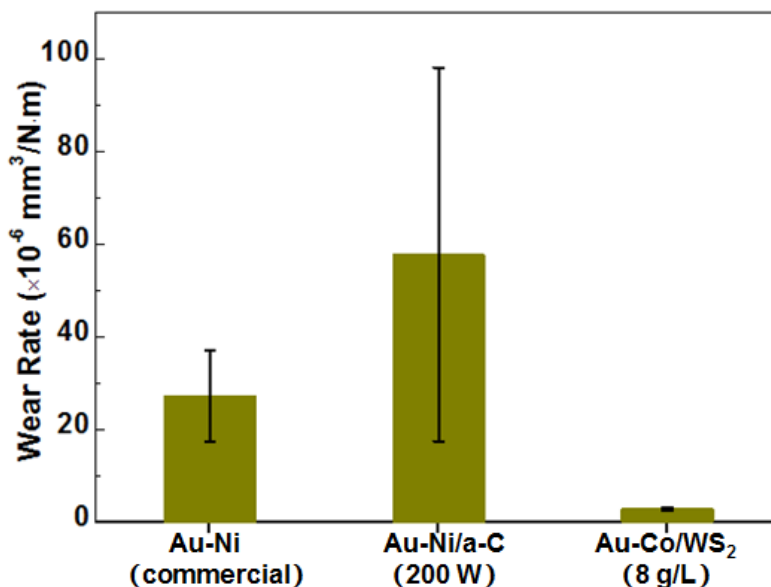


Figure 5-37 Wear rate of different coatings in N<sub>2</sub> atmosphere

The wear rates of the coating were shown in Figure 5-37, the wear rate of the Au-Ni commercial coating is  $2.7 \times 10^{-5} \text{ mm}^3/\text{N}\cdot\text{m}$ . The wear rate of Au-Ni/a-C (200 W) is  $5.7 \times 10^{-5} \text{ mm}^3/\text{N}\cdot\text{m}$ . The Au-Co/WS<sub>2</sub> shows very low wear rate and the value is  $2.9 \times 10^{-6} \text{ mm}^3/\text{N}\cdot\text{m}$ .

## 5.4 Discussion

In this chapter, two self-lubricating composite coatings were developed by magnetron sputtering and electroplating and their tribological performances were evaluated.

- Au-Ni/a-C composite coating

There are two forms of C atom in the Au-Ni/a-C composite coatings, alloying in Au-Ni crystal lattice or accumulating as a-C clusters. Especially for the C atoms that were alloyed in the Au-Ni lattice, a significant solution hardening effect to the Au-Ni matrix was observed. During tribological tests, the generation of C lubricating film was observed in the wear track. However, as C material can't work efficiently under high vacuum condition, the CoF and wear rate of the Au-Ni/a-C composite coating are similar to the Au-Ni coating. In addition, the electrical resistivity of the composite coating is about 3 times higher than the pure Au coating. So, if the Au-Ni/a-C composite coating can't be proved to be more thermal stable (hardness, diffusion resistance) than the Au-Ni coating in the future study, it's not suitable for the application in the ITER ICRH RF sliding contact.

- Au-Co/WS<sub>2</sub> composite coating

This coating was proved to have excellent tribological performance. The Au-Co/WS<sub>2</sub> coatings that developed were verified to have lower Co contents than the ITER limit. However, suppressing the Co content impairs the mechanical performance of Au-Co matrix. As Ni is a compatible element for nuclear application, the achievement of Au-Ni/WS<sub>2</sub> composite coating, which has high Ni composition, could achieve even better tribological performance compared with the Au-Co/WS<sub>2</sub> developed in this study. Au-Ni/WS<sub>2</sub> composite coating is thus very promising and could be developed in future work. Besides, WS<sub>2</sub> is a semiconducting material. Thus, the generation of WS<sub>2</sub> tribofilm on the wear track, which serves as solid lubrication, can impair the electrical performance of the contact. The effects of compounding WS<sub>2</sub> in the coating to the coating's electrical performance needs to be investigated in the future.



## Chapter 6 Conclusions and prospect

### 6.1 Conclusions of this thesis

ICRH system is one of the auxiliary heating systems for the ITER tokamak, which can supply a total heating power of 20 MW to the plasma. RF sliding contacts are embedded in the ITER ICRH antenna to absorb thermal expansion and to allow the assembly and maintenance of the ICRH antenna by remote handling, while insuring the RF current continuity. The development of sliding RF contacts is a challenge, as the foreseen maximum steady-state operating current density is 4.6 kA/m in the ITER vacuum environment. In addition, the 250°C baking operation and the neutron bombardment further constraints the material selection of the RF sliding contacts.

The aims of this thesis are to understand the failure mechanisms of the RF sliding contact under the specific ITER operating conditions and to find suitable materials for design and manufacturing of satisfactory contacts. The main contributions developed in this thesis are:

- The analysis of the failure mechanisms of ITER RF sliding contacts based on a prototype of the Multi-Contact<sup>®</sup> LA-CUT<sup>®</sup> product. A test campaign was carried out on the CEA T-Resonator testbed. An RF current of 1.9 kA at 62 MHz was achieved during 300 s, but burn failure happened with higher current. From a FEM model and by performing electrical-thermal and thermal-hydraulic analyses, it was found that the steady-state operating temperature of the RF contact louver linearly increases with the contact resistance ( $R_c$ ) increase. In order to maintain the temperature of the RF contact louver below 250°C, it has been calculated that the  $R_c$  should be lower than 6.5 m $\Omega$ /louver. This parameter drives the choice of the materials to be used to reduce the operational contact louver temperature. If the RF conductor is made of 316L stainless steel, increasing cooling parameters (such as mass flow rate and velocity) has almost no effect to improve the cooling performance of the contact louver. Actively cooled CuCrZr is strongly suggested as base material of the RF contacts support.
- The development of a multi-functional tribometer which can mimic ITER-relevant vacuum and temperature conditions for material evaluation for the ITER RF sliding contact. Although some commercial vacuum tribometers which could even perform contact resistances exist, no tribometer were found having in addition a sample heating capability. Moreover, any commercial vacuum tribometer needs to be opened to adjust the normal contact force, which is time-consuming and not compatible with the time allowed for the material study

in this thesis, as we needed to adjust the normal contact force frequently. Thus, a multi-functional tribometer which can mimic the ITER environment conditions and be operated conveniently and reliably was developed. This tribometer then been used to characterize the friction and contact resistance properties of various samples of materials. A French innovation patent concerning the loading system has been submitted and authorized.

- The feasibility of applying Au-Ni, Ag, Ag-Sb and Rh as functional coatings for ITER RF sliding contacts have been evaluated from material characterizations. The base material of the RF contact louvers was selected as CuCrZr. The supporting conductor can be made of 316L or CuCrZr. From FEM analyses, the Rc of one louver should be lower than 6.5 mΩ. In order to improve the electrical and tribological performances of the sliding contact, the application of functional coatings have been found to be mandatory. From the commonly used material in the electrical industry, the specific ITER environment conditions of vacuum and temperature lead to the choice of Au-Ni, Ag, Ag-Sb and Rh coatings. Before this thesis, no systematic study and evaluation of common functional coatings under ITER relevant conditions have been made. During this thesis, the above functional coatings were electrodeposited on CuCrZr and 316L substrates and they were deeply characterized regarding their diffusion phenomena with their substrates or with another coating after 250°C thermal aging process. In addition, thermal aging effects on the coatings' morphology, hardness, adhesion performance, crystal structure, electrical and tribological performances were evaluated. The CoF and Rc values have also been measured. All these results provide a good reference for the future studies of ITER RF sliding contacts or other projects.
- The development of Au-Ni/a-C and Au-Co/WS<sub>2</sub> composite coatings and their application as electrical functional coatings in ITER has been investigated.
  - Although Au-Ni and Au-Co are commonly used coatings on electrical and electronic industries, their composite coatings were not deeply considered in the fusion research field. In their lifetime, ITER ICRH RF sliding contacts will face severe adhesive wear during operation and applying solid lubricants on them is very promising. Satisfactory Au-Ni/a-C composite coatings were deposited by magnetron sputtering. A significant hardness improvement has been demonstrated in comparison with Au-Ni coating. However, due to the low lubricating efficiency of carbon materials in vacuum, these composite coatings do not have advantages in minimizing CoF and wear rate compared with Au-Ni coating.
  - An Au-Co/WS<sub>2</sub> electroplating composite coatings process has been developed

and used. A technical breakthrough was made in the  $WS_2$  particle dispersion in aqueous cyanide electrolyte. With the assistance of Triton X-100 surfactant, Au-Co/ $WS_2$  composite coatings were successfully deposited on CuCrZr plates. The coating's mechanical and tribological properties have been assessed. Their high efficiency in minimizing CoF and wear rate under ITER conditions were proved.

## 6.2 Future work

- For RF contact modelling: although a FEM model was created and simulation work was performed on it, only few louvers were considered in this model. The heat loads induced by the contact resistance and bulk resistance were calculated from analytical formulas and then applied on the model as surface heat fluxes. Moreover, two assumptions have been made for the simulation: i) the RF current is uniformly distributed in each louver and ii) no current flows through the stainless steel spring. However, reality is more complex than that. From ANSYS HFSS simulation, more realistic RF current distribution has been obtained and could be used to calculate the heat generation in a RF-thermal modelling in a self-integrated way. A full (or partial) size RF sliding contact model could be in principle be modelled in HFSS to carry out the RF-thermal calculation. However, this workflow would still present a limitation, in the sense that it is not yet possible to setup contact resistances in the RF modelling, which actually exist between the contacts and their supporting and facing materials.
- For material studies: in this thesis, the Au-Ni/a-C composite coating was proved to have no advantages compared with Au-Ni coating in minimizing CoF and wear rate. However, the C atoms in alloyed in the Au-Ni lattice may improve the coating's thermal stability. So, thermal aging investigation of the Au-Ni/a-C composite coating is still interesting to be performed in the future. Concerning Au-Co/ $WS_2$  composite coating, its excellent tribological performance was demonstrated. However, the effects of  $WS_2$  tribofilm generated on the wear track on the electrical performance ( $R_c$ ) were not studied. Besides, as Co content is strictly controlled in ITER, replacing Co by Ni in a Au-Ni/ $WS_2$  composite coating through electroplating is very promising.
- For the engineering design of the new RF sliding contact prototype: in this thesis, a lot of experience in mechanical structure and materials on RF sliding contact were obtained. Based on these experiences, new RF sliding contacts design have been proposed and it would be important to develop and test them on the CEA T-resonator testbed. Among the new proposed RF sliding contacts (not detailed in this thesis), RF contact louvers made of CuCrZr and brazed on the RF conductor

(made of CuCrZr) would improve the cooling efficiency. Thick Ag coating (~100  $\mu\text{m}$ ) is proposed to be applied on the surfaces of these louvers. The counter RF conductor should be made of 316L with a 4  $\mu\text{m}$  Rh coating electrodeposited to minimizing the  $R_c$  and to improve the conductor's wear resistance. For thermal efficiency, a CuCrZr counter RF conductor is a better option. It however requires developing a more satisfactory Rh-coating process on the CuCrZr, for instance by replacing the gold flash layer by a nickel layer.

## References

- [1] H.H. Rogner, World outlook for nuclear power, *Energy Strategy Reviews* 1 (2013) 291-295.
- [2] V.G. Kiptily, On the Core Deuterium-Tritium Fuel Ratio and Temperature Measurements in DEMO, *Nuclear Fusion* 55 (2014) 023008.
- [3] M. Kikuchi, K. Lackner, M.Q. Tran, *Fusion physics*, IAEA: Vienna, 2012.
- [4] P. Norajitra, Divertor development for a future fusion power plant, PhD thesis, KIT, 2014.
- [5] Y.T. Song, S.T. Wu, J.G. Li, B.N. Wan, Y.X. Wan, P. Fu, et al., Concept design of CFETR Tokamak machine, *IEEE Transactions on Plasma Science* 42 (2014) 503-509.
- [6] S. Ciattaglia, G. Federici, L. Barucca, A. Lampasi, S. Minucci, I. Moscato, The European DEMO fusion reactor: Design status and challenges from balance of plant point of view, *Proc. IEEEIC / I&CPS EUROPE*, Milan, 2017.
- [7] Y. Seki, Fusion reactor design and technology program in Japan, *Fusion Engineering and Design* 25 (1994) 49-66.
- [8] <http://www.ccfе.ac.uk/To>.
- [9] M.F. Bashir, Drift Effects on Plasma Waves, PhD thesis, GC University Lahore, 2014.
- [10] K. Ikeda, ITER on the road to fusion energy, *Nuclear Fusion* 50 (2009) 014002.
- [11] N. Holtkamp, An overview of the ITER project, *Fusion Engineering and Design* 82 (2007) 427-434.
- [12] J. Matějčiček, Materials for Fusion Applications, *Acta Polytechnica* 53 (2013) 197-212.
- [13] P. Lamalle, B. Beaumont, F. Kazarian, T. Gassmann, G. Agarici, P. Ajesh, et al., Status of the ITER Ion Cyclotron H&CD system, *Fusion Engineering and Design* 88 (2013) 517-520.
- [14] A. Borthwick, G. Agarici, A. Davis, P. Dumortier, F. Durodie, J. Fanthome, et al., Mechanical design features and challenges for the ITER ICRH antenna, *Fusion Engineering and Design* 84 (2009) 493-496.
- [15] P. Lamalle, B. Beaumont, F. Kazarian, T. Gassmann, G. Agarici, P. Ajesh, et al., Status of the ITER Ion Cyclotron H&CD system, *Fusion Engineering and Design* 88 (2013) 517-520.
- [16] D. Swain, R. Goulding, ITER ion cyclotron system: Overview and plans, *Fusion Engineering and Design* 82 (2007) 603-609.

- [17] F. Ferlay, J. Bernard, C. Dechelle, L. Doceul, D. Keller, J. Wagrez, et al., First analysis of remote handling maintenance procedure in the hot cell for the ITER ICH&CD antenna–RVTL replacement, *Fusion Engineering and Design* 88 (2013) 1924-1928.
- [18] M. Braunovic, N.K. Myshkin, V.V. Konchits, *Electrical contacts: fundamentals, applications and technology*, CRC press: Boca Raton, 2006.
- [19] <http://ec.staubli.com/products/productline/3>.
- [20] D. Hancock, M. Nightingale, R. Bamber, N. Dalton, F. Durodie, M. Firdaouss, et al., Design of the ITER ICRF Antenna, *AIP Conference Proceedings* 57 (2011) 57-60.
- [21] D. Hartmann, Fusion Diacode, IC RF Generator, IC Power Supply and IC Test Facility: Design, Support to the Industrial Development and Preparation of the Technical Specifications, IPP Technical Report, TW3-THHI-GTFDS1, Greifswald, 2004.
- [22] K. Vulliez, JET-EP ICRH antenna finger contact tests, CEA Technical Report, CH/NTT-2003.015, Cadarache, 2003.
- [23] F. Durodié, JET-EP ICRF Description Document, *AIP Conference Proceedings* 595 (2001) 122-125.
- [24] K. Vulliez, G. Lombard, C.H. Harris, Test of Multilam® LA-Cut/0.25 RF sliding contact, CEA Technical Report, CH/NTT-2009.DRAFT, Cadarache, 2009.
- [25] M. Schlesinger, M. Paunovic, *Modern electroplating*, John Wiley & Sons: New Jersey, 2011.
- [26] M. Guan, E. Podlaha, Electrodeposition of AuCo alloys and multilayers, *Journal of Applied Electrochemistry* 37 (2007) 549-555.
- [27] G. Saravanan, Studies on the electrodeposition of chromium and its alloy from Ecofriendly Cr (III) Electrolytes and room temperature ionic liquids-Rtil, PhD thesis, Central Electrochemical Research Institute, 2013.
- [28] I. Mizushima, Electrodeposition of Ni-W Alloy and Characterization of Microstructure and Properties of the Deposits, PhD Thesis, Technical University of Denmark, 2006.
- [29] S. Kumar, S. Pande, P. Verma, Factor Effecting Electro-Deposition Process, *International Journal of Current Engineering and Technology* 5 (2015) 700-703.
- [30] S. Dutta, M. Imran, P. Kumar, R. Pal, P. Datta, R. Chatterjee, Comparison of etch characteristics of KOH, TMAH and EDP for bulk micromachining of silicon (110), *Microsystem Technologies* 17 (2011) 1621.
- [31] D.-M. Tsai, B.-T. Lin, Defect detection of gold-plated surfaces on PCBs using

entropy measures, *The International Journal of Advanced Manufacturing Technology* 20 (2002) 420-428.

[32] M. Buffière, S. Harel, C. Guillot - Deudon, L. Arzel, N. Barreau, J. Kessler, Effect of the chemical composition of co - sputtered Zn (O, S) buffer layers on Cu (In, Ga) Se<sub>2</sub> solar cell performance, *Physica Status Solidi (a)* 212 (2015) 282-290.

[33] Y.H. Joung, H.I. Kang, J.H. Kim, H.S. Lee, J. Lee, W.S. Choi, SiC formation for a solar cell passivation layer using an RF magnetron co-sputtering system, *Nanoscale Research Letters* 7 (2012) 22.

[34] <https://www.zygo.com/>.

[35] <https://www.azom.com/>.

[36] M. Matveeva, Influence of the surface composition and morphology on the reflectivity of diagnostic mirrors in a fusion reactor, PhD thesis, Forschungszentrum Jülich, 2015.

[37] <http://www.microscopy.ethz.ch/sem.h>.

[38] J. Burghardt, G. Buess, Transanal endoscopic microsurgery (TEM): a new technique and development during a time period of 20 years, *Surgical Technology International* 14 (2005) 131-137.

[39] J. Tomastik, R. Ctvrtlik, Nanoscratch test—A tool for evaluation of cohesive and adhesive properties of thin films and coatings, *EPJ Web of Conferences* 48 (2013) 00027.

[40] F. Attar, T. Johannesson, Adhesion evaluation of thin ceramic coatings on tool steel using the scratch testing technique, *Surface and Coatings Technology* 78 (1996) 87-102.

[41] S. Bull, Failure modes in scratch adhesion testing, *Surface and Coatings Technology* 50 (1991) 25-32.

[42] Y. Xie, H.M. Hawthorne, A model for compressive coating stresses in the scratch adhesion test, *Surface and Coatings Technology* 141 (2001) 15-25.

[43] D. Yang, Examining Interfacial Adhesion of Biomedical Coatings Through Scratch Testing and Microanalysis, *Plant & Coating Industry, PCI China*, 2015.

[44] D. Lucca, K. Herrmann, M. Klopstein, Nanoindentation: Measuring methods and applications, *CIRP Annals-Manufacturing Technology* 59 (2010) 803-819.

[45] C.A. Schuh, Nanoindentation studies of materials, *Materials Today* 9 (2006) 32-40.

[46] W.C. Oliver, G.M. Pharr, An improved technique for determining hardness and elastic modulus using load and displacement sensing indentation experiments, *Journal*

- of Materials Research 7 (1992) 1564-1583.
- [47] A.A. Bunaciu, E.G. UdriȘtioiu, H.Y. Aboul-Enein, X-ray diffraction: instrumentation and applications, *Critical Reviews in Analytical Chemistry* 45 (2015) 289-299.
- [48] R. Gou, Y. Zhang, X. Xu, L. Sun, Y. Yang, Residual stress measurement of new and in-service X70 pipelines by X-ray diffraction method, *NDT & E International* 44 (2011) 387-393.
- [49] M. Sowinska, In-operando hard X-ray photoelectron spectroscopy study on the resistive switching physics of HfO<sub>2</sub>-based RRAM, Master thesis, BTU Cottbus-Senftenberg, 2014.
- [50] L. Marot, G. De Temmerman, V. Thommen, D. Mathys, P. Oelhafen, Characterization of magnetron sputtered rhodium films for reflective coatings, *Surface and Coatings Technology* 202 (2008) 2837-2843.
- [51] A. Monshi, M.R. Foroughi, M.R. Monshi, Modified Scherrer equation to estimate more accurately nano-crystallite size using XRD, *World Journal of Nano Science and Engineering* 2 (2012) 154-160.
- [52] V. Mote, Y. Purushotham, B. Dole, Williamson-Hall analysis in estimation of lattice strain in nanometer-sized ZnO particles, *Journal of Theoretical and Applied Physics* 6 (2012) 1-8.
- [53] I. Johansson, P. Somasundaran, *Handbook for Cleaning/Decontamination of Surfaces* Elsevier Science, 2007.
- [54] <http://www.rowbo.info/XPS.html>.
- [55] X. Sun, Investigation of diamond coatings on iron based materials by microwave plasma chemical vapor deposition, Master thesis, University of Saskatchewan, 2014.
- [56] C. Bolsinger, M. Zorn, K.P. Birke, Electrical contact resistance measurements of clamped battery cell connectors for cylindrical 18650 battery cells, *Journal of Energy Storage* 12 (2017) 29-36.
- [57] M. Kim, J.W. Lim, Electrical contact resistance between anode and cathode bipolar plates with respect to surface conditions, *Composite Structures* 189 (2018) 79-86.
- [58] D.M. Pozar, *Microwave engineering*, John Wiley & Sons: New Jersey, 2009.
- [59] J.D. Lavers, R.S. Timsit, Constriction resistance at high signal frequencies, *IEEE Transactions on Components and Packaging Technologies* 25 (2002) 446-452.
- [60] R.S. Timsit, A. Luttgen, Temperature distribution in an ohmic-heated electrical contact at high signal frequencies, *Applied Physics Letters* 108 (2016) 121603.

- [61] K. Miyoshi, Fundamental considerations in adhesion, friction and wear for ceramic—metal contacts, *Wear* 141 (1990) 35-44.
- [62] G. Stachowiak, A.W. Batchelor, *Engineering tribology*, Butterworth-Heinemann: Oxford, 2013.
- [63] F.P. Bowden, F.P. Bowden, D. Tabor, *The friction and lubrication of solids*, Oxford university press: Oxford, 2001.
- [64] K. Kato, Classification of wear mechanisms/models, *Proceedings of the Institution of Mechanical Engineers, Part J: Journal of Engineering Tribology* 216 (2002) 349-355.
- [65] K. Holmberg, H. Ronkainen, A. Laukkanen, K. Wallin, Friction and wear of coated surfaces—scales, modelling and simulation of tribomechanisms, *Surface and Coatings Technology* 202 (2007) 1034-1049.
- [66] J. Archard, Contact and rubbing of flat surfaces, *Journal of Applied Physics* 24 (1953) 981-988.
- [67] J. Denape, Third body concept and wear particle behavior in dry friction sliding conditions, *Tribological Aspects in Modern Aircraft Industry* 640 (2014) 1-12.
- [68] W.O. Akande, Y. Cao, N. Yao, W. Soboyejo, Adhesion and the cold welding of gold-silver thin films, *Journal of Applied Physics* 107 (2010) 043519.
- [69] <http://www.substech.com/>.
- [70] A. Merstallinger, M. Sales, E. Semerad, B. Dunn, Assessment of cold welding between separable contact surfaces due to impact and fretting under vacuum, *ESA Scientific & Technical Memoranda* 279 (2009).
- [71] A. Harsha, U. Tewari, Two-body and three-body abrasive wear behaviour of polyaryletherketone composites, *Polymer Testing* 22 (2003) 403-418.
- [72] <http://cement.flsmidth.com/>.
- [73] B. Bharat, *Fundamentals of tribology and bridging the gap between the macro-and micro/nanoscales*, Springer: Netherlands, 2001.
- [74] I. Kovaříková, B. Szewczyková, P. Blaškoviš, E. Hodúlová, E. Lechovič, Study and characteristic of abrasive wear mechanisms, *Materials Science and Technology* 1 (2009) 1-8.
- [75] D. Berman, A. Erdemir, A.V. Sumant, Graphene as a protective coating and superior lubricant for electrical contacts, *Applied Physics Letters* 105 (2014) 231907.
- [76] M. Cardinal, P. Castro, J. Baxi, H. Liang, F. Williams, Characterization and frictional behavior of nanostructured Ni–W–MoS<sub>2</sub> composite coatings, *Surface and Coatings Technology* 204 (2009) 85-90.

- [77] K. Wong, X. Lu, J. Cotter, D. Eadie, P. Wong, K. Mitchell, Surface and friction characterization of MoS<sub>2</sub> and WS<sub>2</sub> third body thin films under simulated wheel/rail rolling–sliding contact, *Wear* 264 (2008) 526-534.
- [78] Z. He, W. Que, Molybdenum disulfide nanomaterials: structures, properties, synthesis and recent progress on hydrogen evolution reaction, *Applied Materials Today* 3 (2016) 23-56.
- [79] <http://www.medcoat.us/dlc-coatings/>.
- [80] Y. Yang, M. Yan, Y. Zhang, C. Zhang, X. Wang, Self-lubricating and anti-corrosion amorphous carbon/Fe<sub>3</sub>C composite coating on M50NiL steel by low temperature plasma carburizing, *Surface and Coatings Technology* 304 (2016) 142-149.
- [81] S. Dub, Y. Pauleau, F. Thiery, Mechanical properties of nanostructured copper-hydrogenated amorphous carbon composite films studied by nanoindentation, *Surface and Coatings Technology* 180 (2004) 551-555.
- [82] W. Gulbiński, S. Mathur, H. Shen, T. Suszko, A. Gilewicz, B. Warcholiński, Evaluation of phase, composition, microstructure and properties in TiC/aC: H thin films deposited by magnetron sputtering, *Applied Surface Science* 239 (2005) 302-310.
- [83] J. Sánchez-López, D. Martínez-Martínez, C. Lopez-Cartes, A. Fernández, Tribological behaviour of titanium carbide/amorphous carbon nanocomposite coatings: from macro to the micro-scale, *Surface and Coatings Technology* 202 (2008) 4011-4018.
- [84] J. Sánchez-López, D. Martínez-Martínez, M. Abad, A. Fernández, Metal carbide/amorphous C-based nanocomposite coatings for tribological applications, *Surface and Coatings Technology* 204 (2009) 947-954.
- [85] D. Liu, L. Zheng, Y. Liang, H. Li, J. Liu, L. Luo, et al., Preparation, biocompatibility, and biotribological properties of TiN-incorporated graphite-like amorphous carbon bio-ceramic composite films, *Ceramics International* 44 (2018) 6810-6816.
- [86] D. Batory, M. Czerniak–Reczulska, L. Kolodziejczyk, W. Szymanski, Gradient titanium and silver based carbon coatings deposited on AISI316L, *Applied Surface Science* 275 (2013) 303-310.
- [87] C. Corbella, E. Bertran, M. Polo, E. Pascual, J. Andújar, Structural effects of nanocomposite films of amorphous carbon and metal deposited by pulsed-DC reactive magnetron sputtering, *Diamond and Related Materials* 16 (2007) 1828-1834.
- [88] J. Lancaster, A review of the influence of environmental humidity and water on friction, lubrication and wear, *Tribology International* 23 (1990) 371-389.

- [89] S.P. Ingole, P.L. Menezes, M. Nosonovsky, M.R. Lovell, S.V. Kailas, *Tribology for Scientists and Engineers: From Basics to Advanced Concepts*, Springer-Verlag: New York, 2013.
- [90] S. Rengifo, *A Comparison Between Graphene and WS<sub>2</sub> as Solid Lubricant Additives to Aluminum for Automobile Applications*, Master thesis, Florida International University, 2015.
- [91] Z. Rymuza, *Tribology of miniature systems*, Elsevier: North Holland, 1998.
- [92] M. Hoić, M. Hrgetić, J. Deur, Design of a pin-on-disc-type CNC tribometer including an automotive dry clutch application, *Mechatronics* 40 (2016) 220-232.
- [93] Z. Chen, J. Hillairet, V. Turq, Y. Song, Q. Yang, G. Lombard, et al., Multifunctional tribometer development and performance study of CuCrZr-316L material pair for ITER application, *Tribology International* 116 (2017) 208-216.
- [94] R.A. Nevshupa, M. Conte, A. Igartua, E. Roman, J.L. de Segovia, Ultrahigh vacuum system for advanced tribology studies: Design principles and applications, *Tribology International* 86 (2015) 28-35.
- [95] M. Kosinskiy, S.I.-U. Ahmed, Y. Liu, J.A. Schaefer, A compact reciprocating vacuum microtribometer, *Tribology International* 56 (2012) 81-88.
- [96] M. Hasler, K. Schindelwig, B. Mayr, C. Knoflach, S. Rohm, J. van Putten, et al., A Novel Ski–Snow Tribometer and its Precision, *Tribology Letters* 63 (2016) 33.
- [97] K. Kalita, N. Das, P. Boruah, U. Sarma, Design and Uncertainty Evaluation of a Strain Measurement System, *Journal of Metrology Society of India* 31 (2016) 17-24.
- [98] M. Gatzsche, N. Lücke, S. Großmann, T. Kufner, G. Freudiger, Validity of the voltage-temperature relation for contact elements in high power applications, Proc. IEEE 61st Holm Conference on Electrical Contact, San Diego, 2015.
- [99] D. Pavković, N. Kranjčević, M. Kostelac, Design of normal force control system for a pin-on-disk tribometer including active and passive suppression of vertical vibrations, *Automatika* 54 (2013) 364-375.
- [100] J.H. Z. Chen, DISPOSITIF DE MANOEUVRE D'UN ACTIONNEUR DISPOSE DANS UNE ENCEINTE FERMEE AU TRAVERS D'UNE PAROI DE L'ENCEINTE, French Patent 1000407060 (2017).
- [101] M. Rosol, A. Pilat, A. Turnau, Real-time controller design based on NI Compact-RIO, Proc. IMCSIT, Wisla, 2010.
- [102] V. Barabash, Summary of material data for structural analysis of the ITER vacuum vessel and ports, ITER Technical Report, ITER\_ D\_ 229D7N, Cadarache, 2008.

- [103] T. Nicholas, High cycle fatigue: a mechanics of materials perspective, Elsevier: Great Britain, 2006.
- [104] R.B. Sghaier, N. Majed, H.B. Dali, R. Fathallah, High cycle fatigue prediction of glass fiber-reinforced epoxy composites: reliability study, The International Journal of Advanced Manufacturing Technology (2017) 1-15.
- [105] V. Barabash, Appendix A, Materials Design Limit Data, ITER Technical Report, ITER\_D\_222RLN v3.3, Cadarache, 2013.
- [106] L. Doceul, C. Walker, C. Ingesson, E. Ciattaglia, P. Chappuis, C. Portafaix, et al., CEA engineering studies and integration of the ITER diagnostic port plugs, Fusion Engineering and Design 82 (2007) 1216-1223.
- [107] E.J. Wellauer, A. Seireg, Bending Strength of Gear Teeth by Cantilever-Plate Theory, J. Eng. Ind 82 (1960) 213-220.
- [108] M. Reichenbacher, J.W. Einax, Types of errors in instrumental analysis, Springer: Berlin Heidelberg, 2011.
- [109] J. Hillairet, A. Argouarch, R. Bamber, B. Beaumont, J.-M. Bernard, J.-M. Delaplanche, et al., R&D activities on RF contacts for the ITER ion cyclotron resonance heating launcher, Fusion Engineering and Design 96 (2015) 477-481.
- [110] S. Calatroni, R. Perret, W. Vollenberg, RF contacts for the LHC Collimators, Nuclear Instruments and Methods in Physics Research Section A: Accelerators, Spectrometers, Detectors and Associated Equipment 566 (2006) 205-211.
- [111] D. Ramos, Modeling of the RF-shield sliding contact fingers for the LHC cryogenic beam vacuum interconnects using implicit and explicit finite element formulations, Proc. EPAC, Genoa, 2008.
- [112] R.J.M. Konings, Comprehensive Nuclear Materials, Elsevier: Amsterdam, 2012.
- [113] L. Sun, N. Tao, K. Lu, A high strength and high electrical conductivity bulk CuCrZr alloy with nanotwins, Scripta Materialia 99 (2015) 73-76.
- [114] V. Barabash, Summary of material properties for structural analysis of the ITER internal components [Z], ITER Private Communications (2009).
- [115] G. Durashevich, V. Cvetkovski, V. Jovanovich, Effect of thermomechanical treatment on mechanical properties and electrical conductivity of a CuCrZr alloy, Bulletin of Materials Science 25 (2002) 59-62.
- [116] S. Wikman, A. Peacock, O. Zlamal, J. Öijerholm, S. Tähtinen, M. Rödiger, et al., Assessment of materials data for blanket materials within the European contribution to ITER, Journal of Nuclear Materials 442 (2013) 414-419.
- [117] A. Chatterjee, R. Mitra, A. Chakraborty, C. Rotti, K. Ray, Comparative study of

approaches to assess damage in thermally fatigued Cu Cr Zr alloy, *Journal of Nuclear Materials* 474 (2016) 120-125.

[118] R. Niranjana, R. Rout, R. Srivastava, Y. Chakravarthy, P. Mishra, T. Kaushik, et al., Surface modifications of fusion reactor relevant materials on exposure to fusion grade plasma in plasma focus device, *Applied Surface Science* 355 (2015) 989-998.

[119] C. Obitz, J. Öijerholm, S. Wikman, E. Bratu, Erosion corrosion of CuCrZr specimens exposed for simulated ITER operational conditions, *Nuclear Materials and Energy* 9 (2016) 261-266.

[120] L. Morgan, J. Shimwell, M. Gilbert, Isotopically enriched structural materials in nuclear devices, *Fusion Engineering and Design* 90 (2015) 79-87.

[121] Y. Birol, Thermal fatigue testing of CuCrZr alloy for high temperature tooling applications, *Journal of Materials Science* 45 (2010) 4501-4506.

[122] J.H. Zheng, W. Bogaerts, P. Lorenzetto, Erosion–corrosion tests on ITER copper alloys in high temperature water circuit with incident heat flux, *Fusion Engineering and Design* 61 (2002) 649-657.

[123] C. Shueh, C. Chan, C. Chang, I. Sheng, Investigation of vacuum properties of CuCrZr alloy for high-heat-load absorber, *Nuclear Instruments and Methods in Physics Research Section A: Accelerators, Spectrometers, Detectors and Associated Equipment* 841 (2017) 1-4.

[124] D.W. Lee, Y.D. Bae, S.K. Kim, S.H. Kim, B.G. Hong, I.C. Bang, Design evaluation of the semi-prototype for the ITER blanket first wall qualification, *Thin Solid Films* 518 (2010) 6676-6681.

[125] A. Argouarch, R. Bamber, B. Beaumont, J. Bernard, J. Delaplanche, F. Durodié, et al., RF contact development for the ITER ICRH antenna, *AIP Conference Proceedings* 1580 (2014).

[126] A. Argouarch, R. Bamber, J. Bernard, J. Delaplanche, F. Durodié, S. Larroque, et al., Steady state RF facility for testing ITER ICRH RF contact component, *Fusion Engineering and Design* 88 (2013) 1002-1006.

[127] J. Hillairet, Z. Chen, G. Lombard, J.M. Delaplanche, K. Vulliez, Q. Yang, et al., Radiofrequency and mechanical tests of silver coated CuCrZr contacts for the ITER ion cyclotron antenna, *Fusion Engineering and Design* 129 (2018) 29-39.

[128] L. Colas, S. Heuraux, S. Bremond, RF current distribution and topology of RF sheath potentials in front of ICRF antennae, *Nuclear Fusion* 45 (2005) 767-782.

[129] S.I. Hong, M.A. Hill, Mechanical stability and electrical conductivity of Cu–Ag filamentary microcomposites, *Materials Science and Engineering: A* 264 (1999) 151-158.

- [130] L. Zhang, L. Meng, Evolution of microstructure and electrical resistivity of Cu–12wt.% Ag filamentary microcomposite with drawing deformation, *Scripta Materialia* 52 (2005) 1187-1191.
- [131] A. Argouarch, Multilam Contact (LA-CUT/0.25/0 – copper/silver): Thermal conductance, CEA Technical Report, Cadarache, 2011.
- [132] R.F. Tylecote, The solid phase bonding of gold to metals, *Gold Bulletin* 11 (1978) 74-80.
- [133] G. Holmbom, B. Jacobson, J. Sundgren, Composition, Structure & Hardness of Pulse-plated Nickel-hardened Gold Films, Proc. of The AESF Annual Technical Conference. Baltimore, 1995.
- [134] N. Togasaki, Y. Okinaka, T. Homma, T. Osaka, Preparation and characterization of electroplated amorphous gold–nickel alloy film for electrical contact applications, *Electrochimica Acta* 51 (2005) 882-887.
- [135] L. Chalumeau, M. Wery, H. Ayedi, M. Chabouni, C. Leclere, Development of a new electroplating solution for electrodeposition of Au–Co alloys, *Surface and Coatings Technology* 201 (2006) 1363-1372.
- [136] P.G. Slade, *Electrical contacts: principles and applications*, CRC Press: Boca Raton, 2013.
- [137] T.Z.-i. hui, Z. LI Bin, Xiao-yun, L. Ming-hui, S.N.Z.-i. hua, Study of electroplating technology of Ag-Sb alloy coating, *Journal of Aeronautical Materials* 20 (2000) 78-83.
- [138] R. Rudolf, B. Budić, D. Stamenković, M. Čolić, A. Ivanič, B. Kosec, Rhodium platings–experimental study, *Metalurgija* 52 (2013) 337-340.
- [139] M.R. Pinnel, Diffusion-related behaviour of gold in thin film systems, *Gold Bulletin* 12 (1979) 62-71.
- [140] C. Huang, K. Li, W. Lin, M. Liao, The behavior of electroplated hard-chromium on Cr–Mo steel subject to long-term annealing at 250° C, *Materials Science and Engineering: A* 403 (2005) 222-226.
- [141] S. Kim, J. Yu, Recrystallization-induced void migration in electroplated Cu films, *Scripta Materialia* 67 (2012) 312-315.
- [142] J. Ballarre, E. Jimenez-Pique, M. Anglada, S.A. Pellice, A.L. Cavalieri, Mechanical characterization of nano-reinforced silica based sol–gel hybrid coatings on AISI 316L stainless steel using nanoindentation techniques, *Surface and Coatings Technology* 203 (2009) 3325-3331.
- [143] G. Cheng, X. Sun, Y. Wang, S.L. Tay, W. Gao, Nanoindentation study of electrodeposited Ag thin coating: An inverse calculation of anisotropic elastic-plastic

- properties, *Surface and Coatings Technology* 310 (2017) 43-50.
- [144] H.J. Fan, U. Gosele, M. Zacharias, *ChemInform Abstract: Formation of Nanotubes and Hollow Nanoparticles Based on Kirkendall and Diffusion Processes: A Review*, *Small* 3 (2010) 1660-1671.
- [145] M.Z. BUTT, *Review Solid-solution hardening*, *Journal of Materials Science* 28 (1993) 2557-2576.
- [146] T. Gladman, *Precipitation hardening in metals*, *Metal Science Journal* 15 (1999) 30-36.
- [147] K. Ansari, J.A. van Kan, A.A. Bettioli, F. Watt, *Stamps for nanoimprint lithography fabricated by proton beam writing and nickel electroplating*, *Journal of Micromechanics and Microengineering* 16 (2006) 1967-1974.
- [148] T. Kizuka, H. Ichinose, Y. Ishida, *Structure and hardness of nanocrystalline silver*, *Journal of Materials Science* 32 (1997) 1501-1507.
- [149] Z. Dongming, S. Uwe, *Advanced Ceramic Coatings and Interfaces*, John Wiley & Sons: New Jersey, 2007.
- [150] S. Zhou, X. Zeng, Q. Hu, Y. Huang, *Analysis of crack behavior for Ni-based WC composite coatings by laser cladding and crack-free realization*, *Applied Surface Science* 255 (2008) 1646-1653.
- [151] <https://imagej.net/Welcome>.
- [152] K.W. Schlichting, N. Padture, E. Jordan, M. Gell, *Failure modes in plasma-sprayed thermal barrier coatings*, *Materials Science and Engineering: A* 342 (2003) 120-130.
- [153] D.R. Economy, M.J. Cordill, E.A. Payzant, M.S. Kennedy, *Residual stress within nanoscale metallic multilayer systems during thermal cycling*, *Materials Science and Engineering: A* 648 (2015) 289-298.
- [154] K. Khor, Y. Gu, *Effects of residual stress on the performance of plasma sprayed functionally graded ZrO<sub>2</sub>/NiCoCrAlY coatings*, *Materials Science and Engineering: A* 277 (2000) 64-76.
- [155] S. Widjaja, A.M. Limarga, T.H. Yip, *Modeling of residual stresses in a plasma-sprayed zirconia/alumina functionally graded-thermal barrier coating*, *Thin Solid Films* 434 (2003) 216-227.
- [156] A. Belahmar, A. Chouiyakh, *Sputtering Synthesis and Thermal Annealing Effect on Gold Nanoparticles in Al<sub>2</sub>O<sub>3</sub> Matrix*, *Journal of Nanoscience and Technology* (2016) 100-103.
- [157] V. Belous, G. Kalinin, P. Lorenzetto, S. Velikopolskiy, *Assessment of the*

corrosion behaviour of structural materials in the water coolant of ITER, *Journal of Nuclear Materials* 258 (1998) 351-356.

[158] M. Bezzazi, A. Khamlichi, A. Jabbouri, P. Reis, J. Davim, Experimental characterization of frictional behaviour of clutch facings using Pin-on-disk machine, *Materials & Design* 28 (2007) 2148-2153.

[159] S. Islam, R.N. Ibrahim, Mechanism of abrasive wear in nanomachining, *Tribology Letters* 42 (2011) 275-283.

[160] T. Kayaba, K. Hokkirigawa, K. Kato, Analysis of the abrasive wear mechanism by successive observations of wear processes in a scanning electron microscope, *Wear* 110 (1986) 419-430.

[161] S. Jahanmir, N. Suh, E. Abrahamson, Microscopic observations of the wear sheet formation by delamination, *Wear* 28 (1974) 235-249.

[162] D.H. Buckley, *Surface effects in adhesion, friction, wear, and lubrication*, Elsevier 1981.

[163] J. Xu, L. Chai, L. Qiao, T. He, P. Wang, Influence of C dopant on the structure, mechanical and tribological properties of rf-sputtered MoS<sub>2</sub>/a-C composite films, *Applied Surface Science* 364 (2016) 249-256.

[164] M. Čekada, P. Panjan, D. Kek-Merl, M. Panjan, G. Kapun, SEM study of defects in PVD hard coatings, *Vacuum* 82 (2007) 252-256.

[165] P.E. Hovsepian, A. Ehiasarian, Y. Purandare, B. Biswas, F. Pérez, M. Lasanta, et al., Performance of HIPIMS deposited CrN/NbN nanostructured coatings exposed to 650 °C in pure steam environment, *Materials Chemistry and Physics* 179 (2016) 110-119.

[166] E.O. Arregui, M. Caro, A. Caro, Numerical evaluation of the exact phase diagram of an empirical Hamiltonian: Embedded atom model for the Au-Ni system, *Physical Review B* 66 (2002) 054201.

[167] Z. Yang, D.J. Lichtenwalner, A.S. Morris, J. Krim, A.I. Kingon, Comparison of Au and Au–Ni alloys as contact materials for MEMS switches, *Journal of Microelectromechanical Systems* 18 (2009) 287-295.

[168] L. Dubrovinsky, N. Dubrovinskaia, W. Crichton, A.S. Mikhaylushkin, S. Simak, I. Abrikosov, et al., Noblest of all metals is structurally unstable at high pressure, *Physical Review Letters* 98 (2007) 045503.

[169] X. Huang, S. Li, Y. Huang, S. Wu, X. Zhou, S. Li, et al., Synthesis of hexagonal close-packed gold nanostructures, *Nature Communications* 2 (2011) 292.

[170] B.R. Jany, N. Gauquelin, T. Willhammar, M. Nikiel, K. Van den Bos, A. Janas, et al., Controlled growth of hexagonal gold nanostructures during thermally induced

- self-assembling on Ge (001) surface, *Scientific Reports* 7 (2017) 42420.
- [171] R.J. Yeo, *Overview of Amorphous Carbon Films*, Springer: Singapore, 2017.
- [172] L. Gu, P. Ke, Y. Zou, X. Li, A. Wang, Amorphous self-lubricant MoS<sub>2</sub>-C sputtered coating with high hardness, *Applied Surface Science* 331 (2015) 66-71.
- [173] P.K. Chu, L. Li, Characterization of amorphous and nanocrystalline carbon films, *Materials Chemistry and Physics* 96 (2006) 253-277.
- [174] P. Mandal, A.P. Ehiasarian, P.E. Hovsepian, Lubricated sliding wear mechanism of chromium-doped graphite-like carbon coating, *Tribology International* 77 (2014) 186-195.
- [175] A.C. Ferrari, J. Robertson, Interpretation of Raman spectra of disordered and amorphous carbon, *Physical Review B* 61 (2000) 14095.
- [176] F. Zhou, K. Fu, B. Liao, J. Yu, C. Yang, X. Zhang, Effect of carbon content on nanostructural, mechanical and electrochemical characteristics of self-organized nc-ZrCN/a-CN x nanocomposite films, *Applied Surface Science* 327 (2015) 350-357.
- [177] V. Teixeira, Residual stress and cracking in thin PVD coatings, *Vacuum* 64 (2002) 393-399.
- [178] T.C. Totemeier, J. Wright, Residual stress determination in thermally sprayed coatings—a comparison of curvature models and X-ray techniques, *Surface and Coatings Technology* 200 (2006) 3955-3962.
- [179] P. Kadolkar, T.R. Watkins, J.T.M. De Hosson, B. Kooi, N.B. Dahotre, State of residual stress in laser-deposited ceramic composite coatings on aluminum alloys, *Acta Materialia* 55 (2007) 1203-1214.
- [180] F. Mao, M. Taher, O. Kryshnal, A. Kruk, A. Czyrska-Filemonowicz, M. Ottosson, et al., Combinatorial study of gradient Ag–Al thin films: microstructure, phase formation, mechanical and electrical properties, *ACS Applied Materials & Interfaces* 8 (2016) 30635-30643.
- [181] Z. Chen, J. Hillairet, V. Turq, Y. Song, R. Laloo, J. Bernard, et al., Characterizations of thermal stability and electrical performance of Au-Ni coating on CuCrZr substrate for high vacuum radio-frequency contact application, *Thin Solid Films* 659 (2018) 81-88.
- [182] Y. Wang, J. Li, C. Dang, Y. Wang, Y. Zhu, Influence of carbon contents on the structure and tribocorrosion properties of TiSiCN coatings on Ti6Al4V, *Tribology International* 109 (2017) 285-296.
- [183] Y.-C. Huang, S.-Y. Chang, C.-H. Chang, Effect of residual stresses on mechanical properties and interface adhesion strength of SiN thin films, *Thin Solid Films* 517 (2009) 4857-4861.

- [184] Z. Zhou, K. Li, I. Bello, C. Lee, S. Lee, Study of tribological performance of ECR-CVD diamond-like carbon coatings on steel substrates: Part 2. The analysis of wear mechanism, *Wear* 258 (2005) 1589-1599.
- [185] M.R. Gilbert, J.C. Sublet, Neutron-induced transmutation effects in W and W-alloys in a fusion environment, *Nuclear Fusion* 51 (2011) 043005.
- [186] C. Lin, C. Lee, F. Chen, W. Li, Structural evolution and internal stress of nickel-phosphorus electrodeposits, *Journal of the Electrochemical Society* 152 (2005) 370-375.
- [187] Y. Tsuru, M. Nomura, F. Foulkes, Effects of chloride, bromide and iodide ions on internal stress in films deposited during high speed nickel electroplating from a nickel sulfamate bath, *Journal of Applied Electrochemistry* 30 (2000) 231-238.
- [188] T. Fritz, H. Cho, K. Hemker, W. Mokwa, U. Schnakenberg, Characterization of electroplated nickel, *Microsystem Technologies* 9 (2002) 87-91.
- [189] F. Kopnov, A. Yoffe, G. Leitus, R. Tenne, Transport properties of fullerene - like WS<sub>2</sub> nanoparticles, *Physica Status Solidi (b)* 243 (2006) 1229-1240.
- [190] N. Zhou, S. Wang, F.C. Walsh, Effective particle dispersion via high-shear mixing of the electrolyte for electroplating a nickel-molybdenum disulphide composite, *Electrochimica Acta* 283 (2018) 568-577.
- [191] M. Rezrazi, M. Doche, P. Bercot, J. Hihn, Au-PTFE composite coatings elaborated under ultrasonic stirring, *Surface and Coatings Technology* 192 (2005) 124-130.
- [192] R. Mardani, A. Asrar, H. Ershadifar, The effect of surfactant on the structure, composition and magnetic properties of electrodeposited CoNiFe/Cu microwire, *Materials Chemistry and Physics* 211 (2018) 160-167.
- [193] R. Stavitsky, Electroless gold plating solutions, Kanto Chemical Co Inc, US Patent, 1990.
- [194] X. Qi, Y.n. Dong, H. Wang, C. Wang, F. Li, Application of Turbiscan in the homoaggregation and heteroaggregation of copper nanoparticles, *Colloids and Surfaces A: Physicochemical and Engineering Aspects* 535 (2017) 96-104.
- [195] C. Delgado-Sánchez, V. Fierro, S. Li, A. Pasc, A. Pizzi, A. Celzard, Stability analysis of tannin-based foams using multiple light-scattering measurements, *European Polymer Journal* 87 (2017) 318-330.
- [196] Y. Ren, J. Zheng, Z. Xu, Y. Zhang, J. Zheng, Application of Turbiscan LAB to study the influence of lignite on the static stability of PCLWS, *Fuel* 214 (2018) 446-456.
- [197] Q.-A. Poutrel, Z. Wang, D. Wang, C. Soutis, M. Gresil, Effect of pre and

post-dispersion on electro-thermo-mechanical properties of a graphene enhanced epoxy, *Applied Composite Materials* 24 (2017) 313-336.

[198] K. Nayana, T. Venkatesha, Synergistic effects of additives on morphology, texture and discharge mechanism of zinc during electrodeposition, *Journal of Electroanalytical Chemistry* 663 (2011) 98-107.

[199] A. Gomes, M. da Silva Pereira, Pulsed electrodeposition of Zn in the presence of surfactants, *Electrochimica Acta* 51 (2006) 1342-1350.

[200] N. Loukil, M. Feki, Synergistic effect of triton X100 and 3-hydroxybenzaldehyde on Zn-Mn electrodeposition from acidic chloride bath, *Journal of Alloys and Compounds* 719 (2017) 420-428.

[201] H. Wang, Dispersing carbon nanotubes using surfactants, *Current Opinion in Colloid & Interface Science* 14 (2009) 364-371.

[202] R. Rastogi, R. Kaushal, S. Tripathi, A.L. Sharma, I. Kaur, L.M. Bharadwaj, Comparative study of carbon nanotube dispersion using surfactants, *Journal of Colloid and Interface Science* 328 (2008) 421-428.

[203] Y. Geng, M.Y. Liu, J. Li, X.M. Shi, J.K. Kim, Effects of surfactant treatment on mechanical and electrical properties of CNT/epoxy nanocomposites, *Composites Part A: Applied Science and Manufacturing* 39 (2008) 1876-1883.

[204] B. Valaulikar, C. Manohar, The mechanism of clouding in triton X-100: the effect of additives, *Journal of Colloid and Interface Science* 108 (1985) 403-406.

[205] Z. Wang, J.-H. Xu, W. Zhang, B. Zhuang, H. Qi, Cloud point of nonionic surfactant Triton X-45 in aqueous solution, *Colloids and Surfaces B: Biointerfaces* 61 (2008) 118-122.

[206] J. Schroers, B. Lohwongwatana, W.L. Johnson, A. Peker, Precious bulk metallic glasses for jewelry applications, *Materials Science and Engineering: A* 449 (2007) 235-238.

[207] A. Bauer, E.L. Gyenge, C.W. Oloman, Electrodeposition of Pt–Ru nanoparticles on fibrous carbon substrates in the presence of nonionic surfactant: application for methanol oxidation, *Electrochimica Acta* 51 (2006) 5356-5364.

[208] S. Jo, D. Costanzo, H. Berger, A.F. Morpurgo, Electrostatically induced superconductivity at the surface of WS<sub>2</sub>, *Nano Letters* 15 (2015) 1197-1202.

[209] S.P. Vattikuti, C. Byon, V. Chitturi, Selective hydrothermally synthesis of hexagonal WS<sub>2</sub> platelets and their photocatalytic performance under visible light irradiation, *Superlattices and Microstructures* 94 (2016) 39-50.

[210] E. García-Lecina, I. García-Urrutia, J. Díez, J. Fornell, E. Pellicer, J. Sort, Codeposition of inorganic fullerene-like WS<sub>2</sub> nanoparticles in an electrodeposited

nickel matrix under the influence of ultrasonic agitation, *Electrochimica Acta* 114 (2013) 859-867.

[211] X.J. Liu, F. Gao, C.P. Wang, K. Ishida, Thermodynamic assessments of the Ag-Ni binary and Ag-Cu-Ni ternary systems, *Journal of Electronic Materials* 37 (2008) 210-217.

[212] J. Zhong, L. Zhang, Z. Jin, M. Sui, K. Lu, Superheating of Ag nanoparticles embedded in Ni matrix, *Acta Materialia* 49 (2001) 2897-2904.

[213] Q. Liu, C. Wang, W. Zhang, G. Wang, Immiscible silver–nickel alloying nanorods growth upon pulsed-laser induced liquid/solid interfacial reaction, *Chemical Physics Letters* 382 (2003) 1-5.

[214] U. Mizutani, *Introduction to the electron theory of metals*, Cambridge University Press: Cambridge, 2001.

## Appendix A: HV-MTEST Plotting Methods

On HV-MTEST facility, as the stroke of one cycle is 16mm and 0.5s acquisition time is used, which means that there are 32 data points per stroke. When the friction coefficient and contact resistance are being plotted with the sliding cycles, there are two proper techniques: do the average of the 32 points or choose the maximum value.

On HV-MTEST, when the samples that are being tested have slight wear phenomenon, the output from the system looks like Figure1. In that case, the average of one cycle is similar to the maximum value during this step.

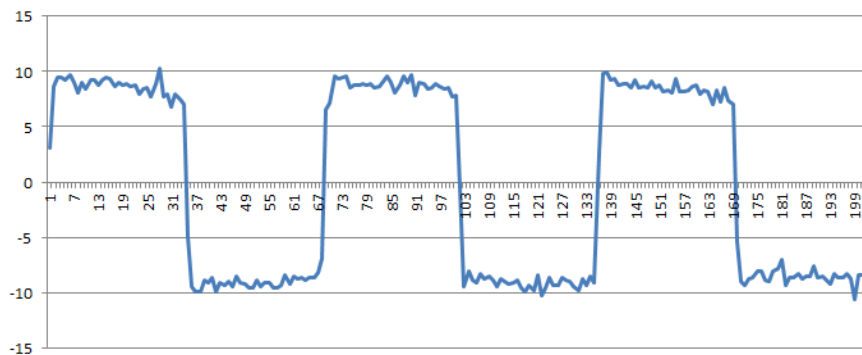


Figure1. HV-MTEST strain output signal with slight wear

However, when the wear phenomenon tends to serious, the output from the system looks like Figure 2, the average can't reveal the true friction phenomenon during this cycle.

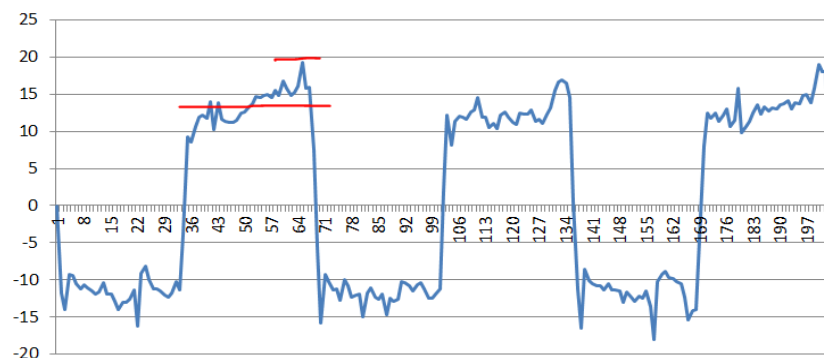


Figure 2. HV-MTEST strain output signal with severe wear

Although the maximum value only happens in short time during the whole cycle, from engineering point of view, choosing the maximum value is more meaningful compared with the averaged value which can guarantee the safety margin of design based on this parameter.

For the contact resistance, as we used the compensation function of the Keithley

DMM7510 facility, which calculates the thermal potential between the contact objectives and gets rid of it from the measurement results during the sliding. So there are obvious noises existing and sometimes minus resistance observed which is not realistic. So, for the plotting of contact resistance, the averaged value per step (32 points) was used which can impair the effects of the noises.

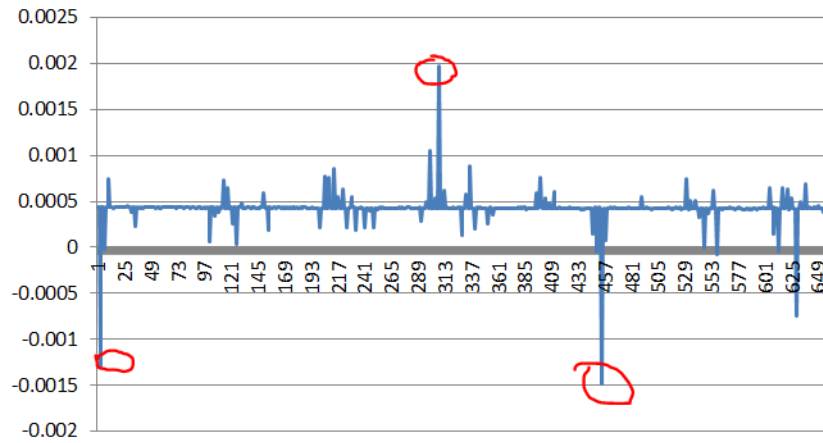


Figure 3. HV-MTEST contact resistance output signal

## Appendix B: Binary phase diagram

### ➤ Ni-Cu phase diagram

The Cu-Ni and binary phase diagram is the simplest type of binary phase diagrams for two metals. Due to the similar atom radius ( $R_{\text{Cu}} = 0.128 \text{ nm}$ ,  $R_{\text{Ni}} = 0.125 \text{ nm}$ ), the same crystal structure (face-centered cubic crystal) and similar electronegativity (Cu: 1.9, Ni: 1.8), Cu and Ni are mutually soluble even at room temperature throughout the entire range of compositions.

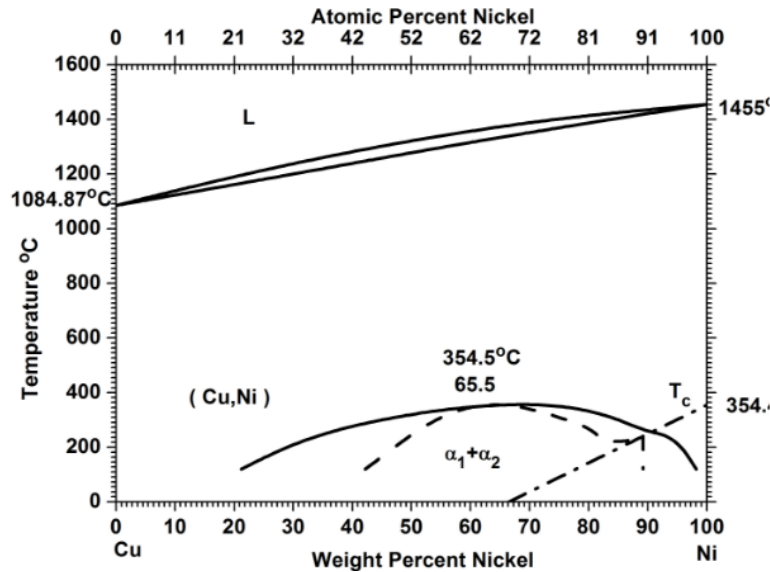


Figure 1 Cu-Ni binary alloy phase diagram

### ➤ Ni-Ag phase diagram

As for the Ag–Ni binary system, their phase diagram shows that there is a eutectic reaction  $[L \rightarrow \text{fcc}(\text{Ni}) + \text{fcc}(\text{Ag})]$  at  $960^\circ\text{C}$  and a monotectic reaction  $[L1 \rightarrow \text{fcc}(\text{Ni}) + L2]$  at  $1435^\circ\text{C}$  [211]. Both Ag and Ni are of fcc structure and with similar atom radius, so the lattice mismatch between Ag and Ni is only 16%. However, the solubility of Ni in Ag is very small, only about 0.2 at.% even at the thermodynamic equilibrium melting point of Ag [212]. Silver with high content of Ni is usually obtained by using powder alloying with the process of pressing or sintering and  $\text{Ag}_{80}\text{Ni}_{20}$  was successfully obtained by using laser ablation[213].

Alloy deposition can deposit with properties not obtained by employing electrodeposition of single metals. They can be denser, harder, more corrosion resistant and more wear resistant. Even though the metals are not mutually soluble in the solid state based on their phase diagram, the metals can be co-deposited at low polarization values, the formation of solid solutions or supersaturated solid solutions alloys [25]. In order to obtain the metal alloy, one of the important preconditions is

that the alloy elements should have the same or nearly the same individual deposition potentials. As the standard electrode potentials of Ag and Ni are +0.799 V and -0.257 V respectively, the co-electroplating of Ag-Ni is very difficult.

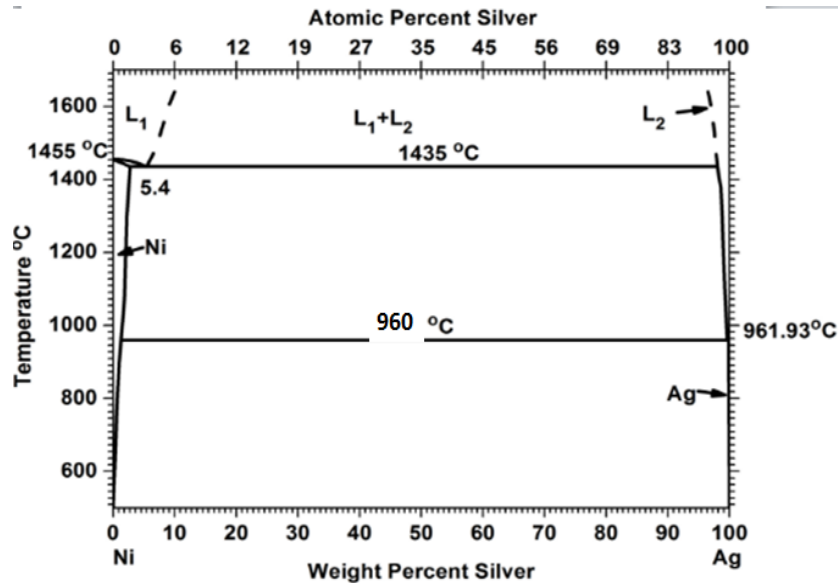


Figure 2 Ag-Ni binary alloy phase diagram

➤ Au-Ni phase diagram

Adhesive wear is one of the main disadvantages of gold coatings intended for sliding contact applications. It can be overcome by alloying gold with other elements such as Ni, Co, Cd, Sb, Cu, Ag and Pd. The introduction of small additives (tenth of percent) of nickel into gold, for example, increases the coating hardness several times. Also, it was shown that alloying reduces the grain size by one or two orders of magnitude, i.e., from 1–100 to 0.01 mm. Here in this study, we chose Ni as the co-alloying element in Au.

Although gold and nickel have the same crystal structure (fcc structure) and they can form a continuous solid solution under relatively high temperature. However, based on the Au-Ni binary phase diagram there is nearly no solid solubility over the entire range of composition under the temperature lower than 200°C. Moreover, the fast decrease of the solid solubility at lower temperatures leads to the decomposition of the single-phase bimetal into two face-centered cubic solid solutions.

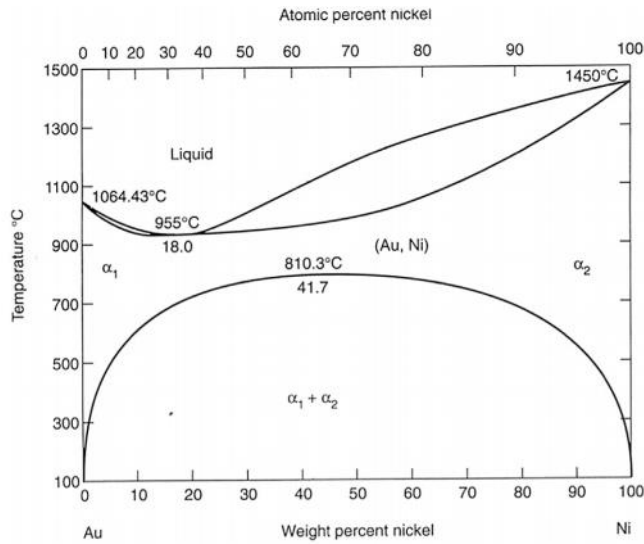


Figure 3 Au-Ni binary alloy phase diagram

➤ Au-Cu phase diagram

With the content of Cu increase, the melting points of the alloy decrease. And with 44 at.% of Cu inside the melting point of the alloy reaches to the minimum and then increase again with the increase of the Cu content. In Au-Cu alloys, when the temperature is higher than 410°C, Cu atoms can randomly substitute in the solid phase for Au atoms at all concentrations and generate disordered fcc crystal. Even though the Au and Cu atoms still occupy the lattice sites as original periodic crystal lattice, the conduction electrons are scattered because the periodic potential is disturbed by the random occupation [214]. Under low temperature, the solid solution will turn from disordered to few ordered intermetallic compounds ( $\text{Au}_3\text{Cu}$ ,  $\text{AuCuI}$ ,  $\text{AuCuII}$ ,  $\text{AuCu}_3\text{I}$  and  $\text{AuCu}_3\text{II}$ ).

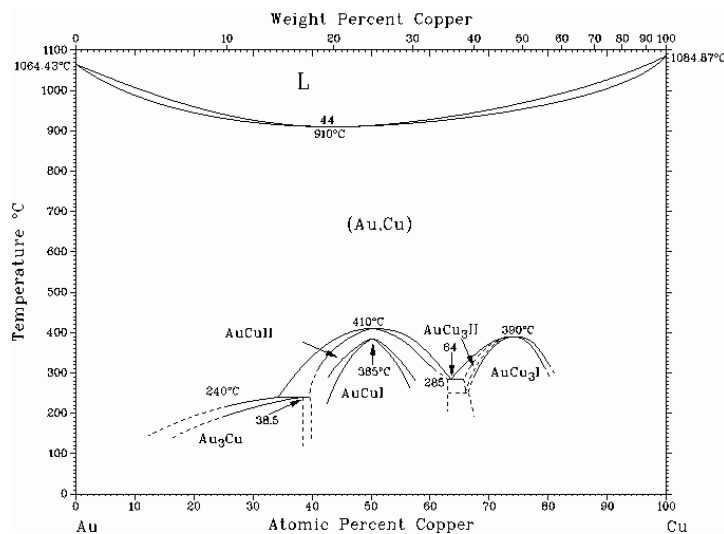


Figure 4 Au-Cu binary alloy phase diagram

➤ Rh-Cu phase diagram

The Cu–Rh phase diagram indicates a peritectic reaction at 1100°C which suggests that a single phase exists in Cu–Rh alloys at 25°C as primary solid solution of  $\alpha$ -CuRh between 0 and 20 at.% Rh and  $\alpha$ -RhCu between 90 and 100 at.% Rh. The alloys of intermediate compositions are two-phase mixtures of  $\alpha$ -CuRh and  $\alpha$ -RhCu.

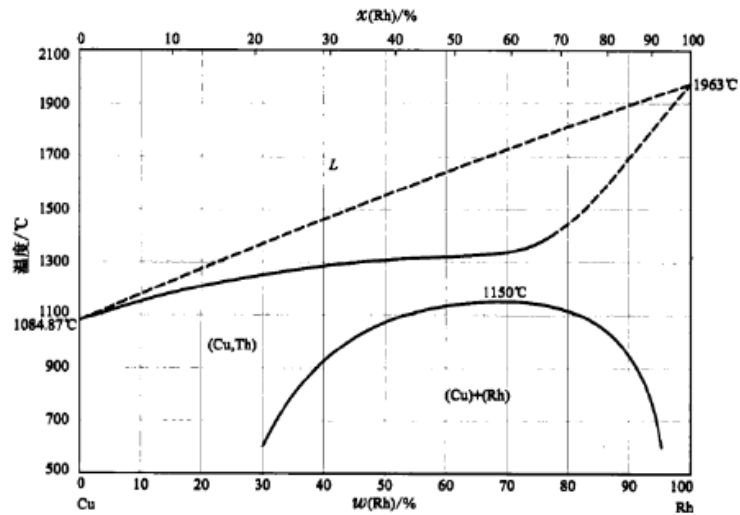


Figure 5 Rh-Cu binary alloy phase diagram

➤ Rh-Au phase diagram

From the Rh-Au binary diagram, it shows that Au and Rh are immiscible in almost the entire composition range. The Au-Rh system can form an fcc solid solution with a maximum Rh solubility of 1.6 at.% in Au and only 0.5 at.% Au in Rh. The low miscibility of Au and Rh especially under low temperature indicates that, the diffusion resistivity of the Au-Rh pair should be high,

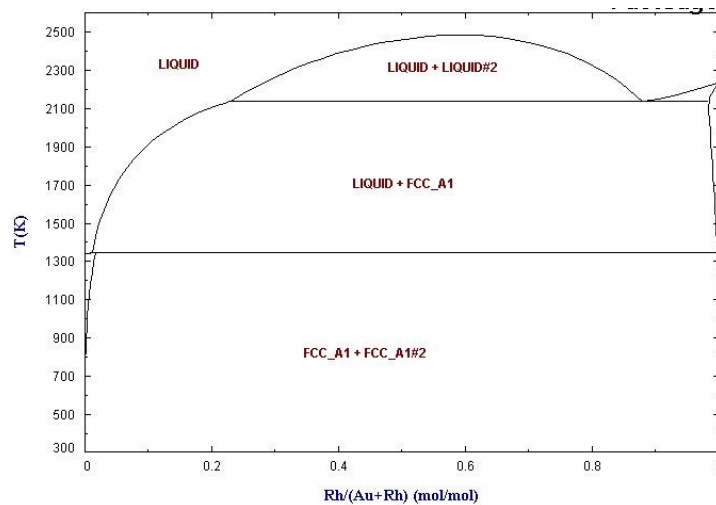


Figure 6 Rh-Au binary alloy phase diagram

➤ Rh-Ag phase diagram

The solid solubility of Rh in Ag is very small and before reaching the melting of silver, there is almost no Rh solute inside. However, the solid solubility of Ag in Rh is much higher and the maximum is about 10 at.%.

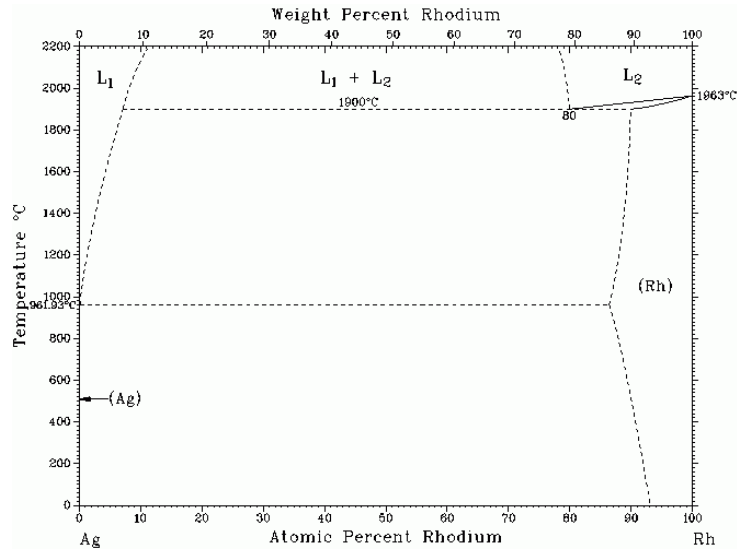


Figure 7 Rh-Ag binary alloy phase diagram

➤ Cu-Ag phase diagram

Although Cu and Ag seem to follow the Hume-Rothery rules, Figure 8 shows that they do not form a complete solid solution. The critical difference is that their atomic radii are not that similar.

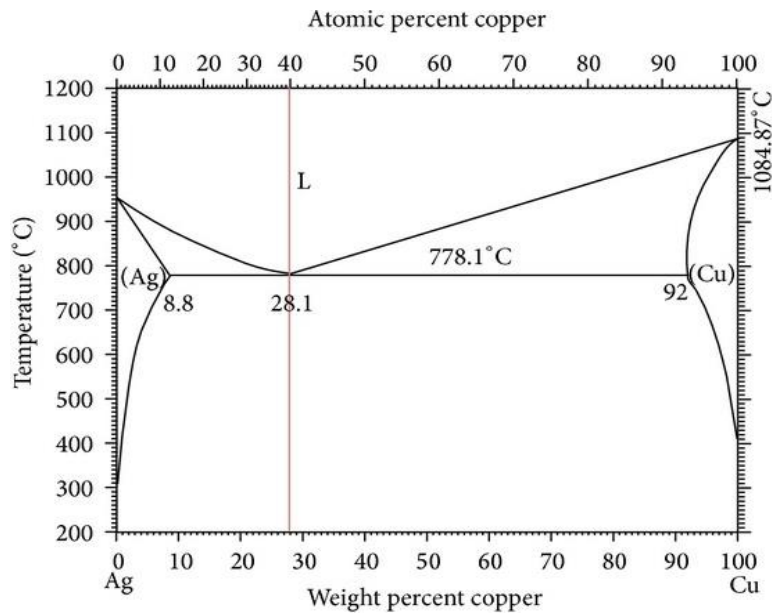


Figure 8 Cu-Ag binary alloy phase diagram



## Appendix C: Investigation of the generation of the top layer

The cross-sectional surface of the Au-Co/WS<sub>2</sub> was prepared by using cross-polisher. When the cross-sectional sample prepared, a top layer was observed on the coating surface (Figure 1). The compositions of this top layer was studied by using EDS (Figure 2), which shows that the top layer is composed of Au, Cu and Ni.

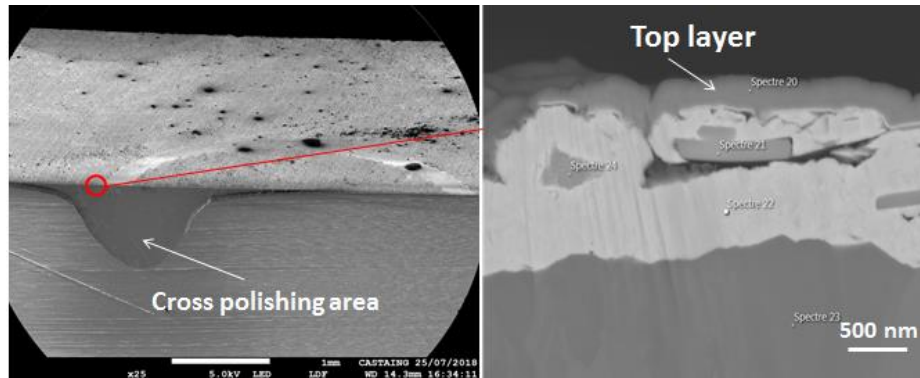


Figure 1: Cross-polishing area and top layer on the coating

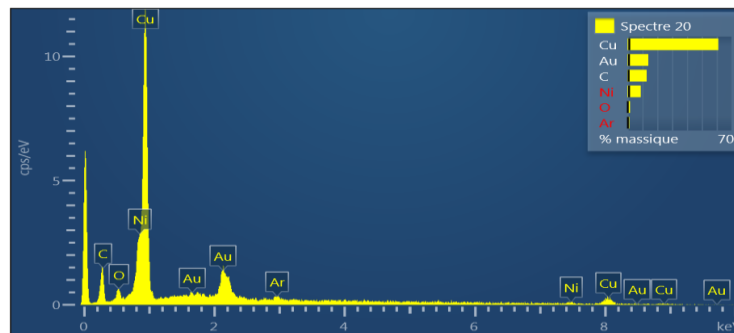


Figure 2: EDS result of top layer

In order to make sure that this top layer was generated during the cross-polishing process other than electrodeposition process (due to the pollution of the Au-Co electrolyte), a further investigation was performed. As shown in Figure 3, by checking the top surface of the cross-polished sample, very different EDS results were obtained between the areas near to the cross-polishing surface and far from the cross-polishing surface. Near to the cross-polishing surface, there is a high content of Cu in the coating, however, there is no copper observed in the coating far from the cross-polishing surface. In a word, the top layer is generated due to the deposition (PVD deposition) during cross-polishing process, other than during electroplating process.

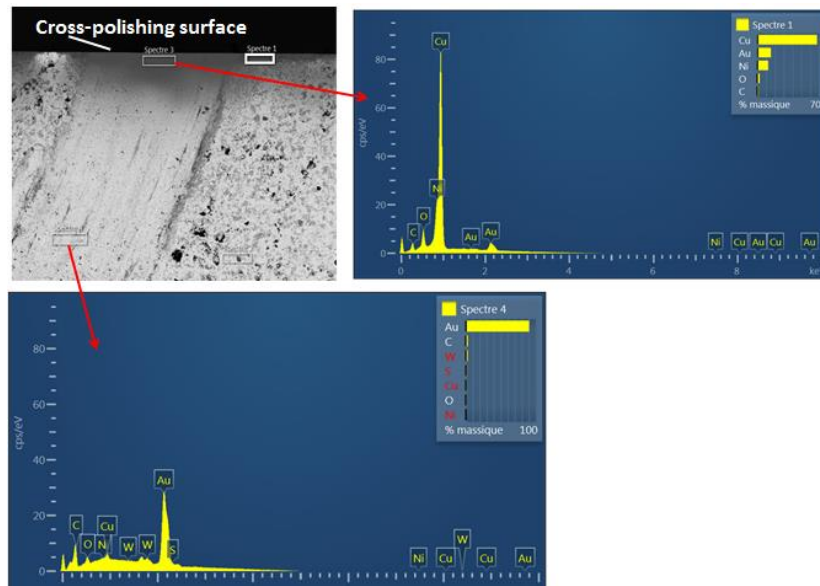


Figure 3: SEM and EDS results of cross-polished sample

### **Publications:**

- [1] Z. Chen, J. Hillairet, V. Turq, Y. Song, Q. Yang, G. Lombard, et al., Multifunctional tribometer development and performance study of CuCrZr-316L material pair for ITER application, *Tribology International* 116 (2017) 208-216.
- [2] Z. Chen, J. Hillairet, V. Turq, Y. Song, R. Laloo, K. Vulliez, et al., Multi-physics modeling and Au-Ni/Rh coating assessment for ITER ion cyclotron resonance heating radio-frequency sliding contacts, *Electrical Contacts, 2017 IEEE Holm Conference on Electrical Contact, 2017*, 26-33.
- [3] Z. Chen, J. Hillairet, V. Turq, Y. Song, R. Laloo, J. Bernard, et al., Characterizations of thermal stability and electrical performance of Au-Ni coating on CuCrZr substrate for high vacuum radio-frequency contact application, *Thin Solid Films* 659(2018), 81-88.
- [4] Z. Chen, J. Hillairet, V. Turq, Y. Song, R. Laloo, K. Vulliez, et al., Study of thermal ageing effects on Rh coating's mechanical performance upon CuCrZr substrate through modeling and experimental methods, *Vacuum* 154 (2018), 227-234.
- [5] J. Hillairet, Z. Chen, G. Lombard, J. Delaplanche, K. Vulliez, Q. Yang, et al., Radiofrequency and mechanical tests of silver coated CuCrZr contacts for the ITER ion cyclotron antenna, *Fusion Engineering and Design* 129 (2018) 29-39.

### **Patent:**

- [1]. Zhaoxi Chen, Julien Hillairet, DISPOSITIF DE MANOEUVRE D'UN ACTIONNEUR DISPOSE DANS UNE ENCEINTE FERMEE AU TRAVERS D'UNE PAROI DE L'ENCEINTE, French invention patent 1000407060 (granted)